The Smart Rotor Concept on Wind Turbines

Actuators and Structures

Proefschrift

ter verkrijging van de graad van doctor
aan de Technische Universiteit Delft,
op gezag van de Rector Magnificus prof.ir. K.C.A.M. Luyben,
voorzitter van het College voor Promoties,
in het openbaar te verdedigen op vrijdag 11 november 2011 om 15.00 uur

door

Anton Werner HULSKAMP

Werktuigbouwkundig ingenieur,
geboren te Amsterdam

Dit proefschrift is goedgekeurd door de promotoren:
Prof. ir. A. Beukers
Prof. dr. ir. G.A.M. van Kuik

Copromotor:
Dr. ir. H.E.N. Bersee

Samenstelling promotiecommissie:

Rector Magnificus,	Voorzitter
Prof. ir. A. Beukers,	Technische Universiteit Delft, promotor
Prof. dr. ir. G.A.M. van Kuik,	Technische Universiteit Delft, promotor
Dr. ir. H.E.N. Bersee,	Technische Universiteit Delft, copromotor
Prof. Dr.-Ing. T. Bein,	Fraunhofer-Gesellschaft, Duitsland
Prof. dr. D.A. Saravanos,	University of Patras, Griekenland
Prof. dr. O.T. Thomsen,	Aalborg University, Denemarken
Prof. dr. M. Verhaegen,	Technische Universiteit Delft
Prof. dr. G.J.W. van Bussel,	Technische Universiteit Delft, reservelid

This research was carried out within the Delft Univeristy's wind energy institute DUWIND, sponsored by the European Commission's FP6 program UpWind, project reference 019945 (SES6)

ISBN 978-90-8891-341-9

Cover design: A.W. Hulskamp
Photography: A.W. Hulskamp, T. Barlas, J.W. van Wingerden and R. Garritsen

Printed in the Netherlands by BOXPress

Voor Claartje en Ton

Summary

In this thesis the structural and actuator issues concerning the implementation of a smart rotor on wind turbines are addressed. Wind turbines convert the kinetic energy in the wind into mechanical torque, but this process is all but constant. Due to for instance changes in inflow, gravity and wave loading on off-shore turbines, there are heavy load fluctuations on the machines, causing fatigue issues.

The smart rotor system is a concept by which, through spanwise distributed devises, such as flaps or tabs, the way the flow around the blade is converted into mechanical loading can be controlled. Current dynamic load alleviation mainly involves pitching the whole blade which puts a very heavy strain on the pitch system if it would have to be done continuously. Controlling the aerodynamics at different spanwise positions, on the other hand, is very elegant because it enables controlling the loads locally. In the research that this thesis is a part of, it is studied how such a system should be implemented and how it would affect the performance of the turbine.

It was decided to base the actuator on so called smart materials because these provide a very high power density and can be applied throughout the structure, limiting the impact of partial failure. Moreover, by applying these materials to turbine skins, morphing surfaces can be obtained. A morphing surface has several advantages over rigid, hinged control surfaces from an aerodynamic point of view since, for instance, morphing flaps go into stall at higher flap angles and produce less noise and drag than their rigid counterparts.

In Chapter 2 an overview of 'smart' aerodynamic load control concepts on aircraft wings and helicopter rotors is presented, as well as the current state of the art in proposed load control devices and concepts for wind turbine rotor blades. Additionally, a spoiler flap concept is presented of which the aerodynamics are analysed using 2D, steady state CFD calculations. The calculations show that a ΔC_L of ± 0.1 is attainable with only a flap deflection of 2% of the chord. Also in Chapter 2 an overview of the demands for smart rotor systems in terms of speed, deflection and size is provided.

For the actuation speed two ranges are considered: a small one, covering the low frequency, but high load spectrum up to 1.4Hz and a range up to 12Hz which covers nearly all disturbances.

For creating an active, morphing load control surface two materials are specifically under investigation, which are Shape Memory Alloys (SMAs) and piezoelectric ceramic based materials. They are selected because they provide the highest power density and the highest Technology Readiness Level (TRL). SMAs derive their actuator function from a temperature driven, reversible phase transformation. The material can be deformed heavily at lower temperatures and this deformation will start to be recovered once the material is heated above a certain temperature threshold. In this process, not only large deformations can be recovered, but also large forces are exerted by the SMA material if the recovery is restrained. However, the material's response is highly non-linear. Piezoelectrics, on the other hand, are driven by an electric field. Typical piezoelectric ceramics will strain around $\sim$0.1% under a field of $\sim$1MV/m. The maximum deformation is much less than the shape memory alloy, but the material can undergo this actuation cycles at very high frequencies. Moreover, the response is much more linear. However, it is decided to continue with SMAs to develop an actuator on because its specific force, displacement and actuation speed characteristics are very suitable for load control surfaces on wind turbines. In Chapter 3 the functionality of SMAs, piezoelectrics and other adaptive materials is discussed.

First the feasibility of the smart rotor concept is investigated in a series of wind tunnel experiments. The experiments indicate that the interaction between the disturbance spectrum and the dynamic modes of the blade is important to take into account. The non-rotating experiments show that transient loads as a result of a step on the angle of attack can be controlled. For the rotating experiments, the dynamic behaviour of the blade was taken into account in the system design and up to 60% of dynamic load reduction was observed.

Then the focus shifts towards the development of a morphing load control surface, dedicated to MW-sized turbines. In Chapter 5 a series of measurement on a specific alloy is performed to provide a full overview of the wire behaviour and to compare testing measurement methods. Infra Red (IR) camera measurements prove to be inaccurate but for non-quasi-static temperature measurements, it is the only available method. The wire that is to be used, a SmartFlex 0.4mm diameter, shows very stable behaviour with comparable Clausius Clapeyron constants to a generic NiTi wire. However, the transition band is rather narrow, which limits the controllability in

certain set-ups because the wire goes through the transition very fast.

In the subsequently Chapter 6 this wire is used in a newly developed actuator. The actuator is aimed at increasing the bandwidth of a SMA as embedded wire as well as the controllability by creating internal channels in which the wires are placed. The wires are heated by Joule heating, but through the channels they can also be actively cooled by controlled, forced convection. A direct Fuzzy Logic Controller is developed to test the performance of the actuator. As inputs the set point, set point rate and error on the displacement are chosen. The controller has three outputs; two heating signals in the form of a power set point for a current - one for each side - and a cooling signal. The cooling signal is split depending on its sign and consists of a voltage that controls the valve which in turn control the airflow trough the cooling channels. The controller/actuator system was subjected to a series of trials, consisting of several set point types that the actuator had to track. These trials show that the actuator is able to track deflection set points at at least 0.6Hz. Above this frequency, the actuator looses track of the set point due to the dynamic behaviour of the beam.

Subsequently, in Chapter 7, a novel, thermoplastic blade concept is elaborated that provides certain key features that are important for blades with flexible trailing edges. Thermoplastic Composites (TPCs) are remeltable and thus a modular structure with ribs and additional strengthening elements can be employed. For smart rotor blades this provides load paths around actuator slots and mounting points for actuators. The demonstrator is made from APA-6 and a design optimisation study shows that replacing the sandwich structure with other stiffening elements is possible. This possibility is enabled by the thermoplastic composite material and its accompanying production techniques. This demonstrator is used to implement the SMA actuator as a flat extension, with the ribs being used as mounting points. This concept is discussed in Chapter 8.

The main conclusion of this work is that from a purely functional point of view there are little hurdles remaining for the implementation of a smart rotor on a wind turbine. However, issues like reliability, availability, power consumption and cost of the system, especially when implementing a SMA-based actuator, will have to be balanced against the benefits that the system provides.

Samenvatting voor niet-ingewijden

Het Slimme Rotor Concept voor Windturbines

Actuatoren en Constructie

Windturbines[1] leveren een steeds groter deel van onze energiebehoefte. Dit komt door de groeiende wetenschap dat fossiele bronnen ooit uitgeput zullen raken en dat de verbranding van fossiele brandstoffen negatieve bijeffecten voor mens en milieu heeft. Tot slot worden, door de economische en politieke opkomst van o.a. China, India en Brazilië, de beschikbare fossiele bronnen met een groeiend aantal afnemers gedeeld waardoor alternatieven aangewend moeten worden.

Windturbines kennen echter nog een aantal verbeterpunten. Een van de grootste technische punten van aandacht is de manier waarop met vermoeiingsbelasting wordt omgegaan. Vermoeiing is het verschijnsel dat een constructie maar een deel van zijn maximale belasting kan (ver)dragen als die belasting een wisselend karakter heeft. Op den duur kan een relatief kleine belasting op die manier tot scheurtjes en zelfs tot het falen van de gehele constructie leiden.

Windturbines zijn onderhevig aan extreme vermoeiingsbelastingen; zowel in termen van grootte van de wisselingen (amplitude) als de hoeveelheid cycli. Dit komt met name doordat de wind die de turbine aandrijft niet constant in sterkte en richting is. Maar moderne turbines zijn zo groot dat de wisselende zwaartekrachtbelasting (door het draaien van de rotor) voor extra vermoeiing zorgt. Ook worden turbines steeds vaker op zee geplaatst waar ze onderhevig zijn aan deining van golven. Bovendien is het bij turbines op zee, nog meer dan op land, belangrijk dat de machines lang

[1] 'Windturbine' is de technische benaming voor een moderne windmolen die elektriciteit levert

kunnen draaien zonder onderhoud en inspectie omdat dat moeilijk en dus duur is.

Aan de moderne turbine is echter het laatste decennium weinig veranderd wat betreft de manier waarop met (wisselende) belastingen wordt omgegaan, terwijl de grootte van de machines die gebouwd worden, verdubbeld is. Dat maakt het moeilijk om traditionele regelconcepten te gebruiken voor vermoeiingsvermindering omdat daarvoor het hele blad (de 'wiek') bewogen moet worden. Aan de andere kant nemen de amplitudes van de belastingen alleen maar toe met grootte. Daarom is er een nieuw concept uitgedacht waarbij er kleine, snelle regelsystemen langs het blad worden geïnstalleerd om locaal de stroming rond het blad te beïnvloeden en daarmee de belasting op het blad en de hele turbine constant te houden. De werking is vergelijkbaar met de manier waarop bij een vliegtuig de rolroeren in de vleugel gebruikt worden om te manoeuvreren.

Dit proefschrift beschrijft een onderzoek naar de ontwikkeling van een rolroer, specifiek voor windturbines, en de toepassing ervan in diens rotorbladen. Allereerst wordt er een overzicht gepresenteerd van concepten uit de luchtvaart waarmee een soortgelijk doel wordt nagestreefd bij vliegtuigvleugels en rotorbladen van helikopters. Ook worden een aantal concepten voorgesteld voor windturbines. Vervolgens wordt in Hoofdstuk 3 de werking van zogenaamde actieve materialen uitgelegd. Veel van het werk in dit proefschrift is gebaseerd op dergelijke materialen.

Zo wordt in Hoofdstuk 4 een serie windtunnel experimenten beschreven waarin op kleine schaal het belastingsreguleringsconcept getest wordt. Zowel de stuurvlakken als de sensoren in de bladen zijn gebaseerd op (actieve) piëzo-elektrische materialen, die onder een elektrisch veld een klein beetje vervormen, maar andersom ook een elektrische ladingverplaatsing afgeven onder een opgelegde vervorming. De testen laten zien dat een significante belastingsreductie mogelijk is. Wel moet bij het ontwerp van het systeem goed rekening worden gehouden met het trillingsgedrag van de bladen.

Hierna wordt de ontwikkeling en toepassing van een vervormend oppervlak besproken. Met een 'vervormend oppervlak' wordt een paneel bedoeld dat actief en controleerbaar buigt onder een (elektrisch) aansturingsignaal. Een dergelijk paneel kan de stroming om het windturbineblad beïnvloeden, en dus de manier waarop krachten op het blad worden gegenereerd. Extra voordelen van dergelijke oppervlakken, in vergelijking tot scharnierende panelen, is dat ze lichter uitgevoerd kunnen worden en er geen knikken of sleuven in het oppervlak van het turbineblad zitten die de stroming kunnen verstoren. In het onderzoek wat in dit proefschrift besproken wordt, wordt de verbuiging gerealiseerd door actieve materialen in te bedden die, wanneer

ze op de juiste manier gestimuleerd worden, het paneel waarin ze ingebed zijn, vervormen.

In dit onderzoek is gekozen voor geheugenmetaal waarvan grote vervormingen teruggewonnen kunnen worden door het op te warmen. Als het materiaal daarin beperkt wordt, bij voorbeeld door het in te bedden, dan oefent het grote krachten op zijn omgeving uit. Een probleem met geheugenmetaal is dat het reageert op warmte. Het kan heel snel opgewarmd worden door er een elektrische stroom doorheen te sturen, maar het ingebedde materiaal kan zijn warmte alleen kwijt door geleiding, hetgeen tijd kost en daarmee de snelheid van de vervorming beperkt. In het onderzoek wat hier besproken wordt, is een actief paneel ontwikkeld waarin het geheugenmetaal in interne koelkanalen wordt ingebed. Door de koelkanalen kan lucht geblazen worden en metingen laten zien dat de koelsnelheid daardoor vertienvoudigd wordt. Om de werking van het actief vervormbare oppervlak aan te tonen is een regelaar ontwikkeld die het aanstuurt. Deze regelaar is gebaseerd op zogenaamde Fuzzy Logic ('wazige logica'). Met een dergelijke regelaar kunnen moeilijk regelbare systemen, zoals geheugenmetaal aangestuurd worden omdat de staat van het materiaal omschreven kan worden. Dit is van belang voor het regelen van geheugenmetaal omdat het gedrag afhankelijk van de thermo-mechanische staat van het materiaal is. De combinatie van vervormend oppervlak en regelaar is stabiel tot ongeveer 0.6Hz, waarmee een groot deel van de vermoeiingsbelastingen van een windturbine weggenomen kan worden. Het geheugenmetaal wat gebruikt is en de ontwikkeling van het actieve oppervlak worden in respectievelijk Hoofdstuk 5 en 6 besproken.

Dergelijke vervormende oppervlakken kunnen echter niet zonder meer het bestaande oppervlak van een windturbineblad vervangen. In Hoofdstuk 7 wordt de ontwikkeling van een innovatieve blad lay-out besproken die de integratie van actieve, maar slappe oppervlakken vergemakkelijkt. Dit is een concept op basis van thermoplastische composieten omdat hiermee kleine onderdelen snel en goedkoop gemaakt en geassembleerd kunnen worden waardoor lokaal versterkende en dragende elementen aan het blad toegevoegd kunnen worden. In Hoofdstuk 8 wordt een concreet integratie concept uitgewerkt waarbij het actieve oppervlak als een platte extensie op de achterrand van het blad wordt toegepast.

Het onderzoek laat zien dat het 'slimme blad' concept grote potentie heeft om de vermoeiingsbelasting te reduceren. De andere hoofdconclusie is dat geheugenmetalen een zeer aantrekkelijk uitgangspunt vormen om een actief oppervlak op te baseren. Het grootste obstakel vormt momenteel echter nog de duurzaamheid van het materiaal zelf.

Contents

Nomenclature

Abreviations and acronyms

AM (and MA)	Austenite-to-matensite (and v.v.)
BEM	Blade Element Momentum
CBL	Critical Buckling Load
CCA	Concentric Cylinder Assembly
CFD	Computational Fluid Dynamics
CFRP	Carbon Fiber Reinforced Plastic
CLT	Classical Laminate Theory
CPB	Centraal Plan Bureau (Netherlands Bureau for Economic Policy Analysis)
CTE	Coefficient of Thermal Expansion
DARPA	Defense Advanced Research Projects Agency (of the USA)
DSC	Differential Scanning Calorimetry
EA	Evolutionary Algorithm
ECN	Energie Centrum Nederland (Energy Research Center of the Netherlands)
(E)DAP	(Enhanced) Directionally Attached Piezo
FB	Feedback
FE(A/M)	Finite Element (Analysis/Method)
FF	Feedforward
GA	Genetic Algorithm
GFRP	Glass Fiber Reinforced Plastic
HAWT	Horizontal Axis Turbine
IPC	Individual Pitch Control
LiPCA	Lightweight Piezo-composite Curved Actuator
LVDT	Linear Variable Displacement Transducer
MFC	Micro Fiber Composite
MIMO	Multiple-Input-Multiple-Output
NCF	Non Crimp Fabric
OJF	Open Jet Facility (TU Delft wind tunnel)

Abreviations and acronyms (continued)

PSD	Power Spectrum Density
RC	Repetitive Control
RPT	R-Phase Transition
SISO	Single-Input-Single-Output
SMA	Shape Memory Alloy
SME	Shape Memory Effect
SMP	Shape Memory Polymer
SRW	Sequential Resistance Welding
Thunder	THin layer UNimorph ferroelectric DrivER
TPC	Thermoplastic Composite
UAV	Unmanned Aerial Vehicle
UCS	Ultimate Compressive Strength
UD	Uni-Directional
URT	UpWind Reference Turbine
UTS	Ultimate Tensile Strength
WECS	Wind Energy Conversion system

Polymer and chrystal names

APA-6	Anionic Poly-Amide-6
PET	Polyethylene terephthalate
PVDF	Polyvenyldiphosphate
PZT	Lead-Zirconium-Titanate

Symbols (Arabic)[2]

a	Axial induction factor [-]
	Acceleration [m/s^2]
a'	Tangential induction factor [-]
A	Area [m^2]
$A_{s/f}$	Austenite start/finish temperature [K]
c_p	Heat capacity [J/kg·K]
C	Clausius Clapeyron constant [Pa/K]
	Aerodynamic coefficient (lift, drag, moment)
d	Matrix of piezoelectric charge or strain constants [m/V] (or [C/N])
D	Aerodynamic drag [N]
	Electric displacement component vector [C/m^2] (or [N/V])

[2]Symbols may be in text font when part of a sentence.

Symbols (Arabic, continued)

e	Error
	Permittivity matrix [F/m] (or [N/V^2)]
E	Electric field vector [V/m]
	Young's modulus [Pa]
f	Frequency [Hz]
G	Shear modulus [Pa]
h	Heat transfer coefficient [W/m^{2}K]
I	Second moment of inertia [m^4]
k	Effective coupling coefficient [-]
K	Controller (in a control scheme)
L	Aerodynamic lift [N]
	Length [m]
M	(Aerodynamic) moment [N]
$M_{s/f}$	Martensite start/finish temperature [K]
p	Elastic loading factor [-]
P	Power [W]
	Plant (in a control schema)
q	Heat flow [W]
	Distributed load on a beam [N/m]
r	Radial position along a a blade [m]
	Stiffness ratio [-]
R	Radius of a rotor [m]
S	Material's compliant matrix [m^2/N]
t	Time [s]
	Thickness [m]
T	Temperature [K]
	Torque [Nm]
u	Controller output
U	Wind speed [m/s]
V	Volume [m^3]
	Speed [m/s]
w	Width [m]
x, y, z	Spatial parameters [m]
x	In- or output parameter of the Fuzzy Logic Controller

Symbols (Greek)

α	Angle of attack [°]
δ	Deflection [m]

Symbols (Greek, continued)

ϵ	Strain vector [-]
ϵ_L	Free strain [-]
η	Energy conversion coefficient [-]
θ	Twist angle [°]
	Tuning parameter of the feedforward controller [-]
Θ	Thermal strain component [Pa/K]
κ	Curvature of a beam [1/m]
λ	Tip speed ratio [-]
ν	Poison ratio [-]
ξ	Martensitic fraction [-]
ρ	Density [kg/m^3]
σ	Stress [Pa]
ω	Frequency of disturbances [Hz]
Ω	Rotational speed of a turbine [rad/s]
	Transformation tensor (SMA) [Pa]

Sub- and superscripts

A	Concerning austenite
c	Concerning the controller
cr	Critical
d	Detwinned (martensite)
D	Concerning drag
g	Concerning the generator
	Glass transition (temperature)
i, j, k, m	Running coordinate (1,2,3...6)
L	Concerning lift
m	Melting (temperature)
max	Maximum
min	Minimal
$model$	Concerning a model
M	Concerning martensite
ref	Reference
t	Twinned (martensite)
w	At the wall
∞	At great distance

Chapter 1

Introduction

This chapter firstly presents an introduction into economical and technological aspects of wind energy, rotor blade design and control. From this introduction the drive towards the smart rotor concept is explained and the thesis outline is presented.

1.1 An introduction to wind energy and rotor blade technology

Today people are looking for alternatives to the burning of fossil fuels for the generation of electricity. There are two reasons for this: First, energy security is becoming important. On the demand side, global economic growth, but especially in emerging economies such as those in India and China, is leading to an increase in the demand for energy sources. But on the supply side, the known reserves for the vast majority of available oil are in politically unstable regions such as the Middle East and Western Africa and newly discovered oil and gas fields are becoming increasingly harder to reach. Secondly, there is a growing notion that the emission of the products of burning fossil fuels leads to negative environmental effects on the short term (smog, acid rain) and climate change on the medium term.

Therefore there is a drive towards the development of alternatives. Nuclear fission is mentioned as an option while a few decades ago the public was calling for its abolition. But also renewable sources such as bio-, solar, tidal and wind energy are gaining interest. Off these so called renewable energy sources wind turbine technology currently provides the lowest cost of energy and for densely populated regions like north-western Europe it is the most predominantly available source of renewable energy.

1.1.1 Wind turbines

Wind turbines basically convert the kinetic energy of the wind into mechanical energy (loading and movement on the blades) which accumulates in a torque on the main shaft which in turn is converted into electrical energy by a generator. Therefore turbines are also called a Wind Energy Conversion Systems (WECS) in general. The most predominant WECS-concept is the Horizontal Axis Wind Turbine (HAWT), shown in Figure 1.1. Multiple variants of the HAWT have been implemented over the last decades [1]. The variation can be found in the way the drive train[1] is arranged. With all modern HAWTs, two or three blades produce torque on the hub to which they are mounted. With most designs, the low speed, high torque on the hub is converted by a gearbox to a high speed, low torque on a shaft which drives a small, high speed generator. Since the gearboxes are often weak points in the wind turbine designs, some turbine manufacturers have chosen implement gearboxless, direct drive designs in which the hub is directly connected to a large, low speed generator. Until today there is no consensus in industry as to what is the optimal design.

The beauty of generating power from wind is that the power source, the kinetic energy of the air, is free and there is no emission of toxic, greenhouse or otherwise harmful residual substances during the conversion into electricity. However, there are high costs involved in building, erecting, financing and maintaining a turbine. These costs will have to be earned back by selling the energy that is generated over the turbine's life span, which is usually around 20 years. Maintenance and stand-stills are acceptable to a certain extend if they can be anticipated and planned.

From the above, several ways of increasing the profitability of wind turbines, from a turbine manufacturer or operator point of view, can be concluded:

- By increasing the rated energy yield that a turbine generates for a given investment.
- By increasing (the accuracy of the prediction of) its life span.
- By reducing the needed investment which consist of hardware and installation costs.
- By decreasing the down-time and (the incidence of) maintenance.

Every feature of the turbine should be designed such that the price per kilowatt hour is minimised. From the above list, it can be concluded that a

[1] The subassembly of shaft, generator and -if there is one- gearbox is called the drive train. The pod-like structure on top of the tower in which it is installed and on which the rotor is mounted is called a nacelle.

Figure 1.1: Off-shore horizontal axis wind turbine. Courtesy of Vestas Wind Systems A/S

reduction in energy price cannot only be attained by reducing the needed investment, but also indirectly by reducing component failure (and thus maintenance) or by producing more power with the same turbine. This makes a trade-off between different turbine technologies a difficult and nontrivial task.

1.1.2 Wind energy in the light of global developments

Currently the price per kilowatt hour of wind energy is almost competitive with other means of electricity generation, but still higher than coal or gas fired plants. The future of wind energy in the light of geopolitical, technological and economic developments has been researched by the Dutch CPB [2], an agency which also calculates the effect of government plans, and the Energy research Centre of the Netherlands (ECN). They present a very thorough analysis on the attainability of economically profitable off shore wind energy on the North Sea. Their assessment is that a crude oil price of 45 to 70 dollar per barrel - depending on economic, political and technological developments - will make 6000MW offshore wind energy by 2020 profitable. The report asserts that large scale offshore wind energy is

thus not profitable, since the long term oil price is predicted to be 25 to 35 dollar per barrel. However, the world has changed a lot since the publication of the report in 2004. The oil price has not been below 35 dollar per barrel and even though an economic crisis has broken out in 2007, the price has only dipped at 50 dollar and has stabilised at about 75 dollar over 2009 and 2010. The International Energy Association asserts that this will remain the case on the medium term because the crisis also leads to a reduction in investments on the supply side [3].

Moreover, the CPB/ECN report assumes that a globalised economy is not beneficial for the profitability of wind energy since in this scenario the carbon emission trade system is abandoned in 2020 and the interest in renewable energy sources is limited. Indeed, the Copenhagen climate conference in 2009 has not led to a new carbon emission treaty, but the interest in renewable sources has remained unaffected and is increasing with global economic leaders like China and the United States.

Furthermore, the report concerns offshore technology. A vast amount of onshore turbines has been installed already, especially in countries like Denmark, Germany, and Spain. Until now, onshore wind turbines have much lower installation costs and are therefore more profitable. The mentioned countries already produced respectively 21, 12 and 7% of their electrical power from wind energy in 2007, mainly from onshore machines [4]. Globally, the total amount of installed power has shown exponential growth, up to 94GW in 2007 and doubling in Europe between 2003 and 2008, which was driven by the geopolitical and economic trends described above. Both the size and the number of turbines that were installed over the last decade has increased very fast (see figure 1.2). The increase in size is driven by the fact that the power conversion by a wind turbine increases with the square of the rotor's diameter.

1.1.3 Technological issues

The trends described above force manufacturers to rapidly increase production capacity and to upscale existing blade designs. However, the boundaries of current technologies are being approached and component costs will also increase with turbine size. For instance, historically the mass of blades has increased with the radius to the power 2.4 [6] to 2.65 [7], depending on how the trend line is fitted. Thus the mass and with it the costs regarding materials and installation of a blade increase faster than the power it captures, which increases with the square of the rotor diameter. This is more acceptable for offshore turbines than for their onshore counterparts because a large part of the costs, such as foundations, is related to the amount of

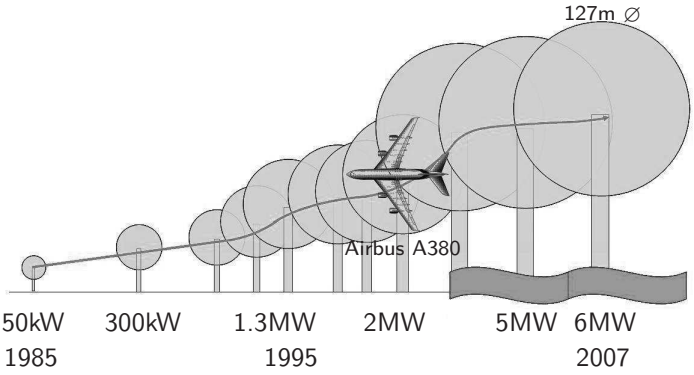

Figure 1.2: The increase of turbine state of the art size in time. Figure adapted from van Kuik in [5].

turbines, rather than the installed power. Increasing the yield per turbine will therefore decrease the costs per kilowatt-hour.

In this thesis we will focus on HAWTs and specifically on the design of their rotor blades. Therefore a small introduction into rotor blade design is presented first.

1.1.4 Rotor blade design

Since the wind turbine extracts kinetic energy from the wind, the air flow going through the rotor slows down and expands. The so called induction factor a denotes the amount with which the air has slowed down on the rotor plane, compared to the free stream airspeed. The power that a turbine converts in mechanical shaft power equals [1]:

$$P = \frac{1}{2}\rho A U^3 a(1-a)^2 \tag{1.1}$$

In which U is the free stream air velocity, A is the rotor area and ρ the air density. The air flow produces loading on the blade because the wind turbine blades are given aerofoils as cross-section. The aerofoil at a certain spanwise position of the blade experiences an airflow which results from the resultant of the wind and rotational speed of the blade. See figure 1.3. The air flow produces a pressure distribution over the blade's surface of which the resultants can be expressed as lift (L) and drag (D) forces and a pitching moment M. θ denotes the local twist angle of the blade with respect to the rotor plane and a' is the tangential induction factor, similar to a. Because the lift drives the turbine, aerofoils are usually designed for

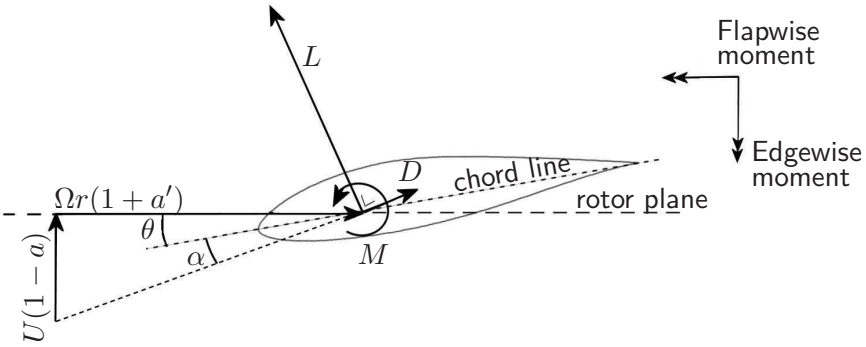

Figure 1.3: Flow and load vectors.

a high lift-over-drag ratio.
The lift that the aerofoil generates increases linearly with the angle of attack α, up to about 10°. At higher angles, the flow separates on the suction side and it goes into stall, generating relative low lift and high drag forces. This mechanism is actually implemented on some turbines as a means of load and power control. Usually a Blade Element Momentum (BEM) model [1] is used to determine the chord and twist distribution along the span of the blade. The local twist and chord is determined such, that constant power conversion is attained over the whole rotor plane, leading to a constant induction factor a.

The shape of the profiles along the span is driven by aerodynamic considerations, but thicker profiles are implemented towards the root in order to increase the moment of inertia, the geometrical part of the bending stiffness. From the aerodynamic and structural considerations usually a blade results with increasing chord towards the root, changing into a circle at the blade-hub interface. Furthermore, the chord line of the tip profile lies almost in the rotor plane, whereas towards the root there is a increasing twist angle to limit the angle of attack. See Figure 1.4 for a typical, large HAWT blade.

The lift and drag forces in turn result in bending moments in the blade which are usually defined with respect to the rotor plane. The out-of-plane direction is called the flapwise direction and these loads are typically larger than the in-plane edgewise bending moments which produce torque on the hub and actually drive the turbine. Besides the aerodynamic loading on the blade, large blades are also loaded by centrifugal and gravitational loads.

The internal structure of the blade is designed to cope with these loads. Modern blade designs usually have the following topology: The main flapwise bending loads are carried by spar caps on the thickest part of the

Figure 1.4: A wind turbine blade mounted to a test-jig. Courtesy of LM Wind Power.

profile. Spar caps are thick laminates unidirectional (UD) lay-up where the fibres are placed along the span of the blade. They can be seen in Figure 1.4 as the relatively dark strip running from the blade root towards the tip. These take up the normal loads as a result of flapwise bending. Usually one or two shear webs are employed to transfer the shear loads between the two spar caps under bending and to add torsional stiffness. The outer shell of the blade actually takes up most of the torsional and the normal stresses as a result of edgewise loads and is therefore sometimes reinforced with UD in the trailing edge to increase the edgewise stiffness. Components that are loaded in shear, either due to bending (webs) or torsion (shells) usually contain a considerable amount of $\pm 45^{\circ}$ orientated plies. The used composite material is usually a Glass Fibre Reinforced Plastic (GFRP), and sometimes the more expensive Carbon Reinforced Plastic (CFRP) is applied in the spar caps. In modern blades the implemented matrix polymer is an epoxy, either applied through vacuum infusion or in a pre-preg. See [7] for an overview of different materials systems. This blade concept is mainly implemented in two variants [8] which can be seen in figure 1.5.

In one variant, a central spar box is constructed which forms both the spar caps and two webs in one part. The outer shells are subsequently adhered to the sparbox. In both cases a maximum of four components is produced and jointed by means of an adhesive. Other variants include blades of which the preform is infused in one shot. This complicates the laying up and bagging of the preform, but cuts out the assembly step. In all cases, the outer shells and webs are usually designed as sandwich structures to provide the parts with resistance against out-of-plane deformations due

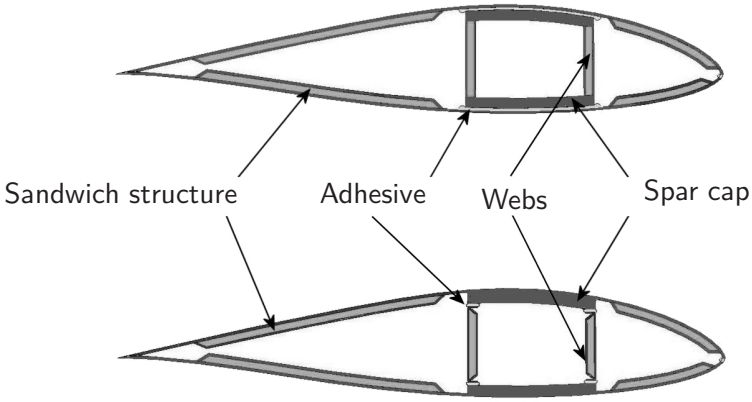

Figure 1.5: Typical blade cross-sectional lay-outs. Top: Design in which the spar caps and shear webs are incorporated in one part. Bottom: Design in which the spar caps are incorporated in the shells.

to bending or buckling loads. Usually high density foam or balsa wood is used as a core material in the skin. See [9] for other, older concepts, such as concepts with a load carrying D-nose.

So concluding, it can said that in industry many manufacturing concepts for large wind turbine blades exist, but that most of them can be reduced to the same structural topology, which is basically a tapered, hollow beam constructed from a minimum amount of components.

1.1.5 Load fluctuations

From this, the increasing mass of turbines with increasing size can also be understood. In order to maintain an acceptable level of stress in the blade and in order to keep the blade from colliding with the tower, the laminates have to be upscaled more than linearly with the rotor size [10]. Mass and size increases have several negative effects, beside higher material costs. First of all, installation cost increase because the heavy rotor has to be lifted to hub height. Secondly, at a certain point in time gravitational loading becomes a serious design driver. This fluctuating load comes on top of the already high fatigue loads that a turbine has to suffer because of fluctuating aerodynamic loading. These are caused by changes in the wind field and by the rotation of the blade through this wind field. Examples of these are wind shear, yaw misalignment, tower shadow and fluctuations in inflow. These loads will also increase with increasing size, for instance through the more severe wind shear experienced by larger machines. In fact, fatigue is already one of

the biggest design drivers and current blades are dimensioned for at least 10^8 cycles. Mitigating the amplitude of the fluctuations could lead to a longer service life of blades, but also to lighter blades and a reduced down time due to fatigue load induced component failure. In general mitigating fatigue loads will lead to a large reduction in the price per kilowatt hour and will provide the designer with an expanded design envelope. For instance, blades can be made lighter, mounted downwind, or operated with an extended life span.

1.1.6 Current load control on wind turbines

Wind turbines have always had some system to control their aerodynamic loading. With old wind mills, sails could be adjusted and with modern turbines, a number of systems have been implemented to control the loads and the power output. Most of these systems comprise of a combination of variable or fixed rotational speed and pitch angle. Currently, the most widely implemented system [11] is the variable speed, variable pitch machine. These machines maintain an optimal tip speed ratio λ below rated wind speeds and the blades are pitched to regulate power above rated wind speeds. λ is the ratio between the wind speed and the tip speed as a result of the blade's rotation. Usually pitching to feather[2] is implemented. The controller is based on the rotational speed and the generator torque signals. The system is mainly in place to control the quality of the power output and the mean loading of the turbine, but it can also alleviate transient loading. Above rated wind speeds, an increase in loading will lead to an increase in generator torque and the controller will react to this increase by pitching the blades to feather. Pitching can be implemented with all blades being pitched collectively or with an actuator pitching each blade. If each blade is driven by its own pitch actuator, two control systems can be distinguished. In one case there exists one controller and the blades are pitched with a 120° phase difference. This so called cyclic pitch control is used to mitigate 1P loads due to wind shear and yaw misalignment, in which P relates to the rotational speed of the turbine. With true individual pitch control (IPC) each blade is really controlled separately, based on local flow or load measurements. See Figure 1.6 for the control loop of a variable speed, variable pitch turbine above rated wind speeds.
Here Ω stands for rotational speed, T for torque, β for the pitch angle and θ for the scheduling parameter that is tailored as the operating point of the turbine changes. The subscript g indicates that it concerns the generator

[2]Pitching towards feather, in contrast to pitching towards stall, means lowering the angle of attack (counter-clockwise in Figure 1.3), thus lowering the loading of the blade.

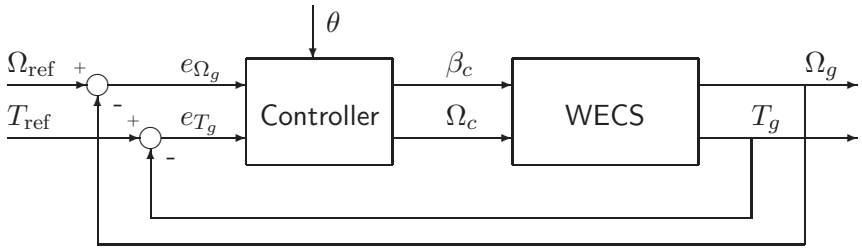

Figure 1.6: Variable speed, variable pitch control scheme for above rated wind speeds. (Figure adapted from [12]).

and c that it's a control signal. However, numerous other concepts exist [12]. These include concepts where the loading above rated wind speeds is controlled by active or passive stall. Also passive control systems such as the FLEXHAT have been developed where a part of the blade is passively pitched as the rotational speed increases because it reacts to centrifugal forces.

Some concepts have been proposed with the goal of mitigating root bending moment fluctuations, such as teetering hinges in the hub and (active) cyclic pitch control. Also, a passive concept, called bent-twist coupling, exists. In this concept the UD laminate in the main bending load carrying spar caps is placed under an angle. In this way, as the blade bends, it will twist [13]. Both twisting toward feather and to stall is possible [14, 15]. In the first case the angle of attack is lowered and thus the aerodynamic loading. In the second case the blade is pushed into stall and is thus subjected to low lift and height drag forces. The concept is passive and it requires the implementation and very accurate placement of expensive carbon fibres to be successful.

Many of the systems in use today react to the rotational speed of the rotor or generator torque. This means that the peak loads are dampened after they occur and that the main source of fluctuations - the way in which the airflow around the blade is locally converted into mechanical loading - is not controlled, nor loading of the individual blades. Many other concepts are passive which is a disadvantage because the loading of the turbine is hard to control and stability issues may arise. Moreover, passive systems only react to the type of signals to which they are tuned (e.g., centrifugal loading for the FLEXHAT or blade bending with bend-twist coupling). Stall control seems to be a very simple way to control the loading of turbines, but it cannot mitigate load fluctuations. Blades that go dynamically in and out of stall are actually subjected to very high fluctuations in loading thus

increasing the fatigue loads.

Active systems, based on feedback control, could dampen all possible load fluctuations which are picked up by sensors in the blade (e.g., strain gages), regardless of the source. The most widely implemented active load control system, variable speed and variable (individual) pitch control on turbines, also has the potential to actively mitigate load fluctuations. However, controlling the loads this way puts a heavy strain on the pitch bearings and hydraulics. Furthermore, the actuation speeds are limited because the whole blade needs to be pitched. Finally, pitching the blade results in a change in angle of attack and thus loading over the whole span of the blade. Having the capability to control the aerodynamics along the span would give much greater control over the dynamics of the blade and the other components of the turbine at a much smaller effort. Moreover, having distributed control along the span of the blade will become more important when future designs will grow even larger, in which case the inflow angle and speed may vary heavily along the span of the blade.

1.1.7 The smart rotor concept

With the above mentioned limitations of the current control systems in mind a new concept is proposed: by controlling the aerodynamics at different stages along the blade's span, the way the blade is loaded can be controlled, thus counter-acting the disturbances and mitigating the fatigue loads. This, in combination with appropriate sensors that measure the loads or structural response and a controller that computes an actuation signal, is defined as the *smart rotor* concept. Such an aerodynamic load control system has been intensively researched for helicopter blades and recently also feasibility studies for wind turbine blades have been performed [16–24]. The goal of the system would be to react both to deterministic loads, such as wind shear and tower shadow, as to indeterministic loads such as gusts and turbulence.

1.2 Research objectives

In this thesis the following definition of the smart rotor used:

> *The research field of smart structures applied to wind turbine technology, in order to actively control the lift and drag characteristics along the span of the blade. The ultimate goal of which is to mitigate load fluctuations on the blades, drive train, tower and bearings.*

Smart structures is a widely used term, but here it will be referred to only if it concerns a full system with sensors, actuators and a controller. In contrast, materials that change their physical properties under an external stimulus and that can thus act as actuator or sensor will be referred to as *adaptive materials*. The definition of the smart rotor system above implies that, for instance, concepts that add structural damping or concepts that are passive, are ignored. But even with such a demarcated definition of the smart rotor, many facets exist. This thesis will focus on the issues regarding the structure of a smart rotor. This mainly concerns the development of an actuator that is suitable for load control on wind turbines. A solution that leads to an integrated adaptive structure is sought because of maintenance and weight considerations. Ideally a construction would be obtained that can deform to the designer's wishes by dissolved actuators. This deformation can be a flapping motion of the trailing edge, blade twist or activating a control surface. Here the focus is on variable trailing edge geometry because of several reasons. Firstly, the trailing edge contributes little to the load carrying capability of the blade, especially in the outboard section of the blade where the load control features are to be installed. Therefore replacing this part of the blade with a flexible, non-load carrying actuator will require minimal additional structural reinforcement and stiffening of the base structure. Secondly, controlling the aerofoil's geometry at the trailing edge is a very effective way of controlling the pressure distribution over the whole profile. 'Effective' means that a small deflection of the trailing edge leads to a relative large pressure change in the suction peak near the leading edge, while the pressure over the trailing edge, which determines the power needed to drive the device, is small. A final advantage of a *morphing* trailing edge flap is that the flow over the stays attached for larger flap angles and that less noise is generated, as compared to a hinged, rigid flap.

The focus will be on adaptive materials for actuation purposes because they are not subjected to wear and require no lubrication. Therefore their implementation will lead to a structure that can stay in service with little inspection and maintenance. Moreover, adaptive materials offer a very high power-to-weight ratio [25, 26]. That leads to the first research objective of this thesis:

> *The selection of a suitable adaptive material, the development of an actuator based on this material and integration of the actuator in the blade's structure. The actuator should be able to act as a morphing surface on the trailing edge of the blade.*

Another important aspect of the smart rotor concept is the integration of the actuator into a feasible *system*. Both the interaction with the aerodynamic and control aspects of the technology, as well as the integration into the blade's structure are important. That leads to the second objective of this thesis:

> *Performing a proof-of-concept of the smart rotor in which dynamics, system design and rotor-specific aspects are addressed.*

The implementation of the smart rotor concept is not merely a matter of adding a flap to certain stations of the blade since the dynamics of the turbine and the performance of the system has to be taken into account.

1.3 Thesis Outline

This thesis is divided in two parts in which the two objectives mentioned above are addressed. The first three chapters of the thesis addresses both topics. After the introduction in this chapter, in Chapter 2 an overview of devices in smart wing and helicopter blade technology is presented. Also, proposed lift control devices for wind turbine rotor blades are discussed, together with a introduction into control algorithms and sensor systems in which the implemented device has to function. Finally, a reference turbine and specifications for the project are defined. Subsequently, in Chapter 3 an overview of adaptive material technology is presented. These chapters set a baseline and reference for the two parts that are discussed in this thesis.

In the first part, which consists of Chapter 4, the second research objective is discussed through a series of experiments in which the feasibility of the smart rotor concept is tested on a scale model of a rotor blade and a scaled rotor. Actuator, sensor and control issues, and the interaction with blade dynamics are addressed here.

In part two the development and structural integration of a full scale actuator is discussed. In Chapter 5, the results of characterisation experiments on a selected shape memory alloy (SMA) wire are presented. This wire is implemented in an actuator of which the design and analysis is discussed in Chapter 6. Subsequently, the issues for blade design with regard to integration of the actuator in the blade's structure are addressed. Specifically, the possibility of a multi-component thermoplastic blade design is studied in Chapter 7 because such a design will allow for locally deformable surfaces. How such a design can be implemented is explained in Chapter 8 where the design and manufacturing of a demonstrator is described, which

incorporates the actuator discussed in Chapter 6. Finally, in Chapter 9, conclusions are drawn. The link between the different chapters in the two parts is illustrated in figure 1.7.

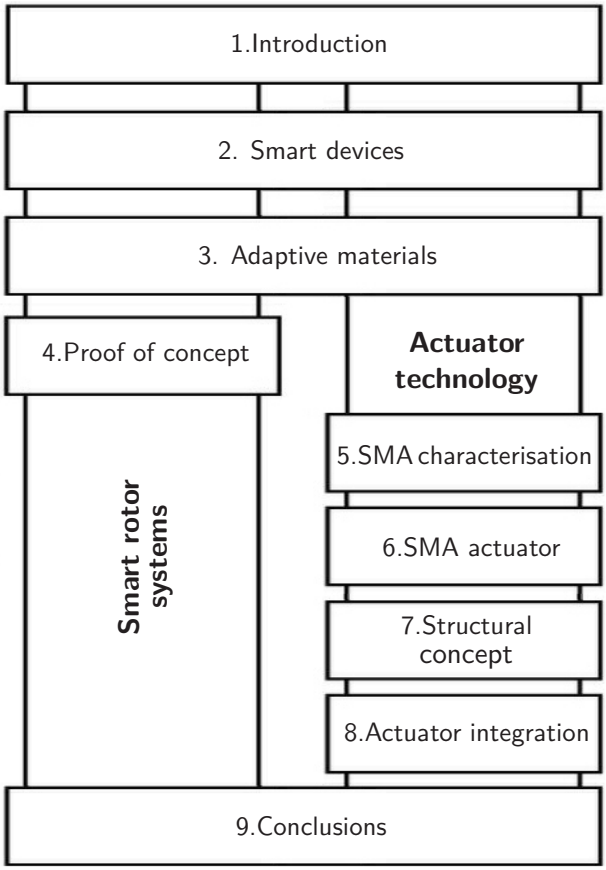

Figure 1.7: Flow chart of the thesis outline

1.4 Structure of the thesis work

The work in this thesis does not stand alone. The focus is on actuator development and structural issues with the smart rotor concept, but as can be observed with the research objectives and thesis outline, there are large interfaces, and even overlap, with control and wind turbine aero-servo-elasticity topics. Within the TU Delft's wind energy research institute DUWIND this

has taken shape in the form of a strong cooperation with the Delft Center for Systems and Control (DCSC) and the Wind Energy group of the Faculty of Aerospace Engineering. The topics of rotor control and rotor aero-servo-elastic performance are somewhat interwoven in this thesis, but van Wingerden [27] and Barlas [28] provide more in depth dissertations on these topics respectively.

1.5 Chapter summary

In the light of global economic developments, there is a need for large scale implementation of renewable energy sources. Currently, wind turbines have a large potential to meet this demand, but in order to bring down the cost of a produced kilowatt hour novel concepts are needed. One of the issues currently encountered by wind turbines is fatigue due to large load fluctuations. A way of reducing these fluctuations is the smart rotor concept with which the load is controlled along the span of the blades by distributed devices. In this field of research, this dissertation discusses the implementation of morphing surfaces based on adaptive material technology.

References

[1] T. Burton, D. Sharpe, N. Jenkins, and E. Bossanyi. *Wind Energy Handbook*. John Wiley and Sons, 2001.

[2] A. Verrips, H. de Vries, A. Seebregts, and M. Lijesen. Windenergie op de noordzee - een maatschappelijke kosten-batenanalyse, 2005. ISBN 90-5833-232-2.

[3] International Energy Agency. Medium-term oil market report 2009. `http://www.iea.org/publications/free_new_Desc.asp?PUBS_ID=2103`, 2009.

[4] European Wind Energy Association. Wind energy, the facts. `http://windfacts.eu/`, 2009.

[5] K. Hanjalic, R. van de Krol, and A. Lekic, editors. *Sustainable energy technologies - options and prospects*. Springer, 2008.

[6] D.A. Griffin. Windpact turbine design scaling studies technical area 1. composite blades for 80- to 120-meter rotor. Technical report, National Renewable Energy Laboratory (NREL), USA, 2001.

[7] P. Brøndsted, H. Lilholt, and A. Lystrup. Composite materials for wind power turbine blades. *Annual Review of Materials Research*, 35: 505–538, 2005.

[8] O.T. Thomsen. Sandwich materials for wind turbine blades - present and future. *Journal of Sandwich Structures and Materials*, 11:7–26, 2009.

[9] S. Joncas. *Thermoplastic Composite Wind Turbine Blades - an integrated design approach*. PhD thesis, Delft University of Technology, 2010.

[10] M. Zaayer. Developments in the concept and scale of wind turbines for offshore application. In M. and J. Roux, editors, *Wind Turbines: Types, Economics and Development*. 2009 Nova Science Publishers, Inc., 2009.

[11] A.D. Hansen and L.H. Hansen. Wind turbine concept market penetration over 10 years (1995-2004). *Wind Energy*, 10:81–97, 2007.

[12] F.D. Bianchi, H. De Battista, and R.J. Mantz, editors. *Wind Turbine Control Systems - Principles, Modelling and Gain Scheduling Design*. Springer, 2007.

[13] W. C. de Goeij, M.J.L. van Tooren, and A. Beukers. Implementation of bending-torsion coupling in the design of a wind-turbine rotor-blade. *Applied Energy*, 63(3):505–538, 1999.

[14] D.W. Lobtiz and P.S. Veers et al. The use of twist-coupled blades to enhance the performance of horizontal axis wind turbines. Technical report, Sandia, 2001.

[15] D.W. Lobitz and D.J. Laino. Load mitigation with twist-coupled HAWT blades. In *Proc. of the ASME Wind Energy Symposium*, January 1999.

[16] T.K. Barlas and G.A.M. van Kuik. Review of state of the art in smart rotor control research for wind turbines. *Progress in aerospace sciences*, 46:1–27, 2010.

[17] K.J. Standish and C.P. van Dam. Computational analysis of a microtab-based aerodynamic load control system for rotor blades. *Journal of the American Helicopter Society*, 50(3):249–258, 2005.

[18] E.A. Mayda, C.P. van Dam, and D. Yen Nakafuji. Computational investigation of finite width microtabs for aerodynamic load control. In *Proc. of the 43rd AIAA Aerospace Science Meeting and Exhibit*, January 2005.

[19] S. Basualdo. Load alleviation on wind turbine blades using variable airfoil geometry. *Wind Engineering*, 29(2):169–182, 2005.

[20] T. Buhl, M. Gaunaa, and C. Bak. Potential load reduction using airfoils with variable trailing edge geometry. *Journal of Solar Engineering*, 127: 503–516, 2005.

[21] S. Joncas, O. Bergsma, and A. Beukers. Power regulation and optimization of offshore wind turbines through trailing edge flap control. In *Proc. of the 43rd AIAA Aerospace Science Meeting and Exhibit*, January 2005.

[22] J.K. Rice and M. Verhaegen. Robust and distributed control of a smart blade. *Wind Energy*, 13:103–116, 2010.

[23] P.B. Andersen, M. Gaunaa, C. Bak, and T. Buhl. Load alleviation on wind turbine blades using variable airfoil geometry. In *Proc. of European Wind Energy Conf. and Exhibition*. European Wind Energy Association, Brussels, 2006.

[24] P.B. Andersen, L. Henriksen, M. Gaunaa, C. Bak, and T. Buhl. Deformable trailing edge flaps for modern megawatt wind turbine controllers using strain gauge sensors. *Wind Energy*, 13:193–206, 2010.

[25] R. Barrett and J. Stutts. Design and testing of a 1/12th-scale solid state adaptive rotor. *Smart Materials and Structures*, 6:491–497, 1997.

[26] D.C. Lagoudas, editor. *Shape Memory Alloys - Modeling and Engineering Applications*. Springer, 2008.

[27] J. van Wingerden. *Control of Wind Turbines with Smart Rotors: Proof of Concept & LPV Subspace Identification*. PhD thesis, Delft University of Technology, 2008.

[28] T. Barlas. *Active aerodynamic load control on wind turbines, Aeroservoelastic modeling and wind tunnel experiments*. PhD thesis, Delft University of Technology, 2011.

Chapter 2

Smart aerodynamic load control devices

Prometheus came to inspect the distribution, and he found [...] that man alone was naked and shoeless, and had neither bed nor arms of defence. The appointed hour was approaching when man in his turn was to go forth into the light of day; and Prometheus [...] stole the mechanical arts of Hephaestus and Athene, and fire with them and gave them to man.

From Plato's 'Protagoras', *translation by B. Jowett*

2.1 Introduction

In this chapter we will address the topic of smart structures and adaptive materials. Firstly, an overview of smart aerospace structures is presented because they pose the best benchmark for wind turbine rotor blades. Secondly, the focus will shift towards proposed solutions for wind turbines. In this section, also requirements for to be developed systems, derived from a reference turbine are discussed, as well as possible control strategies for the aerodynamic load control device that is to be implemented. After all, a 'smart' rotor does not only require capability to change lift through spanwise distributed devices, but also an algorithm to compute an actuator action and sensor signals to base the controller action on.

2.2 Smart aerofoils and wings

A very comprehensive explanation of smart aerofoils is presented by Campanile [1]. Campanile presents in a historic overview that an adaptive wing

was firstly aimed at in man's first attempts to fly and that even the Wright's brother's aircraft had morphing wings for flight control. Campanile asserts that because of the ever more severe demands for load carrying capability, maneuverability and speed (thrust), the tasks were separated in the wing box, flaps or ailerons and engines. But according to Campanile reintegration should be sought which would lead to lighter, aerodynamically more efficient structures. In the end that is also the goal of the smart rotor research. However, there is one mayor difference between aircraft wings and wind turbine rotor blades regarding flow control. Aircraft wings have had a control function from the first day they have been around, whereas for wind turbine blades actively controlling the aerodynamic loading is relatively new and with the exception of tip brakes, spanwise aerodynamic load control has not been implemented on any commercial turbine. In general wind turbine blades are not designed to house any system - they are passive fiber reinforced plastic components that are bolted to the hub, which possibly houses a pitch system. Still, the research into (smart) wings provides interesting insights since both structures have the same task - generating lift.

One of the goals of smart wings is the replacement of current control features into the wing to form an integrated structure. These control surfaces comprise of flaps, slats and ailerons. Their common denominator is that actuating them induce a change in camber. This is also what is mostly aimed for in the research into spanwise distributed devices for wind turbine blades [2]. Monner [3, 4] presents a system where linked plate-like elements form deformable ribs, so called "fingers". The fingers have to be actuated only at one point. A kinematic mechanism distributes the work over the finger and thus the finger is gradually deformed. See Figure 2.1. Monner allows for deformability of the outer skin by a flexible, sliding metallic skin.

Campanile presents a concept called the belt-rib design [5]. See Figure 2.2. The principle of the belt-rib design is based on the idea that for camber control on a continuous body, of the pressure and suction side, one side must lengthen and the other shorten depending on the direction of defection. In stead of straining both surfaces, it can also be conceived that transporting material from the suction to the pressure side, or vice verse attains the same effect. In the belt-rib design this is attained by implementing the aerofoil outer surface as a 'belt': circulation of the belt around the leading edge leads to a flapping motion of the trailing edge. Ribs inside the belt assure that actuation of the belt only leads to a change in camber and only little change in aerofoil shape and thickness.

A disadvantage of this concept is that the whole aerofoil needs to be

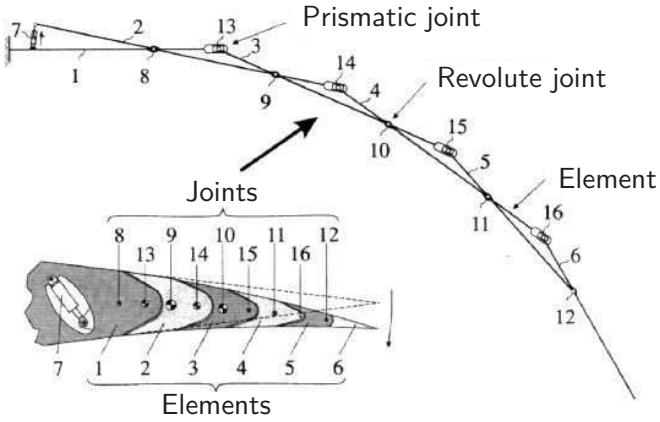

Figure 2.1: Kinematics and outline of Monner's finger mechanism (Figure adapted from [4]).

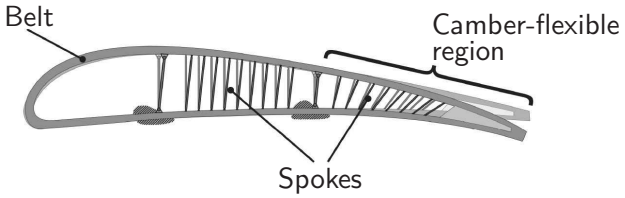

Figure 2.2: The Belt-rib-concept by Campanile.

deformed. With other trailing edge concepts like Monner's finger concept or phase two of the DARPA project Smart Wing [6], the central, load carrying part of the wing is often left unchanged. But combining full deformability in chordwise direction with bending stiffness in the flapwise bending direction of the blade, is not that straight forward.

Another concept that aims as camber control is presented by Inthra et al. [7]. Here genetic algorithms (GA) [8] are implemented to determine the optimal distribution of piezoelectric stack actuators to induce a distributed deformation in the trailing edge. GAs are also a powerful tool in designing compliant mechanisms. Many concepts for morphing wings are compliant structures in the sense that they comply to an actuator signal in a predetermined way and that they rely on the compliance of the material of which the structure is made. In general the ultimate goal is to distribute or to lever the control action of a discrete actuator through the body's volume in a predetermined manner. Or to optimally distribute an array of actuators for a certain control action, like in [7]. GAs are very suitable for designing

these structures because the user only supplies the input and the parameters that should be optimized. If the algorithm is correctly constructed it will determine the optimal material distribution of the structure to achieve, for instance, maximal control action for minimal weight.

Figure 2.3 schematically shows a compliant mechanism concept by Saggere and Kota [9]. They elaborate the concept for a deformable leading edge, a so called drooped nose. Trease [10] presents a similar concept which just aims at deforming the trailing edge, but in this case for biomimenic propulsion in water. Trease does not elaborate on the means of actuation, but calls it a 'smart actuator driven' concept. Kota also reports commercial implementation by the Flexsys company [11]. Recently they have also moved into the wind turbine engineering field as an application of their product.

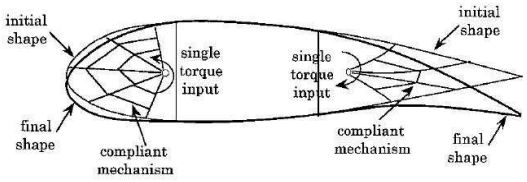

Figure 2.3: Schematics of compliant mechanisms for load control by deformable leading and trailing egde (Figure adapted from [9]).

Two types of compliant mechanisms can be distinguished: lumped and continuous compliance. The disadvantage of lumped compliance - where the deformability is concentrated in discrete points - is that stress concentrations occur around the flexible points, whereas with distributed compliance the strain is distributed over the whole mechanism.

A second form of smart wings aims at flight control through wing twist. Gern [12] mentions that wing twist can be employed to reduce roll reversal due to flap actuation. Wing twist requires a large amount of distributed actuators because the entire wing needs to be deformed to get a significant change in angle of attack. Stanewski [13] also mentions the suitability of adaptive materials for this task because of their high power density and the possibility of distributed actuation, which is needed when deforming a wing though gradual torsional deformation, either on the wing itself, like Krakers [14] suggests, or by an added torsion tube, like Jardine [15] has implemented.

Shape change of an aerofoil is also used for reconfiguration. In this case the aerofoil is deformed to set an optimal shape for different flight modes,

e.g., from sub- to transonic flight or from landing to cruising mode and vice versa. Reconfiguration concepts [16, 17] are often similar to other morphing aerofoil concepts, but the needed actuation speeds are much lower. Therefore it opens up new possibilities for low frequent control concepts and adaptive materials such as shape memory alloys and shape memory polymers (SMP) [15, 18–20].

A final application of adaptive materials in aircrafts is vibration control. On the subject of adaptive materials for vibration reduction in general numerous publications exist, but here the focus will be on vibration reduction of aerodynamically excited panels and wings. Vibration suppression usually involves increasing aeroelastic damping. With increasing size, flutter might also become an issue for wind turbine blades [21] because the first bending and torsion mode move closer to each other, so it is an interesting topic for the wind turbine community as well. Guo [22] reports increased stability of a panel by activating embedded SMA wires. Wu [23] achieves vibration suppression by adhering PZT patches to a panel of a F15 fighter that suffers from aeroelastic excitation. These patches are connected to a shunt circuit which is tuned for maximum energy dissipation at specific frequencies. Hopkins [24] reduces the vibration due to twin tail buffeting by adhering PZT patches to the tails and controlling these using feedback control based on accelerometers and strain gages. An increase in aeroelastic stability can not only be attained by actively or passively increasing the structural damping, but also by increasing the aerodynamic damping, e.g., through control of a flap [25, 26].

A program encompassing many of these concepts is the DARPA Smart Wing program. In the first phase of this program wing twist and SMA-activated trailing edge flaps were implemented on a scaled wing of a fighter aircraft [27]. Wing twist was induced by a SMA torque tube [15, 28] and the trailing edge flaps were designed as flexible glass epoxy plates, covered with aluminium honeycomb and silicone sheets to give the trailing edge its shape and smoothness respectively. In the second phase flaps, driven by piezoelectric motors were implemented on a Unmanned Aerial Vehicle (UAV) [29]. This concept allowed for a high rate, continuously deforming trailing edge in both chordwise and spanwise direction. As a base structure the same construction as the trailing edge flaps, but aramid in stead of aluminium honeycomb were used. The piezoelectric motors were chosen because of their high power-to-weight-ratio. Interesting conclusions from the program were that active surfaces can indeed be employed but that the actuation bandwidth of SMA material is very low and that the technology readiness level [30] was around five [6]. This means that it is at the level of component

and/or breadboard validation in a relevant environment. This point is also addressed by Boller [31]: smart structures have shown great potential over the last twenty years, but only little real structural implementations have been achieved.

The overview of all these concepts of smart wings leads to some reflections. First of all, a distinguish between different amounts of required deformation can be made: vibration control requires the smallest deformation of the structure since it means controlling the stiffness of a structure through stressing, or actively counteracting the vibration with a force. For wing twist medium strains are required because the resulting twist results from the accumulated strain along the blade's span. For integrated control surfaces relatively large strains are needed. This is also illustrated by the fact that many studies focus on the use of servo or servo-like actuators and that often silicone or latex skins are employed to allow for large strains in the skin, e.g., [29]. Classical concepts mentioned by Campanile [1] often employ surfaces that slide over each other.

Another distinction can be made in the different speeds required for actuation. Active vibration control requires very high actuation frequencies, whereas reconfiguration is quasi-static. Concepts for flight control require medium actuation speeds which are similar to the current control surfaces. Thirdly, for all smart concepts, but especially with wing twist, a trade-off must me made between on one hand the possible weight reduction due to the integration of several functions in one structure and on the other the added actuator mass. A final consideration is the readiness of the technology.

2.3 Smart helicopter rotor blades

A great deal of research on smart (aero)elastic structures has been conducted in the field of helicopter rotors. The research has been into different features such as torsion tubes, active twist control, trailing edge flaps which are actuated in all sort of different ways, et cetera. Straub presents a good overview of early concepts [32]. In the following they are grouped and discussed.

2.3.1 Trailing edge flaps

Although helicopter rotors are much smaller than wind turbine blades and operate at much higher rotational speeds, they still pose an interesting benchmark as smart structures. First of all because the structure under consideration is also a rotor. Secondly, the intended effect, obtaining vibration reduction through load control, is usually the same. And finally

because the flap deflections that are aimed at are roughly the same [2, 33], viz. several decrees for a flap size of $\sim 10\%$ of the chord.

There are several ways at which the flap can be controlled by adaptive materials. The following are elaborated in literature. Lee [34] proposes a so called piezo based 'double L' amplifier which drives the flap. Enekl [35] proposed a similar system which consists of a piezo stack between two leaf springs. The Enekl concept (see Figure 2.4) has been tested on a full scale helicopter rotor.

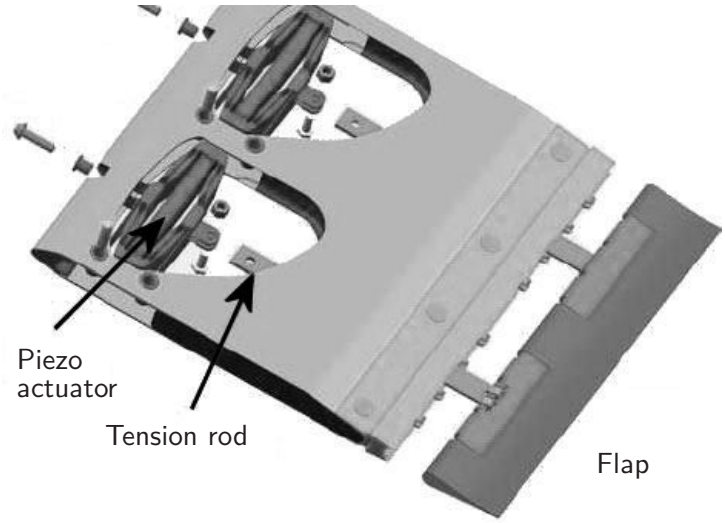

Figure 2.4: The piezoelectric stack driven concept by Enekl (Figure adapted from[35]).

Bothwell [33] elaborates on a magnetostrictive driven torsion tube but he also mentions SMA wires for twisting the tube. Other torsion tube options [36] use pure piezo tubes by evoking twist in the piezoceramic elements. Another way to drive the flap would be to employ the piezoceramic in a bender and to use that bender to actuate the flap close to its hinge, thus amplifying displacement induced by the bender [37–39]. A final application is to use SMA wires to pull the flap in either direction [40].

All these helicopter rotor trailing edge concepts are based on hinged flaps. This is not wanted in wind turbine rotor trailing edge flaps because of maintainability issues. Helicopters are already subjected to mandatory, regular inspections and their rotor blades can replaced if needed.

2.3.2 Active twist

With helicopter blades another option has been researched, although less thoroughly than trailing edge flaps. This is to twist a section of the blade to influence the aerodynamics. Such a system could theoretically replace the cyclic pitch system, but the deflections are not large enough, so the goal remains vibration control [41]. With active twist a piece of the blade at the root can be twisted. Two technical implications can be distinguished. One is to apply adaptive materials under an angle to induce shear and thus torque. The second one is to apply an angled laminate with longitudinal applied adaptive materials. This induces the same type of shear. Possibilities are mentioned by Chopra [37], Strehlow [42] and Barrett [41]. Barrett makes a comparison for different twist inducing configurations for a fin [43] and later for a small helicopter rotor [41]. But according to Boller [31] the solution is only applicable to small rotors.

As with concepts for smart wings, some general considerations can be deducted from this. The first one is that generally the goal of adding smart features to helicopter blades is vibration control and sometimes quasi-static blade tracking. However, it is not meant to replace the current flight control system. For vibration control most research is aimed at active twist or trailing edge flaps, actuated by piezoelectric driven mechanisms since with piezoelectrics high actuation frequencies are attainable.

2.4 Spanwise load control devices and control strategies for wind turbines

For wind turbines similar devices have been proposed, which are discussed in the first part of this section. In the second part of this section, an introduction to control strategies is presented and a reference turbine which is used throughout the thesis is defined.

2.4.1 Flow control devices

Dam et al. [44, 45] focus on microtabs or Gurney flaps. These are small tabs with a height that is in the order of 1% of the chord which are placed near the trailing edge, perpendicular to the flow. The tabs jets the flow in the boundary layer away from the blade's surface, causing a recirculation zone behind the tab, see Figure 2.5.

This effectively changes the circulation around the aerofoil and thus the lift and drag characteristics. Depending on whether they are placed on the pressure or suction side of the aerofoil the lift can be reduced or

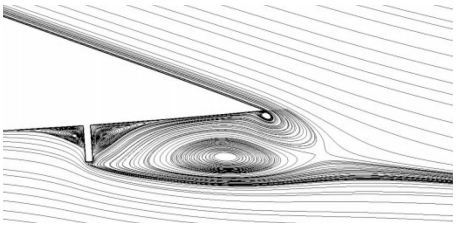

Figure 2.5: Zoom of steemlines around a trailing edge of an Aerofoil, equiped with a microtab on the pressure side. Adapted from [44]

increased and thus the loading of the blade can be controlled. Van Dam has made several studies into this topic, including a Computational Fluid Dynamics (CFD) analysis and wind tunnel experiments, determining the optimal configuration and testing the performance of the device. Another 'add on' device under investigation is the synthetic jet [46]. With this, air is sucked out of, and jetted back into the boundary layer at a very high rate. This can be implemented to control flow separation, but when placed near the trailing edge, at low angles of attack the device has an effect similar to the microtab [47]. Barlas [48] also mentions boundary layer control devices such as vortex generators, plasma generators and boundary layer suction, but these concepts are mainly aimed at stall delay or maintaining laminar flow, not lift control.

2.4.2 Morphing surfaces

However, as mentioned in Chapter 1, here the focus will be on morphing surfaces on the trailing edge. Three possible applications can be foreseen, which are schematically presented in Figure 2.6. Below, the first two are discussed in detail.

Deformable trailing edge

The first option is to to make a part of the existing profile actively deformable. This variant is often referred to as 'flap', whereas its functionality is better compared to an aileron on aircraft wings. These are continuously used during maneuvering of an aircraft, whereas flaps are only deployed quasi-staticly during take-off and landing for so called reconfiguration to a different flying mode. However, to be consistent with literature, dynamically deformable trailing edge geometry on wind turbine blades will be referred to as 'flaps'.

With flaps, when small deflections are needed, a new profile design might

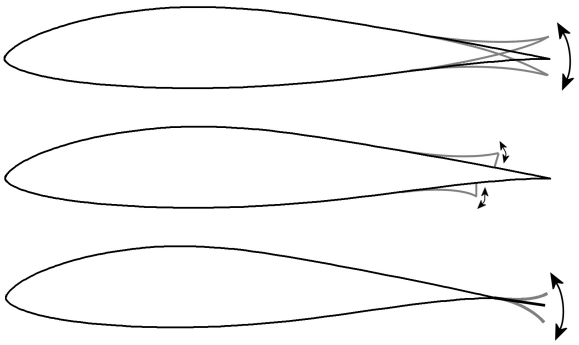

Figure 2.6: Possible implementation of a SMA actuator. From top to bottom: as extension to the trailing edge, as trailing edge wedge or active panels.

not even be needed and also the transition from the undeformable to the active part of the blade is easily made. However, two examples in which this concept was implemented, will illustrate the difficulties involved in such a design.

Lindroos et al. [49, 50] designed and manufactured a blade section with active, monolithic laminates on the pressure and suction side for the trailing edge panels for wind turbines. The problem with this concepts is that the deformation leads to a trailing edge motion that is not purely upward or downward, but rather a 'wagging' deformation of the trailing edge. This also changes the camber of the aerofoil, but not in the way that is required and a large part of the aerofoil needs to be deformable. A second concept that displays large deflections of a prismatic trailing edge was developed by Flexsys [11], which also reports possible application on wind turbines. However, with this concept part of the skin on the pressure side is replaced by a flexible membrane to allow for large (in plane) deformations of the skin.

These two concepts are developed with an application on wind turbines in mind, but they show great similarities with general aerofoil concepts presented in section 2.2, which based on compliance or are driven by internally distributed actuators [5, 7, 18]. However, relatively small deflections or a large part of the aerofoil is allowed to deform in these concepts. To attain large deflections on a small part of the chord there are two options. Either a part of surface has to be made of a material that has a high degree of in plane deformability - a material that is 'stretchy', a silicone skin for instance - or somewhere a cut has to be made, allowing surfaces to slide over each other. Buhl [51] even proposes a completely silicone trailing edge that is driven by pneumatics. The flap can be deployed to either side by

inflating internal chambers. This also eliminates lightning strike issues that are encountered with electrically driven devices.

In general it can be said that in order to realise this concept with a considerable deflection ($\sim 10^{\circ}$) on a relative small part of the chord (10-20%) the high intrinsic stiffness of the triangular shape of the trailing edge must be lowered or removed all together. In other words: a discrete degree of freedom should be created or the compliance of the flap should be high. However, the continuity of the structure is broken and thus its resistance against external (aerodynamic) loading is also lowered.

Spoiler flap

A second option is the spoiler flap. A spoiler flap is positioned on the surface of an aerofoil and is deployed normal to the surface on either the pressure or suction side, or both. Spoiler flaps are implemented on aircraft, but also ons wind turbines [52], as aero-breaks. In that case, the spoiler flap is deployed with large angles which causes a high drag. Scott [53] aims at influencing shock development on an aircraft wing.

On wind turbines, the spoiler flap could change the circulation with a small drag penalty, when deployed at small flap angles. However, until now, spoiler flaps are mostly tested at large angles (10° and larger). At small deflection angles the effect may be similar to the earlier mentioned microtabs, which are already under investigation for load control on wind turbines. Also so called trailing edge wedges are investigated for wind turbine blade profiles by Timmer and van Rooij [54]. They report a higher $C_{L,max}$ for a decreased lift-over-drag, but a detailed analysis aimed at load control is not made.

The big advantage of the spoiler flap concept is that it requires almost no enhancement of the structural rigidity and strength of the blade. As a matter of fact: the only change into the manufacturing of the base blade, in comparison to current designs, would be that locally a small bump would have to be made in the shell moulds, resulting in a small cavity in the products in which the actuators can be mounted, see Figure 2.7.

The main question mark about this concept is its aerodynamic effectiveness which is defined by:

1. its ability to change the lift,
2. the drag penalty that is to be paid,
3. the phase behaviour between the flap deflection and the lift.

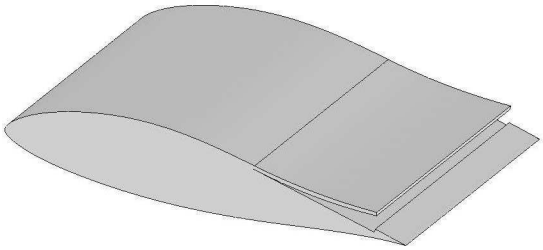

Figure 2.7: Sketch of the implementation of a continuous deformable spoiler flap.

The first two points are clear, but the third one requires some explanation. As mentioned, the concept has many similarities with the so called micro-tabs. However, micro-tabs have been reported to show so called non-minimum phase behaviour [55, 56]. This results from the fact that when the tab is deployed, the initial effect on the lift is adverse to the effect that is envisaged and is attained when the flow reaches a new equilibrium. Consequently, a control problem has been created. The advantage of the spoiler flap may be that, due to its wedge shape, the flow is gradually pushed away from the blade's surface, in stead of bumping into the tab. After all, the phase behaviour is also governed by the speed at which the pressure distribution can reset itself to the tab or flap deflection, which in turn is related to the flow speed and the dimensions of the blade. By gradually disturbing the flow with a continuously deformable flap, this phase delay may be minimised. On the other hand, the attainable change in lift for a given deflection might be smaller with a spoiler flap, as compared to a tab, because its effect on the flow is less dramatic. Furthermore, still a recirculation zone has to form behind the flap, as with the micro-tab. These questions require unsteady CFD analyses to be performed.

Here, as a first evaluation, a series of 2D steady CFD simulations was made, the details of which can be found in Appendix A. The aerofoil under investigation is a 1m chord, DU96-W180 aerofoil, on which a 0.2m flap is projected as a quadratic polynomial. The simulation is run for different flap deflections, which is defined as the normal distance of the blade's surface to the tip of the flap. The tip of the flap is located at 0.95c, both on the pressure as suction side, forming a 0.05c large cavity behind the flap when it is deployed. In this cavity recirculation takes place, changing the Kuta condition at the trailing edge and thus changing the camber of the profile, see Figure 2.8

This changes the pressure distribution over the whole aerofoil. The pressure distribution for the baseline profile, as well as two profiles with

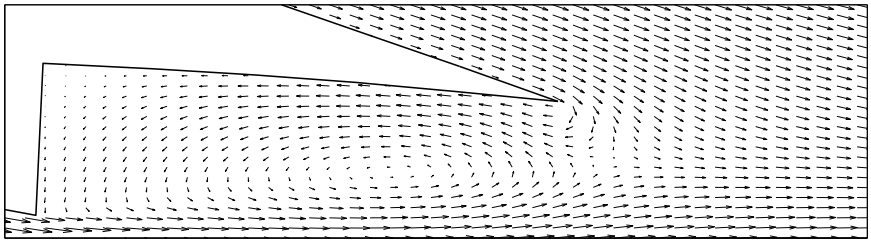

Figure 2.8: Zoom of the trailing edge region of the flow field where recirculation behind the spoiler flap (15mm deflection) can be observed. The length of the vectors represent the flow velocity in a logarithmic manner: $L \sim \log(1 + ||V||)$.

respectively the pressure and suction side spoiler deployed can be seen in Figure 2.9. It can be observed that the relatively small shape change near the trailing edge has an effect on the suction peak.

The pressure distribution can also be expressed in terms of its resultants C_L and C_D. In Figure 2.10 C_L and C_D are presented as function of the flap deflection. It can be seen that the lift coefficient changes considerably, in the order of 0.10-0.15 by a flap deflection of only several percents of the chord, with a limited drag penalty, which is the effect that is envisaged.

However, for small flap deflections on the pressure side, the change in lift is limited or even negative. This can be explained by observing the flow

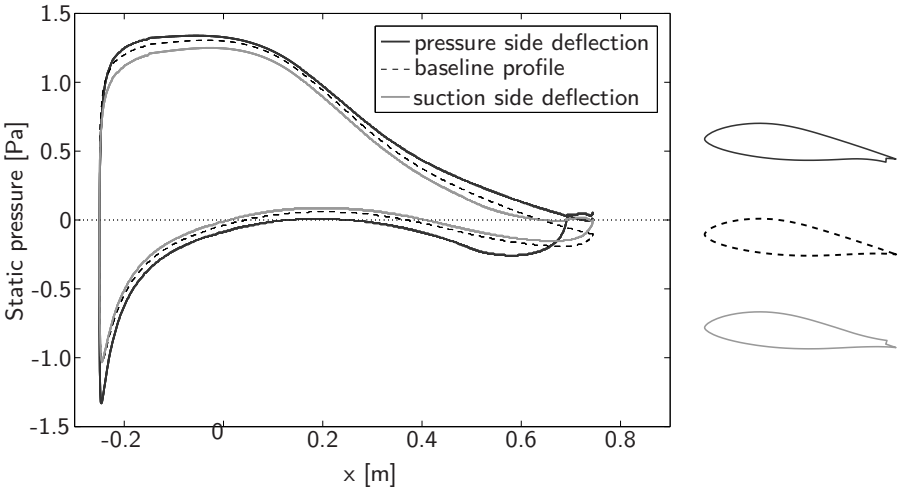

Figure 2.9: Change in pressure distribution over the aerofoil as a result of a spoiler flap deflection on the pressure and section side, as compared to the base DU96-W180 aerofoil.

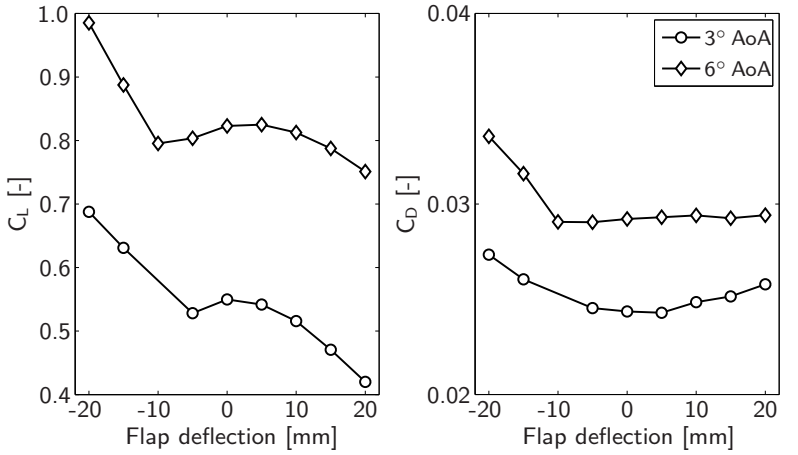

Figure 2.10: Lift and drag characteristics for the DU96-W180 as a function of the spoiler flap deflection, for two different Angles of Attack (AoA). Zero deflection denotes the baseline aerofoil. Positive and negative deflections are related to the suction side and pressure side respectively.

field, see Figure 2.11. For small flap deflection the flow reattaches to the surface before the trailing edge and the Kutta condition is not changed. The effect is even adverse for deployment on the pressure side. This is considered to be a drawback of the concept.

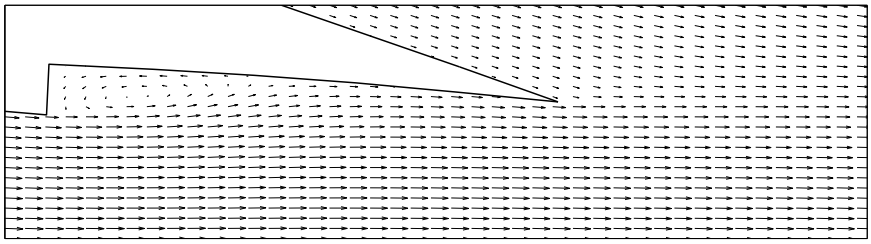

Figure 2.11: Illustration of reattachment of the flow behind the flap for small flap deflections. The length of the vectors represent the flow velocity in a logarithmic manner: $L \sim \log(1 + ||V||)$.

Flat extension

The actuator as a flat extension is already used by Bak [57]. There it was mainly used for validation purposed of an aero-elastic panel code and indeed the concept aerodynamically shows a lot of similarities to the deformable,

prismatic trailing edge described in Section 2.4.2. But from an morphing actuator point of view, it shows a clear advantage because the actuator can be added to the trailing edge and therefore be maintained and/or replaced easily. This concept will be discussed more in detail in Chapter 8.

2.4.3 Sensor and control strategy options

An important aspect of the smart rotor is the sensor and control strategy for the load control features. In Figure 2.12 the possible control possibilities can be observed. Implementation of sensors that measure the structural response is most straightforward. They can be embedded in or attached to the structure. The problem with flow measurements techniques is that they add complexity to the system and some, like Lidar or pressure taps, are not reliable enough yet. However, Lidars have been shown to show great correspondence with cup anemometer data [58] and a nacelle mounted Lidar that measured turbulence in the inflow has been reported [59]. On the other hand, Lidars do not work at all atmospheric conditions. Pitot tubes may be more feasible and are already suggested for control purposes by Larsen [60]. Larsen also mentions that the drawback of measuring the structural response is the phase difference between the load fluctuation and the blade response. Andersen [61] even performed experiments on a blade section equipped with a Pitot tube, to study the potential to mitigate changes in lift that occurred as a result of a pitching motion.

With sensors that measure the blade's mechanical loading, such as strain gages, already some implementations have been seen on wind turbine blades, but not for control purposes. Here the goal was to measure loads to validate the load assumptions in design or for monitoring purposes. For load control measuring the structural response is especially useful if the harmonics of the blade play a large role because the presence of eigenmodes in the load spectrum will amplify certain parts of this spectrum. But in all cases measuring the structural loads will be needed because controlling these is the ultimate goal of the smart rotor concept.

On the other hand, the measuring of inflow could increase the load alleviation potential of the concept. Then so called collocated control [62] is possible, where a local flow sensor directly coupled to a local control surface keeps the local aerodynamic load constant. However, a global control system must be installed too to make sure that the ultimate goal on the system, reducing the load fluctuations, is assured. Keeping the aerodynamic load at certain stations constant does not assure that, because not all stations can be controlled and because non-aerodynamic loading on the blade exist, e.g., wave loading on the tower for offshore turbines. Including inflow

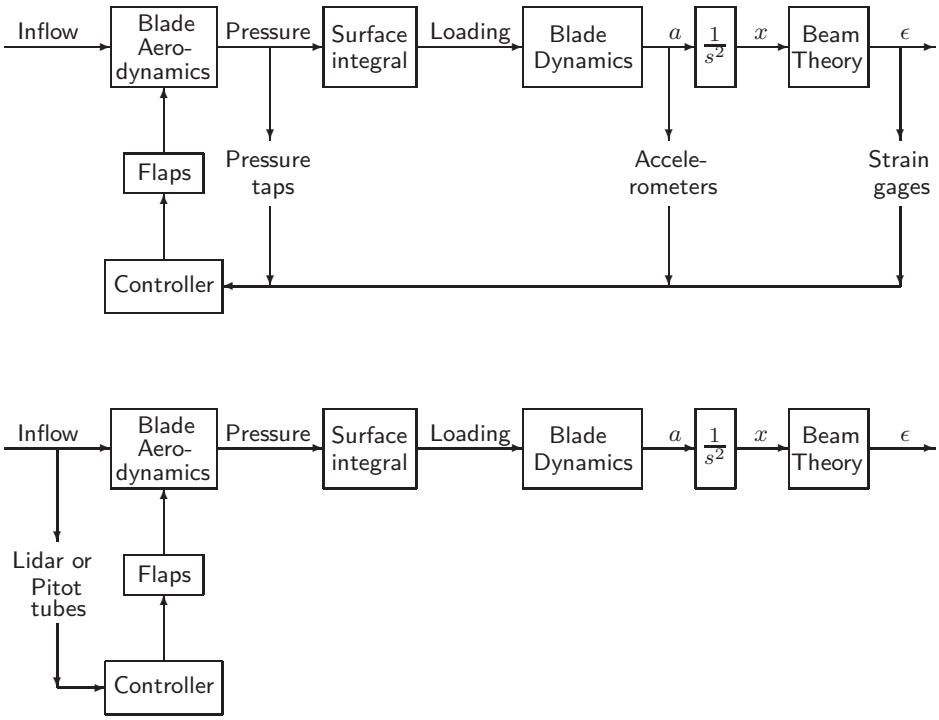

Figure 2.12: Various sensor concepts for feedback (top) and feedforward (bottom) control.

sensors will complicate the control system and it can be questioned whether acting solely on the structural response is not already sufficient to attain a satisfying level of load reduction.

An interesting aspect of the sensor issue is the question which part of the load spectrum is dominant: are the loads dominated by quasi-static components or is the turbulence exciting the dynamics of the blade? MacMartin [62] makes the same distinction: the mitigation of load fluctuation due to forced excitation are referred to as isolation, whereas the suppression of dynamic modes is called active damping.

2.4.4 Requirements for load control devices

In this chapter a series of load control devices for lift generating structures (wings and helicopter and wind turbine rotor blades) have been presented. They all have their advantages and disadvantages, but no statements have

been made about the requirements for a load control devices, in terms of actuation speed, deflection (or ΔC_L) and size. For the UpWind project, in which this research was also conducted, Barlas et al. wrote a report on the requirements for load control systems [63], which in turn was based on the description of the fictitious 5MW UpWind Reference Turbine (URT) [64]. The most important specifications and requirements are summarized in Table 2.1 below.

Parameter	
Rotor Diameter	60m
Rated wind speed	11.4m/s
Rated rotational speed	0.2Hz
First eigenmode of the blade (flapwise bending)	0.68Hz
Target minimum flap frequency	1.4Hz
Target ideal flap frequency	12Hz
Target nominal flap deflection	$\pm$ 12°
Target maximum flap deflection	$\pm$ 15°

Table 2.1: Relevant specifications of, and requirements for load control surfaces on the 5MW URT.

The target flap frequency can be debated; the largest load fluctuations are quasi-static or low-frequent, but the high frequent loads also add to fatigue because they occur more. The widest disturbance bandwidth of interest is up to 6Hz, but since as a rule of thumb actuation bandwidth needs to be a factor two higher than the highest frequency that is to be controlled, the ideal actuation bandwidth is up to 12Hz. Another frequency restriction could be posed by the first natural mode, which lies at 0.68Hz. The largest part of the vibrational energy is concentrated within this low frequency band [65]. A similar discussion can be made with regard to the flap deflection. A smaller flap deflection will give less actuator authority, but since the fatigue life of, for instance, composites typically increase exponentially with decreasing loads, a small reduction in fatigue loads may already pose a significant improvement. This also explains the two different mentioned flap angles in Table 2.1. If only the load fluctuations as a result of normal occurring turbulence and gusts are to be mitigated, the nominal flap deflection can be implemented. If also extreme operating gusts and extreme direction changes are to be controlled, the maximum flap deflection should be used.

2.5 Concluding remarks

In this thesis, this set of requirements and specifications will be used as point of departure in design and analysis. Now that an overview of concepts for load control devices, control stategies and requirements for wind turbine rotor blades have been discussed, a suitable adaptive material has to be selected to base the morphing surface on. As explained in Chapter 1, adaptive materials provide a very high power density and can be applied dispersed throughout the blade. In the next chapter an overview of available materials for actuation is presented. In the subsequent chapters these adaptive materials are applied in the design of an actuator and systems that are used to show the feasibility of the smart rotor concept.

References

[1] L.F. Campanile. *Adaptive Structures, Engineering Applications*, chapter 4, Light Shape-Adaptable Airfoils: a New Challenge for an Old Dream. J. Wiley and Sons, 2007.

[2] P.B. Andersen, M. Gaunaa, C. Bak, and T. Buhl. Load alleviation on wind turbine blades using variable airfoil geometry. In *Proc. of European Wind Energy Conf. and Exhibition*. European Wind Energy Association, Brussels, 2006.

[3] H.P. Monner, T.H. Bein, H. Hanselka, and E. Breitbach. Design aspects of the adaptive wing - the elastic trailing edge and spoiler bump. In *Multidisciplinary Design and Optimization: Proceedings*. Royal Aeronautical Society, October 1998.

[4] H.P. Monner and *et al.* Design aspects of the elastic trailing edge for an adaptive wing. In *Proc. of the RTO AVT Specialists' Meeting on "Structural Aspects of Flexible Aircraft Control"*, October 1999.

[5] L.F. Campanile and D. Sachau. The belt-rib concept: A structronic approach to variable camber. *Journal of Intelligent material systems and structures*, 11:215–224, 2000.

[6] J.N. Kudva. Overview of the darpa smart wing project. *Journal of Intelligent material systems and structures*, 15:261–267, 2004.

[7] P.A. Inthra, R. Sarjeant, M. Frecker, and F. Gandhi. Design of a conformable rotor airfoil using distributed piezoelectric actuators. *AIAA Journal*, 43(8):1684–1695, 2005.

[8] K.-J. Lu and S. Kota. Design of compliant mechanisms for morphing

structural shapes. *Journal of intelligent material systems and structures*, 14(6):379–391, 2003.

[9] L. Saggere and S. Kota. Static shape control of smart structures using compliant mechanisms. *AIAA journal*, 37(5):572–578, 1999.

[10] B.P. Trease, K.J. Lu, and S. Kota. Biomemetic compliant system for smart actuator-driven aquatic propulsion: Preliminary results. In *Proc. of IMECEŠ03*, pages 1–10. ASME, 2003.

[11] Flexsys. http://www.flxsys.com/.

[12] F.H. Gern, D.J. Inman, and R.K. Kapania. Computation of actuation power requirements for smart wings with morphing airfoils. In *Proc. of the 43rd AIAA/ASME/ASCE/AHS/ASC Structures, Structural Dynamics, and Materials Conference*, April 2002.

[13] E. Stanewski. Adaptive wing and flow control technology. *Progress in Aerospace Sciences*, 37(7):583–667, 2001.

[14] L. Krakers. Ductile piezoelectric actuator materials. Technical report, Netherlands Institute for Metal Research, 2006.

[15] A.P. Jardine, J. Bartley-Cho, and J. Flanigan. Improved design and performance of the sma torque tube for the darpa smart wing program. In *Proc. of SPIE Conference on Industrial and Commercial Applications of Smart Structures Technologies*, March 1999.

[16] M.H. Love, P.S. Zink, R.L. Stroud, D.R. Bye, and C. Chase. Impact of actuation concepts on morphing aircraft structures. In *Proc. of the 45th AIAA/ASME/ASCE/AHS/ASC Structures, Structural Dynamics and Material Conf.*, April 2004.

[17] Black. The changing shape of future aircraft. *High Performance Composites*, pages 52–54, September 2006.

[18] J.K. Strelec, D.C. Lagoudas, M.A. Khan, and J. Yen. Design and implementation of a shape memory alloy actuated reconfigurable airfoil. *Journal of Intelligent material systems and structures*, 14(4-5): 257–273, 2003.

[19] D.A. Perkins, Jr. J.L. Reed, and E. Havens. Morphing wing structures for loitering air vehicles. In *Proc. of the 45th AIAA/ASME/ASCE/AHS/ASC Structures, Structural Dynamics and Material Conf.*, April 2004.

[20] B. Dietsch and T. Tong. A review - features and benefits of shape memory polymers. *Journal of Advanced Materials*, 39(2):3–12, 2007.

[21] P. Berring, K. Branner, C. Berggreen, and H.W. Knudsen. Torsional performance of wind turbine blades - part I: experimental investigation. In *Proc. of the 16th International Conference on Composite Materials*.

Japan Society for Composite Materials, 2006.

[22] X. Guo, A. Przekop, and C. Mei. Supersonic nonlinear panel flutter suppression using aeroelastic modes and shape memory alloys. In *Proc. of the 46th AIAA/ASME/ASCE/AHS/ASC Structures Structural Dynamics and Materials Conf.*, April 2005.

[23] S.-Y. Wu, T.L. Turner, and S.A. Rizzi. Piezoelectric shunt vibration damping of F-15 panel under high acoustic excitation. In *Proc. of SPIE Conf. on Smart Structures and Materials 2000: Damping and Isolation*, volume 3989. SPIE, 2000.

[24] M. Hopkins, D. Henderson, R. Moses, T. Ryall, D. Zimcik, and R. Spangler. Active vibration suppression systems applied to twin tail buffeting. In *Proc. of SPIE Conf. on Smart Structures and Materials 1998: Industrial and Commercial Applications of Smart Structures Technologies*, volume 3326. SPIE, 1998.

[25] S. Heinze and Moti Karpel. Analysis and wind tunnel testing of a piezoelectric tab for aeroelastic control applications. *Journal of Aircraft*, 43 (6):1799–1804, 2006.

[26] S. Raja and A.R. Upadhya. Active control of wing flutter using piezoactuated surface. *Journal of Aircraft*, 44:71–80, 2007.

[27] J.N. Kudva and et al. Overview of the DARPA/AFRL/NASA Smart Wing program. In *Proc. of the SPIE Conf. on Industrial and Commercial Applications of Smart Structures Technologies*, March 1999.

[28] C.A. Martin, J. Bartley-Cho, J. Flanigan, and B.F. Carpenter. Design and fabrication of smart wing tunnel model and sma control surfaces. In *Proc. of the SPIE Conf. on Industrial and Commercial Applications of Smart Structures Technologies*, March 1999.

[29] J.D. Bartley-Cho and *et al.* Development of high rate, adaptive trailing edge control surface for the smart wing phase 2 wind tunnel model. *Journal of Intelligent material systems and structures*, 15:261–267, 2004.

[30] D.J. Moorhouse. Detailed definition and guidance for application of technology readiness levels. *Journal of Aircraft - Engineering notes*, 39:190–192, 2002.

[31] C. Boller. *Adaptive Structures, Engineering Applications*, chapter 6, Adaptive Aerospace Structures with Smart Technology - A retrospective and Future View. J. Wiley and Sons, 2007.

[32] F.K. Straub. A feasibility study of using smart materials for rotor control. *Smart Materials and Structures*, 5:1–10, 1996.

[33] M. Bothwell, Ramesh Chandra, and I. Chopra. Torsion actuation with

extension-torsion composite coupling and a megnetostrictive actuator. *AIAA Journal*, 33(4):723–729, 1995.

[34] T. Lee and I. Chopra. Design of piezostack-driven trailing-edge flap actuator for helicopter rotors. *Smart materials and structures*, 10:15–24, 2001.

[35] B. Enenkl, V. Klöppel, D. Preiler, and P. Jänker. Full scale rotor with piezoelectric actuated blade flaps. In *Proc. of the 28th European Rotorcraft Forum*, 2002.

[36] L.R. Centolanza, E.C. Smith, and B. Munsky. Induced-shear piezoelectric actuator for rotor blade trailing edge flaps. *Smart materials and structures*, 11:24–35, 2002.

[37] I. Chopra. Recent progress on the development of a smart rotor system. In *Proc. of the 26th European Rotorcraft Forum*, 2000.

[38] S.R. Hall and E.F. Prechtl. Development of a piezoelectric servoflap for helicopter rotor control. *Smart Materials and Structures*, 5:26–34, 1996.

[39] O. Ben-Zeev and I. Chopra. Advances in the development of an intelligent helicopter rotor employing smart trailing-edge flaps. *Smart Materials and Structures*, 5:11–25, 1996.

[40] K. Singh, J. Sirohi, and I. Chopra. An improved shape memory alloy actuator for rotor blade tracking. *Journal of Intelligent material systems and structures*, 14(12):767–786, 2003.

[41] R. Barrett, P. Frye, and M. Schliesman. Design, construction and characterization of a flightworthy piezoelectric solid state adaptive rotor. *Smart Materials and Structures*, 7:422–431, 1998.

[42] H. Strehlow and H. Rapp. Smart materials for helicopter active control. In *75th Meeting of the AGARD Structures and Materials Panel, AGARD Conf. Proc. 531*, October 1993.

[43] R. Barrett. Aeroservoelastic DAP missile fin development. *Smart Materials and Structures*, 7:55–65, 1993.

[44] K.J. Standish and C.P. van Dam. Computational analysis of a microtab-based aerodynamic load control system for rotor blades. *Journal of the American Helicopter Society*, 50(3):249–258, 2005.

[45] E.A. Mayda, C.P. van Dam, and D. Yen Nakafuji. Computational investigation of finite width microtabs for aerodynamic load control. In *Proc. of the 43rd AIAAAerospace Science Meeting and Exhibit*, January 2005.

[46] A. Glezer and M. Amitay. Synthetic jets. *Anual Review of Fluid Mechanics*, 34:503–529, 2002.

[47] L.W. Traub, A.C. Miller, and O. Rediniotis. Comparisons of a gurney and jet flap for hingeless control. *Jounral of Aircraft*, 41(2):420–423, 2004.

[48] T.K. Barlas and G.A.M. van Kuik. Review of state of the art in smart rotor control research for wind turbines. *Progress in aerospace sciences*, 46:1–27, 2010.

[49] T. Lindroos and M. Sippola. The application of smart structures for large wind turbine rotor blades - related topics at VTT. In *50th IEA Topical expert meeting - The application of smart structures for large turbine rotor*, December 2006.

[50] T. Lindroos, M. Sippola, and J. Koskinen. UPWind - SMA actuated adaptive airfoil. In *Proc. of 56th IEA topical Expert meeting on the application of Smart Structures for large wind turbine rotor blades*, May 2008.

[51] T. Buhl, P.B. Andersen, M. Gaunaa, C. Bak, H. Madsen, F. Zahle, J. Heinz, L. Bergami, L. Na, and A. Fisher. Latest results and tuning activities at Risø DTU withing trailing edge flaps. In *Proc. of 56th IEA topical expert meeting on the application of smart structures for large wind turbine rotor blades*, May 2008.

[52] L.S. Miller. Experimental investigation of aerodynamic devices for wind turbine rotational speed control. Technical report, National Renewable Energy Laboratory, USA, 1995.

[53] R.C. Scott, S.T. Hoadley, C.D. Wieseman, and M.H. Durham. The benchmark active controls technology model aerodynamic data. In *Proc. of the 35rd AIAAAerospace Science Meeting and Exhibit*, January 1997.

[54] W.A. Timmer and R.P.J.O.M. van Rooij. Summary of the Delft University wind turbine dedicated airfoils. *Journal of Solar Engineering*, 125:488–496, 2003.

[55] R. Chow and C.P. van Dam. Computational investigations of deploying load control microtabs on a wind turbine airfoil. In *Proceedings of the 45th AIAA Aerospace Sciences Meeting and Exhibit*, January 2007.

[56] P Bæk, M. Gauna, N.N. Sørensen, and P. Fuglsang. A comparison of two devices for distributed active load control of wind turbine blades. In *Proceedings of the Conference on the Science of making troque from wind*, June 2010.

[57] C. Bak, M. Gaunaa, P.B. Andersen, T. Buhl, P. Hansen, and K. Clemmensen. Wind tunnel test on airfoil risø-b1-18 with an active trailing edge flap. *Wind Energy*, 13:207–219, 2010.

[58] D.A. Smith, M. Harris, A.S. Coffey, T. Mikkelsen, H.E. Jørgensen, J.Mann, and Régis Danielian. Wind lidar evaluation at the danish wind test site in Høvsøre. *Wind Energy*, 9:87–93, 2006.

[59] M. Harris, D.J. Bryce, A.S. Coffey, D.A. Smith, J. Birkemeyer, and U. Knopf. Advanced measurements of gusts by laser anemometry. *Journal of Wind Engineering and Industrial Aerodynamics*, 95:1637–1647, 2007.

[60] T.J. Larsen, H.A. Madsen, and K. Thomsen. Active load reduction using individual pitch, based on local blade flow measurements. *Wind Energy*, 8:67–80, 2005.

[61] P.B. Andersen, C. Bak, M. Gaunna, and T. Buhl. Wind tunnel test of a closed loop controller for an airfoil with trailing edge flaps. In *Proceedings of the Science of making torque from wind conference*, June 2010.

[62] D.G. MacMartin. Collocated structural control: motivation and methodology. In *Proc. of the 4th IEEE Conf. on Control Applications*, September 1995.

[63] T. Barlas, T. Lutz, C. Bak, A.W. Hulskamp, and S. Apiñaniz. Requirements for smart rotor technology. Technical report, UpWind Project, 2010.

[64] Description of the upwind reference wind turbine - version 9. Technical report, UpWind Project, 2007.

[65] T. Barlas, G.J. van der Veen, G. van Kuik, D.-P. Molenaar, and M. Verhaegen. Model predictive control for wind turbines with distributed active flaps: Incorporating inflow signals and actuator constraints. *Wind Energy*, DOI: 10.1002/we, 2010.

Chapter 3

Adaptive materials

3.1 Introduction

In this chapter we will address the topic adaptive materials. In the previous chapter on aerodynamic features, two type of adaptive materials are repetedly mentioned: piezoelectric and SMA material. The two materials indeed they also pose the most potential for wind turbine blades because of their high power density and proven technology. Others can be discarded for adaptive features on wind turbine blades because of the need for heavy coils (magnetostrictives, magneto-rheological fluids) or too low bandwidth (electroactive and shape memory polymers).

3.2 Piezoelectrics

Piezoelectric materials exhibit a coupling between mechanical deformations and dielectric effects. Actually, the term piezo is derived from the Greek word for squeeze or press. Moreover, the piezoelectric effect was firstly discovered in crystals which created a surface charge when strained. This is known as the direct effect. But the effect also works in the inverse manner: the material will strain under the application of an electric field. This is known as the converse effect.

These effects, as well as the governing equations have been documented by many researchers [1–6] and can be written in many forms [1, 5], depending on the electric en mechanical boundary conditions. However, in this thesis only two forms will be written which are relevant to the use of actuator and strain sensor and the appropriate constants that describe the material.

$$\epsilon_i = S_{ij}^E \sigma_j + d_{mi} E_m \tag{3.1}$$

$$D_m = d_{mi} \sigma_i + e_{ik}^\sigma E_k \tag{3.2}$$

$$\text{with: } i, j = 1, 2...6 \quad \text{and } m, k = 1, 2, 3$$

The subscripts are related to the material's coordinate system and the superscripts denote under which constant boundary condition the parameter is assessed - σ for constant stress and E for constant electric field. In equations 3.1 and 3.2 the following variables define the electric and mechanical state of the piezoelectric materials.

- ϵ_i: Strain component.
- σ_i: Stress component.
- D_i: Electric displacement component. Electric displacement is related to the amount of charge q on the electrodes: $q = \iint D dA$
- E_i: Applied electric field component.

The other symbols are the piezoelectric constants and they are defined as follows:

- e: Permittivity. It is the electric field per unit applied electric displacement. e is often related to the permitivity of vacuum: 8.85×10^{-12}F/m
- d: matrix of piezoelectric charge constants. It is the mechanical strain per unit applied electric field or the electrical polerisation per unit mechanical stress applied.
- S: Elastic compliance constant which is defined as the amount of strain in the material per unit applied stress.

There are many ways to rewrite these equations into other forms. The IEEE [1] and Moulson [5] present a good overview. These are chosen here because equation 3.1 is very useful in describing the behavior of piezoelectrics as actuator and equation 3.2 as sensor. Moheimani [2] describes very well how these equations can be applied to patches and Waanders [3] to stacks. Another very important piezoelectric parameter is the effective coupling coefficient, k, which is a measure for the ability of the material to convert mechanical energy in electrical energy, or vice versa:

$$k^2 = \frac{\text{converted energy}}{\text{input energy}} \tag{3.3}$$

k can also be expressed in terms of piezoelectric constants described above:

$$k_{ij}^2 = \frac{d_{ij}}{s_{ij}^E \epsilon_{ij}^S} \tag{3.4}$$

However, the total efficiency of a piece of piezoelectric material is not only defined by k, but also by the way it is incorporated into a mechanical system. Giurgiutiu [7] defines r as the ratio between the (internal) stiffness of the piezoelectric material and the (external) stiffness of the structure against which it acts, subsequently deriving the total energy conversion coefficient:

$$\eta = \frac{1}{4}\left(\frac{k^2}{1 - k^2 \frac{r}{r+1}}\right) \tag{3.5}$$

Note that these equation holds for low frequent and quasi static applications. Many dynamic analyses [3, 5, 7] of piezoelectric materials in electromechanical systems exist.

3.2.1 PZT

PZT, or lead zirconium titanate, is the most widely used piezoelectric material. It is a very brittle ceramic. Below the Curry temperature the ceramic crystal exhibits a lattice structure with a dipole because of tetragonal symmetry. Crystals with adjoining dipoles are grouped in domains, called Weiss domains, which are randomly oriented in the material. Therefore the material has no nett dipole. However, applying an high electric field just below the Curie temperature lets the domains which lie in the field direction grow at expense of others. This operation is called poling and causes a nett dipole in the material. The matrix of piezoelectric strain constants is of the form:

$$\begin{bmatrix} 0 & 0 & 0 & 0 & d_{15} & 0 \\ 0 & 0 & 0 & d_{15} & 0 & 0 \\ d_{31} & d_{31} & d_{33} & 0 & 0 & 0 \end{bmatrix} \tag{3.6}$$

In the case of a patch, the 3-direction denotes the out of plain and poling direction and d_{33} is much larger then d_{31}. 4 to 6 denote shearing. Specific forms and applications of PZT are discussed later.

3.2.2 PVDF

PVDF, or polyvenyldiphosphate, is one of many polymers that can exhibit piezoelectric effects. It is discussed here because it has the highest coupling

coefficient and already some applications exist. Still, the coupling is much lower than that with PZT, but a big advantage of PVDF is that it is very ductile. Making PVDF piezoelectric requires two steps: obtaining the right crystal structure and secondly, obtaining the nett dipole. There are numerous ways to get to a piezoelectric form, but since most available materials consist of so called phase II form, the following procedure is suggested [8].

The first step, obtaining the right crystal structure, is performed by stretching the material at elevated temperature after which it recrystalises in phase I. This form has a non-centrosymmetric crystal, and thus a dipole. However, the crystals are still randomly orientated. Subsequent poling can be achieved by applying a high electric field from a corona at room temperature or a relative low field at elevated temperature. When poling, the PVDF's constitutive units are rotated around their chain bonds and thus a net dipole is attained. Hundred percent alignment with the field is not possible because some of the chains may have a vector component in the poling direction.

For piezoelectric PVDF sheets the charge constant d which links a field in the out of plane poling direction to in-plane strain, is different for both in-plane directions: $d_{31} \neq d_{32}$ and $d_{51} \neq d_{42}$, because of the uni-axial stretching. Therefore the charge constant matrix has the following form:

$$\begin{bmatrix} 0 & 0 & 0 & 0 & d_{15} & 0 \\ 0 & 0 & 0 & d_{24} & 0 & 0 \\ d_{31} & d_{32} & d_{33} & 0 & 0 & 0 \end{bmatrix} \tag{3.7}$$

Both the charge constants, the coupling coefficient and the compliance of PVDF are much lower than those of PZT, but it is much easier to handle and less brittle. In addition, PVDF with PZT granules dissolved in them have been proposed already years back by Furukawa [9]. This boosts the piezoelectric coupling, while maintaining the ductility of PVDF. However, Furukawa shows that the piezoelectric functionality of the composite can mainly be attributed to the PZT part of the composite.

3.2.3 Single crystal piezoelectrics

A final possible alternative is called Langasite [10]. This is a piezoelectric crystal that is grown under very high pressure. The crystal has a lower coupling coefficient than PZT, but a very high Curie temperature and depolerization field. Thus, when high voltages are applied, similar performances can be attained. It is also much less brittle and lighter than PZT. However, the crystal is very limitedly available and more expensive than PZT. The

structure of the d-matrix is as follows:

$$\begin{bmatrix} d_{11} & d_{12} & 0 & d_{14} & 0 & 0 \\ 0 & 0 & 0 & 0 & d_{25} & d_{26} \\ 0 & 0 & 0 & 0 & 0 & 0 \end{bmatrix} \tag{3.8}$$

Bohm [11] reports that due to the symmetry of the crystal, only two parameters are independent. Usually d_{11} and d_{14} are mentioned.

3.2.4 Piezoelectrics as actuators

Because the coupling between a field in the poling direction is the strongest, it is most obvious to employ this effect. But since the mutual distance between electrodes must remain small to attain a high electric field for a given voltage, special configurations have been developed for employing the d_{33}-effect. First of all, one can stack a series of disks or small patches on top of each other, each patch with its own set of electrodes. This is called a 'piezo stack'. See Figure 3.1. By applying the same voltage to each patch, a high field in the poling direction is attained and because the dimension of the piezoelectric material in its doping direction is increased, so is its displacement. However, the displacements are still very small; a typical stack of several centimeters can only attain displacements in the order of magnitude of $10^2 \mu$m. But large forces can be exerted this way.

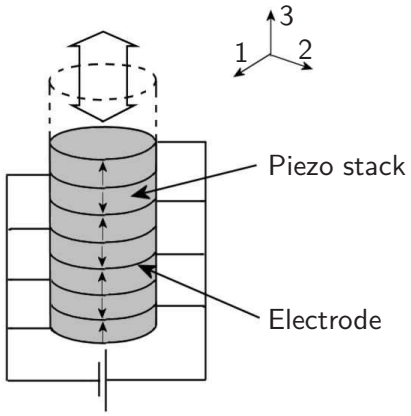

Figure 3.1: Piezo stack configuration (Figure adapted from [12]).

Another concept in which the d_{33}-effect is implemented, is the embedding of fibres that are poled in their longitudinal direction in a polymer with the application of interdigitated electrodes on the surface. These materials are

called Active Fiber Composite [13]. See Figure 3.2. Because these electrodes are placed at small instances, a high electrical field in the poling direction per unit applied voltage is attained. These plies can in turn be embedded into fiber reinforced polymers.

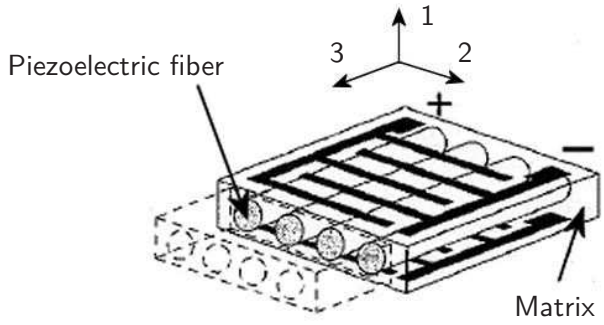

Figure 3.2: The principle of active fiber composites (Figure adapted from[12]).

A special type of these active fiber composites are called MFC's [14] (Macro Fiber Composites), developed by NASA. MFC's are produced by sawing very fine strips from a patch and embedding those in epoxy between Kapton film. See Figure 3.3.

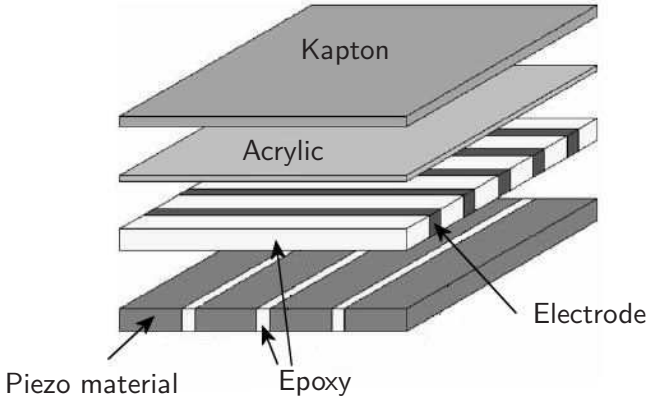

Figure 3.3: The build-up of a Macro Fiber Composite (MFC) (Figure adapted from [14]).

Another way to amplify the displacement of a piezo based actuator is to apply sheet material in a bender, either as an unimorph, with a patch on one side, or as a bimorph with a patch on each side. This way, the small strain of the piezo patch can be used to obtain relatively large deflections

of the bender. The behavior of such a bender is quite accurately described by extending the Classical Laminate Theory (CLT) with piezoelectric effects analogous to thermal expansion. But other models which incorporate out-of-plane shear have also been developed [12]. When applying piezo patches in laminates, one must be aware that a piezo patch strains in all in-plane directions when a field is applied. However, usually straining the construction or substrate in one direction is wanted. Barrett [15] therefore introduced the Enhanced Directionally Attached Piezoelectric (EDAP). With the concepts, narrow strips or special adhesion strategies are used to exploit the induced strain in only one direction.

There are also ways of increasing the deflection of these benders. This is done by introducing a geometrical non-linearity by axially compressing the bender [16] or using the thermal mismatch between the plies to introduce an internal stress state. Two types of benders that make use of the thermal mismatch are called Thunders [17, 18] and LiPCA's [19–21]. The Thunder actuators consist of a piezoceramic sheet that is laminated between a thin steel plate and an even thinner aluminium foil by means of an adhesive. This laminate is consolidated at about 300°C and when it cools, the difference in Coefficient of Thermal Expansion (CTE) causes a bend, slightly domed shape of the bender, depending on the aspect ratios and the presence of tabs. Aimmannee presents a model [18] which accurately predicts the shape of the Thunder. LiPCA's, Lightweight Piezo Ceramic Actuators, are based on the same principle, but they are produced by laminating a piezo patch between glass-epoxy and carbon-epoxy plies.

Mulling [22] makes an analysis of the Thunder under external mechanical loading with different end conditions (e.g., clamping or simply supported). Aimmannee and Hyer [23] focus on the geometrically non-linear deformation of the actuator that results from the production method. But Haertling [24] mentions another effect that might enhance the deflection of Thunder-type actuators under actuation. The residual stresses that occur after cooling from processing at elevated temperature cause additional domain orientation. This increases the piezoelectric charge constant d and thus the coupling between an applied field and the strain of the PZT in the actuator.

Haertling [24] focuses mainly on this effect in the analysis of Rainbow actuators. The concept of this actuator is similar to that of Thunders and LiPCA's, but with Rainbow actuators the layered constitution is obtained by 'reducing' a PZT patch to a certain depth. In this procedure [25], the oxygen from the PZT reacts with a carbon plate on which the PZT is placed at high temperature. This reduced layer has no piezoelectric cou-

pling and has different mechanical properties and CTE than the unreduced layer. In addition, a volume change occurs in the reduction process. This leads to residual stresses after cooling. A Rainbow actuator is therefore not laminated but monolithic.

There are also other ways to mechanically amplify the deflection of piezoelectric actuators. Niezrecki [26] presents an overview including concentric cylinder telescopic actuators, leave springs and lever systems. These mechanical amplifiers are not feasible for integration into active surfaces, but should be regarded as optional, low-wear, stand-alone actuators that could drive other mechanisms in turn.

3.3 Shape memory alloys

3.3.1 Material characteristics

Shape Memory Alloys (SMA) derive their name from the fact that large, plastic deformations to which the material is subjected can be recovered. At low temperatures the material is in martensitic. The martensitic latice structure has two variants, or twins. Loading the martensite above a certain level will lead to 'detwinning'. In this process one variant flips to the other over a certain stress range and the material can be deformed heavily - up to 8% - under a small increase in loading. Upon unloading the deformation remains. This can be observed in Figure 3.4. Here no elaboration into metallurgy is made, but Otsuka [27] offers a comprehensive review.

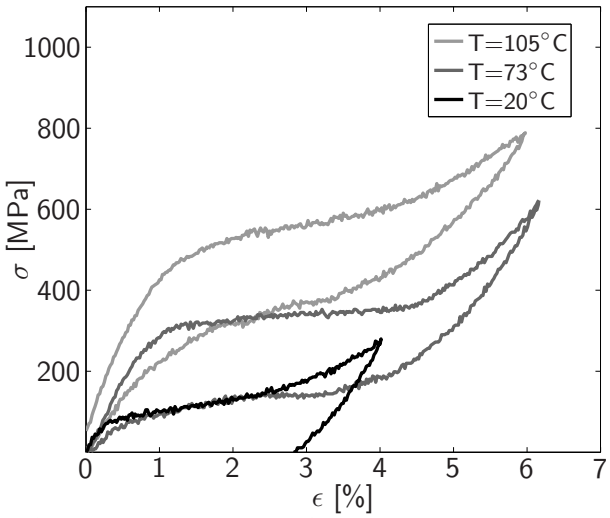

Figure 3.4: Stress-strain curves of a SMA wire at low and high temperatures.

The nearly flat part of the tensile ϵ,σ-curve is called the stress plateau. The deformation is plastic, but fully recoverable by raising the temperature above a certain threshold. Above this threshold the material is austenitic. Austenite has a cubic lattice structure and therefore no variants. The material 'remembers' its undeformed shape because the nett shape of the austenite is the same as of the undeformed variants of the martensite state. When the material is cooled down again the lattice structure becomes multi variant martensite again. This deformation and heating cycle can be observed in Figure 3.5 and is called the shape memory effect (SME).

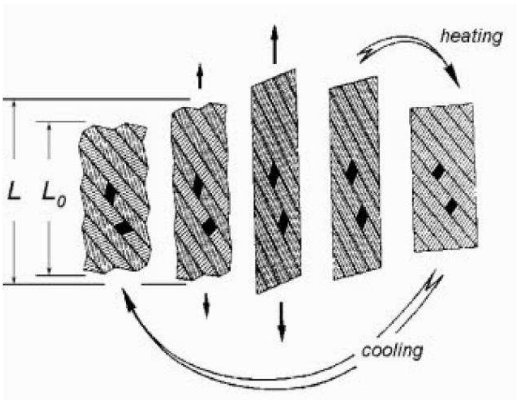

Figure 3.5: The shape memory effect cycle in SMA (Figure adapted from [28]).

The transitions from martensite to austenite and vice versa do not occur suddenly at a certain temperature but they rather occur gradually over a certain temperature range. The temperatures at which the austinite-to-martensite (AM) transition begins (M_s) and finishes (M_f) are different from those where the reverse transition begins (A_s) and finishes (A_f). The latter transition occurs at lower temperatures. See Figure 3.6. Something else that can be observed in Figure 3.6 is that the MA transition is postponed by tensile stresses.

When the temperature is raised until $T > A_f$, this causes the material to also exhibit pseudo-elasticity: stretching a piece of austenitic SMA causes the formation of martensite, so called 'stress induced martensite' or SIM. The deformation that is obtained under the formation of martensite is recovered as the material is transformed back into austenite when the tension is released. See Figure 3.4. The behavior is apparently elastic since all the deformation is recovered, but the physics behind this process is a reversible change in lattice structure, not atomic bond stretching. Moreover, the stress-strain loop shows a considerable amount of hysteresis.

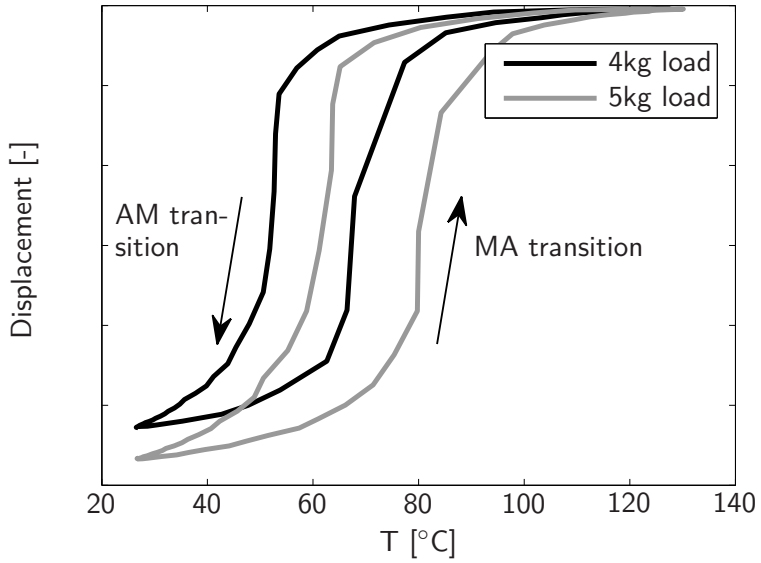

Figure 3.6: The displacement characteristics of an SMA wire as a function of the temperature, under constant loading.

Therefore the SMA is said to have two observable effects during thermal and mechanical load cycles: super- or pseudo-elasticity when A_f is below operating temperature and the shape memory effect (SME) when the material is deformed at $T < M_f$ and then reheated, or a combination of both in between M_f and A_f. A third effect that is reported [27, 29] is the rubber like effect, exhibited by some alloys. With this, the material shows recovery of deformation below M_f. This is usually regarded as an anomaly.

3.3.2 SMA behavior modeling

Usually the mechanical properties of a SMA are described as an ϵ,σ,T-behavior, but actually the underlying, connecting parameter is the martensite fraction ξ. Three types of models can be distinguished to model this behavior: the thermodynamical, the phenomenological and curve fitting models. The Youngs modulus of the low temperature martensite is lower than that of austenite. In all models it is assumed to be linearly decreasing with increasing martensite fraction (ξ):

$$E(\xi) = (1 - \xi)E_A + \xi E_M \tag{3.9}$$

Thermodynamic models are based on potential energy functions. In these models, the possible phases are mathematically represented by 'wells', being local minima of potential energy with respect to the shear length. The shear length is a measure for the lattice shape, with austenite having zero shear length and the two variants of austenite having a certain positive and negative shear length, respectively. The transformation dynamics are described by the probability of a crystal being in one well to overcome the energy barrier to jump to the next using Boltzman statistics. One of the earlier models for SMA behavior by Achenbach [30] is such a model. Others are by Seelecke [28] and Massad [31].

Phenomenological models, like those by Tanaka [32], Liang and Rogers [33] and Brinson [34–36] are also based on thermodynamic potential formulations, but in these models often Gibs and Helmotz free energy functions are employed because they do not rely on entropy as an internal parameter [29]. So called hardening functions are assumed to describe the transformation dynamics. With these models, the martensite fraction of the material is determined by using the σ, T-state of the material. The models differ in the way that transition areas are modeled. Tanaka derives the following constitutive relation from the Helmholtz free energy:

$$d\sigma = Ed\epsilon + \Theta dT + \Omega d\xi \tag{3.10}$$

In this equation E refers to the modulus of elasticity, Θ is related to the coefficient of thermal expansion and Ω is called the 'transformation tensor'. Equation 3.10 can be written in integral form, with constant material properties:

$$\sigma - \sigma_0 = E(\epsilon - \epsilon_0) + \Theta(T - T_0) + \Omega(\xi - \xi_0) \tag{3.11}$$

Tanaka only distinguishes between austenite and martensite and models the stress-temperature dependency of the martensite fraction ξ with an exponential function. For the AM transition:

$$\xi = 1 - \exp^{a_M(M_s - T) + b_M\sigma} \quad \text{for } \sigma \geq \frac{a_M}{b_M}(T - M_s) \tag{3.12}$$

and for the MA transition:

$$\xi = \exp^{a_A(A_s - T) + b_A\sigma} \quad \text{for } \sigma \leq \frac{a_A}{b_A}(T - A_s) \tag{3.13}$$

The coefficients a_M, b_M, a_A and b_A are dependent on the transitions' start and finish temperatures and the stress dependency of these temperatures,

the Clausius Clapeyron constants C_A and C_M. Assuming that the transition is complete with 99% conversion:

$$a_A = \frac{2\ln 10}{A_f - A_s}, \quad b_A = \frac{a_A}{C_A} \tag{3.14}$$

$$a_M = \frac{-2\ln 10}{M_s - M_f}, \quad b_M = \frac{a_M}{C_M} \tag{3.15}$$

The shape functions for phase transition are valid on certain stress dependent temperature domains which can thus be plotted on the T, σ-plane. See Figure 3.7.

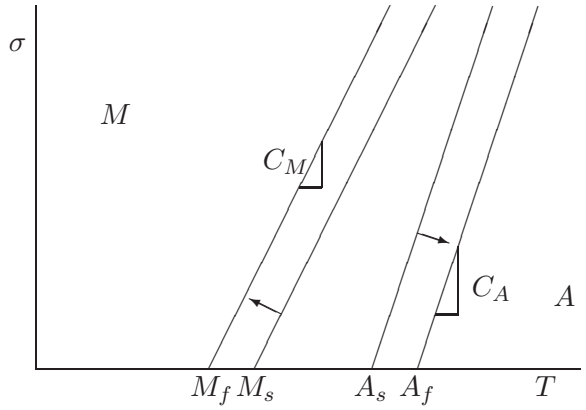

Figure 3.7: T,σ-phase diagram from the Tanaka model. The arrows indicate in which direction of the T,σ-path the phase change occurs.

Here the graphical representation of the Clausius Clapeyron constant can also be seen. Tanaka actually defines b_A and b_M in terms of the hight of the transition band:

$$\Delta\sigma_A = \frac{2\ln 10}{b_A} \tag{3.16}$$

$$\Delta\sigma_M = \frac{-2\ln 10}{b_M} \tag{3.17}$$

This consitutes the same as equations 3.14 and 3.15 because of the definition of the Clausius Clapeyron constants:

$$C_A = \frac{\Delta\sigma_A}{A_f - A_s} \tag{3.18}$$

$$C_M = \frac{\Delta\sigma_M}{M_s - M_f} \tag{3.19}$$

Liang and Rogers propose a similar model, but with a cosine shaped dependency of ξ on T and σ.

For $C_M(T - M_f) - \frac{\pi}{|b_M|} \leq \sigma \leq C_M(T - M_f)$:

$$\xi = \frac{1 - \xi_A}{2} \cos\left(a_M(T - M_f) + b_M\sigma\right) + \frac{1 + \xi_A}{2} \tag{3.20}$$

for the AM transition. For the MA transition the following holds.

For $C_A(T - A_s) - \frac{\pi}{|b_A|} \leq \sigma \leq C_A(T - A_s)$:

$$\xi = \frac{\xi_M}{2} \left[\cos\left(a_A(T - A_s) + b_A\sigma\right) + 1\right] \tag{3.21}$$

with:

$$a_A = \frac{\pi}{A_f - A_s}, \quad b_A = \frac{-a_A}{C_A} \tag{3.22}$$

$$a_M = \frac{\pi}{M_s - M_f}, \quad b_M = \frac{-a_M}{C_M} \tag{3.23}$$

and ξ_M and ξ_A are the start martensite fractions at the beginning of the respective transformations. a_M, b_M, a_A and b_M are slightly differently defined than in the Tanaka model, but they constitute the same physical meaning.

Brinson makes a distinction between temperature induced, multi variant ('twinned') martensite and stress induced, single variant ('detwinned') martensite. The constitutive relation is then rewritten, also taking into account non-constant material properties:

$$\sigma - \sigma_0 = E(\xi)\epsilon - E(\xi_0)\epsilon_0 + \Omega(\xi)\xi_s - \Omega(\xi_0)\xi_{s0} + \Theta(T - T_0) \tag{3.24}$$

Where the subscript s denotes the stress induces, detwinned martensite. Brinson also explains that:

$$\Omega(\xi) = \epsilon_L E(\xi) \tag{3.25}$$

In which ϵ_L is the maximal recoverable strain. Thus equation 3.24 reduces to:

$$\sigma = E(\xi)(\epsilon - \epsilon_L\xi_s) + \Theta(T - T_0) + K_0 \tag{3.26}$$

Where K_0 is a collection of terms that represent the initial conditions:

$$K_0 = \sigma_0 - E(\xi_0)(\epsilon_0 - \xi_{s0}\epsilon_L) \tag{3.27}$$

This parameter is dependent on the loading history of the material. Brinson, like Liang and Rogers, also assumes a cosine-shaped transition path.

Unlike Liang and Rogers, Brinson makes no distinction between the fraction at the start of the AM or MA transition and denotes the state at the beginning of the transition with the subscript '0'. Because of the distinction between twinned and detwinned martensite, below M_s another transition is introduced for the formation of detwinned martensite, also following a cosine-shaped path. For $T < M_s$ and $\sigma_s^{cr} < \sigma < \sigma_f^{cr}$:

$$\xi_s = \frac{1-\xi_{s0}}{2}\cos\left[\frac{\pi}{\sigma_s^{cr}-\sigma_f^{cr}}(\sigma-\sigma_f^{cr})\right]+\frac{1+\xi_s 0}{2} \tag{3.28}$$

$$\xi_t = \xi_{t0}-\frac{\xi_{t0}}{1-\xi_{s0}}(\xi_s-\xi_{s0})+\Delta_{t\xi} \tag{3.29}$$

with, if $M_f < T < M_s$ and $T < T_0$:

$$\Delta_{T\xi} = \frac{1-\xi_{t0}}{2}\cos\left(a_M(T-M_f)+1\right. \tag{3.30}$$

Else:

$$\Delta_{T\xi} = 0 \tag{3.31}$$

Subscript t denotes temperature induced martensite. If the temperature is below M_f the detwinning is only stress dependent. But if the temperature is between M_f and M_s, the model takes into account the formation of detwinned martensite due to cooling through the AM transition zone. This is captured in the $\Delta_{T\xi}$ parameter. If the stress is below σ_s^{cr}, only twinned martensite is formed. For the formation of detwinned martensite above M_s Brinson derives the following.

For $T > M_s$ and $\sigma_s^{cr} + C_M(T-M_s) < \sigma < \sigma_f^{cr} + C_M(T-M_s)$:

$$\begin{aligned}\xi_s &= \frac{1-\xi_{s0}}{2}\cos\left[\frac{\pi}{\sigma_s^{cr}-\sigma_f^{cr}}(\sigma-\sigma_f^{cr}-C_M(T-M_s))\right] \\ &\quad +\frac{1+\xi_{s0}}{2}\end{aligned} \tag{3.32}$$

The function for the formation of austenite above A_s is the same as with Liang and Rogers, but a function for the split in stress and temperature induced martenstite is added:

$$\xi = \frac{\xi_0}{2}\left[\cos\left(a_A(T-A_s)-\sigma/C_A\right)+1\right] \tag{3.33}$$

$$\xi_s = \xi_{s0}-\frac{\xi_{s0}}{\xi_0}(\xi_0-\xi) \tag{3.34}$$

$$\xi_t = \xi_{t0}-\frac{\xi_{t0}}{\xi_0}(\xi_0-\xi) \tag{3.35}$$

As with the model of Tanaka, the different phase regions can be plotted on the T,σ-plane, see Figure 3.8. In a later publication, Bekker and Brinson

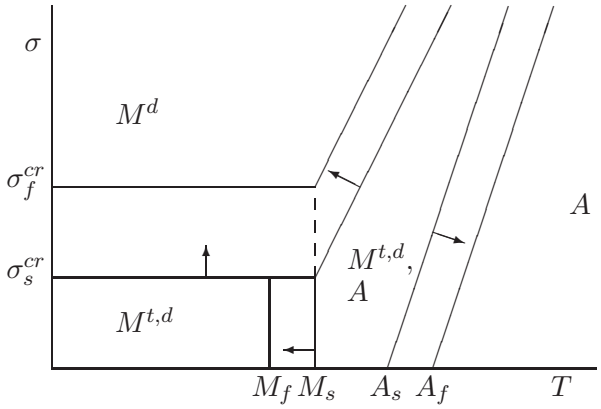

Figure 3.8: T,σ-phase diagram for the Brinson model. The arrows indicate in which direction of the T,σ-path the phase change occurs.

[37] introduced so called switching points. At these switching points, the phase transition is either complete or the σ, T-path reverses. In the model, the start fractions ξ_{s0} and ξ_{t0} are reset. In this way, uncompleted transitions and embedded loops can be modelled.

These models give understanding of the underlying mechanisms of the SME and superelasticity because they map the martensite fraction based on the actual parameters on which it is actually depending: stress and temperature. More importantly: they seem to predict the SMA behavior well [38]. However, the models provide the strain as a function of temperature, stress and load history. Inverting the model is not possible and a solution must be found iteratively. Leo presents a similar model in [39].

With the curve fitting models, like those by Spies [40] and van der Wijst [41], the force-displacement behavior is derived directly from the stress-strain path. The temperature dependency of this path is taken into account by linearizing the ϵ, σ-paths between transition points and shifting these points with the temperature. Van der Wijst does that by mapping the stress-strain envelope onto a ξ, p-plane, where p is the elastic load parameter and ξ is again the martensite fraction, see Figure 3.9. It is stipulated that changes in elastic stress and in martensite fraction cannot occur simultaneously:

$$\dot{p}(t)\dot{\xi}(t) = 0 \; \forall \; t \tag{3.36}$$

Van der Wijst uses the ξ, p-map in conjunction with a set of bilinear equations for stress and strain to determine the state of the SMA material and

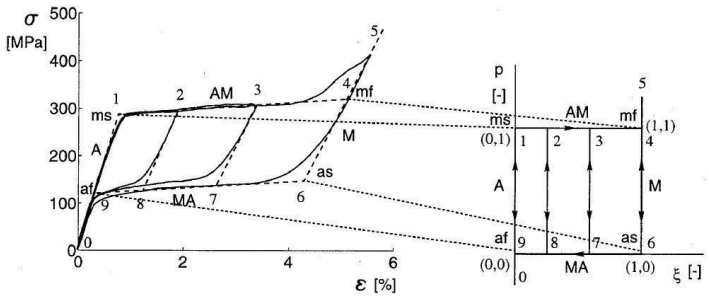

Figure 3.9: ϵ, σ-space to ξ, p-space mapping in the Van der Wijst model.

calculate the corresponding stress and strain state:

$$\epsilon = \epsilon_1 + \epsilon_2 p + \epsilon_3 \xi + \epsilon_4 p\xi \tag{3.37}$$

$$\sigma = \sigma_1 + \sigma_2 p + \sigma_3 \xi + \sigma_4 p\xi \tag{3.38}$$

In this equations, the coefficients are linearly dependent on the temperature:

$$\begin{aligned} \epsilon_1 &= \epsilon_{1a} T + \epsilon_{1b} \\ &... \\ \sigma_4 &= \sigma_{4a} T + \sigma_{4b} \end{aligned} \tag{3.39}$$

To calculate the state from time step to time step the equations are split over the two states and differentiated with respect to time. For the elastic regime (with constant martensite fraction):

$$\dot{\xi} = 0 \tag{3.40}$$

$$\dot{p} = \frac{1}{\epsilon_{,p}} \dot{\epsilon} - \frac{\epsilon_{,T}}{\epsilon_{,p}} \dot{T} \tag{3.41}$$

$$\dot{\sigma} = \frac{\sigma_{,p}}{\epsilon_{,p}} \dot{\epsilon} + (\sigma_{,T} - \frac{\epsilon_{,T}}{\epsilon_{,p}} \sigma_{,p}) \dot{T} \tag{3.42}$$

for the transformation state (with constant elastic load parameter):

$$\dot{\xi} = \frac{1}{\epsilon_{,\xi}} \dot{\epsilon} - \frac{\epsilon_{,T}}{\epsilon_{,\xi}} \dot{T} \tag{3.43}$$

$$\dot{p} = 0 \tag{3.44}$$

$$\dot{\sigma} = \frac{\sigma_{,\xi}}{\epsilon_{,\xi}} \dot{\epsilon} + (\sigma_{,T} - \frac{\epsilon_{,T}}{\epsilon_{,\xi}} \sigma_{,\xi}) \dot{T} \tag{3.45}$$

In these equations a comma denotes a derivative to the subsequent parameter. Coupled with a thermal model for the temperature of the wire

and a model for the external forces on the wire, the wire's behavior can be predicted each time step. The curve fitting models are not based on the thermodynamics behind the material behavior and a linear path is fitted between the transition points, but van der Wijst has shown that they can be a powerful tool for trajectory control, both with feedforward and feedback controllers. However, without feedback on the position of the actuator, good trajectory control is not possible. This is both due to the difficulties in modeling as in uncertainties in the thermal balance of the system.

3.3.3 R-phase transition and some metallurgistic considerations

In the above, the SMA behaviour was mostly discussed on the basis of the austenite-to-martensite transition (and vice-versa). However, some alloys exhibit another transformation when cooling down from the parent phase. This is the rhombohedral or R-Phase Transition (RPT) which occurs in some alloys before the martensitic transition. So in stead of $A \rightarrow M$, $A \rightarrow R \rightarrow M$ occurs [42] during the reverse transition. The recovery transition $M \rightarrow A$ occurs in one step. This RPT is associated with very small strains and its transition stress is highly temperature dependent, expressed by high Clausius-Clapeyron constants. Therefore, for higher temperatures the direct $A \rightarrow M$ transition occurs. See Figure 3.10.

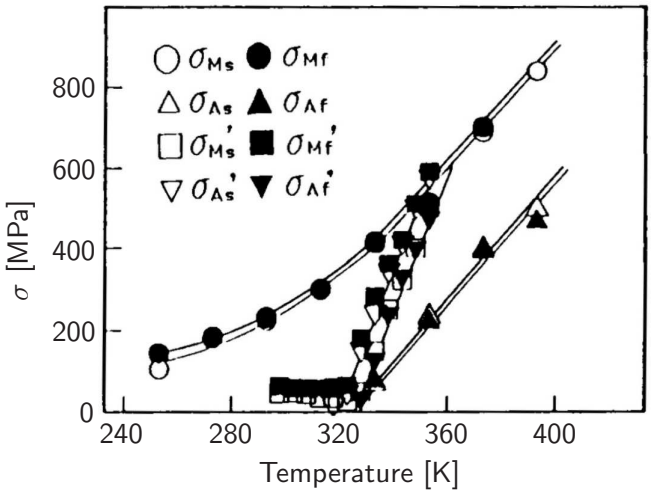

Figure 3.10: RPT and martensitic and reverese transition in the stress-temperature diagram. The RPT is indicated by an apostrophe in the legend. Figure adapted from [43]

Otsuka [44] makes a very elaborate discussion about the metallurgy of SMA materials, including those that exhibit the R-phase transition. The occurrence of the RPT is related to many factors, which include: the presence of precipitates, dislocations or certain non-Ni or Ti atoms. These factors all have one thing in common: they act as a resistance to a (large) lattice deformation, which the martensitic transformation is. The austenite to R-Phase transition is associated with much smaller deformations and is therefore hardly influenced by the presence of precipitates or a dislocation network. High Ni-content precipitates can be formed by aging the alloy at several hundred degrees. Dislocations are introduced by grain refinement through cold work. Stachowiak [42] reports that after cycling under isobaric loading, the RPT is overruled by the martensitic transition because the latter shifts to higher temperatures. Tobushi [45] reports the same effect.
The advantage of the RPT is that high forces can be exerted with it in restrained recovery, while the fatigue life of the alloy is much higher than when the 'traditional' martensitic transition is employed. However, the RPT can only be employed over a limited strain range.

Thermal and mechanical treatments do not only have a influence on the occurence of RPT, but also on the SME en superelasticity as a whole - in other words: on how the SMA functions as, for instance, actuator or damper. The specific metallurgistic fundamentals are out of the scope of this research, but here it is relevant to mention that it is reported [44] that cold work, followed by a ~ 1hour aging step at $\sim 400°$C leads to very stable super-elastic behaviour and SME. This is the case because cold deformation leads to small grain size and aging causes the formation of fine precipitates which prevent slip.

3.3.4 Applications

SMAs are mainly employed in the form of wires and ribbons. To be applied as an actuator, the SMA material must be prestrained and prestressed and attached to, or embedded in the structure. When the SMA material is heated it will start to recover its deformation. The structure will resist the deformation and the resulting stresses will postpone the formation of austenite. The structure or a bias force (spring, mass) will also have to force it back to its original position because typically the SMA is employed with one-way behavior. In addition, two wires can be set to act against each other.

If the structure is stiff enough, the behavior of a SMA can be described as restrained recovery: the strain remains negligible in comparison to the maximal recoverable strain, and it reduces to a σ, T-behavior. This still

shows a considerable amount of hysteresis and the behavior is non-linear. The restrained recovery force can be used to determine the deflection of structures.

Restrained SMA wires can exert high forces, up to several hundred MPa. The force that can be exerted increases linearly for moderate amounts of prestraining, but it flattens off for high rates of prestraining [46]. Practical functionalities of (embedded) SMA wires and ribbons include tuning of dynamic behavior [47] and increasing aeroelastic stability [48], increasing critical buckling loads [49] and increased impact resistance [50]. Practical applications are mentioned by [29] and [27]. They mention pipe couplings that do not require fasteners and deforming cheyfrons on jets in order to change the jet oulet from low noise configuration during landing and take off to optimal performance while cruising. SMA material is also often implemented in bio-mechanical engineering, because of it's good biocompatibility. Use of the SME in bio-mechanical engineering can be found in stents to open arteries and in minimal invasive surgical equipment. See also [51].

SMA materials seem very suitable for application for control surfaces on MW-sized turbines because of their high power density, high actuation force and/or strain capability and because their bandwidth is in the required range. However, several drawbacks exist:

- Like all conductors, they are susceptible to lightning strike.
- The goal of the control system of which the actuator is a part is to alleviate fatigue loads on the blade. However, SMA material itself shows poor fatigue properties. Several options exist to increase the fatigue life:
  - Only subject the material to partial cycles
  - Implement materials that exhibit the R-phase transition
  - Use special high fatigue alloys
- The bandwidth that is mentioned in literature [29] is only attainable in laboratory conditions. In applications the bandwidth is limited by the cooling rate that the system can impose on the SMA material.
- Typically, the heat that is put in to drive the transformation cannot be recovered, resulting in a energy loss. This makes the power consumption of SMA materials relatively high as compared to, for instance, piezoelectrics.

3.4 Ionic polymers

The functionality of ionic polymers is similar to that of polymeric piezoelectrics [52, 53]. Ionic polymers consist of gels in which certain atoms or atomic groups can move freely. When these groups have an electric charge and they bind water, water can be transported from one side of a strip to the other by applying an electric field through the thickness. This process is called electrophoresis and is also used in DNA-tests. This will let one side of the strip swell (expand), while the other shrinks (contracts). This leads to a bending deformation, which is actually quite fast and very large. The steps in figure 3.11 were taken with a 0.5s interval.

Figure 3.11: Motion of an IPMC under a low voltage

Since electrodes are needed, they are usually referred to as 'Ionic Polymer-Metal Composites' or IPMC's. However, for application in structures, the same objections as with PVDF hold: the forces that can be exerted are very small. Moreover, they must be submerged in water, which limits the applicability. An often mentioned application is artificial muscles.

3.5 Electrostrictive materials

Electrostrictive materials have the same actuation characteristics as piezoelectrics. They strain under the application of an electric field. Additionally, the maximum strain is also in the order of 0.1% [12]. However, the physical principle is quite different. With electrostrictives, strain is obtained through the alignment of otherwise arbitrarily oriented domains under an electric field. The response of strain to a applied field is quadratic, but saturates at a certain field. Since electrostrictives are very sensitive to temperature variations they are usually used in underwater or in vivo applications.

3.6 Magnetostrictive materials

Magnetostrictives show a straining behavior under the application of a magnetic field. Heavy coils are needed to induce the field and the resulting strains. This makes their application mostly feasible in situations where weight is of lesser importance, such as engine mounts with active dampening. The maximum attainable strain is about 0.2%, typically twice that of a piezoelectric.

3.7 Shape memory polymers

Shape Memory Polymers (SMP) can be given a "programmable" shape by shaping the polymer above a certain temperature. Reheating the polymer above that transition temperature will cause the transition to the old shape. An often used polymer in this, is a certain type of poly-urethane. This is a block copolymer which consists of hard and soft segments. Between the melting temperature of the soft segments (T_{ms}) and that of the hard segments (T_{mh}) the material is in a rubbery state and it can be deformed [54]. When the temperature is lowered, the material is frozen in the altered shape. When the material is reheated to a temperature between T_{ms} and T_{mh}, the stored elastic deformation in the hard segments forces the material back into its original shape.

However, since this shape change is very slow, SMPs are mostly implemented in R&D programs for quasi-static shape control such as reconfigurating aerofoils from sub- to transonic flight.

3.8 Magneto-rheological fluids

With magneto-rheological fluids their viscosity can be actively altered by applying a magnetic field. The objection to this material for lightweight adaptive structures is the same as with magnetostrictive materials: the weight of the coils of the magnet to apply a field. But magneto-rheological fluids are also not suitable for shape control, since their viscosity can be altered, not their shape. Magneto-rheological fluids are mostly employed as controllable dampers.

3.9 Concluding remarks

In helicopter research, which poses a very good benchmark for the wind turbine smart rotor research, piezoelectrics have been mostly implemented

for dynamic control [55–57] and shape memory alloys (SMA) for quasi static control, so called blade tracking [58, 59]. However, the requirements for wind turbine blades are different, especially with respect to the required bandwidth and the dimensions of the blade, which were already described in in Section 2.4.4. Although the ideal bandwidth of the load control device has been determined to be 12Hz, the largest part of the power spectrum density (PSD) up to three times the rotational frequency constitutes the largest part of the vibration energy. Another bandwidth restriction is posed by the first dynamic eigenmode. Being able to actuate on this frequency will mitigate transient vibrations and could increase the aeroelastic stability. The UpWind reference turbine [60] was used in this research, of which the 3P frequency is 0.60Hz and the first vibrational mode lies at 0.68Hz.

This lies within the theoretical operation bandwidth of the SMA material. Moreover, a SMA has a very high power density and, in contrast to piezoelectrics, does not have to be operated by means of a high voltage and is easily upscalable to large flap sizes. However, several issues remain, such as the limited fatigue life, limited bandwidth if the wire is to be embedded in the structure and lightning strike.

Therefore for the development of a morphing surface will be based on SMA material. In Chapter 5 the characterisation of a specific SMA wire which is to be used in a actuator is discussed. In the subsequent chapter, this wire is implemented in a novel actuator design that primarily addresses the bandwidth and controllability issues. Then, two chapters are dedicated to the feasibility of the smart rotor concept and how it affects blade design. And finally in Chapter 8 it is discussed how the SMA actuator can be used as an actuator in this blade.

However, in the next chapter firstly a proof-of-concept of the smart rotor concept is presented. This is done on small blades which rotate and vibrate at much higher frequencies than the reference MW-sized turbine, which is described in Section 2.4.4. Because of the required high operation frequencies, the flaps of the blades will be based on PZT technology. Also, sensor technology will be based on PZT-material.

References

[1] A.H. Meitzler, D. Belincourt, G.A. Coquin, III F.S. Welsh, H.F. Tiersten, and A.W. Warner. Ieee standard on piezoelectricity. Technical report, IEEE, 1988.

[2] S.O.R Moheimani and A.J. Fleming. *Piezoelectric Transducers for Vibration Control and Damping*. Springer Verlag, 2006.

[3] J.W. Waanders. *Piezoelectric Ceramics - Properties and Applications*. Philips Components, 1991.

[4] J. Sihora and I. Chopra. Fundamental behavior of piezoceramic sheet actuators. *Journal of Intelligent Material Systems and Structures*, 11: 47–61, 2000.

[5] A.J. Moulson and J.M. Herbert, editors. *Electroceramics: Materials, Properties, Applications*. John Wiley and Sons, Ltd, 2003.

[6] D.J. Leo, editor. *Engineering Analysis of Smart Material Systems*, chapter 4. John Wiley and Sons, Ltd, 2007.

[7] V. Giurgiutiu and C.A. Rogers. Power and energy characteristics of solid-state induced-strain actuators for static and dynamic applications. *Journal of Intelligent Material Systems and Structures*, 8:738–750, 1997.

[8] G.M. Sessler. Piezoelectricity in polyvinylidenefluoride. *Journal of the Acoustical Society of America*, 70(6):1596–1608, 1981.

[9] T. Furukawa, K. Ishida, and E. Fukada. Piezoelectric properties in the composite systems of polymers and pzt ceramics. *Journal of Applied Physics*, 50:4904–4912, 179.

[10] L. Krakers. Ductile piezoelectric actuator materials. Technical report, Netherlands Institute for Metal Research, 2006.

[11] J. Bohm and *et al.* Czochralski growth and characterization of piezoelectric single crystals with langasite structure: $La_3Ga_5SiO_{14}$ (LGS), $La_3Ga_{5.5}Nb_{0.5}O_{14}$ (LGN) and $La_3Ga_{5.5}Ta_{0.5}O_{14}$ (LGT), Part II, Piezoelectric and elastic properties. *Journal of Crystal Growth*, 216:293–298, 2000.

[12] I. Chopra. Review of state of art of smart structures and integrated systems. *AIAA Journal*, 40(11):2145–2187, 2002.

[13] H.Y. Zhang and Y.P. Shen. Three-dimensional analysis for rectangular 1-3 piezoelectric fiber-reinforced composite laminates with the interdigitated electrodes under electromechanical loadings. *Composites: Part B*, 37:603–611, 2006.

[14] H.A. Sodano, G. Park, and D.J. Inman. An investigation into the performance of macro-fiber composites for sensing and structural vibration applications. *Mechanical Systems and Signal Processing*, 18: 683–697, 2004.

[15] R. Barrett and *et al.* Active plate and wing research using EDAP elements. *Smart Matererials and Structures*, 1:214–226, 1992.

[16] R. Barrett and *et al.* Post-buckled precompressed piezoelectric flight control actuator design, development and demonstration. *Smart Ma-*

terials and Structures, 15:1323–1331, 2006.

[17] S. Aimmannee and M.W. Hyer. Deformation and blocking force characteristics of rectangular thunder-type actuators. In *Proc. of the International Conf. for Emerging System and Technology (ICEST 2005)*, May 2005.

[18] S. Aimmannee and M.W. Hyer. Analysis of the manufactured shape of rectangular thunder-type actuators. *Smart Materials and Structures*, 13:1389–1406, 2004.

[19] K.J. Yoon and *et al.* Design and manufacture of a lightweight piezo-composite curved actuator. *Smart Materials and Structures*, 11:163–168, 2002.

[20] K.J. Yoon and *et al.* Analytical design model for a piezo-composite unimorph actuator and its verification using lightweight piezo-composite curved actuators. *Smart Materials and Structures*, 13:459–467, 2004.

[21] K.Y. Kim and *et al.* Performance evaluation of lightweight piezo-composite actuators. *Sensors and Actuators A*, 120:123–129, 2005.

[22] J. Mulling and *et al.* Load characterization of high displacement piezoelectric actuators with various end conditions. *Sensors and Actuators A*, 94:19–24, 2001.

[23] M.W. Hyer and A.B. Jilani. Deformation characteristics of circular rainbow actuators. *Smart Materials and Structures*, 11:175–195, 2002.

[24] G. Li, E. Furman, and G.H. Haertling. Stress-enhanced displacements in plzt rainbow actuators. *Journal of the American Ceramics Society*, 80:1382–1388, 1997.

[25] Q.M. Wang and L.E. Cross. Analysis of high temperature reduction processing of rainbow actuator. *Materials Chemistry and Physics*, 58: 20–25, 1999.

[26] C. Niezrecki, B. Diann, S. Balakrishnan, and A. Moskalik. Piezoelectric actuation: State of the art. *The Shock and vibration digest*, 33:269–280, 2001.

[27] K. Otsuka and X. Ren. Recent development in the research of shape memory alloys. *Intermetallics*, 7:511–528, 1999.

[28] S. Seelecke. Shape memory alloy actuators in smart structures: Modeling and simulation. *Appl. Mech. Rev.*, 57(1):23–46, 2004.

[29] D.C. Lagoudas, editor. *Shape Memory Alloys - Modeling and Engineering Applications*. Springer, 2008.

[30] M. Achenbach. A model for an alloy with shape memory. *International Journal of Plasticity*, 5:371–395, 1989.

[31] J.E. Massad, R.C. Smith, and G.P. Garman. A free energy model for thin-film shape memory alloys. In *Proc. of the SPIE, Smart Structures and Materials 2003: Modeling, Signal Processing, and Control*, March 2003.

[32] K. Tanaka. A thermomechanical sketch of shape memory effect. *Res Mechanica*, 18:251–263, 1986.

[33] C. Liang and C.A. Rogers. One-dimensional thermo mechanical constitutive relations for shape memory alloys. *Journal of Intelligent Material Systems and Structures*, 1:207–234, 1990.

[34] L.C. Brinson. One dimensional consttitutive behavior of shape memory alloys: Thermomechanical derivation with non-constant material functions and redefined martensite internal variable. *Journal of Intelligent Material Systems and Structures*, 4(2):229–242, 1993.

[35] L.C. Brinson. Deformation of shape memory alloys due to thermo-induced transformations. *Journal of Intelligent Material Systems and Structures*, 7, 1996.

[36] L.C. Brinson and M.S. Huang. Simplifications and comparisons of shape memory alloy constitutive models. *Journal of Intelligent Material Systems and Structures*, 7(1):108–114, 1996.

[37] Bekker and L.C. Brinson. Phase diagram based description of the hysteresis behavior of shape memory alloys. *Acta Materialia*, 46(10): 3649–3665, 1998.

[38] H. Prahlad and I. Chopra. Comparative evaluation of shape memory alloy constitutive models with experimental data. *Journal of Intelligent Material Systems and Structures*, 12:383–395, 2001.

[39] D.J. Leo, editor. *Engineering Analysis of Smart Material Systems*, chapter 6. John Wiley and Sons, Ltd, 2007.

[40] R.D. Spies. An algorithm for simulating the isothermal hysteresis in the stress-strain laws of shape memory alloys. *Journal of Materials Science*, 31:6631–6636, 1996.

[41] M. van der Wijst. *Shape control of structures and materials with shape memory alloys*. PhD thesis, University of Eindhoven, 1998.

[42] G.B. Stachowiak and P.G. McCormick. Shape memory behaviour associated with the R and martensitic transformations in a NiTi alloy. *Acta metallurgica*, 36:291–297, 1988.

[43] H. Tobushi, K. Tanaka, K. Kimura, T. Hori, and T. Sawada. Stress-strain-temperature relationship associated with R-phase transformation in TiNi shape memory alloy. *JSME International journal, Series 1*, 35: 278–284, 1992.

[44] K. Otsuka and X. Ren. Physical metallurgy of Ti-Ni-based shape memory alloys. *Progress in materials science*, 50:511–678, 2005.

[45] H. Tobushi, S. Yamada, T. Hachisuka, A. Akai, and K. Tanaka. Thermomechanical properties due to martensitic and r-phase transformations of TiNi shape memory alloy subjected to cyclic loadings. *smart Materials and structures*, 5:788–795, 1996.

[46] Rogers and Liang. One dimensional constitutive relations of shape memory materials. *Journal of Intelligent Material Systems and Structures*, 1(2):207–234, 1990.

[47] J. Epps and R. Chandra. Shape memory alloy actuation for active tuning of composite beams. *Smart Materials and Structures*, 6:251–264, 1997.

[48] X. Guo, A. Przekop, and C. Mei. Supersonic nonlinear panel flutter suppression using aeroelastic modes and shape memory alloys. In *Proc. of the 46th AIAA/ASME/ASCE/AHS/ASC Structures Structural Dynamics and Materials Conf.*, April 2005.

[49] S. Choi, J.J. Lee, D.C. Seo, and S.W. Choi. The active buckling control of laminated composite beams with embedded shape memory alloy wires. *Composite Structures*, 47:679–686, 1999.

[50] H. Jia. *Impact Damage Resistance of Shape Memory Alloy Hybrid Composite Structures*. PhD thesis, Virginia Polytechnical Institute and State University, 1998.

[51] M. Langelaar. *Design optimization of Shape Memory Alloy Structures*. PhD thesis, Delft Technical University, 2006.

[52] P.G. de Gennes, Ko Okumura, M. Shahinpoor, and K.J. Kim. Mechanoelectric effects in ionic gels. *Europhysics letters*, 50(4):513–518, 2000.

[53] M. Shahinpoor and Kwang J. Kim. Ionic polymerŰmetal composites: Part I. fundamentals. *Smart materials and structures*, 10(4):819–833, 2001.

[54] Han Mo Jeong, Sang Yoon Lee, and Byung Kyu Kim. Shape memory polyurethane containing amorphous reversible phase. *Journal of Materials Science*, 35(7):1579–1583, 2000.

[55] B. Enenkl, V. Klöppel, D. Preiler, and P. Jänker. Full scale rotor with piezoelectric actuated blade flaps. In *Proc. of the 28th European Rotorcraft Forum*, 2002.

[56] S.R. Hall and E.F. Prechtl. Development of a piezoelectric servoflap for helicopter rotor control. *Smart Materials and Structures*, 5:26–34, 1996.

[57] T. Lee and I. Chopra. Design of piezostack-driven trailing-edge flap actuator for helicopter rotors. *Smart materials and structures*, 10:15–24, 2001.

[58] K. Singh, J. Sirohi, and I. Chopra. An improved shape memory alloy actuator for rotor blade tracking. *Journal of Intelligent material systems and structures*, 14(12):767–786, 2003.

[59] D.K. Kennedy, F.K. Straub, L. McD. Schetky, Z. Chaudhry, and R. Roznoy. Development of an sma actuator for in-flight rotor blade tracking. *Journal of Intelligent material systems and structures*, 15: 235–248, 2004.

[60] Description of the upwind reference wind turbine - version 9. Technical report, UpWind Project, 2007.

Chapter 4

The feasibility of the smart rotor concept

Scarecrow: *Oh, I'm a failure, because I haven't got a brain!*
- Dorothy: *Well, what would you do with a brain if you had one?*
Scarecrow: *Do? Why, if I had a brain, I could...*

Scene from 'The Wizard of Oz', *MGM, 1939*

4.1 Introduction

In the previous chapters an introduction into load control concepts and adaptive materials was presented. In this chapter one of the control algorithms of Section 2.4.3 is elaborated in a proof-of-concept of the smart rotor concept in a series of wind tunnel experiments that where conducted. Moreover, both the sensors and actuators were PZT-based, see Section 3.2 in the previous chapter. The importance of understanding the blade's dynamics as well as how to integrate the load alleviation concept as a sensor, actuator and control system is discussed. The experiments were conducted in two phases, which are discussed separately here. Firstly, a series of non-rotating experiments was performed in a closed wind tunnel and secondly, experiments were performed on a rotating set-up in an open wind tunnel. Details on the controllers are addressed by [1, 2]; here the focus will be on the design and performance of the system. Parts of this chapter were published in [3], and [4].

4.2 Preliminary non-rotating load alleviation experiments

In a first approach these experiments were performed on a non-rotating blade. In these experiments the blade operates as a cantilever beam with uniform cross-section - the DU96 W180 aerofoil profile. In principle this is a 2D experiment because the blade has a constant cross-section. On the other hand, the blade is free to vibrate at one end and only part of the blade is equiped with flaps.

4.2.1 Structural design

The blades were designed to be of a glass-epoxy laminate, which was infused in a double rigid mould, after being wrapped around a solid foam core. Thereby, the gap between the mould surface and the foam core was filled with resin and the preform was infused. Through this process, a strong but flexible blade with a smooth outer surface could be obtained. The glass reinforcement was a S303 8H-satin weave (Ten Cate Advanced Composites, Nijverdal, The Netherlands) which was used for its fine tows and good drapability. The employed resin was an Epikote 04908 resin with an Epikure 04908 hardener (Hexion, Rotterdam, The Netherlands). This is a resin that is used in the wind turbine industry, but it was specifically employed here for its long pot life, which was needed for infusion. The chosen foam was a 75kg/m^3 Airex C70.200 (Airex AG, Sins, Switzerland).

The laminate lay-up was used to tune the blade dynamics, stiffness and strength to the desired values. This meant that quite a flexible blade had to be attained. At the same time, however, strength and buckling requirements had to be met. The blade was analyzed using a finite element (FE) model in Abaqus. The FE model consisted of quadratic shell for the skin and solid elements for the foam core with aluminium inserts. The material properties were obtained from manufacturers' data or from previous experiments [5]. The properties of the laminate were adjusted for a lower fibre volume fraction V_f using a micro-mechanical modeller [6]. V_f was relatively low because the fabrication process leads to a lower compaction of the glass weave.

Several analyses were performed with the FE model. Firstly, a static analysis was performed to analyse the strength of the blade. To evaluate laminate strength, a maximum stress criterion was implemented. Finally, a linear modal analysis was used to evaluate the eigenmodes.

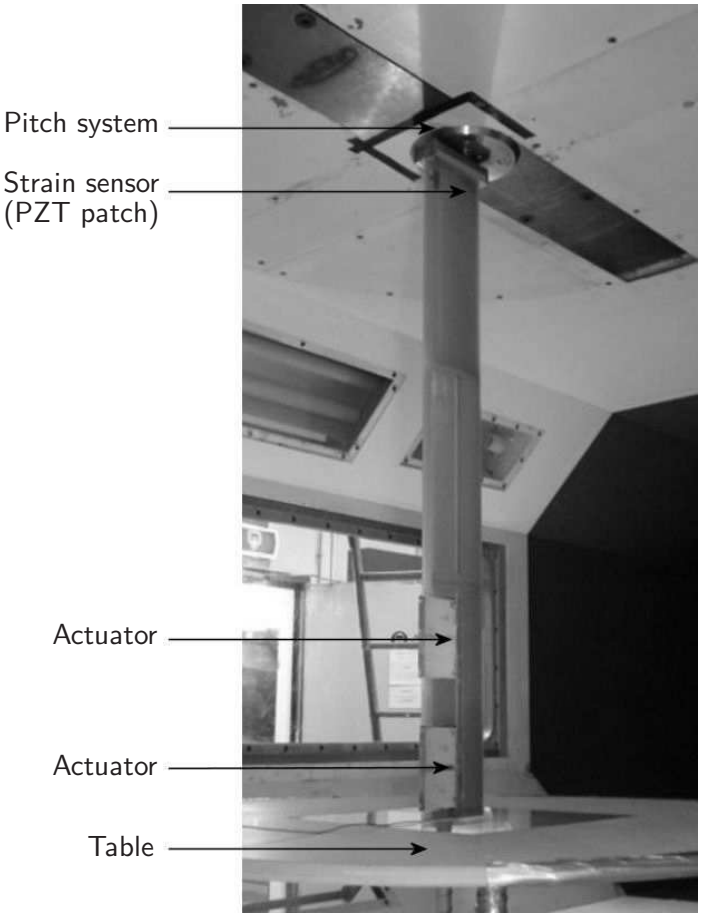

Figure 4.1: Wind tunnel set-up for load alleviation experiments. The airflow goes from right-to-left in this picture.

4.2.2 LST wind tunnel set-up

The blade is mounted onto a pitch system at the wind tunnel's top wall and free to deflect over a table at the bottom side. The pitch system can be used to change the mean angle of attack, as well as inducing the dynamic disturbances that are to be mitigated. Rotational effects are thus not taken into account and the blade, unlike actual HAWT rotor blades, has no twist or taper but constant thickness. The table ensures that there are no tip-effects, because only 2D aerodynamic analyses were made. However, additionally experiments without table were also performed. See Figure 4.1 for a picture of the set-up.

For controlling the aerodynamic loads it was chosen to implement partial

camber control: the aft half of the cord at certain stations in the outboard section of the blade was made deformable by an actuator, therefore enabling a controllable change in camber of that part of the span. Such aerodynamic load control systems were also suggested for wind turbine blades by Buhl [7] and Joncas [8] and intensively discussed before. The actuator is based on a piezoelectric Thunder actuator (Face International Corporation, Norfolk, Virginia, USA), which was discussed in Section 3.2.4. The actuator is covered with a soft polyether foam which in turn is covered with a latex skin to provide a smooth surface. See Figure 4.2 for the actuator design.

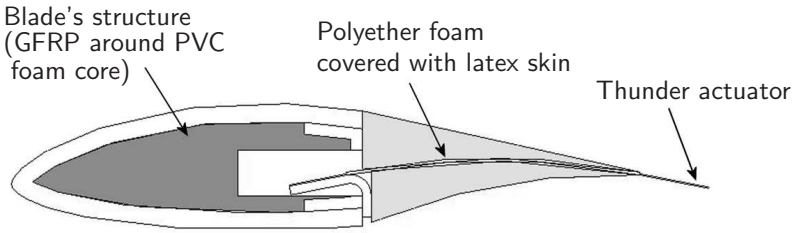

Figure 4.2: Design of the active control surface.

4.2.3 Control

In order to control the actuators and read the signals from the sensors, a dSpace (dSPACE GmbH, Paderborn, Germany) system was employed for both feedforward as feedback experiments. With this system, the sensors signals are converted to a digital signal and sampled. These signals can be recorded as well as fed to a feedback control algorithm. The output of the controller (whether it's feedforward or feedback) is converted to an analogue signal and send to the different actuator amplifiers. The system of processing signals as well as the feedback controller is designed in Simulink (The MathWorks, BV, Gouda, The Netherlands) and compiled onto the dSpace system. In- and outputs for e.g., setting values and plotting and recording signals can also be incorporated and linked to Control Desk, dSpace's virtual instrumentation software that acts as a Graphical User Interface (GUI), see Figure 4.3. From the dSpace hardware, one signal goes to the pitch system actuator, which is a linear motor and two signals go to the high voltage amplifier which drives both sets of piezoelectric benders.

Inputs to dSpace include: the actual pitch displacement (feedback from the pitch system), the actual voltage on the piezoelectric benders (output of the amplifier), strain at the root of the blade and acceleration of the tip.

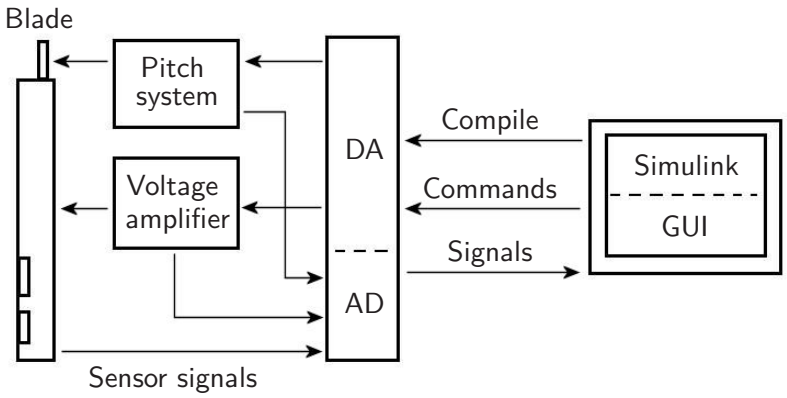

Figure 4.3: Set-up of the control system.

A critical part of the blade's design is the dynamics. The first natural vibration mode should be scaled with respect to two parameters:

1. The frequencies of the disturbances on the blade. HAWT blades are mainly subjected to loads associated with its rotational frequency or multiples of that - 1, 2 and 3P. Proximity of vibrational modes will influence the dynamic response under loading. However, this can also be tuned by changing the frequency spectrum of the disturbances which is controlled by the pitch system.
2. The second type of dynamic effects to take into account, is the unsteadiness of the aerodynamics. This is expressed by the parameter k, called the reduced frequency:

$$k = \frac{\omega b}{V} \tag{4.1}$$

in which ω is the frequency of the disturbances, V the undisturbed airspeed and b the half cord of the aerofoil. With it, frequencies of disturbances can be scaled to the dimensions of the blade and the wind speed. The aerodynamic delay, the phase between a sine on the flap and the resulting lift forces, is dependent on this reduced frequency [9].

The blade is designed to match the frequencies that were derived from these considerations. The target first flapping frequency was determined to be 19.2Hz and in the actual blade the eigenfrequency was 12.5Hz. This was easily compensated for by changing the airspeed and the frequencies of the disturbances to which the blade is subjected. The blade was tuned

by changing the internal structure, viz. the number of glass-epoxy plies and the presence of a spar. A spar was added in the tip because here the actuator slots were cut out. The spar adds additional stiffness and strength and can be used as mounting point for the actuators.

The blade was produced using vacuum infusion in a closed mould and after assembly of the sensors and actuators, it was mounted on the pitch system and connected to the control hardware. Several tests were conducted:

- Feedforward on disturbances with a sinusoid signal.
- Feedback control on a sinusoid signal with a strain sensor at the root.
- Feedback control on a spectrum angle of attack disturbances that resembles the turbulence that an actual blade experiences.
- Feedback control on a step on the angle of attack (simulating gusts and tower shadow)

4.2.4 Results and discussion

The results of the first set are promising. Here the focus will be on the results on the step experiments. See van Wingerden [1] for details. In these experiments a step, simulating a gust, was put on the pitch of the blade which triggered a sudden change in lift. This was firstly done without controlling the flaps and secondly with feedback control. The results in two cases, $\alpha = 6^\circ$ (around maximum C_L/C_D) and α=10° (higher than the static stall angle), can be seen in Figures 4.4 and 4.5. A significant reduction in the vibration behaviour, as well as a reduction of the first peak can be observed.

Observing Figures 4.4 and 4.5 an important conclusion can be drawn: the control system based on structural response is able to considerably increase the aerodynamic damping and to decrease the peak load. Measuring the inflow of the could enhance the performance of the system, although it would also greatly complicate it. Moreover, it can be concluded that regarding the discussion in Section 2.4.3, that suppressing the blade's modes is very important in dealing with the response to a gust.

4.3 Rotating experiments

This issue of interaction between excitation loads and blade resonance, taking into account sampling of higher-P loads due to rotor-wake interaction

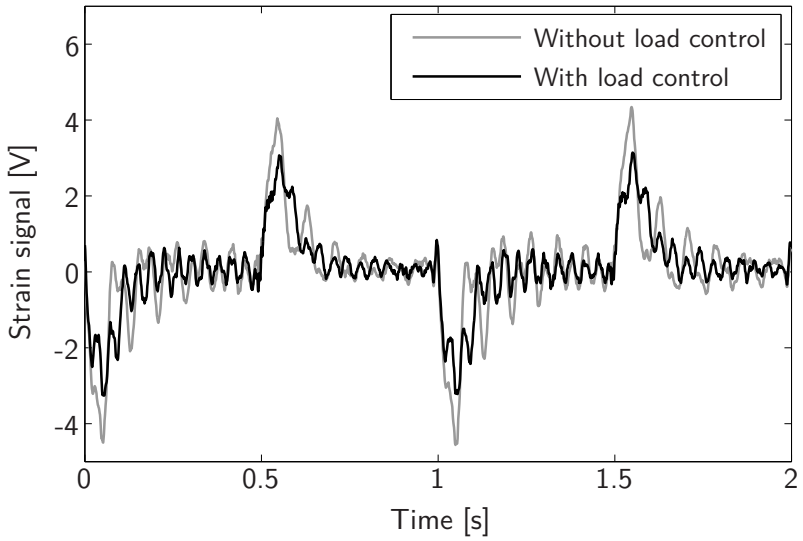

Figure 4.4: Strain signal at the root as a result of a step on the pitch at 6° angle of attack (close to maximum C_L/C_D, desired operating point for the DU-96 aerofoil).

and the presence of multiple blades on a (flexible) turbine has a large influence on the performance of the system. Therefore, tests were performed on a rotating set-up, taking into account all these issues. For this purpose a scaled rotor was built on which to perform load reduction experiments in the TU Delft's OJF wind tunnel. This section discusses the design of the system, encountered the issues and the load reduction potential that was observed.

4.3.1 Design and manufacturing of an aero-elastically tailored blade

Firstly, the design of the different components of the blades, which include the design of the base structure of the blade, the actuators and the sensor array, are discussed. The design on the blades for the rotating set-up has a slightly different aim than the non-rotating set-up. Moreover, the manufacturing is also more complex and the design is more thorough, including a sensor placement analysis and a more elaborate aerodynamic design.

Conceptual design

As illustrated in the non-rotating experiments, an important issue in the design of the system, is the load spectrum that is under consideration because

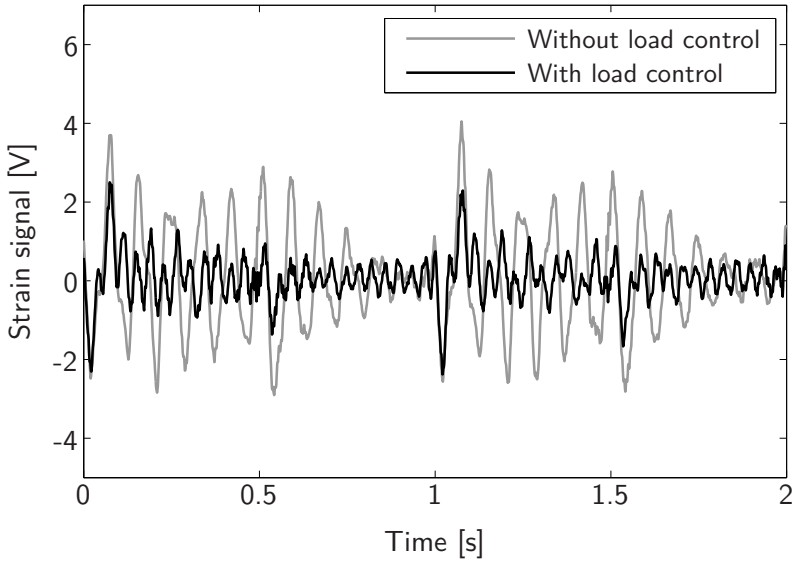

Figure 4.5: Strain signal at the root as a result of a step on the pitch at 10° angle of attack (higher than the static stall angle).

of the interaction between rotational speed and blade harmonics.

A turbine is subjected to several disturbances, most of which are related to the rotation of the rotor through a wind field with spatial variations and thus they occur with the rotational frequency of the rotor. Examples of these variations are tower shadow and wind shear and due to sampling of these 1P (once per rotation) disturbances, because multiple blades are mounted to one hub, the blades also experience multiple P loads. The interaction between the first flapwise bending mode and these multiple P excitation loads is an important aspect in the control of the rotor and for the reduction of fatigue loads. After all, disturbances for which the frequency is close to a natural mode excite the blade more severely, as compared to low frequency, quasi-static disturbances. This should be incorporated in the scaled experiment.

Summarizing, the load spectrum and dynamic behaviour of the scaled turbine should reflect that of the full scale reference design. This was achieved by scaling the first flapwise bending mode frequency of the blades with the rated rotational frequency of the turbine:

$$\frac{f_{model}}{\Omega_{model}} = \frac{f_{ref}}{\Omega_{ref}} \rightarrow f_{model} = \frac{f_{ref}\Omega_{model}}{\Omega_{ref}} \tag{4.2}$$

in which f relates to the frequency of the first flapwise bending mode and

Ω to the rotational frequency. The subscript ref refers to the 5MW Up-Wind reference turbine and $model$ to the scaled model. See Table 4.1 for the operational and design parameters that were employed in scaling. The rotational speed of the rotor was set to 7Hz, which sets the target for the first bending mode to 24Hz. Reynolds scaling was not employed, nor scaling to the reduced frequencies k, see equation 4.1, because these proved to be secondary effects during the non-rotating experiments.

	Reference Turbine	Scaled Turbine
Rated Rotational speed [rpm]	12.1	430
Rated wind speed [m/s]	11.4	10
Rotor Diameter [m]	60	1.8
Design TSR [-]	7	5
First flapwise bending mode [Hz]	0.68	24

Table 4.1: Operational parameters that are used for scaling and the aerodynamic design.

Aerodynamic design

The aerodynamic design was based on the operational parameters, while keeping the structure and the actuator design in mind. The design parameters that determined the shape were the twist and chord distribution along the span and the shape of the profile at different radial stations.

The profile shapes along the length of the blade, which determined the absolute thickness of the blade, were initially left open to be determined in the structural optimization process because these had a large influence on the stiffness of the blade. However, after some iteration, it was determined that a slender DU96-W180 profile along the whole span of the blade was needed in order to obtain the desired structural properties, i.e. a relative low frequency for the first eigenmode.

The twist and chord distribution were primarily based on the aerodynamic performance of the turbine and derived using a Blade Element Method (BEM)-based optimizer. In this optimization procedure, a restriction was formed by the installation of the actuators. To successfully implement the actuators in the tip, a straight tip - without twist and taper - was desired. A chord of 12cm was chosen for this section. These specific dimensions were chosen because of experiences obtained in the previous experiments. Here it led to a tip Reynolds number of $2.4 \cdot 10^5$, which was much lower than the

reference turbine. However, as mentioned before, it was not tried to employ Reynolds scaling in this work. For the performance of the aerofoil sections with actuators, XFOIL [10] calculations were performed on the adapted aerofoil shape (also see 'Actuator design' below). The calculations were corrected for rotational effects [11].

With these requirements and the turbines operational settings in mind, the aerodynamic design could be optimized. Due to the restrictions mentioned above, attaining an aerodynamically optimal design turned out to be impossible. But obtaining an optimally performing turbine was not the goal of this project, so the design was adapted to fit the shape requirements. Moreover, the predicted loading was enough to drive the turbine and provide an observable and distinctive sensor signal. The derived twist and chord distribution can be seen in Figure 4.6.

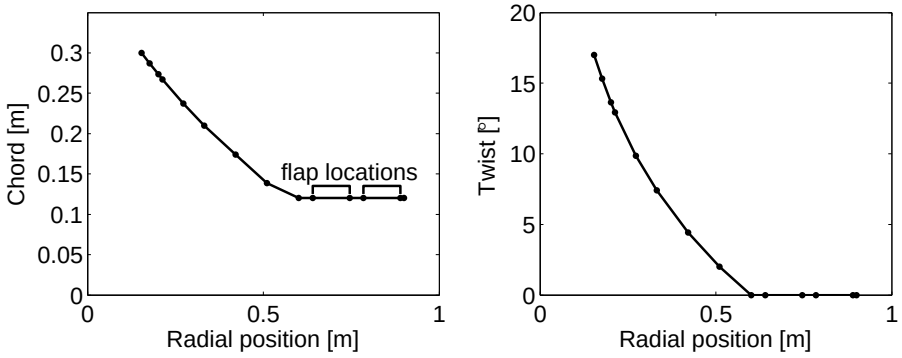

Figure 4.6: Twist and chord distribution of the blade.

Structural design

For manufacturing, the same technique as with the blade in the non-rotating experiment was used; infusion of a preform that was wrapped around a foam core in a double rigid mould. In addition, the same fiber and resin material was used. For the foam core, however, a 200kg/m^3 Airex C70.200 foam was implemented. This high density foam was chosen because it allowed for high accuracy milling and because it provided good support for the skin, which is much thinner than with the prismatic, non-rotating blade.

Unfortunately, in a second series of tests, which were performed after the one described in Section 4.2, the non-rotating blade failed at the root. The lessons learned from this failure are expressed in three design features. Firstly, the foam core was fitted with a steel instead of aluminium foot to mount the blade to the hub. Steel was used because it adheres better than

aluminium and also the foot extended further into the blade. Secondly, the foot was designed such that the skin laminate shape-locks around the foot. In addition, an UD roving is wrapped around the foot so the laminate cannot fail on its splices. Finally, two 5mm holes were drilled through the foam, one at, and the other just behind the pitch axis along the length of the blade. One hole was used to fit the sensor and actuator cables and the other to fit a safety cable which was attached to both the steel foot and an insert at the tip. If the laminate would fail, the blade would at least stay attached to the hub.

The straight outboard section was equipped with a glass-epoxy spar. The spar was prefabricated and assembled with the foam core and steel inserts before infusion of the skin. The spar acted as mounting point and reinforcement where the actuator slots were cut out after resin infusion of the skin. It consisted of 8 plies of the same glass-reinforcement and epoxy materials as the skin.

As in the previous experiments, the laminate lay-up was used to tune the blade dynamics, stiffness and strength to the desired values. As mentioned, a target eigenfrequency of 24Hz for the flapwise bending mode was the goal. Again, a FE model was set up, this time in Ansys, The loads for the analysis were obtained from the BEM analysis and stresses and eigenmodes were evaluated. In addition Plantema's theorem was used to evaluate for skin wrinkling [12]. An iterative design procedure proved that with a laminate thickness of 0.5mm the stresses stayed within allowable limits and skin wrinkling would not occur. A linear modal analysis predicted a first flapwise bending mode frequency of 33Hz, which was higher than the target frequency of 24Hz, but linear modal analyses typically overestimate eigenfrequencies. Moreover, the blade mounting to the hub was more flexible than modelled.

Actuator design

Camber control was achieved by sawing slots at two locations in the blade's straight outboard section, as indicated in Figure 4.6. The outer slot was placed as far outboard as possible in order to have as large an effect as possible on the root bending moment when actuating the flap. The second slot was placed as far inboard on the straight section as possible so the actuators can also control higher modes, which would require exerting a moment at the tip by opposite flap motion. Here we focused on the first bending mode, in which case both flaps work synchronously. The slots were fitted with the actuators. In contrast to the actuators on the blade for the non-rotating experiment, Thunder actuators were placed in line with the

suction side of the aerodynamic profile. See Figure 4.7.

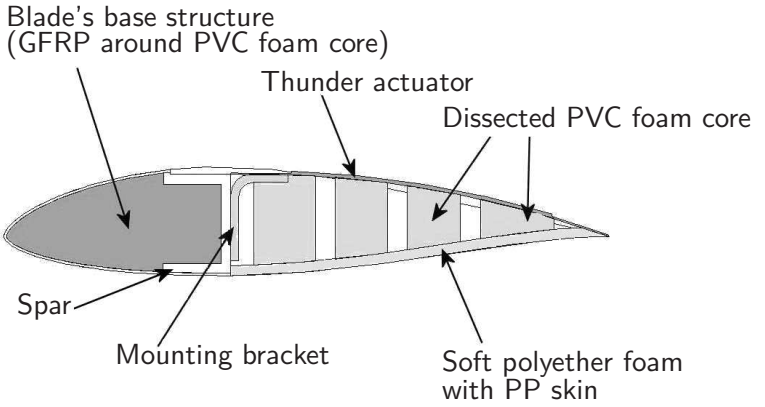

Figure 4.7: Design of the morphing camber control surface

The actuators are much larger in chordwise sense than would be needed on full scale blades, but here they were implemented as 60% of the chord for the purpose of producability of the flaps and flap authority. The curvature of the actuators coincided fairly well with the curvature of the profile as can be seen in Figure 4.8. Placing the actuators here would assure a smooth and solid surface on the suction side. This was needed for more predictable performance of the actuator and to have a qualitative good boundary layer over the actuator. This is believed to be an improvement over the actuator design of Figure 4.2. Here, the slight mismatch in surface curvature between the baseline profile and actuator surface was considered acceptable.

The remainder of the shape of the aft part of the profile was achieved by filling the slot with foam and covering it with a polypropylene (PP) film. Two types of foam were implemented: dissected rigid foam filled the largest part of the space; this was covered with a soft polyether foam patch to smoothen the sections of the rigid foam, see Figure 4.7. The rigid foam was implemented to prevent the suction side from denting under the aerodynamic pressure, which was also observed in the previous experiments. The Thunder actuators were attached to the blade by means of an aluminium bracket to which it was adhered. This method of mounting increased the first eigenfrequency of the bender to about 90Hz, compared to the 40Hz that was observed when using a bolted connection. A weak part of the actuator design is still the flexible skin on the pressure side, because it does not pose a hard, smooth surface. Predictions on flap performance were based on XFOIL calculations for rigid flaps. The shape of the profile was obtained using measurements of the actuator shape and deflections. It was,

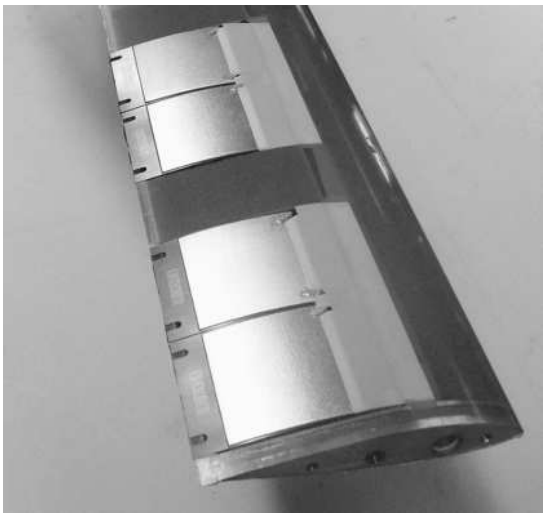

Figure 4.8: Installed Thunder actuators, suction side view

though, quite hard to estimate actual flap angles. This means that it is not known what the induced ΔC_L is. However, for the controller the flap is part of the system's black box, and this information is not required.

Blade and sensor testing

A different set of experiments was conducted to evaluate the blade's behaviour and the sensor performance. Three strain sensors were evaluated; strain gages, PVDF-patches [13] and MFCs (Smart Material Corp., Sarasota, Florida, USA) [14]. The blade was subjected to several dry tests outside the wind tunnel to test the sensor performance and to validate the FE model. Firstly, the blade was excited at the outboard section by a sinusoid signal and the sensor signals were recorded.

All sensors seemed to capture the excitation signal well, although with different signal to noise ratio's. In addition, a free vibration test was performed. From the different tests, conclusions about the performance of the different sensors can be drawn. In Figure 4.9 the response of different sensor signals to a transient vibration can be seen.

The magnitude of the sensor signals could be amplified, but several conclusions can be drawn about the quality of the signal. First of all, the PVDF film showed a clear spike at 50Hz. Because of its low capacitance it easily picked up electro magnetic interference. The MFC signal followed the behaviour of the captured strain well. Actually, the MFCs proved to give the best signal and, in contrast to strain gages, the signal required no amplifier.

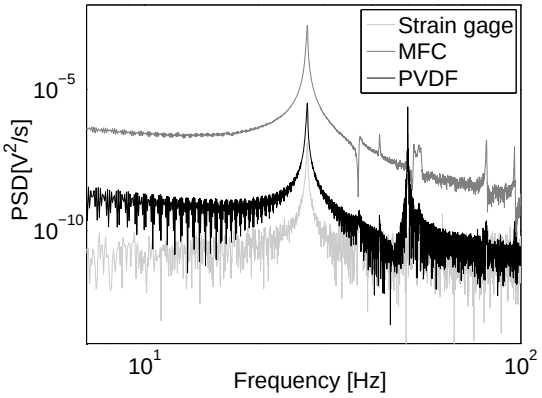

Figure 4.9: PSD of the sensor signals to a transient load

However, because of their high impedance they are quite susceptible to electromagnetic noise, but not as severe as the PVDF. Here, proper shielding and filtering mitigated the noise. The electrodes of the MFC were bridged by a resistor and a capacitor. In this way, effectively a sensor with a high pass filter was obtained. Two MFCs were adhered to each blade - one on the pitch axis to measure normal stresses that arose from a flapwise bending moment and one on the leading edge to measure the strains associated with an edgewise bending moment. The optimal location was determined using a harmonic analysis. Through this analysis the strain magnitude and phase behaviour (sometimes referred to as 'delay' in the wind energy community) at different locations on the blade surface as a result of an excitation force can be derived.

The goal is to obtain so called collocated behaviour [15, 16]. With collocated control, the sensor and actuator are associated with the same degree of freedom of the system. This is obviously the case when a displacement transducer and actuator are placed at the same location. But in the case of vibration of a cantilevered beam which is measured by a strain sensor, the displacement at the actuator location is associated with a strain elsewhere. This relation, as a function of excitation frequency, can be determined with the harmonic analysis. One of the features of a collocated sensor-actuator pair is that when observing the Bode plots, the gain plot is characterized by alternating resonance and anti-resonance peaks. In the phase diagram this results in a phase lag between 0 and -180 degrees. As can be seen in Figure 4.10, this is obtained for excitation at the inboard flap, but not for the outboard flap. However for the frequency range of interest the behaviour is acceptable.

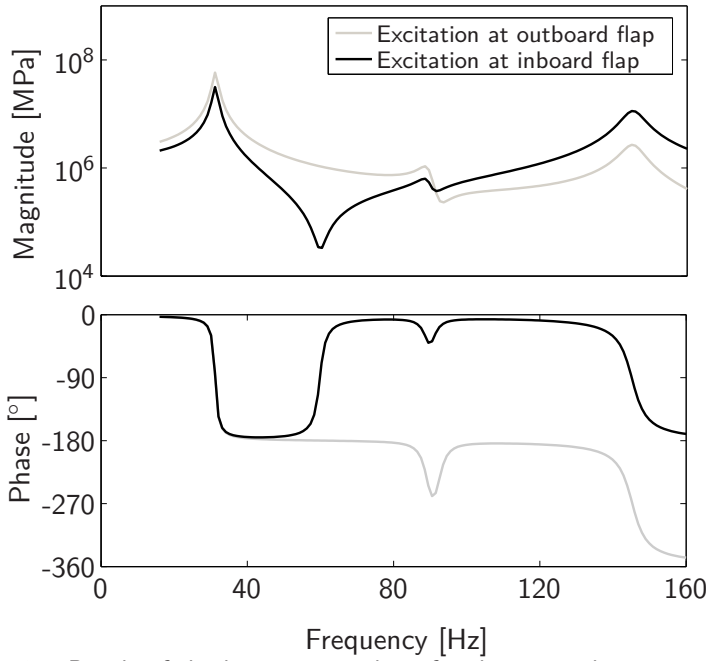

Figure 4.10: Result of the harmonic analysis for the sensor location on the pitch axis to a flapwise bending excitation.

Finally, a static experiment was performed and only 4% deviation in stiffness between the FE model and the test blade was observed.

4.3.2 Wind tunnel set-up

In this section the set-up in the wind tunnel is discussed, which includes the specifications of the tunnel itself, an overview of the whole system and the design of the controller. The controller was based on a measured state space model of the turbine, using system identification techniques. Thus the controller was designed and tuned using data obtained from experiments on the blades mounted on the turbine.

Wind tunnel and turbine

The experiments were conducted in the OJF wind tunnel [17]. This tunnel has a closed circuit with an open test section. The air travels through the circuit in the following manner. Starting just before the rotor plane, it enters the test section through an octagonal nozzle, creating a steady jet with an

effective diameter of 3 meter. There are little or no wall effects because the section is 6 meter wide and 6.5 meter high; much larger than the jet. See Figure 4.11.

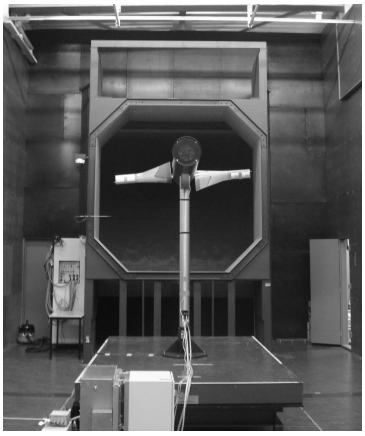

Figure 4.11: The turbine in the test section, with the rotor in the jet. Picture was taken in the direction opposite to the airflow.

The air is collected at the back of the test section, cooled, and fed back into the tunnel's fan after the flow direction is reversed around two 90° corners with a series of corner vanes. After the fan, the flow direction is again reversed around a set of corner vanes. Before it is blown through the nozzle back in to the test section, it enters a settling chamber with several rows of wire meshes to reduce the turbulence levels, which are measured to be 0.1%. The tunnel's fan is powered by a 500kW motor with which a maximum air speed of 35m/s in the jet is attainable.

The blades were mounted to a small turbine in the wind tunnel, see Figure 4.12. The turbine is designed specifically for model tests in the OJF. Its generator is actually a synchronous AC servo motor, with a maximum power of 5kW. If the turbine works as a WECS and the shaft torque is negative, then the motor works as a generator and electric power is dissipated by a dissipator.

Feedback of the rotor speed and position is done through an encoder. The rotor plane is 1m upwind of the tower so the blades experience no tower shadow. The conical hub is mounted to a shaft that runs along the whole length of the nacelle. The front end of the nacelle between the hub and the generator, that is installed on top of the tower, only contains the drive shaft. The aft section contains the slip rings that transferred signals from and to the fixed world. The hub has a diameter of about 30cm. The tower has a diameter of about 15cm and a helical cable is wound around the tower (see

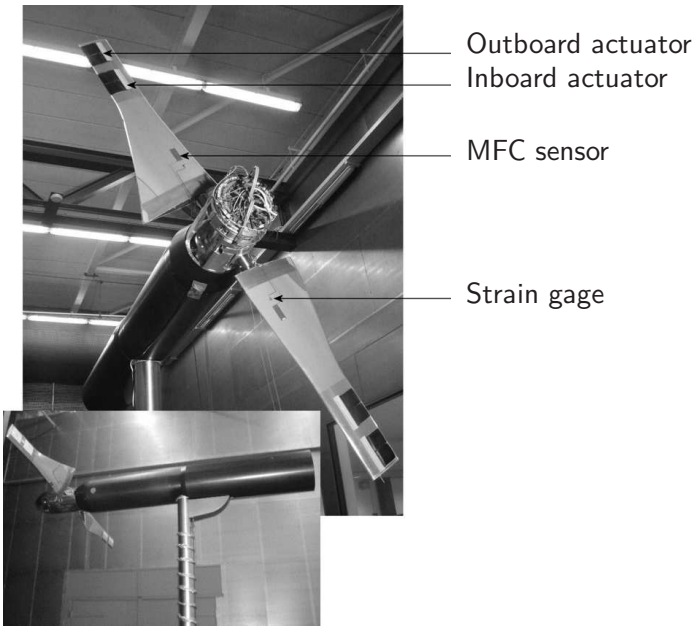

Figure 4.12: Wind tunnel set-up for load alleviation experiments. At the bottom the fully installed turbine can be seen. The air flows from left to right.

Figure 4.12) to suppress flow separation and tower vibrations resulting from that. The turbine's controller is programmed through a LabVIEW system (National Instruments Netherlands BV, Woerden, The Netherlands) which acts as a GUI. The actual operational parameters, such as generator speed and torque, are also fed into this LabVIEW system to be displayed on screen for monitoring purposes. In the experiments discussed here, the control of the generator was set to speed control.

All actuator and sensor cables of the blades were connected according to the scheme in Figure 4.13. The signals were fed through the hub and then transferred over slip rings to and from the fixed world. The hub was also powered by a 7V DC voltage. This was used to power the accelerometers in the blades and the strain gage amplifiers. The signals of the MFCs were transferred unamplified. The actuation signal for the flaps was amplified on the ground and then transferred to the blades over the slip rings.

As with the non-rotating experiments, the controller for the flaps was designed and programmed in a Matlab and Simulink environment and compiled to the dSPACE real time control system. Commands, such as manual flap control and controller gains, could be altered in the ControlDesk Graphical User Interface (GUI). Moreover, the measurement signals were

also plotted in ControlDesk and recorded on the hard disk. All signals to and from the blade as depicted in Figure 4.13 were transferred to the hub in two fold; one set for each blade.

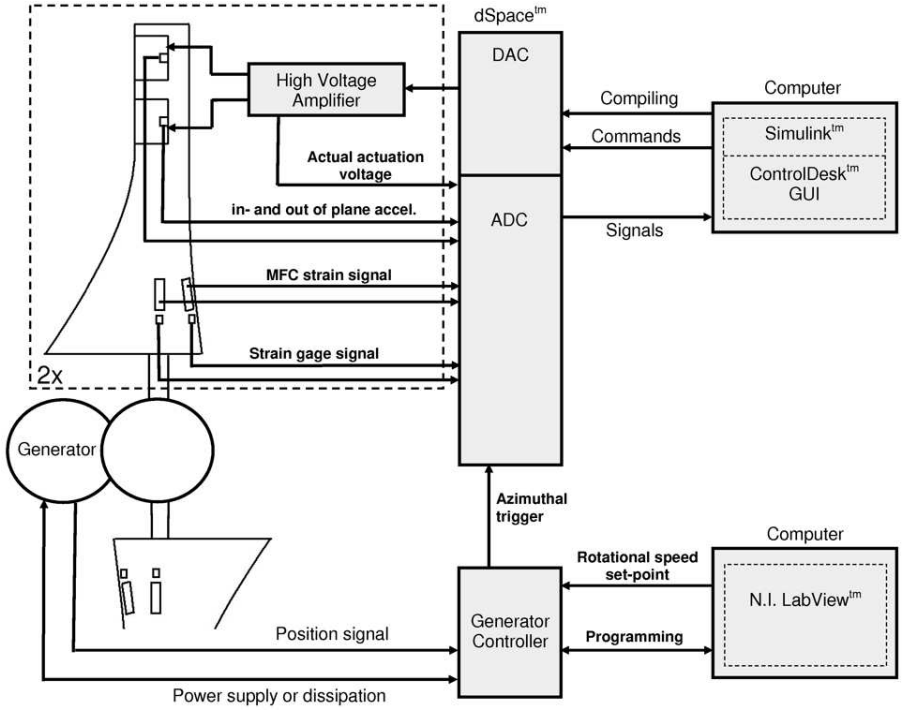

Figure 4.13: Control scheme of the smart rotor

As can be seen in Figure 4.13, the turbine and rotor control systems were fully separated, except for the recording of the azimuthal trigger. The only task of the LabVIEW-controlled system was to maintain constant rotor speed. The dSPACE system, on the other hand, was only concerned with the loads on the rotor blades. It had no control over the rotor speed or torque. The two systems were separated in order to have constant operational conditions of the turbine when the rotor was subjected to different external fluctuations.

Operational conditions

A series of experiments was performed. Here we focus on the results of the rotor in yaw. 0 and 5° yaw were tested. The no-yaw condition was tested as a baseline, but this case already posed a significant load case as we will see later. The rotational speed was set to 370rpm although the

rated rotational speed is 430rpm. This had to be done, because of problems with controlling the rotor speed at high rpm. Although the rotational speed in the experiments presented here was not the rated speed, a similar interaction between rotationally induced disturbances and the first flapwise bending mode was observed because the 4P loads were still close to the first flapwise bending mode, see Figure 4.14. The wind speed was changed to 7m/s. This resulted in a slightly higher TSR than as designed. This was done in order to increase the power conversion.

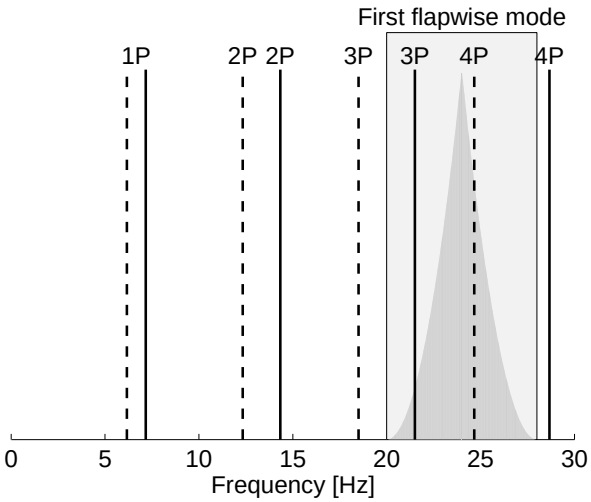

Figure 4.14: Interaction between the rotational frequency and the blade's first eigenmode. The dashed lines mark 370rpm and the solid lines 430rpm. The frequency range over which there was an interaction between the multiple-P loads and the first flapwise bending mode, is indicated as the light-grey area. In this, the resonance peak is schematically represented in grey, with its peak at 24Hz.

The exact operation point of the turbine, in terms of thrust and power coefficient, was hard to determine because the thrust and torque measurement capability of the turbine was not available when the tests were performed.

Controller design

A dynamic state space model was obtained through system identification [18]. The system's inputs were the control signals to the high voltage amplifiers that drove the Thunder actuators and the system's outputs consisted of the MFC sensor signals. The flaps were given a GBN-noise signal, a block signal with a fixed amplitude and a certain bandwidth, and the response of

the blade was measured through the MFCs. In all experiments reported here the in- and outboard flap were being controlled by the same actuation signal, as depicted in Figure 4.13. This effectively reduced both flaps to one flap, but in future experiments, the flaps can be operated individually. The results can be seen in Figure 4.15. This figure displays the transfer from a signal to the flaps on the respective blades, to the strain signal on both blades, as a function of the actuation frequency. There was a considerable amount of coupling, indicated by the high values for the transfer between flap actuation on one blade to the sensor on the other. (See the top-right and bottom-left graphs in Figure 4.15).

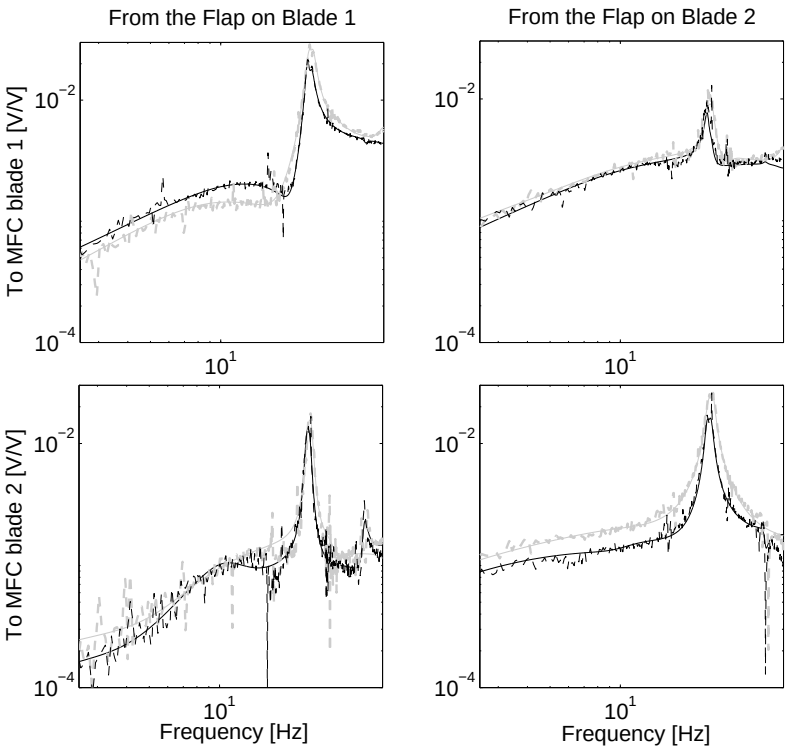

Figure 4.15: Bode gain plots of the measured flap actuation to blade load measurements and the fitted state space model. Grey depicts the model for 420rpm and black for 370rpm. The dashed lines represent the measurement data and the solid lines the obtained model.

Several controllers were designed using this state space model. Firstly, a Single Input, Single Output (SISO) PID controller, similar to those used in previous experiments [1] was implemented. Two SISO controllers, one for each blade, worked parallel to each other, but the two gains were tuned

successively. The controllers took their input signal from the MFC on each respective blade and provided a single actuation signal for both flaps on that same blade. Secondly, a $\mathcal{H}_\infty$ Multiple Input Multiple Output (MIMO) feedback controller with the same in and outputs was designed with a combination of notches at 1, 2, 3 and 4P loads, as well as added damping to the first flapwise bending mode.

In addition, the potential of feedforward control was investigated. The controller was tuned by Repetitive Control (RC) [19] scheme. Because it is less common, its implementation requires some explanation. RC is a form of feedforward control and can be applied to systems which are excited by the same disturbance over and over again, which is clearly the case for rotating turbines. With RC, the error signal over a certain cycle, called a trial, is captured and after each trial the controller parameters are updated. Moreover, the number of parameters that is to be tuned can be reduced by selecting a certain set of base functions, resulting in a so called structured feed forward signal. Here, a sine and cosine function was chosen with a frequency that was equal to the rotational speed of the turbine because the objective was to reduce the 1P loads:

$$u_k^{(ff)} = \theta_k^s \sin(\omega t) + \theta_k^c \sin(\omega t) \tag{4.3}$$

In equation 4.3, θ_k^s and θ_k^c are the parameters to be tuned and are updated every trial, ω is the rotational speed of the turbine and the subscript k denotes the k^{th} trial. The technique was attractive because an accurate dynamic model of the system was not needed. A scheme for the feedforward controller, including a feedback controller, can be seen in Figure 4.16.

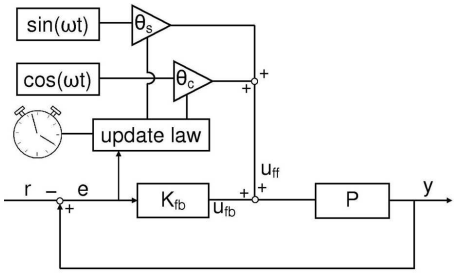

Figure 4.16: Scheme for feedforward control, including a feedback controller. P denotes the plant and K_{fb} the feedback controller.

Both the feedforward and the feedback controller acted on the error signal and provided an actuation signal, but the feedforward controller provided a preselected signal - here the sum of a sine and cosine function - for which the gains were tuned by an update law. The timer was added in Figure 4.16

to the update law to indicate that the update law was not a continuous process, but was executed once every trial. On the smart rotor turbine the timer was implemented in the form of the azimuthal trigger that generated a pulse when the rotor was in a certain azimuthal position. Therefore, small errors in rotational speed did not disturb the update process, as would be the case when the update law had been executed every assumed time period.

The challenge was to tune θ^s and θ^c. Algorithms were implemented in collaboration with the DCSC, see [19] and [2] for details.

4.3.3 Results

In this section the results obtained with the setup and the different controllers as discussed above are presented. Three cases are discussed. First, the load reduction attained with two uncoupled SISO controllers will be shown. Second, the results of the MIMO controller and finally, the load reduction attained by the MIMO controller, in combination with adaptive feed forward control on the 1P loads will be presented. An overview of the load cases and the different controllers used in those respective cases are depicted in Table 4.2.

Controller configuration	Controller type	Case 1	Case 2	Case 3
SISO	PD with notch filter	X		
MIMO	$\mathcal{H}_\infty$		X	X
Feedforward	Repetitive Control			X

Table 4.2: Different load cases with controller types.

SISO control

The results obtained with the SISO controllers for different yaw angles can be seen in Figure 4.17 and 4.18. In these spectra plots the 1, 2, 3 and 4P load spikes, as well as the resonance peak at 24Hz - as designed - are clearly visible. Also, the amplification of the 4P spike because of the interaction with the first bending mode can be observed. Comparing both figures, one would have expected a higher induced loading for the 5° yaw load case, but this is not the case. The exact reason for this is yet to be determined, but it could be that in the 0° load case the induced disturbances were so large that the added effect of a small yaw angle posed only little additional loads. Also, a difference of the behaviour of blade 1 and 2 can be observed. This could be attributed to small differences in blade manufacturing and a slight

unbalance of the rotor. Regarding the performance of the SISO controller, it can be concluded from the figures that the SISO controller failed to add damping to the first mode for blade 2.

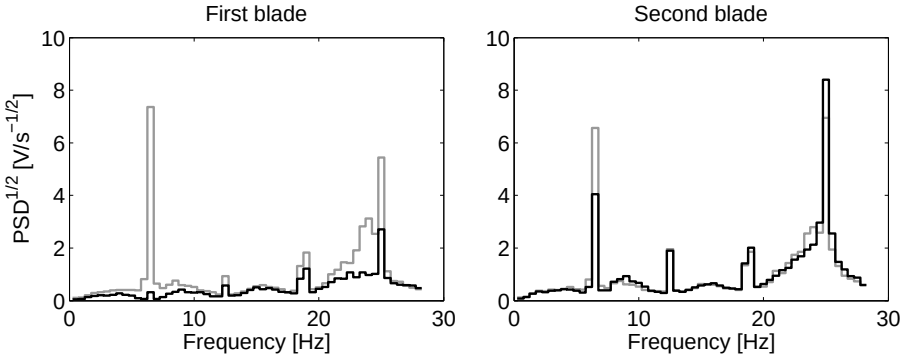

Figure 4.17: Load PSD with (black) and without (grey) SISO feedback control at 0° yaw.

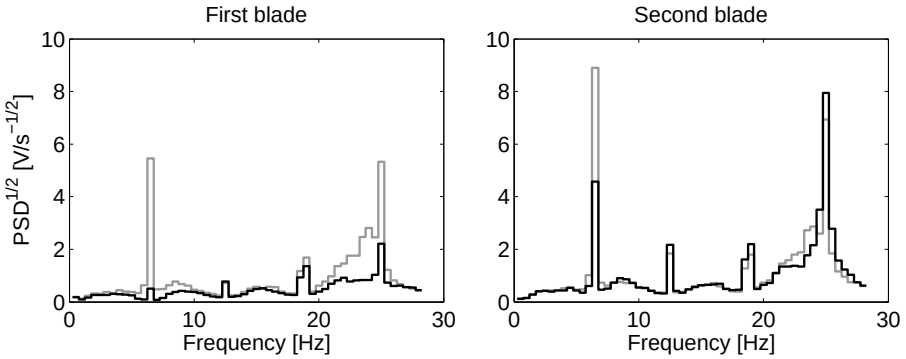

Figure 4.18: Load PSD with (black) and without (grey) SISO feedback control at 5° yaw.

However, the controllers on the two blades were acting independently, even though the action of each controller had a large effect on the response of the other blade, because of the high degree of coupling present in the system. Therefore, with parallel SISO control, the controllers might have been working against each other.

MIMO control

As a result of these issues that were encountered with SISO control, MIMO control was implemented; the results of which can be seen in Figures 4.19

and 4.20. The same load spectrum (without controller) as with the SISO controller was observed and the 5° yaw load case posed no significantly different spectrum. The load reduction was much higher than with parallel SISO control and it maintained high load reduction at a 5° yaw angle for both blades. In particular, the blade dynamics were damped much better, at the expense of the reduction of the 1P loads.

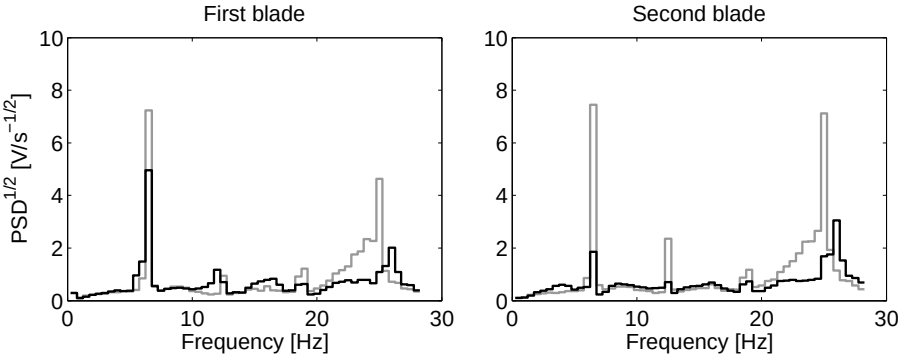

Figure 4.19: Load PSD with (black) and without (grey) MIMO feedback control at 0° yaw.

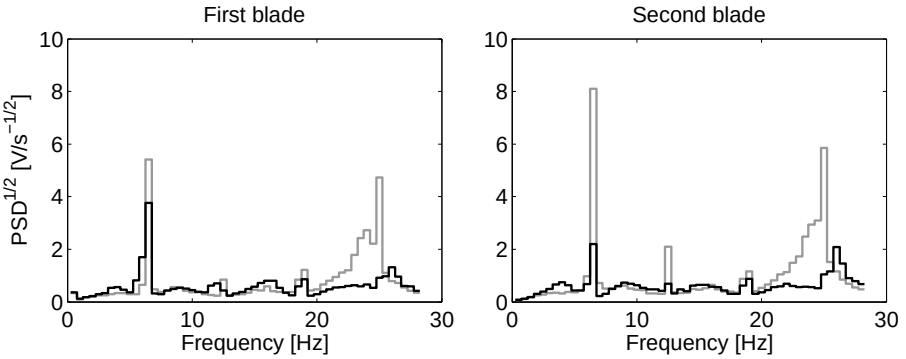

Figure 4.20: Load PSD with (black) and without (grey) MIMO feedback control at 5° yaw.

Combined MIMO and RC control

Subsequently, a combination of the MIMO feedback controller with a feed-forward controller was tested, see Figures 4.21 and 4.22. As can be observed

comparing Figures 4.19 and 4.20 to Figures 4.21 and 4.22, a better performance regarding the 1P loads was attained. For this controller also two time series plots for blade 1 are presented, see Figure 4.23) for 0° and for 5° yaw.

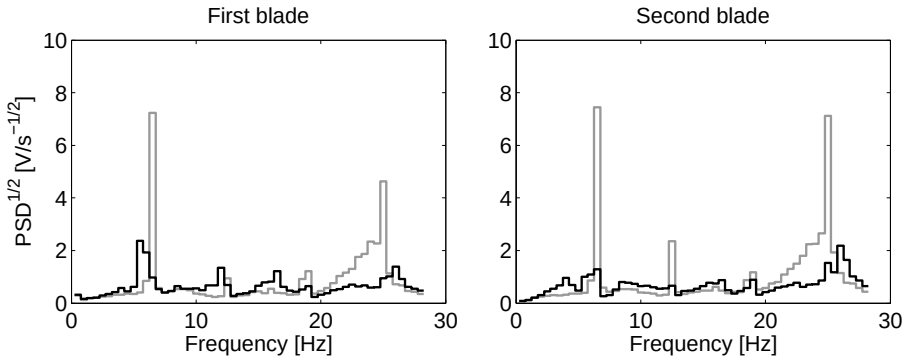

Figure 4.21: Load PSD with (black) and without (grey) feed-forward and MIMO control at 0° yaw.

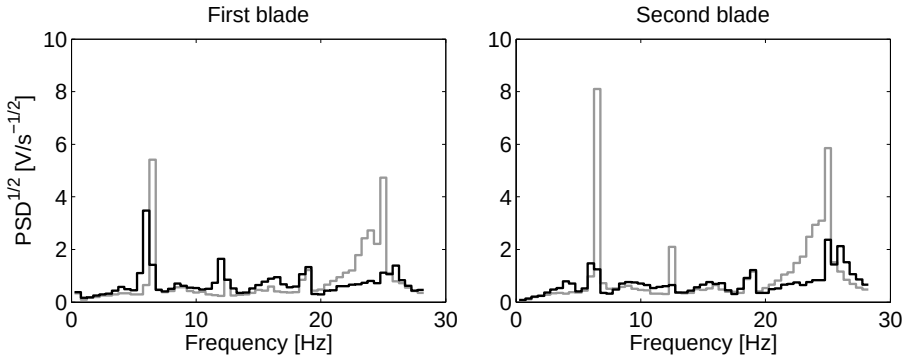

Figure 4.22: Load PSD with (black) and without (grey) feed-forward and MIMO control at 5° yaw.

In these figures the same observed behaviour as in the PSD figures can be seen. The 1P load with a period of about 0.16s was greatly reduced, especially for the zero yaw case, but there was a penalty to be paid in the form of high frequency disturbances. The same holds for the 5° yaw load case, although there seemed to be a high frequency component which was less mitigated.

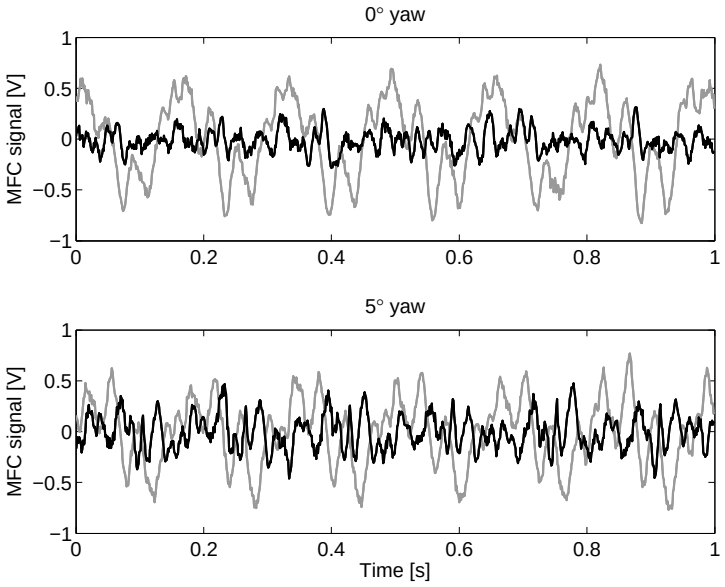

Figure 4.23: Time series of blade 1 with feedforward and MIMO control for two yaw cases

Controller comparison

Finally, the standard deviation of the MFC signal is presented, relative to the same load case without any controller. Thus, a value of 1 equals the standard deviation for the respective load case without a controller:

$$\text{Rel. standard deviation} = \frac{std(\text{MFC}_{\text{with control}})}{std(\text{MFC}_{\text{without control}})} \tag{4.4}$$

Where $\mathrm{std}(\text{MFC})$ is the standard deviation of a captured time series of the MFC signal. This provides a good estimation of the reduction in dynamic loads, see Figure 4.24. The SISO controller obviously worked well for blade 1, but hardly any reduction was seen for blade 2. This was also consistent with the PSDs in Figure 4.17 and 4.18 and it was because the gains of the controller were tuned for blade 1 first. Subsequently, a good controller for blade 2 was hard to obtain. The MIMO controllers with and without feedforward control showed similar results, although the one with feedforward control at 1P seemed to perform slightly better in total standard deviation reduction.

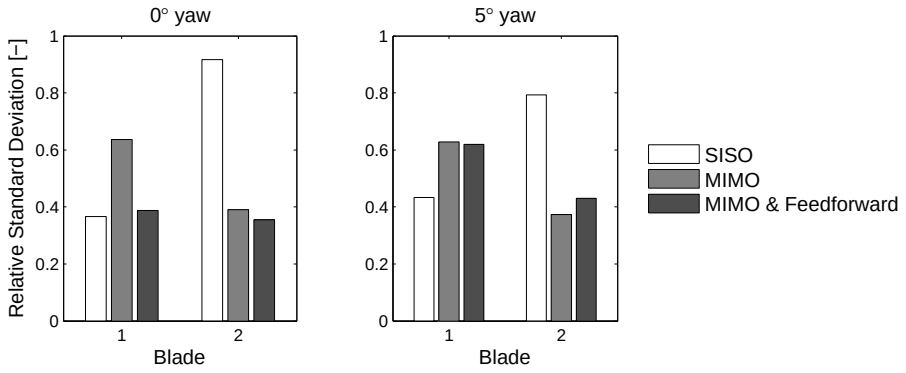

Figure 4.24: Standard deviation, relative to the corresponding uncontrolled load-case for the different controllers.

4.3.4 Summary and future work

In this chapter the design procedure for a smart rotor, equipped with variable trailing-edge geometry was discussed. After initial non-rotating experiments in which the potential of the concept was tested on a set-up with which the disturbances were controllable, it was decided to design and test a set of smart rotor blades that were tested on an actual turbine. The dynamic behaviour of the blades was analysed, also with sensor selection and placement in mind. Different controllers were designed, based on the measured behaviour of the system. Both feedback and feedforward controllers were based on the structural response of the blade to dynamic loading.

The rotor was tested under different yaw conditions with the different controllers. In general, significant reductions of the dynamic amplitude were attained with all controllers. The SISO feedback control gave some load reduction, but mainly for the blade to which the controller gains were tuned first. The MIMO controller gave better performance, but the performance at 1P was slightly increased when an adaptive feed-forward controller, aimed at the 1P loads, was added. However, some penalty was paid for reducing loads at the multiple-P and around the first natural frequency of the blade by a slight increase in loads in other parts of the spectrum. In general, the results showed that a large dynamic load reduction is attainable, but that the coupling between the different blades on a rotor has to be taken into account in controller design.

Thus, through presenting a design procedure for - and experiment on - a smart rotor this research provided a framework for successful implementation of load control to a rotor. However, for implementation on a full scale

turbine several topics are still to be addressed, such as the design of the flaps on that scale and the reliability and stability of the system.

In the future other load cases than operating the scaled rotor in yaw should be tested. Also different controllers will be developed to target the different deterministic and stochastic loads. Increasing the flap authority through a better actuator shape and greater deflection could greatly increase the load reduction potential of the system.

Now that the feasibility of the system has been shown, the question remains how to implement control surfaces on the MW-sized turbines. In the next two chapters the development of such an actuator based on SMA material will be described and the Chapter 7 and 8 the integration of the actuator in a novel blade structure is discussed.

References

[1] J.W. van Wingerden, A.W. Hulskamp, T. Barlas, B. Marrant, G.A.M. van Kuik, D.P. Molenaar, and M. Verhaegen. On the proof of concept of a 'smart' wind turbine rotor blade for load alleviation. *Wind Energy*, 11:265–280, 2008.

[2] J.W. van Wingerden, A.W. Hulskamp, T. Barlas, G.A.M. van Kuik, D.P. Molenaar, and M. Verhaegen. Two-degree-of-freedom active vibration control of a prototyped 'smart' rotor. *Journal of IEEE transactions on control system technology*, page published online, 2010.

[3] A.W. Hulskamp and H.E.N. Bersee. *Wind power generation and wind turbine design*, chapter 14, Implementation of the 'smart' rotor concept. WIT Press, 2010.

[4] A.W. Hulskamp, J.W. van Wingerden, T. Barlas, H.E.N. Bersee, G.A.M. van Kuik, and M. Verhaegen. Design of a scaled wind turbine with a smart rotor for dynamic load control experiments. *Wind Energy*, page published online, 2010.

[5] K. van Rijswijk. *Thermoplastic composite wind turbine blades: vacuum infusion technology for anionic polyamide-6 composites*. PhD thesis, Delft University of Technology, 2007.

[6] R. de Vries, E. Lamers, S. Wijskamp, B. Villa Rodriguez, and R. Akkerman. U20mm: The University of Twente micromechanics modeller. `http://www.utwente.nl/ctw/pt/research/Tools/`.

[7] T. Buhl, M. Gaunaa, and C. Bak. Potential load reduction using airfoils with variable trailing edge geometry. *Journal of Solar Engineering*, 127, 2005.

[8] S. Joncas, O. Bergsma, and A. Beukers. Power regulation and optimization of offshore wind turbines through trailing edge flap control. In *Proc. of the 43rd AIAA Aerospace Science Meeting and Exhibit*, January 2005.

[9] J.G. Leishman. Unsteady lift of a flapped airfoil by indicial concepts. *Journal of aircraft*, 31:288–297, 1994.

[10] XFOIL, http://raphael.mit.edu/xfoil/. website.

[11] Z. Du and M.S. Selig. A 3D stall-delay model for horizontal axis wind turbine performance prediction. In *Proc. of theAIAA, Aerospace Sciences Meeting and Exhibit, 36th, and 1998 ASME Wind Energy Symposium*, January 1998.

[12] L. Fagerberg. Wrinkling and compression failure transition in sandwich panels. *Journal of Sandwich Structures and Materials*, 6:129–144, 2004.

[13] G.M. Sessler. Piezoelectricity in polyvinylidenefluoride. *Journal of the Acoustical Society of America*, 70(6), 1981.

[14] H.A. Sodano, G. Park, and D.J. Inman. An investigation into the performance of macro-fiber composites for sensing and structural vibration applications. *Mechanical Systems and Signal Processing*, 18, 2004.

[15] D.G. MacMartin. Collocated structural control: motivation and methodology. In *Proc. of the 4th IEEE Conf. on Control Applications*, September 1995.

[16] André Preumont. *Vibration Control of Active Structures - An Introduction, 2nd edition*. Kluwer, 2004.

[17] Open Jet Facility, http://www.lr.tudelft.nl/live/pagina.jsp?id=264683f6-4e46-4b40-8d9f-b47d2577c073&lang=en. website.

[18] M. Verhaegen and V. Verdult. *Filtering and system identification: A least squares approach*. Camebridge University Press, 2007.

[19] S. van der Meulen, R.L. Tousain, and O.H. Bosgra. Fixed structure feedforward controller design exploiting iterative trials: Application to a wafer stage and a desktop printer. *Journal of Dynamic Systems, Measurement, and Control*, 130(5), 2008.

Chapter 5

Characterisation of SMA wire material

Every act of perception, is to some degree an act of creation, and every act of memory is to some degree an act of imagination.

Oliver Sacks in 'Musicophilia'

5.1 Introduction

In Chapter 3, the choice for shape memory alloy wires as adaptive material to develop a load control surface for wind turbine blades has been discussed. The specific bandwidth and high power density were the main reasons for selecting a SMA. In this chapter a study into the characterisation of two available SMA materials will be described. The first SMA is a NiTi-alloy that has undergone a specific thermo-mechanical treatment by the manufacturer to obtain good properties to act as an actuation wire. These specific properties constitute high recovery forces, small hysteresis and good fatigue properties. In addition, this wire was also stabilised after receiving it, by subjecting it to thermal cycles under constant load. It concerns the Smartflex wire of Saes Getters (Milan, Italy), with a diameter of 0.41mm and an estimated A_f temperature of 90°C.

Secondly, a 'basic' NiTi-alloy, with an estimated A_f of 60°C and a diameter of 0.4mm is selected. It is the M-alloy wire of Memry GmbH (Weil am Rhein, Germany). It is heat treated at different temperatures for different times lengths. Consequently, the wire is also subjected to thermal cycles under constant load to stabilise the behaviour. It is used to benchmark the specific actuator wire.

5.2 Characterisation procedure

Lagoudas [1] and Prahlad [2] describe the procedure to characterize the material for application that are related to its phase transition. This implies determining the borders of the transition zones in the σ, T-phase diagram. The following tests are proposed:

- Differential Scanning Calorimetry (DSC) measurements to determine the stress free transition temperatures, M_s, M_f, A_s and A_f.
- Tensile test below M_f to determine σ_s^{cr} and σ_f^{cr}
- Tensile test above A_f to determine the stress dependency of the transitions' start and finish temperatures. Alternatively, it is possible to do recovery experiments under constant loading (isobaric tests). The first gives vital information on the superelastic behavior and the second the ability of the materials to exert work. Both test will provide another set of points on the transitions' borders (the first being the result of the DSC measurements).

Lagoudas further mentions that it is also important to determine the stabilizing behavior under cyclic loading, especially if more than one cycle is part of the functionality. Prahlad compares the results from a model, based on the characterization experiments with experimental results for restrained recovery. Here the procedure described by Lagoudas is used to compare the different wire materials.

5.3 Test set-ups

In this section, the different set-ups that were used to perform the tests, as described in section 5.2, are discussed.

5.3.1 Isothermic tensile test

The isothermal tests were performed on a 10kN MTS testing machine. The wire clamps, one of which was connected to the load cell and the other to the testing machines actuator, extended into the oven through holes in the oven wall. The wire was thus completely clamped and tested inside the oven. A thermocouple was placed in the oven, close to the wire. The oven was closed and the tensile test was not started before the oven had reached a constant, set temperature.

The tensile tests were performed such that full transition was obtained - usually through straining the material 5-6%. The tensile speed was set such

that the cycle is performed in 4 minutes. This constitute a very small strain rate of about 0.05%/s. A sample tensile test and the way the different transition start and finish temperatures were derived, can be seen in Figure 5.1.

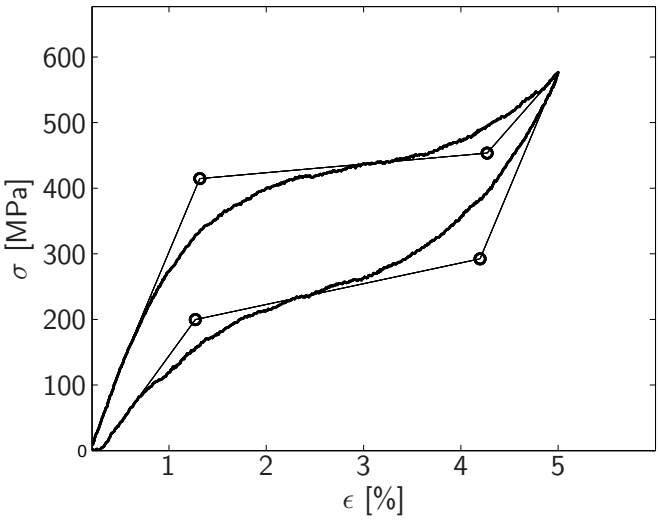

Figure 5.1: Example of a tensile test with the way the different transition stresses are calculated

5.3.2 Isobaric temperature cycle tests

Oven test

The isobaric tests were performed with the SMA-wire in an oven. On one end, the wire was attached to the oven wall and on the other it was elongated by a steel cable which extended outside the oven and runs over a steel rod, covered with a Teflon sheet, providing a very low friction bearing. At the end of the wire a weight was attached which's displacement was recorded by a Linear Variable Differential Transformer (LVDT). Two thermocouples measured the temperature in the oven at a point very close to the wire. In addition air circulated in the oven, which assured a homogeneous temperature distribution and good heat transfer from the air to the wire. Thus, due to the small rate in temperature change, the good heat transfer between the air and the wire and the small diameter of the wire, it was assumed that the temperature of the wire and the oven are the same.

See Figure 5.2 for a schematic representation of the setup. The wire was subjected to thermal cycles by heating and cooling the oven very slowly at 1°C/min.

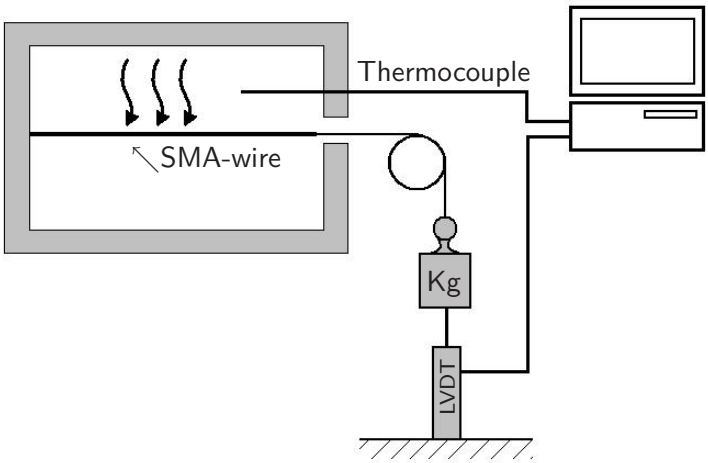

Figure 5.2: Oven set-up for isobaric tests

The temperature and displacement were both recorded simultaneously. A sample result of the measurements can be seen in Figure 5.3.

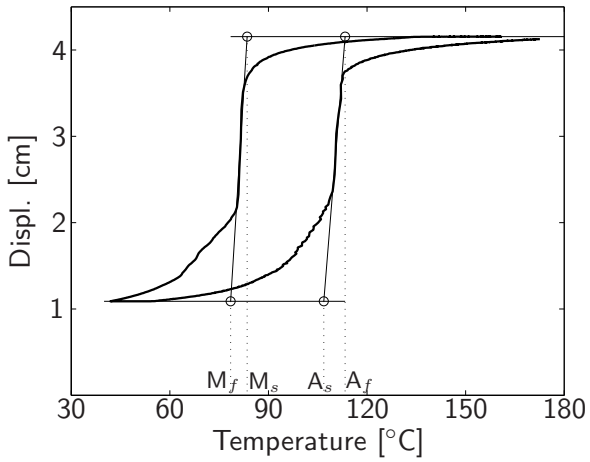

Figure 5.3: Example of an isobaric test with the determination of the temperatures A_s, A_f, M_s and M_f.

Joule heating

Alternatively, the wire can also be heated by joule heating, while the temperature of the wire is measured by an IR-camera. The IR-camera provides a method for temperature measurements which does not influence the temperature of the wire. In contrast, in order to get a good measurement with a thermocouple, it must be electrically isolated from the SMA wire, but at the same time there must be good heat transfer and the presence of the thermocouple must not influence the temperature of the wire. These two requirements of direct temperature measurement and non-invasiveness are hard to fulfill at the same time with a thermocouple and therefore an IR-camera is used. Tests with Joule heating were also performed and a schematic representation of the set-up can be seen in Figure 5.4.

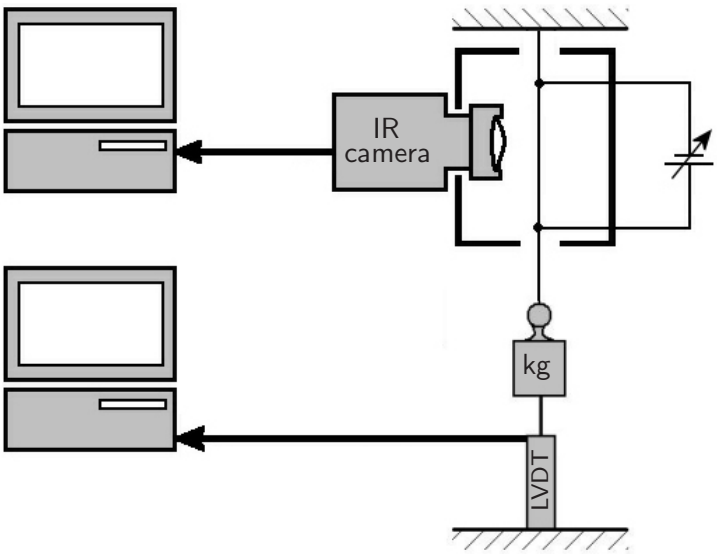

Figure 5.4: Set-up of the isobaric tests with Joule heating and an IR-camera.

This set-up has two main differences with with the one discussed in the first part of this section. First, the heating is not attained by heat from convection, but by electrical resistance heating. Because the physical nature of the heating methods are completely different, so will be the wire response. When the wire is heated through resistance heating and grains make the phase change to austenite, their resistance will change, and thus will the nature of the subsequent heating process. Secondly, the way the temperature is measured is different. In the oven the temperature is measured at some distance from the wire. It is assumed that these temperature

measurements are also valid for the wire because the rate of temperature change is very low (1°C/min). However, critical comments can be made on the way the temperature is measured with the IR-camera. Although the wire is very close to the lens, the wire still only spans a few pixels across and it is highly curved. Thus, although the wire is made mat black, it is very difficult to make a good correlation between the measured photon intensity and the temperature, mainly because the emissivity of the surface may be $\lesssim$1. Finally, the wire may move slightly due to its transformation, leading to a unfocused view of the wire. These three effects (an emissivity that is lower than one, a wire surface that is small and highly curved and a possibly unfocused image of the wire) lead to a measured temperature that is lower than the actual one. The method of heating also adds to this because the internal temperature will never be lower than its surface temperature, which is measured by the camera even though its diameter is very small. This is also observed when compare both methods of measurement are compared. See Figure 5.5. The displacement is normalised because the wire length in both tests was not equal. As can be seen, the AM-transition apparently occurs at 10°C lower temperatures when temperature is measured in to oven than by IR-camera. For the MA-transition this is about 20°C.

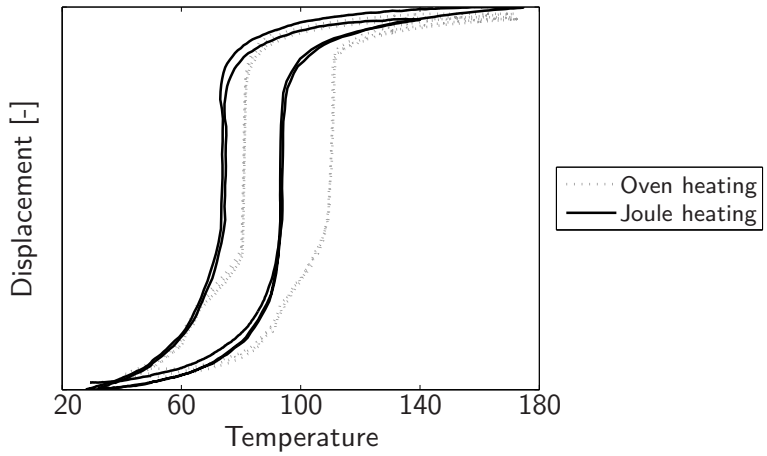

Figure 5.5: Comparison between Joule heating and oven measurements for isobaric testing. The displacement is normalised.

However, in some cases working with an IR-camera is the only option, for instance when performing non-quasi-static measurement, *in situ* measurements on a wire that acts as an actuator in or on another structure, or measurements on a wire that is heated by Joule heating.

5.3.3 DSC

The DSC measurements were performed on a Perkin Elmer Sapphire DSC. A thermal cycle from 130°C to 20°C and back, with a temperature rate of 7.5°C/min was executed. The DSC-curve can be seen in figure 5.6.

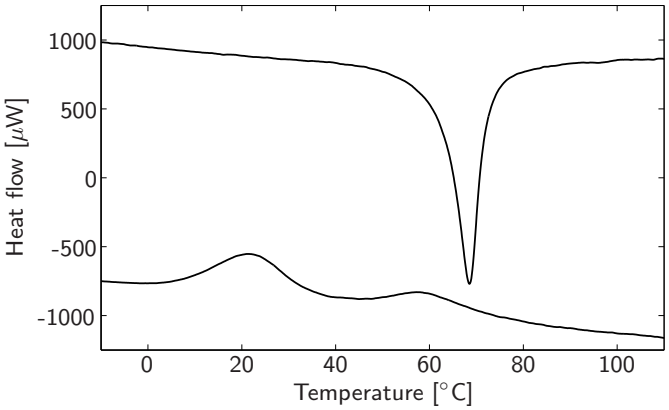

Figure 5.6: DSC-curve for the Smartflex wire

As can be seen, the Smartflex exhibits the R-Phase Transition (RPT) upon cooling because of the two peaks in the cooling curve. The first (high temperature) peak is associated with the A→R transition and the second one with the R→M transition.

5.3.4 Restrained recovery

A restrained recovery test does not directly provide any data along the axis of the stress-temperature diagram. However, important information about the capability of the wire to exert force can be derived. In contrast to the other measurements, the test is not performed in an oven, but the wire is heated by Joule heating. The temperature is recorded by a infra-red (IR) camera. The tests are also performed on the 10kN MTS machine, inside a box which is spay painted with mat black paint to prevent interference from radiation from external sources. The part of the wire where the IR-camera is focused on, is also painted black. Synchronisation between the camera and the force measurement is achieved by a trigger: the testing machine sends out a pulse when the test starts, which starts recording of the IR images by the camera.
Although the IR-camera has proven to give temperature measurements that are inconsistent with the quasi-static oven tests, this method is used here

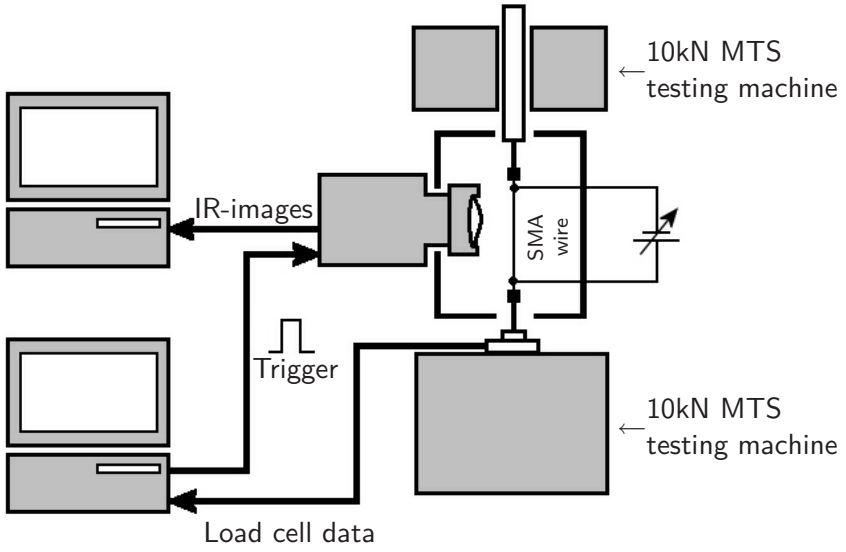

Figure 5.7: Restrained recovery set-up

for a number of reason. First, the restrained recovery set-up is the test that most closely resembles the state of the material in an morphing surface (see the next chapter, Chapter 6), which is heated by Joule heating. Also related to the work described in Chapter 6, the tests are performed in a non-quasi-static manner, up to a temperature rate of $10^{2\circ}$C/s, which requires a method of measuring the temperature externally, instead of deducting it from the oven temperature. The IR-camera is the only non-invasive method available.

The results of a restrained recovery test on a wire can be seen in Figure 5.8 below. The wire was strained 3% of which 1.6% permanent strain remained after unloading. Test for 4% and 5% gave similar results.

5.4 Results

5.4.1 Phase diagrams

The results of the tests are illustrated in Figure 5.9. The results from the isobaric and the isothermal tests seem to follow the same trend line very well and also the DSC tests are in line with the same trend, at least for the A_f and A_s lines.

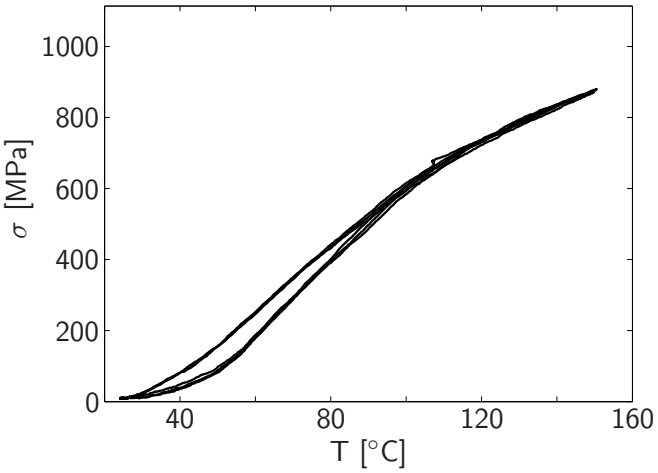

Figure 5.8: Results of the restrained recovery experiments.

5.4.2 The comparison between Smartflex and M-alloy

In Figure 5.10 the stress-temperature phase diagram of the M-alloy can be seen. Of course, the stress free transition temperatures of the M-alloy lie at lower temperatures than the Smartflex because the alloy was designed this way.

However, only tensile and DSC tests were performed on this wire as a new batch of M-alloy was ordered for further tests. But the new batch behaved very differently. See Figure 5.11. Moreover, it was impossible to stabilise the new batch in cyclic loading. The comparison is therefore limited and on the part of the M-alloy wire solely based on the tensile tests.

One of the quantitative conclusions that can be drawn from the comparison is that both alloys have very similar Clausius-Clapeyron constants and that the M-alloy shows a similar hysteresis, but with wider transition bands - the distance between A_s and A_f lines and the M_s and M_f lines, respectively. The narrow transition bands of the Smartflex wire make it difficult to control the temperature of the wire to a specific state in which $0 < \xi < 1$, where ξ is the martensite fraction. Being able to control the wire to this intermediate states is important to control the actuator in which the materials is implemented to intermediate positions, as apposed to binary control. However, this appears to be mostly an issue with the isobaric load case and less with the restrained recovery-like behaviour in a morphing surface and the reproducible and stable behaviour of the Smartflex wire are considered important advantages of the material. Therefore, it was decided to proceed with this material in actuator development.

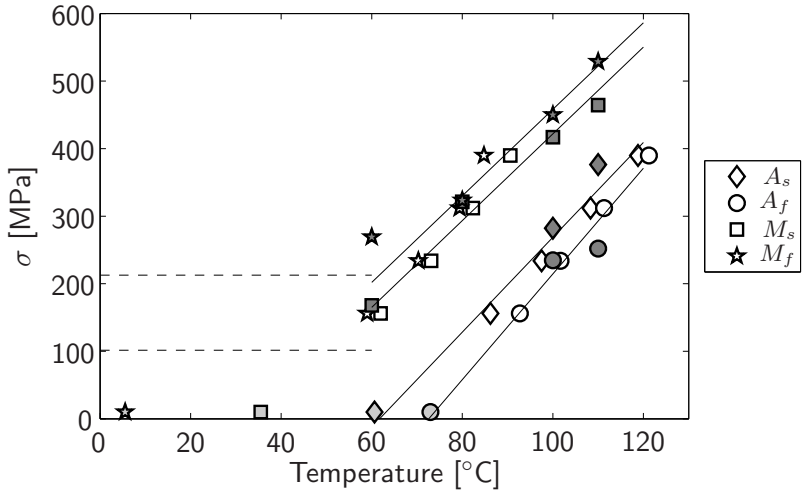

Figure 5.9: Phase diagram of the Smartflex wire. White marker color indicates that the data was obtain though the isobaric test, light grey through the DSC test and dark grey through tensile tests. A linear fit to the different transition points is also indicated as a solid line for $T > M_f$ and dotted for $T < M_f$ (detwinning of martensite).

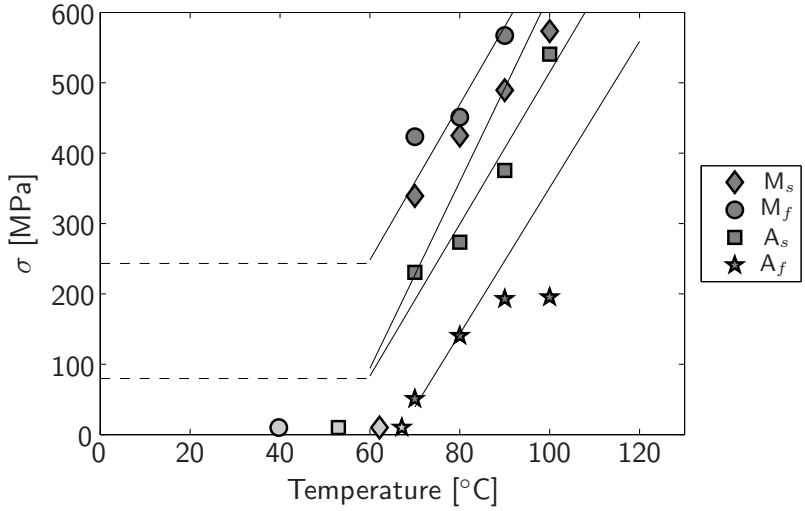

Figure 5.10: Stress-Temperature diagram of the M-alloy wire, annealed at 400° C for 35minutes.

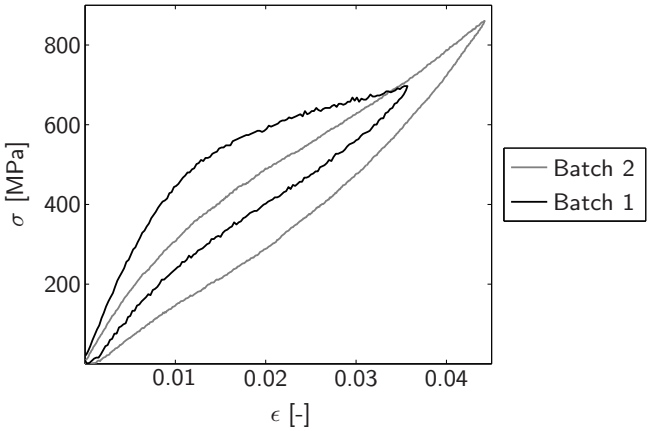

Figure 5.11: Two tensile tests at 100°C on the same wire (M-alloy, heat treated at 350°C for 45min. and isobarically cycled) from two batches.

5.5 Conclusions and discussion

5.5.1 Test methods

A clear conclusion about the test methods, is that measurements with the IR-camera show a clearly different result than the oven tests, as observed in Figure 5.5. It is believed that the inaccuracy is in the IR-camera measurement because they are not consistent with the other measurements and because there are numerous reasons that explain the observed difference with the oven tests. The test results of the restrained recovery might therefore be inaccurate from an absolute thermal point of view. The tests do, however, provide valuable information on the recovery force and the amount of hysteresis in the stress-temperature cycles.

Moreover, the isobaric and tensile tests on the Smartflex, both performed by oven heating, show great correspondence, illustrated by the close fit of the trendlines in Figure 5.9 to both data sets.

5.5.2 Actuator wire behaviour and performance

Based on the experimental results, the choice was made to proceed with the specific actuator wire. This was mostly driven by its ability to exert high forces and its good fatigue behaviour.

However, there are also some aspects against it. The hysteresis, when we define it as the difference between the A_f and M_s or M_f and A_s line, is still some 25 to 30°. Moreover, both the AM and the MA transition band

are relatively narrow. For instance the Smartflex wire goes so fast through its transition in isobaric tests that the transition can almost be regarded as adiabatic. This was also observed in a temperature change, opposite to the rate in temperature, needed to go through the transition. For instance, during cooling the exotherm of the AM-transition is observed as a small increase in temperature (see Figure 5.12)

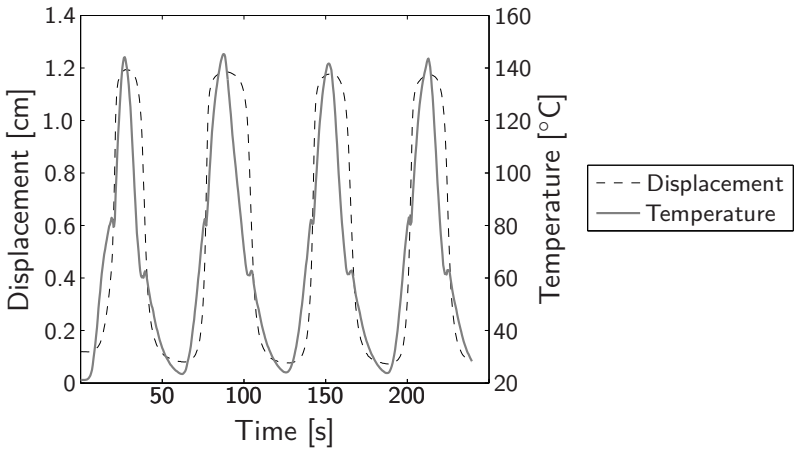

Figure 5.12: Temperature and displacement during isoabaric tests on a Smartflex wire under 3kg load.

Finally, it is important to note that the A_f of the Smartflex wire is slightly higher than that of the M-alloy. This has an advantage because when the wire is at elevated temperature and cooling is required, the temperature difference between the wire and surrounding is larger, and thus the cooling rate. On the other hand, the temperature that can be reached with a wire is limited when the wire is to be embedded in a polymer material or composite because of the restrictions posed by the polymer's T_g or T_m.

References

[1] D.C. Lagoudas, editor. *Shape Memory Alloys - Modeling and Engineering Applications*. Springer, 2008.

[2] H. Prahlad and I. Chopra. Comparative evaluation of shape memory alloy constitutive models with experimental data. *Journal of Intelligent Material Systems and Structures*, 12, 2001.

Chapter 6

Development of a high-rate SMA actuator

6.1 Introduction

As argued in the previous chapters, a SMA as the basis for morphing load control surfaces on wind turbine blade is a very powerful concept because of its high power density, large attainable actuation strains and theoretically attainable bandwidth. However, this bandwidth is only attainable under lab conditions, not when the material is embedded in a plate. In this chapter the possibility for a high rate SMA actuated active surface, based on active, controllable cooling, is addressed. This would increase the bandwidth of the embedded SMA into the range required for active control surfaces for wind turbine blades, while at the same time limiting its power consumption -as compared to wires subjected to continuous forced convection- and increasing the controllability.

The development of the actuator was carried out in four major stages 1) Design and manufacturing of an actuator with internally mounted SMA wires 2) characterisation of the thermal behaviour and evaluation of the cooling potential, 3) development of the controller, to be able to test the system's behaviour 4) Testing the performance of the actuator-controller combination in set-point tracking experiments.

6.2 Design the actuator

6.2.1 The concept

The concept of the developed actuator is to embed SMA wires inside a beam or plate-like structure inside channels. The SMA wire is prestrained and when the wire is heated, it tries to recover that deformation and in the process it exerts a force on the actuator. The channels are placed out of the neutral axis of the actuator and the wires are placed on the most outer part of the channel. In this way, a force exerted by the wire results in the highest attainable bending moment on the actuator, and thus in the largest curvature. The wires are mechanically constrained at their ends.

Through the channels air - or any other fluid - can be forced to cool the wires at a high rate. The incorporation of the channels requires a certain thickness of the actuator. To limit the bending stiffness of the actuator, it is constructed from pure polymer as opposed to GFRP. The Young's modulus is much lower than reinforced plastics and it has a high level of formability.

Two sets of wires are implemented; one on each side of the actuator. See Figure 6.1. Controlling the actuator therefore requires two heating and two cooling signals. There are two reasons for this approach. Firstly, it makes it possible to deflect the actuator in both directions. Secondly, in this configuration - called an antagonist configuration - the wires work against each other.

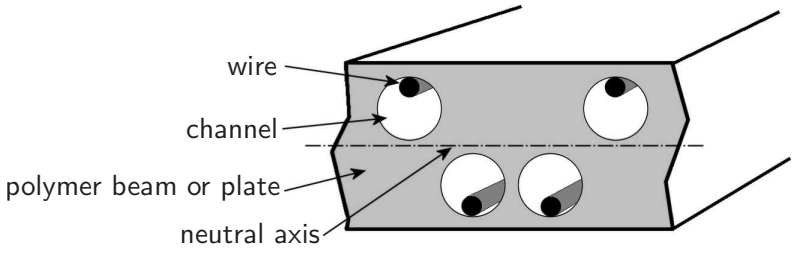

Figure 6.1: Schematics of a unit cell of the actuator concept.

The antagonistic configuration is schematically depicted on the left side of Figure 6.2. If two prestrained wires are acting against each other, together they can induce a motion in both directions. This is needed with one-way shape recovery because the wire can only recover its previously applied strain and a bias force is needed to regain that prestrain after it is heated. In the antagonistic set-up the wires supply this bias force for each other.

In the case of the actuator, however, a large part of the bias force is formed by the elasticity of the actuator itself, see the right part of Figure

6.2, in which this elasticity is represented by springs. In fact, the strain in the actuator is relatively small, as compared to typical actuation strains of the SMA material [6]. Therefore the springs in Figure 6.2 are very stiff and the SMA behaviour almost reduces to so called restrained recovery.

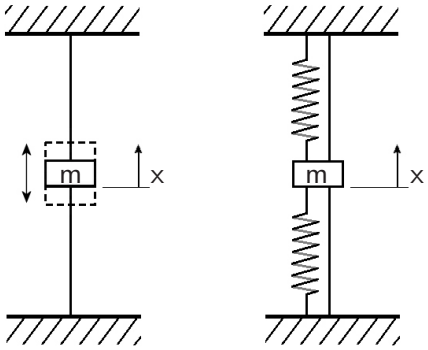

Figure 6.2: Schematic representation of an antagonistic configuration (left) and for the actuator (right).

In any case, the antagonistic configuration also allows for faster position control because the second wire can be heated while the first one is still cooling down. Normally this poses a disadvantage of the antagonist configuration because, if both wires are heated in alternating manner, but the cooling capacity is not sufficient, the actuator might become unstable due to the build-up of heat in both sets of wires. With the actuator discussed here, the cooling rate of the wire that is cooling down is increased because of the flow through cooling channels, limiting simultaneous heating of both sets of wires.

Concluding, it can be said that the configuration of the wires in the actuator is of an antagonistic nature and that the concept of the actuator is very suited for that because of the active cooling. However, the compliance and dynamics of the beam also play a role.

6.2.2 Detailing and manufacturing

To obtain a plate or beam with narrow, straight channels, 1.8mm diameter, cylindrical, removable inserts were tensioned in a aluminium mould which was filled with a casting resin. After curing, the inserts were removed and the product demoulded. The inserts were placed such that 0.6mm of polymer remains between the channel and the outer surface of the actuator. Since the thickness of the actuator is 6mm, this means that the whole channel lays on one side of the neutral axis. See Figure 6.1.

The implemented material system is a modified PA-6, a form of nylon [9]. An advantage of the system is that the properties of the polymer are tuneable to some extent and because the thermoplastic actuator could be welded to other thermoplastic structural elements. Moreover, it's a low cost material. After demoulding and removal of the inserts, the the excess resin was removed and connections for the wires and the pressurised air were made.

The implemented wires were the 0.4mm diameter SmartFlex wires from Saes Getters that were already discussed in Chapter 5. The diameter was chosen to obtain a good balance between force and obtainable cooling rate. Large diameter wires can exert higher forces, but the volume to surface area is too large for rapid cooling. Initial measurements on this wire and calculations on the actuator deflection showed that this wire would attain the required performance. The wires in the actuator were prestrained 3%, slightly stressed and clamped at their ends. Holes were drilled in both ends of the actuator for entry into and exit from the channels for the air.

6.3 Thermal characterisation

The most important conceptual feature of the actuator is its increased cooling capacity in comparison with fully embedded wires. In order to make predictions about its behaviour and performance, the thermal behaviour was characterised. This was done by heating the wire to a certain temperature by Joule heating and subsequently cutting the power. The temperature decay was measured with an infra red (IR) camera and an exponential function $T = a \exp bt$ was fitted to the data, see Figure 6.3.
From the exponential decay the heat transfer could be calculated using basic heat equations [2]. The heat loss per unit length is given by:

$$q' = -hA(T_w - T_\infty) \tag{6.1}$$

With h being the heat transfer coefficient - the parameter of interest - A the circumference of the wire (or the surface area per unit length), T_w the temperature of the wire and T_∞ the temperature of the flow. It was assumed that the flow did not heat up significantly when passing the wire because the air speed was very high, i.e. T_∞ remained constant. The temperature change as a result of the heat dissipation is defined as:

$$\frac{dT_w}{dt} = \frac{q'}{V \rho c_p} \tag{6.2}$$

In which, V is the cross-sectional area (or volume per unit length), ρ and c_p the density and heat capacity of the wire respectively. ρc_p was taken from

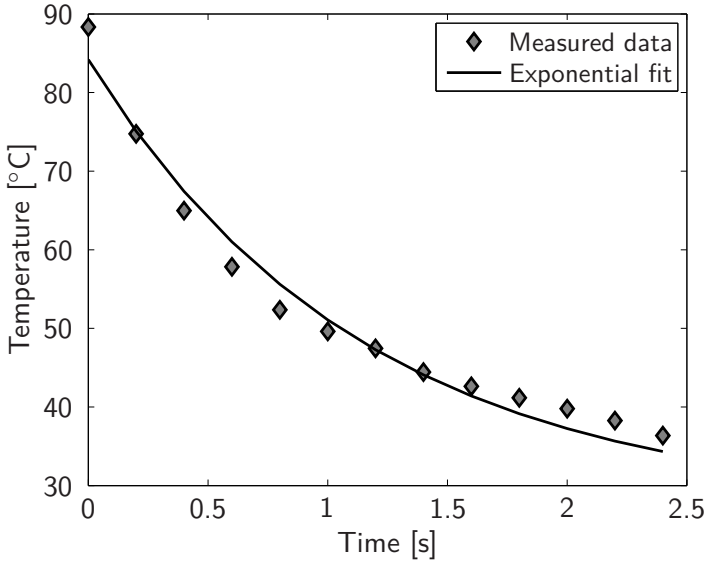

Figure 6.3: Example of exponential fit to the measured temperature data.

[3] and good correspondence was observed with the measurements. The value can be obtained from the measurements when looking at the instant that the wire starts heating up from T_∞. At this moment the heat loss is zero because the temperature difference with the ambient temperature is still zero and the relation between the input power and heat-up can be derived from equation 6.2, with q' the generated heat through Joule heating, per unit length. Combining equations 6.1 and 6.2 gives:

$$\frac{dT_w}{dt} = \frac{-hA(T_w - T_\infty)}{V\rho c_p} \tag{6.3}$$

This is a first order differential equation with the solution:

$$T(t) = T_\infty + (T_0 - T_\infty)\exp\frac{-hA}{V\rho c_p}t \tag{6.4}$$

With T_0 the temperature at $t = 0$. In Table 6.1 the fits of the measured data can be seen. The resulting heat transfer coefficient is plotted in Figure 6.4.

Figure 6.4 and Table 6.1 indicate that the cooling of the wire is increased up to tenfold by active cooling. Moreover, the heat that is dissipated is quickly blown away, whereas it would have to be dissipated through the actuator in the case of a fully embedded wire. This build-up of heat would

Airflow			h	
[L/min]	a	b	[W/Km^2]	R^2
0	95.6	-0.211	55	0.99
7	77.5	-1.01	260	0.99
11	85.2	-0.93	240	0.98
15	65.4	-1.38	356	0.98
18	69.9	-1.4	361	0.98
21	77.5	-1.62	417	0.97
23	81.8	-1.94	499	0.98
25	70.4	-2.28	587	0.97

Table 6.1: Exponential curve fit to the measured data.

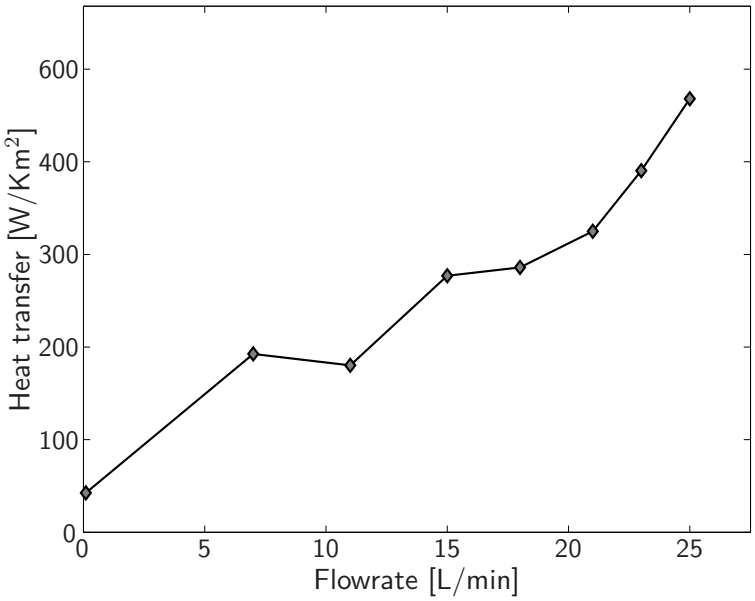

Figure 6.4: Measured heat transfer coefficient.

change the thermal boundary conditions of the wire and with it its response. This in sharp contrast with active cooling through forced convection in the channels. Additionally, the power consumption can be kept under control in comparison to externally mounted wires on a wind turbine, because the cooling can be switched off if the wire needs to be heated. The system therefore does not only have the potential to increase the actuation speed but also to increase the controllability and energy efficiency.

6.4 Controller

Controllers for SMA actuated structures usually aim at tackling the hysteresis and non-linearities. Webb [10], for instance, uses the error between a reference signal and the actual displacement to update an adaptive hysteresis model to compute the actuation signal through a thermal model. Here, it was chosen to implement fuzzy logic control [4] to control the actuator. Ahn [1] implemented a fuzzy logic supervisor to update the proportional, integration and derivative gain of a PID controller to perform displacement control with SMAs. Kumagai [5] used neural networks to train the fuzzy controller. Here, a fuzzy logic controller was heuristically tuned and it directly controlled the plant. The implementation of (direct) fuzzy logic was motivated by the non-linear characteristics of the system and the complexity of the set-up with its multiple controller outputs for only one degree of freedom of the plant (deflection of the actuator). The non-linearities arose from the non-linear behaviour of the SMA material, especially the hysteresis when going through actuation loops and the fact that the force and deflection flatten off at higher temperatures, see Chapter 5. Secondly, the asymmetry of the temperature control system had to be taken into account. This asymmetry is caused by the different physical nature of the heating and cooling mechanisms. Heating is done by resistance heating, whereas cooling is attained by forced convection. Although forced convection is very effective in dissipating heat from the wire, it is still much slower than resistance heating in terms of attainable rate of temperature change $|dT/dt|$. Also, the inertia and compressibility of the air leads to a delay between the control signal and the actual cooling. In this section relevant fundamentals and how fuzzy logic control was implemented on the system are discussed.

6.4.1 Fuzzy logic controller

With fuzzy logic control, three steps are executed to compute a control signal from the controller's input. See Figure 6.5.

The three blocks in Figure 6.5 were implemented in the following way. First, the input of the actuator is converted to a value between 0 and 1 for different linguistic terms describing the state of the system; the so called degree of membership. For instance, a certain error input value x_{error} may lead to degrees of membership, indicated by μ_1 and μ_2 in Figure 6.5, of 0.4 for 'negative' and 0.7 for 'negative large'. This step is called fuzzification and the relation between an input value and the degree of membership μ is described by membership functions, shown as triangular and trapezoid plots

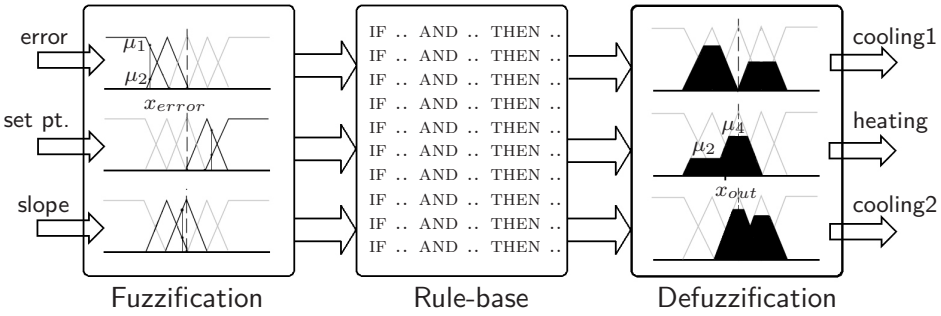

Figure 6.5: Scheme of the fuzzy logic controller, also indicating schematically how the different steps are implemented.

in Figure 6.5.

Here, the following input linguistic variables were chosen. The choice for the error signal is logical. It can be regarded as a proportional part of the controller and it is the error that is to be minimised. The deflection is important because it is related to stress, and thus to the temperature in the wire, which in turn determines the mechanical behaviour of the wire and consequently about its thermal behaviour. For instance, if the actuator is deflected to its fullest extent, it can be assumed that the wires on the compression side are very hot, which in turn would lead to rapid cooling when the heating is cut - even without forced convection. The slope of the set point is implemented because it determines the required speed of heating or cooling which is directly related to the required input power or valve set point. The number of inputs is limited because the number of rules in the rule base (and with it the computational time) increases exponentially with the amount of input parameters. Five linguistic terms and accompanying membership functions were defined for each input linguistic variable.

Subsequently, a rule-base is executed in which the occurrence of non-zero input membership grades is linked to an output fuzzy set through 'if-then' statements (second block in Figure 6.5). This linguistic approach of the rule base is very suitable for the kind of control that was sought. Because of the delay in cooling and the response of the SMA wire, smooth control of the cooling and actuating quickly with a heating signal over that cooling signal is wanted. The rule base controller makes it possible to minimize concurrent heating and cooling which limits the power consumption. Additionally, the controller was implemented in such a manner that still coupling between heating and cooling control is obtained. This is important to prevent jittering. Therefore, for instance, the rule base was chosen such that

a dead zone exists around a zero error for the cooling.

Finally, a weighted average of the different results of the rule-base is computed using output membership functions, which forms the output of the controller. This is called defuzzification. For the heating signal seven linear (triangular and trapezoid) functions are used. For the valve output four output membership functions are defined: Three triangular functions and one singleton. The singleton is implemented such, through the rule base, that it is executed when the opposite wire set is being heated and the side that is to be cooled is not. The goal is to prevent heat build-up in the actuator. The Center of Area method is used for computing the output value, meaning that the output signal is computed using the following relation [7]:

$$x_{out} = \frac{\int_{x_{\min}}^{x_{\max}} x f(x) dx}{\int_{x_{\min}}^{x_{\max}} f(x) dx} \tag{6.5}$$

Where $f(x)$ are the combined, activated output membership functions, x is the output parameter and $x_{\min}$ and $x_{\max}$ denote the domain over which x is defined. The Center of Area method is also schematically indicated in Figure 6.5. Three output signals are computed this way: a valve setting for each side of the actuator and one power control signal for the current generators. The heating signal is split to wires on each side of the actuator, based on its sign. If the heating output is positive, power is fed to the wire set on one side of the actuator and if it is negative, to the other set. So there are four inputs to the plant, whereas the fuzzy controller only has three output linguistic parameters, see Figure 6.6. The power signal consists of voltage and current set points for the current generators which are adjusted for the change in electrical resistance due to the lattice transition from austenite and martensite or vice versa [8]. On the other hand, for the cooling response, sometimes it is needed to cool both sets of wires at the same time. This also prevents the build-up of heat in the bender, which increases the controllability. Therefore two separate output signals for the cooling signals are needed.

The controller was implemented on in LabVIEW 9.0 (National Instruments Netherlands BV, Woerden, The Netherlands). The digital-to-analogue and analogue-to-digital converters were National Instrument NI 9215 input and 9263 output modules on a NI cDAQ 9172 board. The control loop was executed at 50Hz.

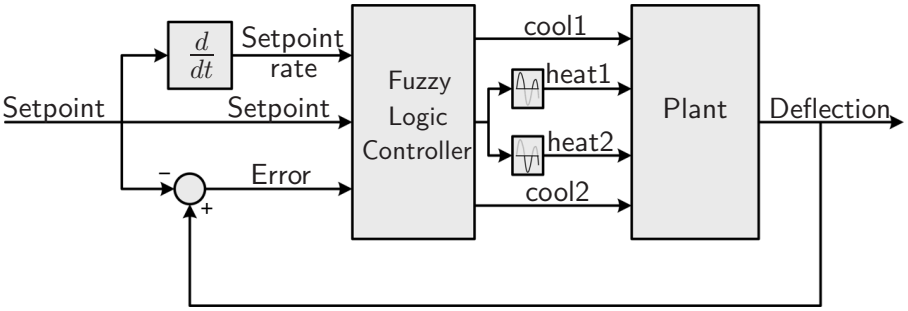

Figure 6.6: Control scheme for the fuzzy logic controller.

6.4.2 Controller performance

In order to investigate the performance of the controller separately from the actuator performance, an antagonistic set-up was built. See Figure 6.7. The set-up is schematically presented by the left side of Figure 6.2. In this case a laser target was mounted in the middle of a wire with a 3% prestrain. To both sides of the target, electrodes and cooling channels, as intended on the actuator, were applied. In this way, *de facto* two separately controllable wires were obtained. A laser displacement sensor was aimed at the laser target. This was used as the feedback signal. Heating the wire on one side, causes recovery of the strain in that part of the wire, simultaneously straining the other part further. Subsequent cooling of this side of the wire results in relaxation of the actuation force and simultaneous heating of the other side causes the laser target to move in opposite direction. The controller

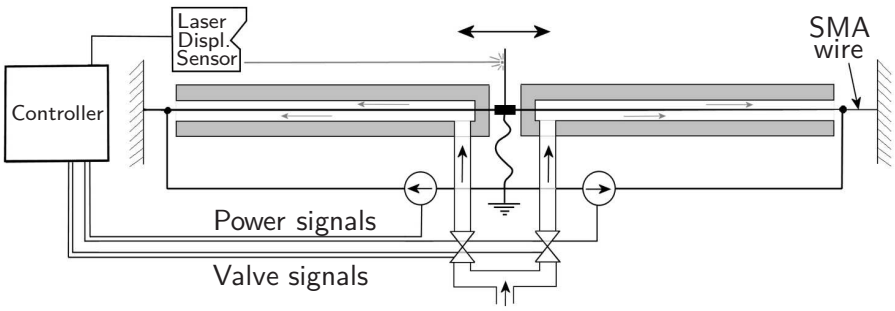

Figure 6.7: Schematics of the antagonistic set-up.

was manually tuned to the specific behaviour of the set-up and a series of tests was performed in which the target tracks a sinusoidal reference signal. The reference signal, the actual displacement and controller outputs were

recorded. For a set point amplitude of 1.5mm and frequency of 0.6Hz can be seen in Figure 6.8.

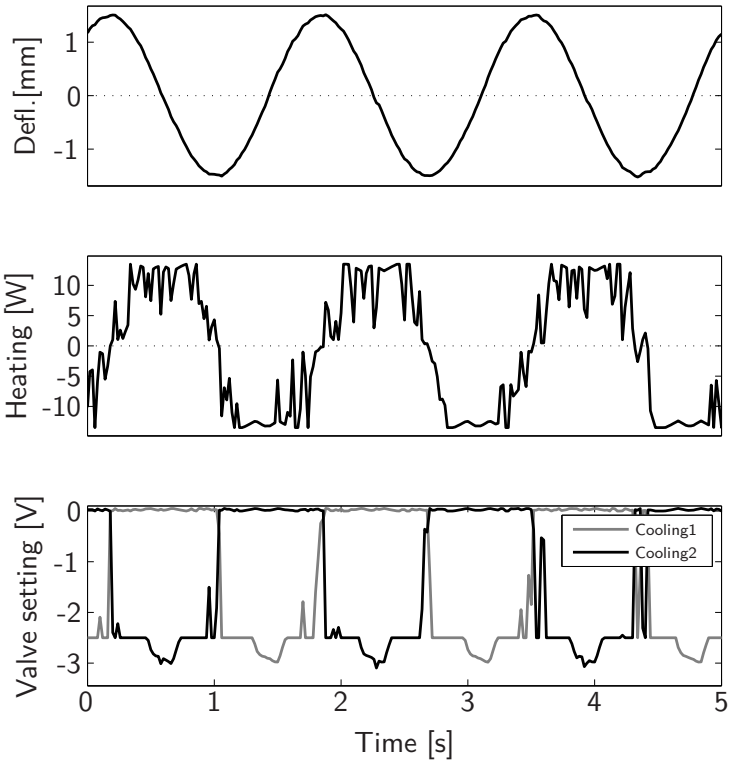

Figure 6.8: Response of the antagonistic set-up when tracking a set point with an amplitude of 1.5mm and 0.6Hz. From top to bottom: the deflection of the system, the heating and the cooling output of the controller.

The figure shows that the response was as wanted: the wire that was not being heated, was cooled by a relative smooth signal. When the set point time derivative was at its maximum, the valve was opened slightly more. The heating signal response was much more irregular than the cooling response because the controller mainly used the current generators to minimize the error. A series of experiments tracking sinusoidal reference signals with different amplitudes and frequencies was performed. The results of the tests are presented in several ways. First of all, the error between the reference signal and the actual displacement was plotted. See Figure 6.9.

As expected, the controller failed in controlling the set-up for higher frequencies and amplitudes. But the error remained very small for all am-

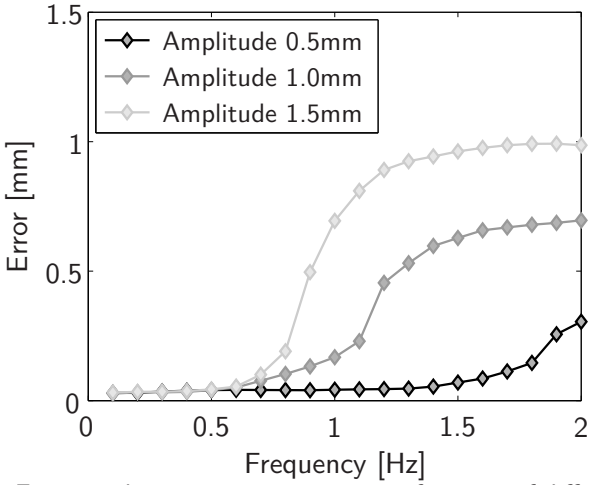

Figure 6.9: Error on the antagonist set-up as a function of different amplitudes.

plitudes up to 0.6Hz, which covers an important part of the frequency spectrum that is under consideration for large MW-sized wind turbines, as explained in Section 2.4.4. However, when observing the nature of the response above 0.6Hz (See Figure 6.10), it was noticed that the error was caused by a reduction in amplitude and a phase delay while the response maintained a sinusoidal shape. Therefore, the transfer between the reference signal and the actual response of the signal can be presented in the form of a Bode plot of the closed loop system. In Figure 6.11 it can be seen.

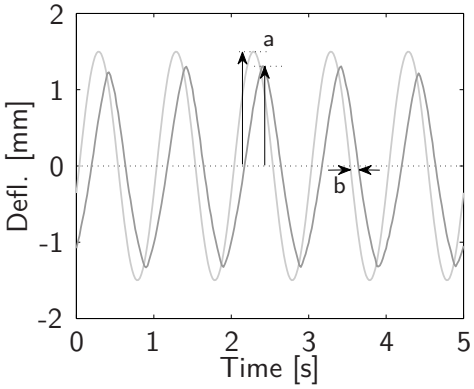

Figure 6.10: Time series of the antagonist set-up tracking a sinusoidal reference signal. a) illustrates the difference ('transfer') between the amplitude of the set point signal and actual displacement. b) illustrates the phase change.

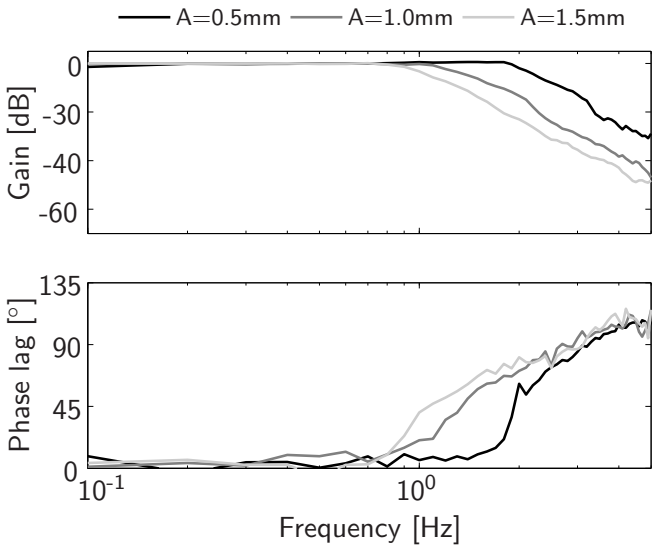

Figure 6.11: Bode-like plot of the antagonistic set-up for different amplitudes.

The conclusions are similar as with the error plot of Figure 6.9: for higher amplitudes the cut-off frequency decreases. The closed loop system seems to perform as a third order system because the slope of the roll off is 60dB per decade. The bandwidth of the closed loop system, where it passes the -3dB, seems to be at least 1Hz for all amplitudes. This knowledge can also be used to design a controller around the actuator system.

6.5 Actuator performance

Now that the potential and controllability of the actuator system were shown, experiments on the actual actuator were performed. To study its performance, a set of experiments was conducted of the same kind as on the antagonistic set-up. Because of the similar nature of the system (compare Figure 6.7 to Figure 6.12) the same controller structure was employed. The actuator is after all based on the same SMA wires and cooling channels and the wires were also applied in an antagonistic configuration. On the other hand, the SMA behaviour moves from a temperature-strain to a temperature-stress dominated controlled configuration because of the small strain fluctuations the SMA wire experiences in the actuator. Thus, the membership functions and rules had to be changed to accommodate for the different deflection behaviour of the actuator as compared to the antagonistic set-up. Moreover, the displacement of the actuator is induced by bend-

ing, whereas the antagonistic set-up describes a translational movement. Thus, these tests also provide information about the dynamic response of the beam actuator, as compared to only the SMA and thermal behaviour as tested on the antagonistic setup.

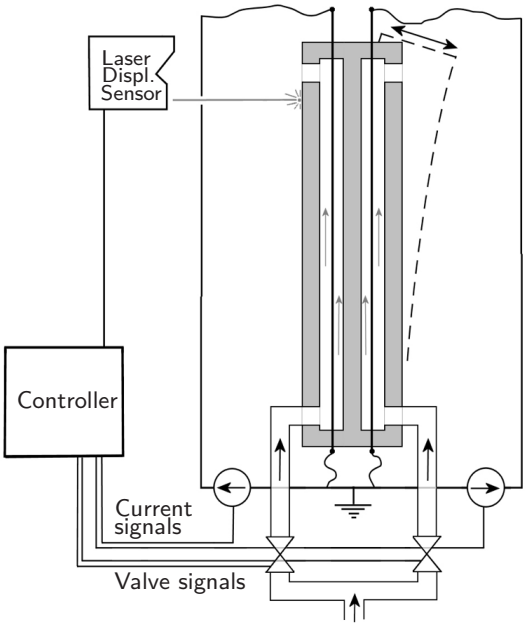

Figure 6.12: Schematics of the actuator test set-up.

6.5.1 Sinusoidal reference signal tracking

The actuator was set to track a sinusoidal set point signal, with the displacement transducer aimed at the tip as feedback signal. In Figure 6.13 the response to a low frequent reference signal can be seen, including the control signals. The response and the control signals seemed to be symmetric and the tracking was fairly good. However, the power control was somewhat irregular, with high spikes. The execution of the singleton output membership function for the valves can be seen as the constant cooling signal of -2V when the deflection of the actuator is around its maximum.

For higher frequencies the actuator response are presented in Figure 6.14. As can be seen, the bender behaviour became increasingly unstable with increasing frequency. The actuation frequency was maintained, but the response was not sinusoidal; the actuator was jumping from side to side.

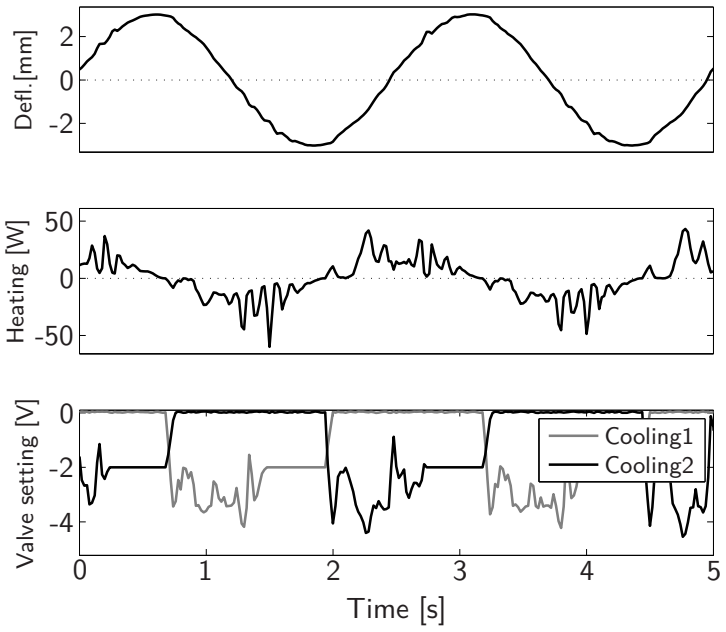

Figure 6.13: Response of the actuator to a 0.4Hz reference signal.

This was ascribed to snap-through behaviour around the neutral position of the bender which was caused by the space that the wires have in the channels. When the actuator moves through the neutral position, the wires move from one side of the channel to the other, see Figure 6.15.

The sign of the moment that a wire exerts, does not change because the channel is on one side of the neutral axis of the actuator, but around the neutral axis there are two stable positions. This was also substantiated by looking at the quality of a fit of a sine ($a\sin(bt+c)$, where t is the time and a, b and c are the parameters that were fitted to the measured data). R^2, the square of the correlation between the measurement data and the fitted values, is plotted in Figure 6.16 for the response of the antagonistic set-up and the actuator. It is a measure for the quality of the fit. Here it indicates whether the signal remained a sinusoidal shape, even if tracking of the reference signal was lost. $R^2 = 1$ indicates a perfect sinusoidal response.

From the figure it can be concluded that the actuator response lost its sinusoidal shape at much lower frequencies than the antagonistic set-up. This can only be attributed to the specific beam dynamics because the SMA material and the control system were the same.

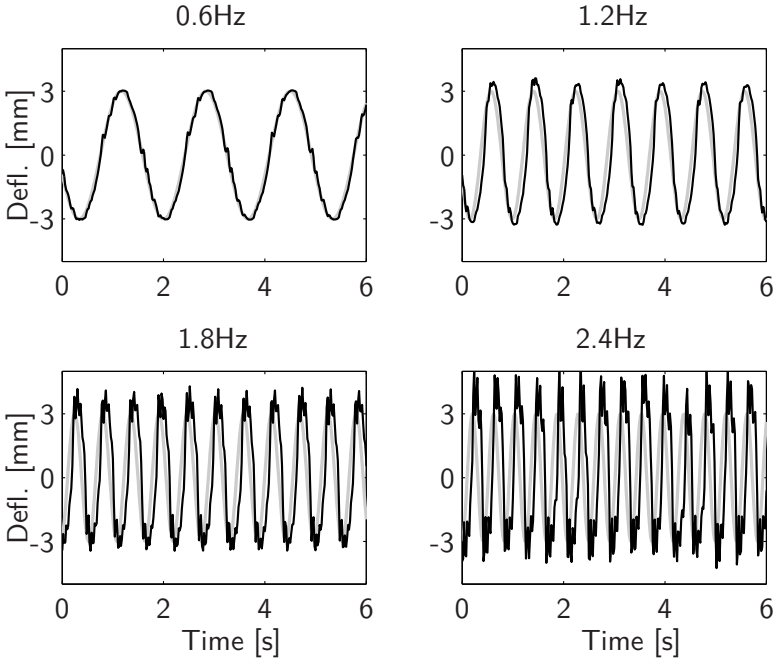

Figure 6.14: Performance of the bender in tracking sinusoidal signals with different frequencies and an amplitude of 3mm. The set point is depicted in grey and the response in black.

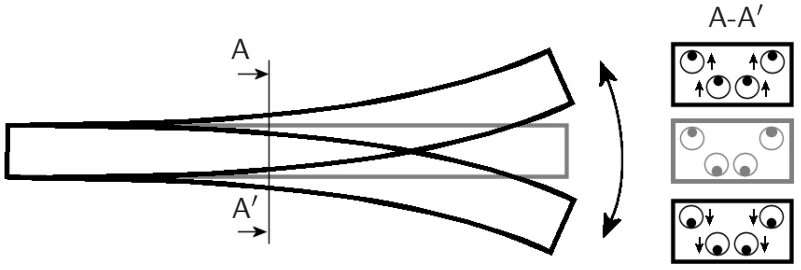

Figure 6.15: Schematic representation of the wires moving in their channels, causing an unstable neutral position (shown in grey).

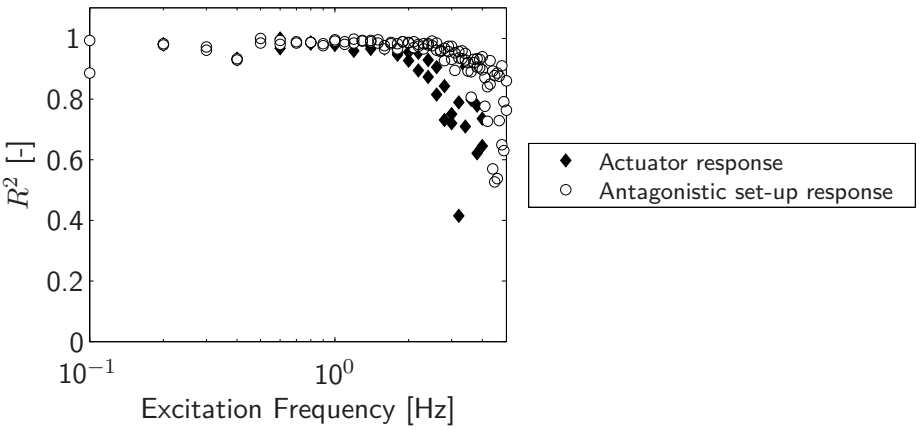

Figure 6.16: Square of the correlation for the response of the actuator and the antagonistic set-up

6.5.2 Composite sinusoidal reference signal tracking

Normally, the wanted deflection of the actuator, needed to counter blade vibrations, consists of a combination of different frequency components. To study the effect, a series of measurements on composite sinusoidal signals was performed. Moreover in such experiments it is also possible to see the response of the high frequency component with varying mean. The response and the set point for different frequency combinations are presented in Figure 6.17.

Here the snap-through behaviour, especially around the neutral position can also be seen in the form of jittering around the reference signal. The controller was unable to minimize the error because the actuator position was unstable around zero deflection. When the reference signal increased or decreased, tracking was restored again.

6.5.3 Step response

Finally, the closed loop response to a step on the set point is presented. This was an interesting case because a sinusoidal reference signal posed a constantly varying signal, but with the response to a step, the system had to act quickly with a small overshoot. Because this required a different type of response of the controller, it was an interesting case to subject the system to. The response to a step of $\pm$3mm can be seen in Figure 6.18 below.

The controller also seemed to perform well in this case. The wire set that is on the extension side is constantly cooled and the controller controls the

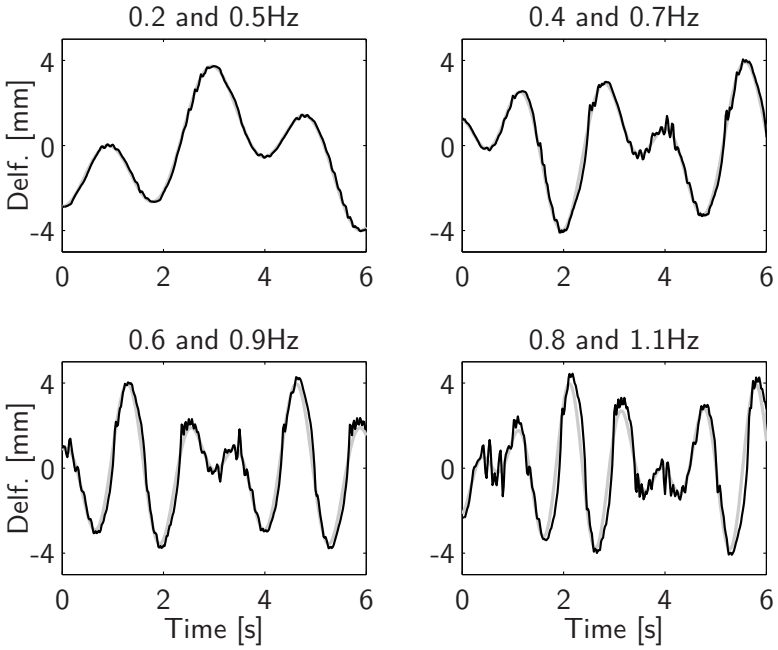

Figure 6.17: Performance in tracking composite sinusoidal signals of different frequencies. The reference signal is plotted in grey and the actual response in black.

actual position of the actuator through the heating signal. However, there was some overshoot and the response seemed to be asymmetric. Because the controller is completely symmetric, this has to be ascribed to the beam behaviour. Moreover, when a zoom of the steps is observed (see Figure 6.19), an acceleration of the deflection when it passes the neutral position between -1 and 1mm deflection, in both directions, can be seen. This could be attributed to the snap-through behaviour. Moreover, during the overshoot, a vibration is observed which has the same frequency of the first natural vibration of the actuator.

6.6 Concluding remarks

6.6.1 Discussion

An actuator was designed and manufactured, aimed at serving as a morphing surface. The design specifically tackled the bandwidth issue, associated with the dynamic use of SMA material to drive an actuator. From the thermal experiments we can conclude that the cooling channels, as they are

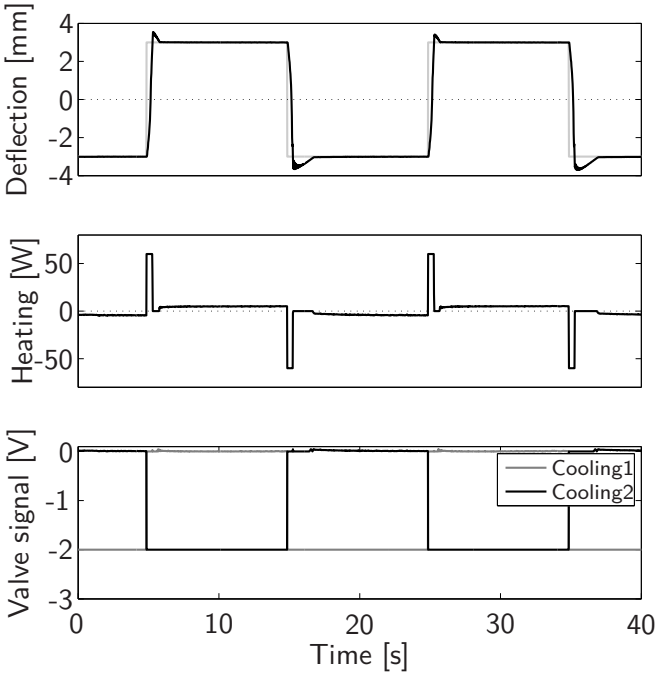

Figure 6.18: Response of the actuator to steps on the set point signal

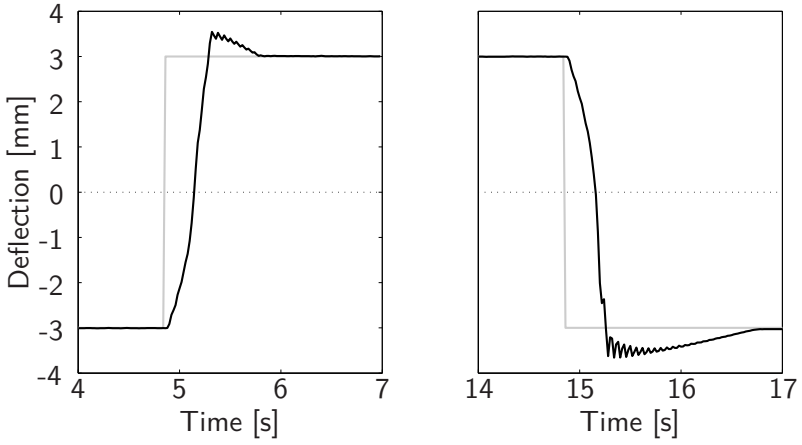

Figure 6.19: Zoom of the step response around the steps.

intended in the actuator, greatly increases the cooling rate, up to ten times in comparison to the same set-up without forced convection. Moreover, the advantage of cooling via internal channels over external cooling is that

the cooling rate can be controlled, limiting the power consumption and increasing the controllability because the dissipated heat is blown away and therefore there is no heat build-up in the actuator.

To study the performance of the bender a fuzzy logic controller was designed because of the non-linearities involved in the bender and the SMA material, and because of the linguistic nature that the controller offers. Tests with the actuator showed that a reference signal up to 0.6Hz could be tracked, which covers a large part of the load spectrum associated with MW-sized turbines.

Although the transition and hysteris band of the Smartflex material is rather narrow, the controller seems to be able to control the actuator to intermediate positions between zero and maximum displacement. On the other hand, the Clausius-Clapeyron constants of the SmartFlex material is not larger than with the reference NiTi material, as explained in Section 5.4. Therefore the temperature range over which the near restrained recovery transformation takes place in the actuator is still considerable.

Finally, although this work was aimed at obtaining a morphing surface for aerodynamic load control on wind turbines, the actuator concept could also be applied to any similar application requiring $\sim$1Hz actuation.

6.6.2 Ongoing and future work

For implementation as an actual flap several design improvements will have to be made, mainly regarding the shape of the cooling channels. Now the channels are relatively high as compared to the thickness of the actuator. In order to keep the channels on their respective side of the neutral axis, a thick actuator was constructed because the actuator has to be thicker than two times the height of the channel. This, however, limits the deflection of the actuator because its stiffness increases faster than the moment arm of the wire. After all, for a given wire, the curvature κ is defined by:

$$\kappa = \frac{M}{EI} \sim \frac{t}{t^3} = \frac{1}{t^2} \tag{6.6}$$

With M the moment exerted by the wire, t the thickness and EI the bending stiffness of the actuator. Moreover, the tip deflection of the actuator increases quadratically with curvature. Making the cooling channels flatter and wider will allow for a thinner actuator design and at the same time will minimize, if not remove the snap-through behaviour. Work is already progressing in this direction and a beam with flat cooling channels has already been manufactured, see Figure 6.20, also including the improvement of wire clamping and on the way that pressurised air is applied to the cooling channels.

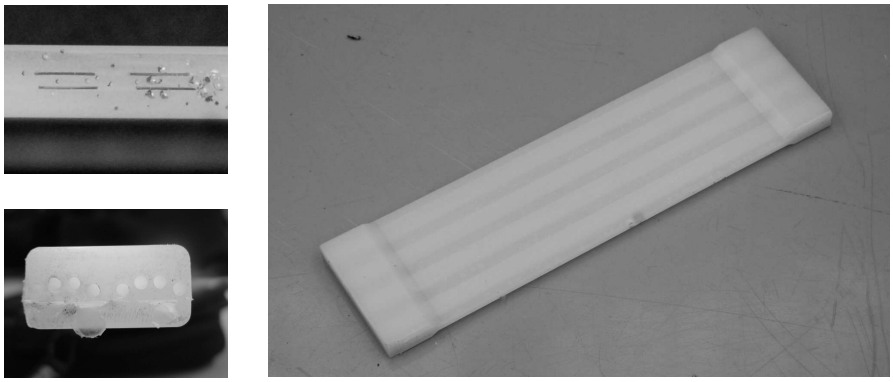

Figure 6.20: Actuator photo's. On the left: channel shape and configuration of the new actuator (top) and the actuator discussed in this chapter (bottom). On the right: new actuator.

It is asserted that a feedback controller is needed to control the actuator, especially if it is to be subjected to external loading. Moreover, further characterisation and modelling efforts will increase the controller's performance. Finally, as already discussed in Section 3.3.3, the durability of the SMA wire in the actuator can be increased by implementing a wire which exhibits the R-phase transition.

Further aspects regarding the integration of the actuator in an opperational wind turbine blade will be addressed in Chapter 8.

References

[1] K.K. Ahn and B.K. Nguyen. Position control of shape memory alloy actuators using self tuning fuzzy pid controller. *International Journal of Control, Automation, and Systems*, 4:756–762, 2006.

[2] A. Bejan. *Heat transfer*. John Wiley and sons, 1993.

[3] J.G. Boyd and D.C. Lagoudas. Physical metallurgy of TiŰNi-based shape memory alloys. *International Journal of Plasticity*, 12, 1996.

[4] J. Jantzen. *Foundations of Fuzzy Logic Control*. John Wiley and sons, 2007.

[5] A. Kumagai, T.I. Lui, and P. Hozian. Control of shape memory alloy actuators with a neuro-fuzzy feedforward model element. *Journal of Intelligent Manufacturing*, 17:45–56, 2006.

[6] D.C. Lagoudas, editor. *Shape Memory Alloys - Modeling and Engineering Applications*. Springer, 2008.

[7] NI. *LabVIEW - PID and Fuzzy Logic Toolkit User Manual*. National Instruments, June 2009.

[8] K. Otsuka and X. Ren. Physical metallurgy of tiŰni-based shape memory alloys. *Progress in Materials Science*, 50, 2005.

[9] K. van Rijswijk. *Thermoplastic composite wind turbine blades: vacuum infusion technology for anionic polyamide-6 composites*. PhD thesis, Delft University of Technology, 2007.

[10] G. Webb, L. Wilson, D. Lagoudas, and O. Rediniotis. Adaptive control of shape memory alloy actuators for underwater biomimetic applications. *AIAA journal*, 38:325–334, 2000.

Chapter 7

Rotor blade design

We will now discuss in a little more detail the Struggle for Existence.

Charles Darwin in 'The Origin of Species'

7.1 Smart and thermoplastic rotor blades

Recently Thermoplastic Composite (TPC) materials for wind turbine rotor blades have become of great interest to the industry. This is firstly driven by the several superior mechanical properties of TPCs over traditional thermosets, but also because of the potential of recyclablility with some polymers. Moreover, the material allows for some topological changes which may lead to an increase in blade quality and a reduction in production costs and which also benefits smart blade technology.

A smart rotor blade does not necessarily have to be designed from TPC, but there are several reasons why both technologies can go hand-in-hand. First of all, almost all flap concepts involve chordwise deformability or movement with loss in spanwise load carrying capability of the blade. After all, the flap itself must be able to move relative to the blade's base structure. Therefore, stiffening and reinforcing elements will be needed to create load paths around the actuator slots. TPCs are very suitable for creating structures with added reinforcing elements because they can be produced and assembles fast and cheaply. Secondly, for morphing flap technologies often thin, deformable skins are employed, sometimes with spanwise stringers because such a panel still has a considerable spanwise load carrying capability, while at the same time being deformable in cordwise direction. Thill presents a elaboration of the concept [1]. Typically, (amorphous) thermoplastics are tougher than thermosets, which is an advantage for the morphing struc-

tures because in principle the polymer allows for large deformations. The morphing surface which is discussed in Chapter 6 was constructed from a pure (unreinforced) thermoplastic polymer.

So concluding, it can be said that smart and TPC blade technologies are not directly linked, but that TPCs show clear advantages for smart rotor blades in design. Therefore, in this chapter and Appendix B the development of a TPC blade topology concept is discussed. The integration of the morphing surface will be discussed in Chapter 8.

In this chapter, firstly different manufacturing processes that are available for TPCs, and glass/APA-6 specifically, are discussed. Secondly, it is discussed how this leads to a different design concept. Finally, the design concept is materialised in a technology demonstrator. This chapter solely addresses the design of the blade's structure and the integration of the actuator technology is discussed in the next chapter.

7.2 A design and manufacturing concept

For TPC blades, a similar design similar to current thermoset blades is possible, but several properties of the materials and accompanying production techniques enable, but also ask for a different design topology and assembly methods. Here, we will address these issues and explain how this leads to a different design. But first the physics behind thermosets and thermoplastics that drive this change are briefly explain.

7.2.1 Basic polymer physics

Current polymer materials used in composite blade design are thermosets. Thermoset composites are typically produced by having a (monomer) resin polymerise in between its fiber reinforcement. The formed polymer has a high degree of cross-linking, forming a network that is not remeltable, nor can the monomers be reobtained from the polymer. Moulding of a thermoset part is therefore an irreversible process. Also, the process takes some time - at least minutes, but usually hours - because the polymerisation reaction does not occur instantaneously.

In contrast, thermoplastic polymers form linear, entangled chains on a molecular scale. These chains have some freedom of movement with respect to each other and a thermoplastic polymer is therefore typically much tougher then thermosets, if its degree of crystallinity is not too high. In addition, the chain movement increases at elevated temperatures, making the polymer meltable when heated. Finally, the thermoplastic polymers have

an almost indefinite shelve life, whereas thermoset resins and prepregs often need to be kept at refrigerated storage conditions.

Due to their meltability, with thermoplastics it is possible to use production methods based on the melting and (re)consolidation cycle. This temperature driven, physical cycle can be executed much faster than the chemical polymerisation reaction. TPCs are therefore very suitable for parts that have to be produced in large volumes in a cost-effective way. In the next section two of these production methods are briefly discussed.

7.2.2 TPC melt processing techniques

Firstly, a very powerful method for assembling TPC components, based on their (re)meltability, is welding. Welding methods include resistance welding [2], ultrasonic welding and induction welding. Induction welding is only possible with magnetically susceptible materials, such as carbon fibers. Resistance welding results in a very strong bond, of which the attainable static lap shear strength has been reported to be higher than that of co-consolidated joints, with similar fatigue properties [3].

However, sufficient pressure must be applied during welding in order to obtain a strong bond. When parts are assembled by means of a adhesive, there is some tolerance in the part shape because the adhesive can fill gaps, in order to obtain, for instance, the blade's outer shape from two half shells. So concluding, welding as assembly technique will lead to high part tolerances, but it also requires high tolerances or at least some flexibility of the subcomponents that are to be assembled.

A second issue is that currently with welding only a limited weld width is feasible. This is because a considerable amount of power is needed to attain welding temperature and the needed power increases with the weld's surface. Secondly, several bars of pressure have to be applied to obtain a high quality bond. Producing large welds is therefore impractical. Robotizing the process through Sequential Resistance Welding (SRW) [4–6] is under development, but for the conceptual design of the blade section we have decided to implement only line connections between different parts. However, if the issues of applying pressure and current are dealt with, which is usually a matter of designing the appropriate tooling, a high quality bond can be obtained very fast.

A second production technique which uses the possibility to melt thermoplastic polymers, is rubber forming [7]. Through rubber forming products can be shaped from flat semipreg plates by heating the material and pressing it in a mould with a rubber stamp, which produces an even pressure distribution during consolidation of the formed part. Thus parts can be

produced cheaply and fast, but the part size is limited by the size of the employed press and only thin parts can be produced in any case. For large parts of dimensions in the order of magnitude of 10^1m and larger, or parts that are thicker than $\sim$1cm, such as rotor blades for MW-sized turbines, resin infusion is really the only available manufacturing technique. Recently, resin infusion for thermoplastic composites has been developed, although the number of available resin systems is still limited. The technology is discussed in the next section for a specific polymer.

7.2.3 Reactive processing of APA-6

One of the thermoplastic material systems under investigation is Anionic Polyamide-6 (APA-6), a form of Nylon that is synthesized through ring-opening polymerisation [8]. The system was originally meant as a casting resin but in the last few years the curing dynamics have been adapted to make it suitable for resin infusion [9]. This has been an important breakthrough in the production of thermoplastic wind turbine blades [10] because traditionally TPCs are processed through melt processing of semi-pregs where extremely high, autoclave-like pressures are needed to obtain a properly consolidated product. This is not feasible with large parts like wind turbine spars and shells.

APA-6 is a semi-crystalline polymer and it has several material properties that are very attractive for wind turbine blades, such as retained toughness at low temperatures, good abrasive properties and the potential for recycling. Moreover, the material is cheap, especially considering the properties that it provides. Finally, the base materials have an almost infinite shelf life, as long as they are kept in a moisture-free environment.

In-situ polymerisation of TPCs enables the manufacturing of thick and large thermoplastic parts like wind turbine blade shells and spars by out-of-autoclave techniques. Through vacuum infusion the monomer Caprolactam is infused, together with a reaction initiator and activator. The mould and preform are heated to polymerization temperature (between 140 and 180°C) and the curing reaction takes place between the fibers.

In this, the initiator firstly reacts with the activator and forms a complex with a cation that has been disscociated from the initiator. This reaction, and formation of the complex with the cation from the initiator takes some time and this provides the time window for infusion. The formed complex can disscociate protons from the Caprolactam monomer, forming new reactive anions which react with the complex, by cutting open the ring of the end group. Subsequently a linear molecular chain is formed, hence ring opening polymerisation. This step (proton dissociation and reaction of the

anion) occurs easily, increasing the reaction rate after the complex formation. Moreover, the functional groups are not lost in the anion addition and thus the reaction can reoccur over and over again, leading to the formation of long, linear chains.

This polymerisation takes place at a temperature below the melting and crystallisation temperature and thus the process is more energy efficient than melt processing. Moreover, it is possible to control the crystallinity and molecular weight to some extent by choosing the process parameters, such as the curing temperature. The most important material properties of the glass/APA-6 composite and its epoxy benchmark are depicted in Table 7.1.

Property	GFR APA-6	GFR epoxy
Compressive Modulus [GPa]	26	25
Compressive Strength [MPa]	473	392
Tensile Modulus [GPa]	26	26
Tensile Strength [MPa]	495	476

Table 7.1: Comparison between the static and dynamic material properties of glass/APA-6 and glass/epoxy composites. Specimens were produced using a 8H satin weave. Specimens are tested dry as moulded. The implemented weave is a 8H satin weave. GFR stands for Glass Fiber Reinforced. Adapted from [9]

.

The fatigue properties of glass/APA-6 are reported by [9] to be slightly worse than glass/epoxy because of a poor fiber-to-matrix bond, but new sizings are under investigation.

7.2.4 Design considerations

State of the art blade design concepts

As explained in Chapter 1, current blade designs usually comprise of two shells adhered to each other with one or two shear webs to transfer shear loads. Most design variation can be found in the way the spar cap is incorporated. On some designs it is infused with the shells, but sometimes the spar caps and shear webs are produced as an integral sparbox. Thus, blades are usually assembled from three or four subcomponents, but also blades infused in one shot are reported. These designs are manufactured in this way because curing and bonding of the fiber reinforced (thermoset) plastic is a time consuming process, so the amount of components that is to be assembled, is minimized.

However, this group of concepts has some disadvantages. First of all, in order to assure stability of the panels in the leading and trailing edge sections of the blade, especially under compression, large areas of sandwich structures are implemented. In principle, a sandwich construction is a very effective way of applying bending stiffness to a panel with a low weight penalty because a high second moment of inertia is attained by mostly implementing a very low density material.

However, core materials constitute a large part of the material cost for wind turbine blades [11] and machining the material to size and shape is a labor intensive production step. Moreover, in wind turbines sometimes heavy core materials such as balsa wood are employed. These materials also take up a large amount of resin [12], especially in highly curved parts of the blade where the core materials needs to be dissected. Furthermore, a sandwich structure may provide the panels with a high bending stiffness, but if the core material is damaged or if the core-to-facing adhesion is lost, its load carrying capability is severely reduced [13]. The panel is therefore quite sensitive to local defects, introduced during production, impact or due to moisture uptake.

Finally, when bent in flapwise direction, blades are susceptible to so called Brazier effects due to ovalisation of the cross section, as reported by Jensen et al. [14]. This is an issue because flattening of the cross-section leads to a reduction in bending stiffness and stress concentrations in the sparcap-to-web region. Implementing a different stiffening structure, both for the panels as for the main loading structure itself, could therefore lead better performing blades. This possibility is provided by TPCs.

Thermoplastic composite blade design concept development

The most important design implication of the melt processing of TPCs, is that the economically driven concept of a blade that comprises of as little as possible components is not necessarily dominant because smaller components can be produced and assembled with the main structure cheaply and fast. A topology optimization performed by Joncas [15] already led to the conclusion that ribs in blades are favorable for dealing with a typical combined load case for a blade section, but ribs are only economical feasible if they can be produced and assembled quickly, which is the case for TPCs. Moreover, designs with a central, load carrying sparbox and attached rib stiffened trailing and leading edge panels is not new to aerospace, nor to the wind energy industry. The design was only abandoned for wind turbine blades because having as little as possible components to assemble the blade from, was considered favourable.

Furthermore, alternative methods of panel stiffening of these sections also become feasible with ribs. Traditionally, core materials such as foam or balsa wood are used to create a sandwich structure. Also, sandwich structures are proposed as spar cap reinforcement for very large blades [16]. However, with the ribs in the front and aft sections of the blade, providing panel stability in chordwise direction, other stiffening topologies can be considered. In aerospace industry, usually stringer stiffened panels are implemented, with ribs perpendicular to the main loading direction. A similar design could be implemented on wind turbine blades, considering the properties of the TPC.

On the other hand, stringer stiffened panels are also flexible in chordwise bending, providing the flexibility needed for a good fit of the parts in assembly. The ribs, which can be formed with very high accuracy, subsequently force the shell in the exact profile shape with minimal residual stresses while at the same time removing their chordwise flexibility.

Finally, with stringer stiffened panels, the same stringer geometry may be used throughout the whole blade, making it possible to implement them in a modular form and to produce them using (cheap) mass production techniques. The design of panels stiffened by top-hat stringers is addressed in the second part of this chapter and Appendix B. In the next section, the design and manufacturing of a thermoplastic blade section is addressed in which the integration of the TPC material, available manufacturing processes and design is addressed.

7.3 Manufacturing of a thermoplastic blade section

With these design considerations in mind, a demonstrator was manufactured. It was chosen to fabricate the demonstrator without skin stiffening - sandwich or stringers - because this section is meant as manufacturing demonstrator. Currently work on a full section which is structurally optimized is in progress.

7.3.1 Shape and size

The fact that the demonstrator is both an integrated material, production and structural design demonstrator as well as a test bed for smart rotor technologies, poses a design conflict. For structural design, the transition section of a blade is most interesting. This is the part where the cross-section of the blade transforms from the pitch circle at the root to an aerodynamic profile with a round nose, sharp tail and a relative thickness of tens of percents. This transition section is close to the root, so the blade

loading in considerable. But the profile is slender and it has a large chord, so this part of the blade is most critical in terms of strength and panel stability.

On the other hand, the spanwise positions where span wise distributed devices are to be implemented are located in the outboard section of the blade. Since the demonstrator should also be suitable for wind tunnel testing of integrated actuator technologies, for which the aerodynamic properties are a very important issue, it was chosen to design the demonstrator as a tip section of a blade.

It is therefore decided to proceed with a DU96-W180 profile, which is a typical tip profile. The demonstrator will still be used to demonstrate the concept of the internal lay-out, which is the same throughout the blade, as well as to integrate the different production methods in design. But the detailing of the design to meet different design criteria will be less critical.

The DU96-W180 profile has 18% thickness and the chord is set to 0.6m. This is big enough to attain representative Reynolds numbers and small enough to fit the profile in the TU Delft's smaller wind tunnel without blockage issues. The span is set to 1.8m, resulting in a span-over-chord ratio of 3, which is needed for proper wind tunnel testing. Moreover, the span-over-profile-thickness ratio becomes $16\frac{2}{3}$-to-1. A large span-over-thickness is needed to perform a represenatative (structural) bending test.

From this, it can be concluded that the outer shape is a compromise between different requirements and factors that have to be taken into account, but that all demands can be met. When the outer shape was set, the internal, structural design of the profile could be detailed.

7.3.2 Detailed design

Considering the possibilities and limitations of the production techniques within a laboratory environment, the following design concept is chosen. A central sparbox is employed, made out of two halves which are welded together in the middle of the shear webs. This is the point where maximum shear stresses as a result of bending occur, but welds are very capable of transferring these loads and the weld flange acts as a stringer along the web. It was decided to make the sparbox out of two halves so they could be produced by vacuum infusion without the need for very costly moulds and tooling.

The parts of the sparbox that form the spar caps also forms the outer skin. Consequently, the height tolerance of the welding process is utilized to the fullest and no large weld areas are needed to join the skin with the sparbox, as done in some traditional blade designs. The leading and trailing

edge panel sections are welded to the sparbox at the cap-to-web transition. The parts are given variable thickness, from 1.5mm for the skins up to 7mm for the sparcaps. This blade section is meant as a fabrication demonstrator, but still some detailing, such as the laminate thickness, is performed to obtain a representative product. See Figure 7.1 for a drawing of its cross-section.

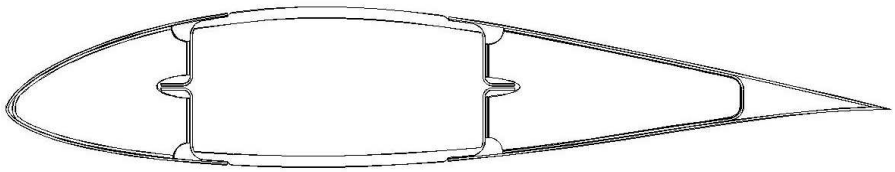

Figure 7.1: Sketch of the blade section design

The demonstrator is a 60cm chord, 90cm span prismatic section with a DU96-W180 profile as its outer contour. Three sets of ribs in the nose and tail section are placed at a 45cm pitch. Although often buckling of the sparcap is reported as a failure mode [13, 14], it is believed that ribs in the nose and tail will also improve the stability of the sparcaps because they provide lateral support to the webs, thus limiting the effects of the Brazier loads.

At this point it should be noted that this is *a* design concept, just like multiple design concepts exist for thermoset blades. Other considerations, such as maintaining natural laminar flow, are not made. Taking this into account may lead to a design without the nose-to-sparbox transition in the outer surface. However, as explained, this concept is aimed at addressing many of the design issues and possibilities that TPC blades pose.

Concluding, the possibilities and restrictions resulted in a design which consists of a central spar box which carries the main flapwise bending load. To this spar box the leading and trailing edge sections are attached by means of line welding. The leading and trailing edge are designed as open boxes with ribs to increase the shape stability. See figure 7.1

7.3.3 Manufacturing

All parts are made from a $0/90^{\circ}$ layup of a 8h satin weave and infused with the APA-6 resin. In addition, a plat plate is infused from which the blanks for the ribs are machined. The ribs are subsequently rubber formed from their blanks. In Figure 7.2a a blank, the rubber forming moulds and the final rib for the nose section can be seen. This process is sufficiently

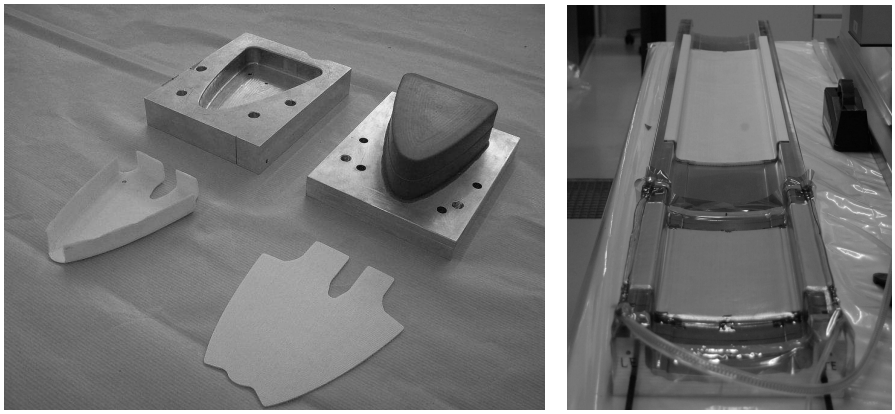

a b

Figure 7.2: Fabrication processes. a) Rubber forming. Flat blank, moulds and finished nose rib. b) Vacuum infusion. In front: bagged preform ready for infusion. In the back: finished part.

accurate so that trimming of the parts afterward is not needed.

Vacuum infusion followed by in-situ polymerisation is used to fabricate the large parts - the nose and trailing edge skins as well as the sparbox halves, see Figure 7.2b The half fabricates are trimmed afterwards to remove the excess material of the infusion in and outlet and the runners. Due to the shrinkage of the resin during polymerisation, with both sparbox halves some inward residual deformation of the webs was observed, but this had no influence on the assembly of the parts.

Subsequently, the different parts were assembled. The ribs were welded to the leading edge skin using a jig which accurately placed the ribs prior to welding and which was equipped with a rubber bladder between the part and the tool to apply pressure during welding. A pressure of 4 bars was applied. Subsequently, the trailing edge skins of the pressure and suction side were welded together on the trailing edge to form a V-shaped part. This subassembly was placed on the pressure side mould and the ribs were welded to the skin (see Figure 7.3b). This was also done using a welding jig for the ribs, as well as a special support which was placed over the suction side panel to keep it in place when the welding pressure was applied. The two sparbox halves were welded together by placing them both in their respective moulds and placing these on top of each other. Welding pressure was applied by adding weights to the top mould until a pressure of about 1 bar was attained.

Finally, the leading and trailing edge sub-assemblies were welded to the

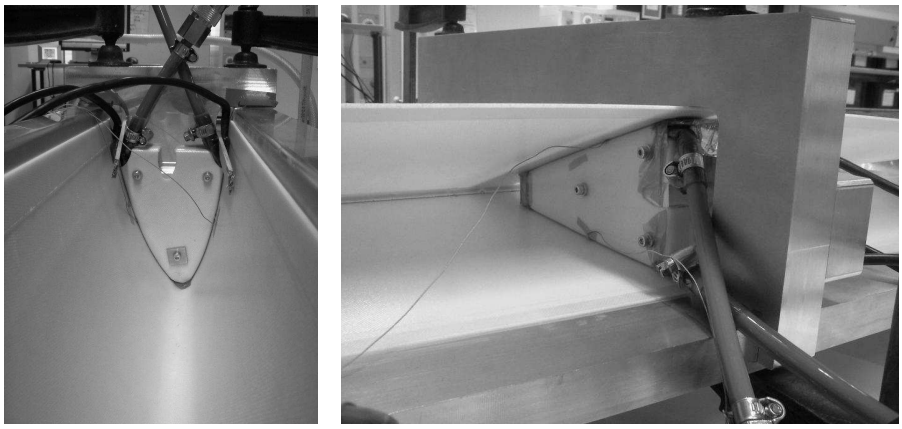

a b

Figure 7.3: Welding proces. a) Nose weld. b) Tail weld. In both cases the power cable (black) and tubes supplying air pressure to the blatters (grey with hose clamps) can be seen. The respective welding jigs are on the back of the ribs, but the bolts with which the ribs are bolted to the jigs can be seen. In b) also the support holding the suction side panel in place can be seen.

sparbox. Here, welding pressure was applied by adding clamps. The finished product can be seen in Figure 7.4a. In Figure 7.4b a zoom in of the sparbox-to-nose transition can be seen where the high tolerance of the welding process is visible. Because the shape of the nose is governed by the ribs and the nose-to-sparbox weld and because the nose itself is quite flexible in chordwise bending due to the absence of sandwich panels, very high shape tolerances are attainable here. The same holds for the tail section, of course.

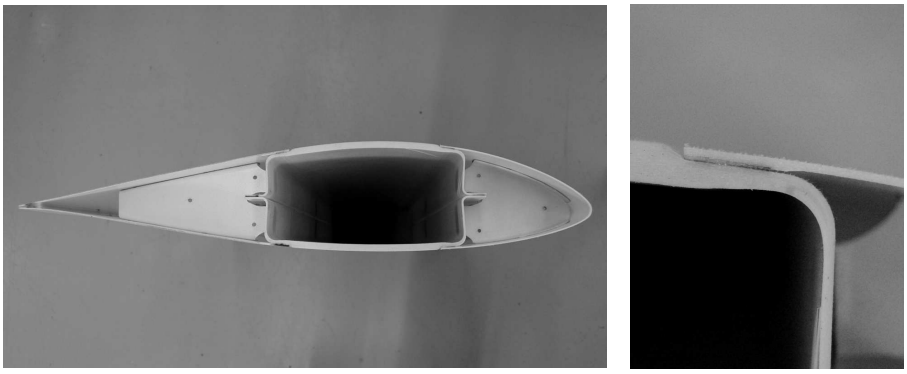

a b

Figure 7.4: Finished blade (a) with zoom of the spar-box to nose panel weld (b).

7.4 Detailing the design

The manufacturing demonstrator that was discussed in the previous sections is completely made from a $0/90^{\circ}$-oriented 8h satin weave because at the time of manufacturing this was the only suitable fiber material that was available. However, it is projected that in the near future UD tapes will become available. Therefore, using the moulds from the manufacturing concept and scaling down from the Upwind Reference Turbine (URT), a detailed laminate lay-up is derived and the issue of panel stiffening is addressed. The mould shape was already designed using the similarity rules that are discussed in the next section, but also some flexibility with respect to the laminate lay-up was incorporated into the mould design. Moreover, the matter of scaling is mostly important when detailing the laminate.

7.4.1 Scaling

The outer shape of the blade was given by the shape of the profile. What was left to do was to dimension the design in terms of laminate lay-up. Because no load requirements are known for the section, the design is scaled from the r=47.7m$\sim$0.75R section of the URT. For this, so called similarity rules are employed. These are analytically derived rules on how loads, stiffnesses, stress and masses scale as a function of the turbine size. Similarity rules are mostly employed to analyse technological development over the years against a theoretical trend because turbine size has only increased in time. For instance, it can be derived that the mass would theoretically scale with the rotor size cubed, whereas the historic trend has shown a growth with a factor of about 2.5, as already mentioned in Chapter 1. Moreover, these rules are used to make extrapolations to future, larger designs, but here they are employed to scale down an existing, large design to a manufacturable size. First, the similarity rules will be derived and secondly they will be applied to the design. When using similarity rules, the following assumptions are made [17]:

1. All dimensions of the structure scale linearly with R.
2. The blade profile at r_2 is the same as at r_1, when $r_2/R_2 = r_1/R_1$, with the subscripts 1 and 2 referring to similar blades of different size.
3. The rotational speed is inversely proportional to R.

The last point is easily defensible, by assuming that turbines operate at the same rated tip speed, independent of their size (which is more or less the case). In this case, however, 'all dimensions' is interpreted as 'all profile dimensions'; excluding the laminate thickness. Thus, it is derived how loads

and deflections scale with size but decissions about the laminate thickness are made *a posteriori*.

Loads

The power that a turbine converts, increases with R^2. The root bending moment follows from the converted power in the following way:

$$P_{\text{blade}} = P_{\text{turbine}}/n = M\Omega \quad \rightarrow \quad M = \frac{P_{\text{blade}}}{\Omega} \sim \frac{R^2}{R^{-1}} = R^3 \tag{7.1}$$

Where M is the root bending moment in the blade, n the number of blades and ω the rotational speed. So the root bending moment scales with R^3.

Stresses

For a thin walled profile, the moment of inertia of a cross-section increases with the thickness of the profile, cubed, if the wall thickness is not changed. After all, if the flapwise bending stiffness is dominated by the sparcaps, their contribution is defined as:

$$I = Ay_1^2 + Ay_2^2 \tag{7.2}$$

With A the cross-sectional area of the sparcaps, which is assumed to be equal for both caps, and y_1 and y_2 the distance between the respective sparcaps and the neutral axis of the profile with regard to flapwise bending of the blade. Thus, $y_1 + y_2$ equals the total thickness of the profile. y_1, y_2 and A all increase linearly with R. If the laminate thickness is not changed, A increases with R linearly because the width of the sparcap increases with $\sim R$. Thus: $I \sim R^3$. The stress in the sparcap is defined as:

$$\sigma = \frac{My}{I} \sim \frac{R^3 R}{R^3} \sim R \tag{7.3}$$

Where y is the distance between the neutral axis of bending and the sparcap and it also increases with $\sim R$. So the stresses increase linearly with the size of the blade, if the thickness of the laminate is not changed. Therefore, to maintain equal stresses, the laminate must also increase linearly with the size of the turbine.

Consequently the blade's mass increases with the cube of R if equal maximum stresses are considered: One order because of the blade length, one order because of the increase of the circumference of the profile and one order from the increase in laminate thickness.

Stiffness

In the previous paragraph linear laminate scaling with profile size has been derived, assuming a certain maximum allowable stress. In the following, stiffness scaling will be derived using the assumption of linearly increasing laminate thickness. The tip deflection δ of a cantilevered beam with linearly increasing distributed loads along the span (which is the case for wind turbines) reads:

$$\delta = \frac{11 q_o L^4}{120 EI} \tag{7.4}$$

Where q_o is the load level in N/m at the tip. In this equation an uniform stiffness distribution is assumed, but since all local bending stiffnesses along the span scale with the same order, it is implemented for comparison here. Since q_o increases linearly with R and EI with the forth order of R, the tip deflection will increase linearly with R: $\delta \sim R$. However, since the overhang - the distance between the tip of the unloaded blade and the tower - also increases linearly with turbine size, this is an allowable; the relative tower clearance will remain the same.

Laminate lay-up

With the scaling factor for the laminates known, the given laminate of the reference turbine can be downscaled for the demonstrator to realistic values. The results can be seen in Table 7.2.

Laminate	Reference section	Demonstrator
Sparcap	33	7
Skin	5.6	1.19
Shear webs	5	1.06

Table 7.2: Laminate thicknesses in mm for the r=0.75R section and the scaled demonstrator. As skin and web laminates the sum of the thickness of the respective sandwich facings is taken.

However, Table 7.2 only depicts laminate thicknesses, not the specific lay-up. When determining the laminate lay-up for the demonstrator, of course the lay-up of the reference section should be taken as a starting point. However, there are two issues to be considered. The scaling of the laminate is done considering global blade properties, e.g. bending stiffness of the whole profile. Therefore, the foam core in the sandwich can be left out when considering the global stiffness of the blade. However, for the local

panel properties the specific lay-up and panel stiffening methods are of great importance. When thinking about alternative panel stiffening topologies, as described above, the laminate lay-up should also be (re)considered. For instance, the facing laminate of the sandwich skins of the reference turbine is a triaxial lay-up with only 0°, -45° and 45° plies. This is a very logical lay-up because the ±45° add shear stiffness to the blade and take up the stresses that are induced by blade torsion and edgewise bending. The 0° fibers increase the capability of the blade to take up normal stresses. The core material of the sandwich provides sufficient transverse bending stiffness to the panel, as a result of which the implementation of 90° fibers is not needed. Another restriction is formed by the availability of the different fiber architectures. Basically, two are available: an UD tape and a 8h satin weave. In design, all laminates will be assumed to be made from the satin weave, except for the UD in the sparcaps.

This means that when applying the weave in the skin, adding 0° fiber material will imply the application of an equal amount of 90° fibers. This is actually a desired side effect because of what is explained above: removing the core material decimates the bending stiffness of the skins. In longitudinal direction the global bending stiffness is restored by adding stringers, which also take up a considerable amount of the compressive loads on the panel when the blade is bent. In transversal direction, however, additional reinforcement is needed. Another design study on a vertical tail plane for an aircraft [18], in which a sandwich design is compared to a stringer stiffened design, also showed that quasi-isotropic laminates are needed when applying stringers. Because the scaled thickness is only 1.19mm, only 5 plies can be implemented in the skin and a $[\pm 45, 0/90, \pm 45, 0/90, \pm 45]$ layup is implemented.

7.4.2 Finite element analysis

In the course of the feasibility study of this topology, a FE model was made to determine the amount, locations and geometry of the panel stiffening elements, as well as the rib pitch. The requirement is that the buckling load capacity is equal to that of sandwich panels. The model was used to analyse the part of the blade that is most susceptible to buckling; the spanwise position at maximum chord length. The set-up of the model and the result on the maximum-chord section are described in Appendix B as well as validation experiments on a top-hat stiffened panel and an analysis on the modelling method.

In this study, an algorithm is used that optimises the location of a given amount of stringers with given geometry. The optimiser consists of a evo-

lutionary part that mixes the design parameters of well performing designs, but also randomly explores the design space. A second part of the algorithm executed a targeted mutation, aimed at suppressing local buckling by reducing the distance between stringers at the location where local buckling occurs. To reduce the computation time, only the suction side of the blade section is modelled, with antisymmetric boundary conditions on the section plane. This is not entire accurate because the profile is not completely symmetric, but the model is employed for comparison purposes. The procedure is run for a series of basis values. The details of the analysis for the maximum chord section can be found in Appendix B. The results show that it is possible to attain similar buckling loads as with a sandwich panel with a limited amount of stringers and ribs.

The model is also used to analyse the demonstrator. In this case, no stringers are implemented in the nose because it is hard to apply them with the available tooling due to space restriction. To compensate for this, more ribs are applied in the nose. Three stringers are implemented in the tail section in the optimisation process. Regardless of the stringer position, buckling will occur in the sparcap, according to the simulation. This is probably due to the relatively large sparcap width. This was linearly scaled down, but afterwards extended with two areas which would act as welding zones for the nose and tail sections. But the analysis does show that panel stability is easily attained with few stringers and ribs and omitting the core of the sandwich.

The occurence of buckling in the sparcap makes the application of the optimisation process less relevant. On the other hand, panel buckling is also not a critical failure mode for the r=0.75R section on the full scale URT. The first buckling modes for the demonstrator under four-point-bending can be seen in Figure 7.5.

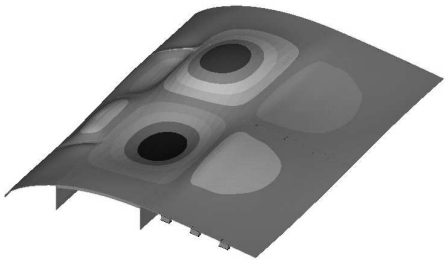

Figure 7.5: Buckling mode of the center 0.9m of the demonstrator under four-point-bending.

7.5 Discussion

In this chapter a design and manufacturing concept for thermoplastic blades was developed. Secondly, using the manufacturing concept, a detailed design was developed to show the potential of alternative panel stiffening methods. In this section the concept and design will be evaluated to learn lessons for the manufacturing of a fully optimised design and to realise an actual thermoplastic smart blade.

7.5.1 Manufacturing concept

The manufacturing concept showed some clear advantages. For instance, very high shape tolerances were attained because of the ribs, despite shape distortion of the shells due the large amount shrinkage of the APA-6 which is caused by the polymerisation reaction and crystalisation. The ribs force the skins into the right shape and the skins allow this because of their flexible nature, as opposed to sandwich shells.

Also, the design makes optimal use of the welding technique by implementing only line welding. Downsides to the concept are the need for a final finish to fill the small surface discontinuity near the nose-to-sparbox and tail-to-sparbox welds. Another issue that needs attention are the mould design. To obtain moulds that are both thermally and chemically compatible with the APA-6 polymerisation process, they were milled from blocks of aluminium. This has several disadvantages. First of all, the moulds become very expensive and heavy. Secondly, the mould has a very high thermal inertia. This does not only mean that heating to processing temperature in an oven takes several hours, but also that infusion has to take place at polymerisation temperature. This limits the infusion window since at this temperature initiation of the polymerisation takes place after about six minutes. The rate of subsequent polymerisation is very high, so the resin becomes viscous very quickly and the resin front comes to a halt.

Ideally one would infuse at a temperature just above melting temperature of the Caprolactam (90-110°C) and increase the temperature to the polymerisation temperature (140-180°C) after that. However, this must be done fast and the thermal inertia of the mould does not allow that as explained above. Therefore, all parts of the demonstrator were infused at 150°C and a limited infusion length was taken into account when determining the infusion strategy.

There are also some design issues with the current demonstrator. For instance, the detailed analysis of the concept shows that buckling of the sparcap is the first occurring failure mode under four-point-bending, which

can be attributed to the large sparcap width. Unfortunately, the results of the panel buckling analysis on the demonstrator are therefore inconclusive.

7.5.2 Alternative concepts

As explained in the previous section, the manufacturing concept that was developed has several drawbacks. Several design choices were made because of the prototyping nature of the demonstrator. With the lessons learned, other topologies could be considered. First of all, since a core material, PET foam, has been found that is chemically compatible with the APA-6 system and that can withstand the processing temperatures, a traditional design lay-out could be implemented. However, then the advantages of the APA-6 come purely from its mechanical properties and the material's full potential in manufacturing and design is not utilized. But since industries are often conservative and like to use proven technologies and designs, it can not be ruled out that APA-6 wind turbine blades will firstly be implemented in this form.

In general the load carrying concept of the blade, and the way that shape stability under loading is retained, could also be changed. With state of the art designs, the main flapwise bending load is carried by a sparbox or by sparcaps which are connected by webs, but also to a large extent by the shell. The normal stresses as a result of edgewise loads are taken up by the nose and tail, which are sometimes reinforced with spanwise oriented UD. In the concept that was discussed here, the same load distribution concept was employed, but the way in which the components are assembled and deal with their loading is changed. Alternative concepts might involve incorporating the edgewise load carrying capability solely in the sparbox or in a D-nose, in which case all loads, including the torsional ones, are carried by a single component, *monocoque*, part. Then non-load carrying panels, attached by welding, could form the tail. Such a concept would combine the advantages of a one-shot design with the strong points of the TPC manufacturing and assembly techniques. These designs are not new to wind energy, as mentioned by Joncas [19], but TPC technology makes their reintroduction very attractive, especially considering that the extremely large chords of large blades are becoming a bottleneck in transportation. Later assembled, non-structural fairings might be a very attractive solution to that issue.

The final conclusion is that the TPC material and processing technologies open up many new design options which are explored in this study. Another conclusion is that an optimal design concept, taking into account aerodynamic considerations and optimising for the final cost-of-energy, is

still to be developed.

In the next chapter, the demonstrator of which the design and build was discussed here, will be used to implement the SMA activated morphing surface of Chapter 6.

References

[1] C. Thill, J.A. Etches, I.P. Bond, K.D. Potter, and P.M. Weaver. Composite corrugated structures for morphing wing skin applications. *Smart Materials and Structures*, 19:doi: 10.1088/0964–1726/19/12/124009, 2010.

[2] D. Stavrov and H.E.N. Bersee. Resistance welding of thermoplastic composites - an overview. *Composites Part A: Applied Science and Manufacturing*, 36:39–54, 2005.

[3] I. Fernandez Villegas and A. Yousefpour H.E.N. Bersee, P. Hubert. Performance analysis of resistance welded and co-consolidated joints in continuous fibre reinforced thermoplastic composites. In *Proc. of the SAMPE 2010 conference*, May 2010.

[4] C.L.T. Lambing, S.M. Andersen, S.T. Holmes, R.C. Don, B.S. Leach, and J.W. Gillespie Jr. Apparatus and method for resistance welding., 1993. United State Patent No. 5.225.025.

[5] S.T. Holmes and J.W. Gillespie jr. Thermal analysis for resistance welding of large-scale thermoplastic composite joints. *Journal of Reinforced Plastics and Composites*, 12, 1993.

[6] S.H. McKnight, S.T. Holmes, J.W. Gillespie, C.L.T. Lambing, and J.M. Marinelli. Scaling issues in resistance welded thermoplastic composite joints. *Advances in Polymer Technology*, 16(4):279–295, 1997.

[7] G. Nino, H.E.N. Bersee, and A. Beukers. Design and manufacturing of thermoplastic composite ribs based on finite element analysis. In *Proc. of the 49th AIAA/ASME/ASCE/AHS/ASC Structures, Structural Dynamics and Materials Conf.*, april 2008.

[8] K. Rijswijk and H.E.N. Bersee. Reactive processing of textile fiber-reinforced thermoplastic composites - an overview. *Composites Part A: Applied Science and Manufacturing*, 38:666–681, 2007.

[9] K. van Rijswijk. *Thermoplastic composite wind turbine blades - vacuum infusion technology for anionic polyamide-6 composites*. PhD thesis, Delft University of Technology, 2007.

[10] K. van Rijswijk, S. Joncas, H.E.N. Bersee, and O.K. Bergsma. Vacuum infused fiber-reinforced thermoplastic mw-size turbine blades: A cost-

effective innovation? In *Proc. of the 43rd AIAA Aerospace Science Meeting and Exhibit*, January 2005.

[11] D. Berry and S. Lockard. Innovative design approaches for large wind turbine blades final report. Technical report, Sandia National Laboratories, USA, 2004.

[12] F. Stoll, R. Banerjee, and D. Griffin. Performance of engineered sandwich cores in large wind turbine blades. In *Proc. of the Windpower conference*, January 2008.

[13] C. Berggreen and B.C. Simonsen. Non-uniform compressive strength of debonded sandwich panels, Part II fracture mechanics investigation. *Journal of Sandwich Structures and Materials*, 7:483–517, 2005.

[14] B.G. Falzon F.M. Jensen, J. Ankersen, and H. Stang. Structural testing and numerical simulation of a 34 m composite wind turbine blade. *Composite Structures*, 76:52–61, 2006.

[15] S. Joncas, M.J. de Ruiter, and F. van Keulen. Preliminary design of large wind turbine blades using layout optimization techniques. In *Proc. of the 10th AIAA/ISSMO Multidisciplinary Analysis and Optimization Conf.*, 2004.

[16] C. Berggreen, K. Branner, J.F. Jensen, and J.P. Schultz. Application and analysis of sandwich elements in the primary structure of large wind turbine blades. *Journal of Sandwich Structures and Materials*, 9: 525–552, 2007.

[17] M. Zaaijer. *Wind Turbines: Types, Economics and Development*, chapter 3, Developments of concept and scale of wind turbines for offshore application, pages 63–94. Nova Science Publishers, 2009.

[18] H.E.N. Bersee, O.K. Bergsma, and et al. Conceptual design vtp-n6. Technical report, TU Delft, The Netherlands, 2003.

[19] S. Joncas. *Thermoplastic Composite Wind Turbine Blades - an integrated design approach*. PhD thesis, Delft University of Technology, 2010.

Chapter 8

Actuator integration

'An idea that is developed and put into action is more important than an idea that exists only as an idea'.

Buddha

8.1 Introduction

In the previous chapter a structural concept for thermoplastic rotor blades was discussed. As stated, the thermoplastic concept poses clear advantages for smart rotor blades, such as the possibility to add local structural elements to reinforce the blade to add mounting points for smart systems. In this chapter the structural integration issue will be discussed, on the basis of the actuator and the structural concept that were already discussed in Chapters 6 and 7, respectively.

The integration heavily depends on the aerodynamic effect that is under consideration. Three ways of implementing the SMA actuator that was developed, or other deformable surface concepts, were presented in Chapter 2. Firstly, the suction and pressure side of the existing profile could be replaced by the actuator, resulting in a deformable prismatic trailing edge. Secondly, the actuator could be mounted near the trailing edge as a spoiler flap. Finally, it could be mounted as a flat extension to the trailing edge as done with piezoelectric Thunder actuators by Bak et al. [1]. In this chapter the integration of the deformable surface into the blade structure as a flat extension will be discussed in more detail. The choice was made because it is relatively easy to implement the flap in this way and, in contrast to the spoiler flap, its performance is relatively known. Moreover, the flap can also be easily inspected and if necessary replaced. But there are also drawbacks.

Most notably, the compliance of the actuator itself is rather high, so its resistance to external loading is limited.

8.2 Structural issues

The issue with implementing a deformable trailing edge into the blade's structure is that the part of the chord carrying the loads on the blade is strongly reduced because it is hard to provide the deformable part with both deformability (compliance) and load carrying capability (stiffness, strength). This has three mayor implication for the structural properties of the blade section where the flaps are to be applied:

1. The edgewise stiffness is reduced because of the reduction in chord.
2. The torsional stiffness is reduced because of the reduction in cross-sectional area of the profile.
3. the transition from the base blade to parts with flaps will lead to additional stress concentrations.

The flapwise bending stiffness of the blade is hardly affected because this is mostly governed by the spar caps at the thickest part of the blade, which remains unchanged by the introduction of the flaps. The edge wise and torsional stiffness could be brought back to the base level by adding an additional spar. For the reduced profile, the reduction in structural rigidity of the base structure is larger than with a truncated profile, which would remain with a prismatic trailing edge flap, for the same fraction of deformable trailing edge, see Figure 8.1. It can be clearly observed how a truncated profile leads to a structure with a higher edgewise and torsional stiffness than one of which the trailing edge part is resized to arrive at the same chord, because there are more (possibilities for) load carrying elements in the trailing edge.

Figure 8.1: Example of a truncated DU96W180 profile (grey) and one with a scaled aft part (outlined), to come to the same reduced chord. The deformable part of the aerofoil is displayed by dashed lines.

Another issue is the transition - in spanwise direction - from the static part of the blade to sections with flaps. A gradual change is proposed, because

it limits stress concentrations and the occurrence of radial flow effects. Furthermore, it will require the design of a new profile, probably based on a DU96-W180 or NACA-64618 profile. Preferably, the nose and sparcap of the profile is the same as the base profile so this part of the blade remains smooth and the bending stiffness of the section is preserved, which is a matter of redesigning the profile.

8.3 Demonstrator

To show how such an actuator concept could be realised a demonstrator concept was built, based on the structural concept described in Chapter 7 and the actuator of Chapter 6.

The actuator was slightly adapted to have a flat trailing edge. In addition, the way that the airflow was applied and the way the wires were clamped on the trailing edge had to be changed as compared to the actuator that was tested in Chapter 6 in order to fit the actuator in the trailing edge. This also constitutes an improvement. The actuator consisted of three actuator units, assembled with small pins. Therefore, there are six air tubes applied; one for each side of each actuator.

A 7.5cm wide section was built, in which three actuators were integrated. Unfortunately, the span-over-chord ratio of this section is much smaller than 1, making it impossible to perform wind tunnel experiments on the section. However, at this stage of the actuator development, making this section already constituted a challenge. Future work on the actuator, as described in Section 6.6.2 will make upscaling in spanwise direction more easy.

The section was equipped with one rib in the nose and two in the tail. To these two ribs a bracket was mounted, illustrating the added value of the multi-component design for smart rotors. The aft panels on the suction and pressure side were not welded together, leaving a gap through which the actuators could extend. No additional spar was added. See Figure 8.2 for a picture of the trailing edge of the section with the actuators mounted to it.
On the other hand, however, this concept can also be realised on thermoset blades. But still the creation of mounting points and load paths remains an issue. Photos of the actuator in its position of maximal positive and negative deflection can be seen in Figure 8.3.

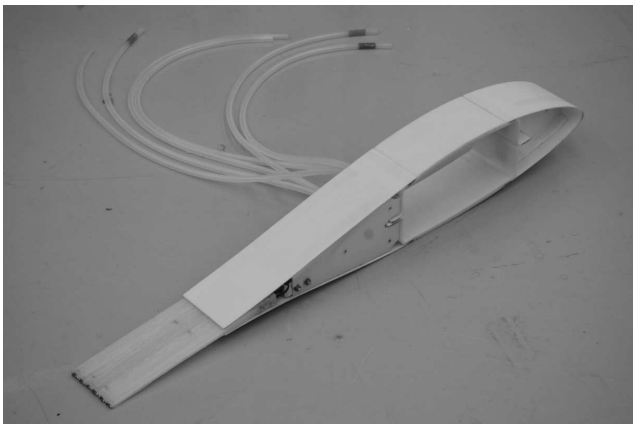

Figure 8.2: 75mm Wide blade section with the SMA actuator as flat extension to the trailing edge. In the back the tubes that apply compressed air to the actuators can be seen.

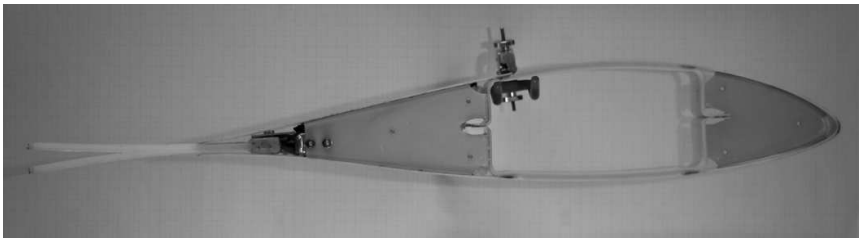

Figure 8.3: Overlay of two photo's of the actuator in maximum up and down deflection

8.4 Sensor and controller issues due to integration

In Chapter 6 feedback control on the flap's deflection was done through a laser at the tip. Feedback control on the actuator deflection or deformation will be needed because of many uncertainties in the actuator's behaviour due to changes in ambient temperature and external loading. Alternatively, a laser displacement sensor could be used to aim back from the blade's main body towards the actuator tip, or optical fibers with Fiber Bragg Gratings (FBGs) could be embedded within the actuator. In any case, a displacement or deformation measurement system should be implemented.

FBGs can also be used to monitor the temperature in the actuator. Temperature measurements or estimation could be very helpful in controlling the actuator. Firstly, since the actuator will heat up slightly during operation, temperature measurements could be used to compensate strain measure-

ments. But more importantly, temperature measurements could be used to monitor the temperature of the wire. In this case, the temperature sensor (being for instance a thermocouple or a specialised FBG grating) should preferably be placed as close to the SMA wire as possible. This would be valuable information for the Fuzzy Logic Controller, especially if fluctuating aerodynamic loading leads to a different deformation for the same actuator signal. Supervising the wire temperature will make the controller more robust and will prevent overheating.

Alternatively, a state estimator [2] could be used because it proves to be hard to measure the internal states (temperature, martensite fraction) of the actuator that are relevant to controlling the actuator. Attempts using the electric resistance of the SMA material have also been made [3], because it varies with martensite fraction, but the response is highly non-linear and ambiguous. Estimating the states using the power and valve settings and considering the external loading as 'noise' could be an option. But in this case also measurements of the actual deflection or deformation will be needed to update the estimates.

8.5 Concluding remarks

In this chapter the implementation of a continuously deformable surface on a wind turbine as a load control surface in the form of a flat extension on the trailing edge of the thermoplastic blade concept was discussed. A large deflection of the actuator was observed, but upscaling in spanwise direction is needed for wind tunnel tests. In Chapter 2 already an alternative application in the form of a spoiler flap was elaborated.

Concluding, it can be said that several concepts exits, but that the final implementation depends on issues like the size of the turbine, the required change in C_L (and thus flap deflection) and the expected external loading on the actuator. The concepts also vary in the ease in which they can be implemented in the aerodynamic and structural design. Furthermore, a detailed analyses of the solid-fluid-interaction for specific devices is needed to make a good assessment of their respective performance, especially if the aerodynamic performance of the device relies on its own compliance, as with the morphing surface.

References

[1] C. Bak, M. Gaunna, P.B. Andersen, T. Buhl, P. Hansen, and K. Clemmensen. Wind tunnel test on airfoil Risø-b1-18 with an active trailing

edge flap. *Wind Energy*, 13:207–219, 2010.

[2] B.N. Datta. *Numerical Methods for Linear Control Systems - Design and Analysis*. Elsevier, London, 2004.

[3] K. Ikuta, M. Tsukamoto, and S. Hirose. Shape memory alloy servo actuator system with electric resistance feedback and application for active endoscope. In *Proceedings of the 1988 IEEE international conference on Robotics and Automation*, pages 427–430, 1988.

Chapter 9

Conclusions and discussion

Gust: Did I ever tell you the story of the Zen master and the little boy? On his 16th birthday, a boy gets a horse as a present. All the villagers say, 'How wonderful!' The Zen master says, 'We'll see.' One day, the boy is thrown from the horse and is hurt and can no longer walk. All the villagers say, 'How terrible!' The Zen master says, 'We'll see.' A short time later, war begins, and all the young men of the village are taken away to be soldiers, but this boy can't fight, so he is spared, and all the villagers say, 'How wonderful!'

- Charlie: And the Zen master says, 'We'll see...'

Gust: You're catching on...

Scene from 'Charlie Wilson's War', *Universal, 2007*

9.1 Introduction

In this chapter conclusions are drawn on the different aspects of the implementation of the smart rotor concept that is discussed in this thesis - actuator technology and integration into a 'smart' system and the blade's structure. Also, a discussion on, and recommendations for the steps that need to be taken towards commercial implementation are presented.

9.2 Actuator technology

9.2.1 Conclusions on the SMA-based actuator

In Chapter 3 an overview of different actuator concepts was presented. A choice was made to continue with SMA based morphing surfaces due to the specific force, deformation and bandwidth properties of the material. In Chapter 5 and 6 further investigations into a specific wire were made and

the gap between the theoretical attainable bandwidth and what is observed with embedded wire was bridged by development of an actuator with internal cooling channels.

From this it can be concluded that SMA material is very suitable for actuation of control surfaces from a thermo-mechanical point of view, provided that active cooling is implemented. Large deflections are attainable and actuation up to $\sim$1Hz are within reach.

9.2.2 Shape memory alloys - applicable on wind turbines?

Limitations

In the previous section, the merits of actuators based on shape memory alloys are discussed. However, for implementation on wind turbines two mayor hurdles remain. The first one is the limited fatigue life of the material. In this thesis the martensite-to-austenite transition was implemented in the actuator, but there is also the possibility to use the R-phase transition. The downside to the R-phase transformation is that the actuation strains are limited, but for SMA material close to the neutral axis of the actuator only small strains are needed to obtain the wanted actuator displacement. Beside the strain limitation, it could be questioned whether material with which the R-phase transition is implemented will attain the fatigue life that is needed for implementation on wind turbines. Of course, the actuator could be replaced during inspection, but it will still have to remain in service for millions of cycles.

The second issue is lightning strike. A thunderbolt making contact with the turbine through an actuator will surely damage the actuator locally. However, any implemented electrically driven actuator, which could be anything from a servo, linear motor or electrically driven adaptive materials, will cause issues with lightning, because the electrical system acts as a lightning conductor and the electric charge of a thunderbold passing through the system will destroy it. Therefore, concepts that are not electrically driven pose a big advantage. For instance, pneumatically driven actuators are proposed [1].

If the actuator is implemented as proposed in this thesis, with Joule heating, that will naturally cause lightning issues on wind turbines. However, the functionality of SMA material also poses another opportunity to deal with the lightning strike issue. The material in principal reacts to heat - no matter how that heat is applied - and the cooling channels that were developed here, make it possible to not only cool, but also heat the internal SMA material through convection. Thus, the SMA material can also be

applied in such a way that it is electrically insulated and does not act as lightning rod in the blade. If the actuator is hit by lightning, locally it will be damaged, but the control system is not and due to the distributed nature of the SMA actuator, it can remain in service. Therefore, SMA based actuators may even pose an even more serious candidate for control surface actuation than already argued in this thesis, if an alternative way of applying heat can be found.

Alternatives

Here, two type of alternatives will be discussed: alternative use of the SMA material and alternatives to the SMA-based actuator. As explained in Chapter 3, SMA material may not only be used as actuator to deform structures. Alternatively, it may also be implemented in its super-elastic form, acting as passive damper. Also, it could be implemented in semi-active form in the blades load carrying structure. In that case, the wire is applied prestrained, in its martensitic form. When heated, the wire will stress the structure. When this is done actively, active damping is applied to the blade's structure. Of course, this will not remove the source of load fluctuations, but it will reduce the blade's dynamic response to those fluctuations in a way that is much simpler than applying load control surfaces.

Alternatives to SMAs for the implementation of control surfaces are also still on the table. For instance, compliant mechanisms or piezoelectric actuation also are viable solutions, although each have their own drawbacks, as mentioned in Chapter 3. For instance, piezoelectric actuators will have to be driven by a high voltage and the attainable deformations are limited.

9.2.3 Recommendations for future work on the actuator

One of the features of the actuator that requires improvement is the shape of the cooling channels. Currently, the cooling channels have a height (diameter) that is much larger than the diameter of the wires. Thus, the wires are free to move in the channels and the beam needs to be made relatively thick to fit the channels. It is a matter of ongoing research to develop an actuator with a flat channel by using a thin strip in stead of a cylindrical inserts to form the channels. See Figure 6.20. This has several advantages:

1. Less snap-through effect.
2. Because the channels can be made thinner, so can the actuator. Thus, it can be designed with a lower bending stiffness.

3. The channel can be made with a large width, so multiple wires can be mounted in one channel.

Drawbacks are that the wire will need lateral fixation in the channel and that a circular channel provides the lowest flow resistance for a given cross-section area, unlike the wide, flat channel.

A second point of improvement is the fuzzy logic controller. Feedback control on the actuator deflection or deformation is needed for three reasons. Firstly because of the non-linear behavior of the SMA material. Secondly because of the thermal uncertainties, for instance fluctuating ambient temperature and flow around the actuator, and finally because the actuator is an elastic body that will deform under external loading. The work in Chapter 6 is performed using controller based on the tip deflection, measured with a laser displacement sensor perpendicularly aimed at the actuator tip. This is not a practical solution on rotating turbine blades, unless a backward looking laser can be installed in the base structure of the blade, as described in Chapter 8. The backward looking laser displacement sensor or, for instance, embedded FBG sensors could prove a durable, robust deflection measurements for feedback control on the flap deflection.

A third point for improvement is the method of clamping of the wire. Currently this is achieved by locally pressing the wire into the polymer of the actuator using a bolt, resulting in high friction and shape locking. Taking the actuator to a higher TRL will require a custom made clamping system with minimal stress concentrations at the wire's ends. Finally, an investigation into different SMA wire materials could be made. This should be mostly aimed at optimal durability, expressed in a long fatigue life and actuator stability.

9.2.4 Final considerations on SMA-based actuators

Thus, taking all considerations into account, it can be concluded that the implementation of SMA material into continuous deformable surfaces has been brought a few steps closer through the work in this theses, but that still issues and good alternatives exist. The final choice for an actuator will depend on the demands that are set for the actuator. These include the aerodynamic effect that is sought (resulting in certain required load and deflection characteristics) and the load spectrum that is under consideration. This does not only imply a certain bandwidth demands for the actuator, but it is also related to the control strategy that is conceived. For instance, the choice could be made to only use the flaps in situations that pose a severe fatigue load spectrum, such as above-rated wind speeds, severe wind shear

or turbulence conditions. In such a case, SMA-based actuators are a very powerful solution because the number of actuation cycles is reduced and the limited fatigue life is less of an issue.

9.3 Smart rotor systems

9.3.1 Sensors

The main conclusion on the implementation of the smart rotor system is that a controller based on the root bending moment provides a considerable load reduction potential, as long as the dynamics of the turbine are taken into account. This is mostly a matter of controller design, but in the design of the turbine and (smart) rotor blades already several steps can be taken to make the load control system effective, of which the most important ones are sensor choice and sensor placement.

In this work, piezoelectric sensors, that are bridged with a high-Ohmic resistance were used. This provides a sensor signal with a high signal-to-noise ratio and the sensor is in principle very durable. Moreover, it can be embedded in the blade's surface and it had an intrinsic high-pass filter. Thus, only the dynamic strains are recorded, but mitigating that is ultimately the goal of the smart rotor concept.

As explained in Chapter 4, the placement of the sensors is important to obtain good phase behavior with the flaps. For quasi static excitation, it is less of an issue, but if it is needed to suppress the blade's dynamic modes as well, it is clearly important. In design, this can be investigated through a harmonic analysis with excitation forces applied at the intended flap locations.

9.3.2 Discussion on the control strategy

When taking the actuator that was developed in this thesis can attain into consideration, as discussed in Chapter 6, its most important limitation is still its bandwidth. 0.6Hz Sinuses are tracked perfectly, and signals up to 1.2Hz can be tracked with an acceptable amount of error, see Figure 6.14. In Chapter 2 a distinction was made between the minimum required actuation bandwidth, and the ideal one. The minimal required bandwidth for the reference turbine was set at 1.4Hz, still slightly higher than what the SMA-actuator can attain. This bandwidth, as compared to the rotational frequency and dynamics of a large turbine is the same as the spectrum that is under consideration in Chapter 4; from quasi-static to a frequency just above the frequency of the first eigenmode (flapwise bending) of the

blade. However, the actuators used in the wind tunnel experiments can attain much higher actuation frequencies.

Therefore recommendations for future work, taking into account the limitations of the SMA-actuator, would include running experiments and simulations with more stringent restrictions on the actuation speed and deflection. In the experiments described in Chapter 4 and references [2] and [3] already saturation of the actuators was observed in some cases; the system wanted more flap deflection than the actuator could provide. Also, in simulations, a certain maximum flap deflection and flap speed is usually imposed on the flap. For instance, Barlas and van der Veen [4] already focused on the 0-2Hz band with accompanying flap speeds. If the bandwidth of the actuator proves to be too low to target the first (flapwise) eigenmode of the blades and turbulence, it would be very interesting to study what kind of load reduction is attainable with a feedforward controller that only focuses on the 1P or 1-to-3P loads.

9.4 Actuator integration

9.4.1 The SMA actuator as aerodynamic feature

Regarding the application of the actuator, several proposals have been made. However, the way in which the actuator is to be implemented is mainly an aerodynamic consideration; how the actuator can lead to a maximum ΔC_L with a minimal drag penalty. Speaking from an actuator point of view, the main criteria are the amount of aerodynamic loading the actuator has to deal with and the complexity of incorporating it in the blade's structure.

The spoiler flap concept seems to be very easy to apply, but little was known about its aerodynamic performance. Therefore, a first-order aerodynamic analysis of the spoiler flap concept was made. The conclusions are that the attainable effect in terms of ΔC_L is similar to microtabs. On the other hand, undesired phase behaviour and initial opposed lift change during dynamic excitation is an issue that should be investigated. From an actuator and structural integration point of view, this way of applying a morphing load control surface is a very attractive solution because of its low impact on the blade's structure.

9.4.2 Structural integration - are TPC and smart blades two sides of the same coin?

However, integration of the actuator in the blades structure will generally require redesign of the blade. As mentioned, the severity of the needed

redesign will depend on the specific actuator choice. But in all cases, even concepts that are researched outside this work, such as microtabs and compliant mechanisms require local reinforcements and stiffening of the blade's structure. The reason for this is threefold:

1. To restore the blades stiffness which is reduced due to a reduction in chord and cross-sectional area.
2. To create load paths around cut-outs, mitigating stress concentrations.
3. To create mounting points for actuators (if a few, large actuators are to be implemented).

As argued in Chapter 7 and 8 this makes the implementation of a TPC blade concept very logical because with this family of polymers locally applied structural elements can be produced and assembled fast and cheaply. Only the spoiler flap seems to be a concept that can be implemented without any notable structural revisions. However, the TPC material and the design concepts that it enables, also pose other merits, such as recyclability and the possibility to greatly reduce the amount of sandwich core material that is implemented in a blade. Resin uptake and sensitivity of sandwich cores to local defects are also important issues with current blade materials and designs, regardless of the smart rotor concept.

So concluding it can be said that for the smart rotor concept, implementing a TPC design seems a logical step, but the other way around that is not necessarily the case: thermoplastic blades can be designed without implementing the smart rotor concept. The reported fatigue properties of the glass/APA-6 system is not at the same level as typical thermoset composites, but work is continuing on this topic on a material level and it can be debated whether implementing the smart rotor concept is the right way to balance inferior material properties. This does illustrate that the design decision to implement the smart rotor system should be made on turbine (system) level, instead of blade or rotor level.

9.4.3 Recommendations on thermoplastic blade design

As explained in Chapter 7, the conceptual design that was developed here, was partly driven by the prototype nature of design and that fact that is has to be both a structural concept and a test bed for wind tunnel testing of actuators. Since a PET foam is available for panel stiffening, a more traditional topology could also be chosen. In that case, however, the production benefits that TPCs pose, are not fully exploited. Also, other design lay-outs like a load carrying D-spar with the trailing edge as a fairing

could be considered. In this case, the fairings could possibly be assembled on-site, reducing transportation issues.

Concluding, it can be said that the thermoplastic blade design poses many new design options, addressing current design issues, but depending on other (aerodynamic) design considerations, such as the implementation of an aerofoil with a flat-back or large inboard chords.

9.5 Final conclusions

9.5.1 Conclusion summary

In this thesis many issues of the smart rotor concept have been addressed. An actuator with specific characteristics for actuation on wind turbines was developed. Secondly, the concept and design issues of smart rotors are discussed. Finally, proposals for implementation of the actuator in the blade's structure are made, although a more thorough analysis on the solid-fluid interaction between the (elastic) actuator and the flow should be made. The complexity of structural integration in the blade strongly depends on the type of control surface, but this is not believed to to be an insurmountable issue when the flap covers a limited part of the chord ($\sim$10%). A new structural concept was presented which tackles many of the structural issues that will are arise with implementing non-load carrying parts, such as flaps. If the actuator is to be an add-on feature, this is not an issue all together.

9.5.2 Smart rotor blades - panacea or fata morgana?

As explained in the introduction to this thesis, the smart rotor concept poses a solution to many of the load problems that current and future (larger) turbines are suffering from. This most of all concerns fatigue, but also gust alleviation and increased aero-elastic stability are possible merits of the system. On the other hand, adding such a system is in contradiction to the notion that a turbine's design should be as simple as possible for the sake of robustness. Therefore the concept has to overcome a certain economic barrier because it will require a higher initial investment and causes concerns about maintenance. Thus, the commercial implementation of the smart rotor concept may be a long time coming, since many practical issues and design options remain. The final decision on the implementation of the smart rotor concept and which actuator to use, will have to be made by the Original Equipment Manufacturers (OEMs), possibly driven by demands from operators to do something about dynamic load issues.

Thus, from a lift control point of view, there are little technical hurdles remaining, some of which are tackled in this thesis. However, to obtain a working, economically feasible *system* on a MW-sized turbine, several steps will have to be taken. Moreover, with the current state of the art, a trade-off will have to be made between load reduction potential on one hand and loss of power conversion and system complexity on the other. Even for the actuator itself such a trade-off is necessary. For instance, with actuation by SMAs, large deflections are possible, but the bandwidth is limited, even with active cooling. With piezoelectrics this is the other way around (high bandwidth, small deflections) and electric motors, for driving compliant mechanisms for instance, will add a lot of weight. At present time it seems impossible in any case to obtain a structure that will deform smoothly, fast, with large deflections but with almost no weight and maintenance penalty - which, as explained in Chapter 3 is the ultimate goal in the field of smart structures.

In the end, making design choices on a wind turbine comes down to a economic assessment and this is not any different for the smart rotor concept. If, when and how load control features along the span of the blade and the accompanying control system will finally be implemented on commercial turbines is something that is up to industry. But the tools and knowledge, both for design and in terms of hardware, are becoming increasingly available and it is believed that this thesis contributed to that.

This research will continue within the DUWind institute and the faculty of Aerospace Engineering of the Delft University of Technology, improving the actuator quality and researching new control concepts.

References

[1] T. Buhl, P.B. Andersen, M. Gaunaa, C. Bak, H. Madsen, F. Zahle, J. Heinz, L. Bergami, L. Na, and A. Fisher. Latest results and tuning activities at Risø DTU withing trailing edge flaps. In *Proc. of 56th IEA topical expert meeting on the application of smart structures for large wind turbine rotor blades*, May 2008.

[2] A.W. Hulskamp, J.W. van Wingerden, T. Barlas, H.E.N. Bersee, G.A.M. van Kuik, and M. Verhaegen. Design of a scaled wind turbine with a smart rotor for dynamic load control experiments. *Wind Energy*, page published online, 2010.

[3] J.W. van Wingerden, A.W. Hulskamp, T. Barlas, G.A.M. van Kuik, D.P. Molenaar, and M. Verhaegen. Two-degree-of-freedom active vibration

control of a prototyped 'smart' rotor. *Journal of IEEE transactions on control system technology*, page published online, 2010.

[4] T. Barlas, G.J. van der Veen, G. van Kuik, D.-P. Molenaar, and M. Verhaegen. Model predictive control for wind turbines with distributed active flaps: Incorporating inflow signals and actuator constraints. *Wind Energy*, DOI: 10.1002/we, 2010.

Appendices

Appendix A

CFD parameters

Grid	
Grid generator	Gambit 2.4.6
Dimensions	2D
Number of cells	$\sim 6{\cdot}10^4$
Cell shape	Quadralitical cells are applied in the wake of the spoiler flap, in the boundary layer and in the far-field flow. Around the profile, triangular cells are applied. None of the cells have mid-side nodes.

Boundary conditions	
Inlet	Uniform flow, U=14.61m/s, resulting in Re_L=$1{\cdot}10^6$. 10% turbulence intensity.
Outlet	Pressure outlet, 0 gauge pressure.
Top and Bottom	Symmetry BCs
Profile	Wall

Boundary layer	
First cell thickness	$2.33{\cdot}10^{-5}$, y^+=1
Grow factor	1.2

Turbulence modeling	
Model type	standard k-ϵ, with standard wall functions.
Model parameters	C_μ=0.09, $C_{1\epsilon}$=1.44, $C_{2\epsilon}$=1.92, Prandtl number: 1

Fluidum properties and flow conditions	
Dynamic viscosity, μ	$1.7894 \cdot 10^{-5}$ kg/m s
Density	1.225kg/m^3
Pressure (at infinity)	101325Pa
Reynolds number	$1 \cdot 10^6$

Solver	
Solver	Fluent 6.3.26
Solver type	Steady, implicit formulation, pressure based.
Discretisation	Second order
Gradient option	Green-Gauss Node-Based
Number of iterations	>5000
Convergence criteria	All residuals $<10^{-4}$ and fluctuations in lift coefficient that are in the order of 10^{-3}.

Grid convergence

For one of the cases a grid convergence study has been made, of which the results can be seen in the graph below. The grid space h is defined as $1/\sqrt{n}$, where n is the amount of cells in the mesh. The coarsest grid is the grid that is used for Figure 2.10 and has about 54000 cells. The finest grid has about 190000 cells.

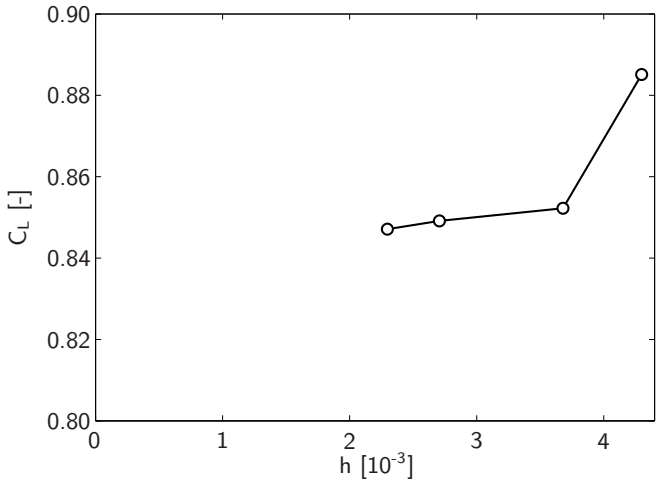

Appendix B

The feasibility of top-hat stringers

As explained in Chapter 7, thermoplastic blades pose both a opportunity and a circumstance to consider different panel stiffening topologies. The opportunity arises from the possibility of introducing additional structural elements and the circumstance from the fact that only limited core materials are available for in-situ polymerisation.

Regardless of the thermoplastic concept, top-hat or omega stringers pose a very attractive way of stiffening panels because they are an efficient manner of providing both global and local bending stiffness to a panel and they can be co-cured with the skin. In that case, they may be draped over trapezium shaped foam stringers, and infused and cured together with the skin. See figure B.1 for a sample of a APA-6/glass panel with co-cured stringers. For APA-6 composite panels, PET-foam was found to be a core material that is both thermally and chemically compatible with the fabrication process, but at present time no other feasible core materials are known. The employed foam can be a low density variant because it is only used as a draping tool. Prefabrication of the stingers is also possible and in that case they can be assembled by welding. The optimal solution depends on the amount and the size of the stringers, but here we will assume co-cured stringers with which half the laminate of the panel forms the skin and the other half is alternately draped over the trapezium foam pieces and on the skin laminate (see also Figure B.1).

Although it is reported that top-hat stringers are not the most cost effective way of providing buckling resistance to a plate [1], they are now being employed on the Boeing 787 Dreamliner's carbon fuselage. Glass Fiber Reinforced Plastic (GFRP) top-hat stiffened structures are also applied in

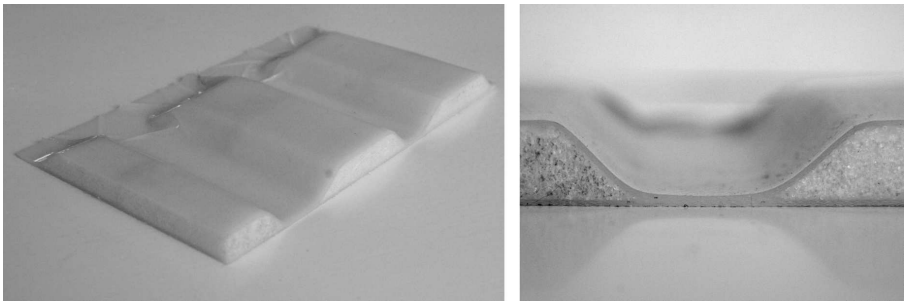

Figure B.1: APA-6 plate with co-infused stringers, draped over PET-foam.

large yachts [2] and even thermoplastic top-hat stiffened bridge decks are proposed [3]. Therefore, in this appendix an analysis is made on the implementation of top-hat stringers for front and aft panels of wind turbine blades. First, a feasibility study is made on the maximum chord section of a 5MW blade by optimising the stringer placement for a given number of stringers and stringer geometry and the method of modelling that is used, is analsysed. Secondly, experiments on a flat stringer stiffened panel are discussed.

B.1 Comparison to the reference design

Before running an optimisation procedure, the reference design is analysed. Here, as for the design of the demonstrator in Chapter 7, the 5MW URT is chosen. A fictive laminate lay-up of the URT blade is derived in the UpWind project that corresponds to the blade's stiffness distribution [4]. The topology of the cross-section of the mayor part of the blade is as follows (see Figure B.2): The skin laminate consists of a triaxial non crimp fabric (NCF), in the thickest part of the blade a strip of unidirectional (UD) material is laminated between the triaxial layers in spanwise direction to form a spar cap and in the front and aft part a dense foam core to form a sandwich. At the transitions from spar cap to sandwich two shear webs are placed, effectively forming a spar box with the spar caps. In the trailing edge a band of spanwise oriented UD is placed to increase the edgewise stiffness.
Because the laminate is described for the whole shell, including sparcaps, the topology would suggest that the blade is assembled from two shells and two webs, in contrast to, for instance, a design with a spar box out of one-piece with to shells adhered to it. But the design is a virtual one (no actual blade exists) and no details were provided.

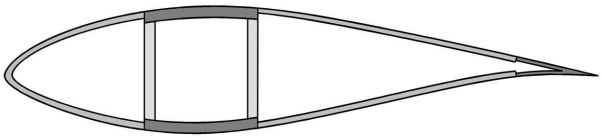

Figure B.2: Lay-out of the reference turbine. Black: GFRP multi-axial laminate. Dark-grey: GFRP UD, Grey: Shell sandwich core. Light grey: web sandwich core.

The main issue with changing the panel topology is buckling. The blade's stiffness in flapwise bending is mainly provided by the spar box-like structure which is left unchanged in this analysis. To analyse the buckling capacity of the reference blade, first a global Finite Element (FE) model of the blade is constructed and used in linear analysis to analyse the buckling mode and to estimate the Critical Buckling Load (CBL) of the blade.

B.1.1 Material properties

The material proporties of the URT are only provided on laminate level. However, to study the feasibility of a different design topology it is necessary to change the laminate lay-up. Therefore, a study of the laminate is made to derive the ply properties, using micro-mechanical modelling (the Concentric Cylinder Assembly (CCA) model [5] in this case) and the Classical Laminate Theory (CLT). The laminae of the URT are assumed to be of the same UD-weave material, except for the shear webs. For the sparcaps all material is placed in a 0° orientation and for the facings a triaxial NCF of the same fiber material is assumed. The lay-up of the triax is derived to be about 50% $\pm 45^\circ$ fiber material and 50% $\pm 0^\circ$ In table B.1 the results of the design study, as well as some experimental validation can be seen. The experiments were performed on a 250kN Zwick testing machine with strain gages attached to the specimen to measure the strain. The specimens' dimensions and test procedure are in accordance with ASTM standard 3039-07 [6]. The lay-up of the triaxial lay-up of the specimens used in the experiments is $[0_2,(+45,-45)_s,0_2,(-45,+45)_s,0_2]$. The total laminate thickness is then 2.85mm, as compared to 2.8mm given for the URT.

However, this concerns a kind of reverse engineering analysis of the URT laminate. For the new design with stringers, half of the 0° plies are replaced by 90°, to enhance the the transverse bending stiffness of the panel. The lay-up used in the Finite Element Analysis (FEA) for the top-hat stiffened panel becomes: $[(45\ -45)_s,90_2,0_4,90_2,(45\ -45)_s]$.

Property name	Derived ply prop.	Derived triax prop.	Measured triax prop.	Given triax prop. [4]
E_1 [GPa]	44.6	26.6	26.9	24.8
E_2 [GPa]	9.9	13.3	14.0	11.5
G_{12} [GPa]	3.9	-	-	4.9
ν_{12} [-]	0.23	0.486	0.498	0.42
UTS [MPa]	-	-	462	436
UCS [MPa]	-	-	346	349

Table B.1: Used and provided material properties. UTS stands for ultimate tensile strength and UCS ultimate compressive strength.

B.1.2 Buckling

The FE model is built in Ansys and consists entirely of quadratic shell elements. When defining the material lay-up, each ply is defined separately. The load case consists of the instant that the maximum flapwise bending moment in the root occur during rated wind speed operation, as modelled in the wind turbine aeroelastic code Bladed. Only the inboard 47 of the 63m span are modelled, up until the point where the UD material in the trailing edge ends. This is done because the tip is not of interest to the model. The tip loads are transfered to the sparbox at the truncation in the form of a flapwise and edge wise moment, shear loads and and a torsional moment. Several iterations are performed because the centrifugal loads are not scalable. As can be expected, buckling occurs at the maximum chord section of the blade in the aft sandwich panel. See figure B.3. Here, the aft suction side panel is 2.3m wide and almost flat. The CBL factor is 6.79, which is quite realistic for such a design. Subsequently, a smaller model with constant cross-section of this local section of the blade is made, similar to the one employed by Lund and Johansen [7]. Consequently, in the optimization procedure on the top-hat stiffened design many design variations can be analysed at low computational cost. The section also consists of quadratic shell elements and only the suction side of the blade is modelled, with anti-symmetric boundary conditions on the chord line. The section is 8 meter long but it is extended 4 meter on both sides. These sections are given very stiff material definitions to distribute the loads, which are introduced as a 1kN compressive load on the sparcaps, over the whole cross section. This model shows a similar buckling shape as on the whole blade model. The reference CBL factor is 1140. This value is used to benchmark the top-hat stringer designs.

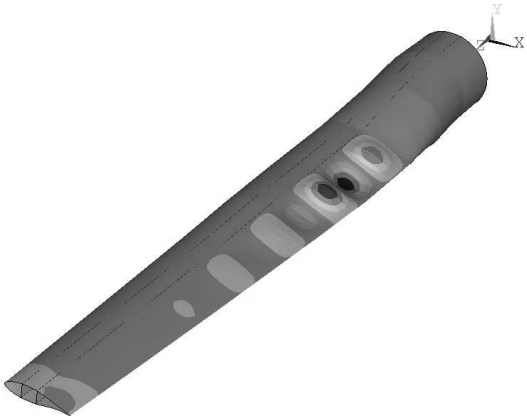

Figure B.3: First buckling mode of the blade.

B.2 Design optimisation with top-hat stringers

B.2.1 Modelling

In order to limit the number of nodes and elements in the model, the top-hat stringer is modelled as sandwich material. Thus, the webs of the stringers are omitted, but the flange is modelled wider than in reality. See figure B.4.

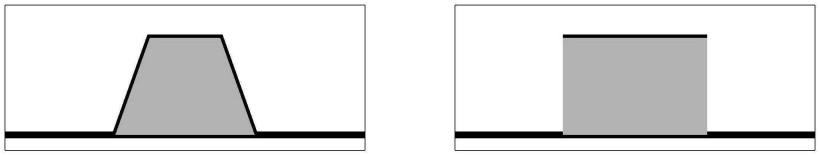

Figure B.4: The stringer as intended, in comparison to its model representation.

An analysis of the moment of inertia of the top-hat stringer, in comparison to its modelled sandwich equivalent using typical values from the optimization procedure showed that both values are equal for a web-to-panel angle of about 69°, which is a very realistic value.

B.2.2 Optimization procedure

A combination of a local optimiser and an Evolutionary Algorithm (EA) is developed in Matlab to optimise the design. In this case, the optimisation constitute finding the optimal stinger placement for a maximum buckling

load. The procedure is run for given material lay-up, rib placement and stringer geometry. Two vectors describe a design, consisting of the width of consecutive subplates between the stringers, starting from the edge of the sparbox. One vector is defined for the leading edge and one for the trailing edge panel (see Figure B.5).

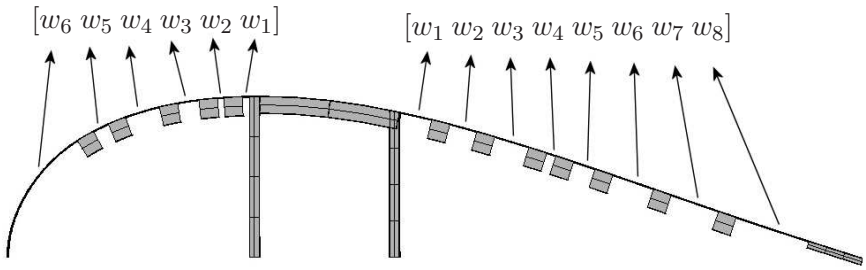

Figure B.5: The stringer as intended, in comparison to its model representation.

A code is written in Matlab which uses the subpanel width values as input and produces an Ansys input file, containing geometrical modelling, meshing, solution and post processing commands. The post processing includes the extraction of the first three CBLs and the location of the occurring buckling in the form of the maximum displacement point of the buckling mode. This data is written to a series of text files which are read by the Matlab script and used to calculate the next generation of designs based on the old ones. The whole optimization procedure can be seen in Figure B.6.

Each optimisation run is based on a certain average subpanel width. Subsequently, the number of stringers that fits on a panel is calculated and a series of random widths with values between 0 and two times the average subpanel width is generated for the front and aft panel. Twenty so called individuals (designs) of these quasi-randomly formed set of vectors form the starting population. For all consecutive generations the population size is twelve. The panels are created in Ansys by placing alternating stringer and panel sections from the sparbox to the trailing and leading edges for respectively the aft and front panel. The number of stringers n is calculated at the start from the average subpanel width and during the optimization procedure it is kept fixed. Fewer stingers are possible if the sum of the stinger spacings until the n^{th} stinger is larger than the panel width and the last stringer is dropped because the end of the panel has been reached when constructing the model. However, typically this will constitute a non-optimal load carrying capability of the panel and the design will not survive.

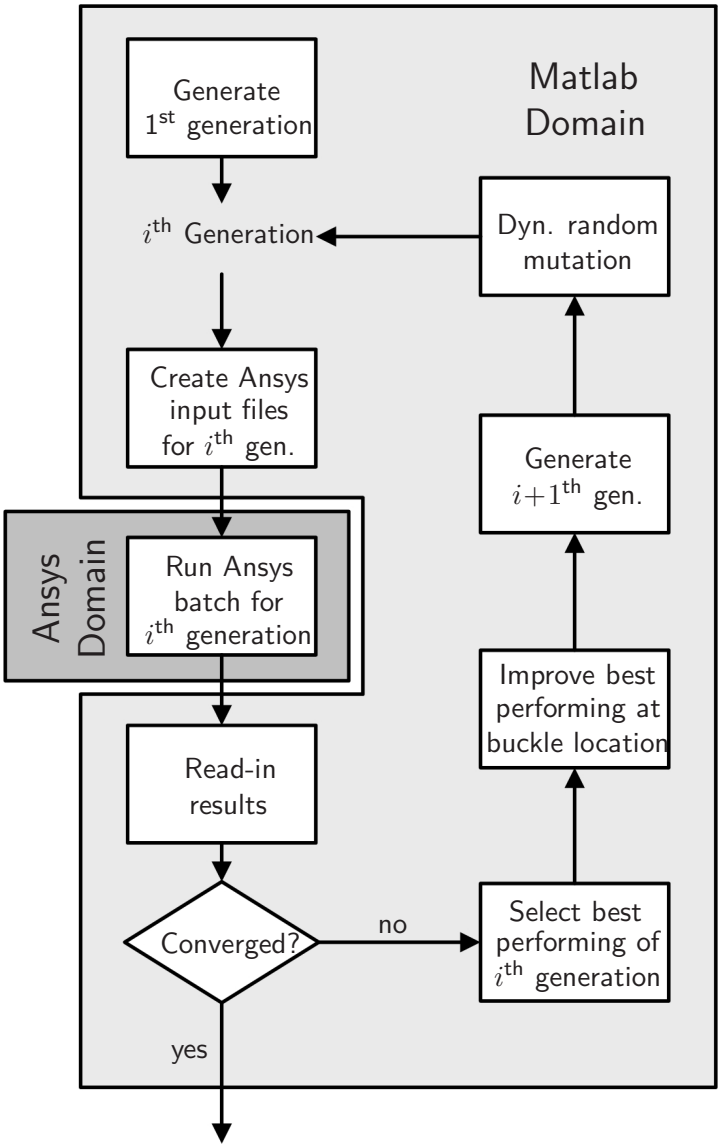

Figure B.6: Optimisation proceedure

After each analysis round, the solution results of the previous generation i are read in. One of the conclusions drawn early in the optimisation process is that high stringers are needed to attain the required buckling load. Since the skin is relatively thin, the optimisation procedure actually constitutes finding a stringer distribution at which no local buckling occurs with the first buckling mode. Therefore, the parent population of each generation

is slightly altered by a local, targeted mutation before executing the EA. The alteration concerns the narrowing of the subpanel width to 90% of its original value at the location of the maximum displacement of the buckling mode, at expense of the other others. See Figure B.7.

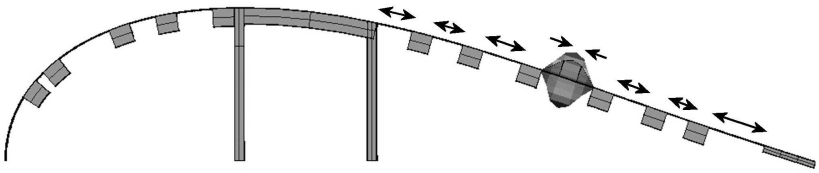

Figure B.7: Local, targeted modification of individuals after analysis.

Subsequently, the EA part of the optimisation procedure is executed. It comprises of parent selection, crossover, mutation and a replacement step [8]. The parent selection is executed through rank selection. In this step, the members of the i^{th} generation are ranked according to their fitness (CBL). The chance for an individual of being selected as parent decreases quadratically with its rank: the top performing individual has a m^2 as high chance of being selected as the m^{th}-ranking individual, where m is the generation size. A multiple point crossover scheme is used to recombine the parent vectors. Both are cut in three pieces at random locations and the child individual is created. In addition, a random mutation is executed. With a mutation a certain element of the vector is randomly changed into a number between 0 and two times the average subpanel width, as done with forming of the first generation. The probability of mutation depends on the spread of fitness in the generation. If the spread is low, it can be assumed that the optimisation is reaching (premature) convergence and the mutation rate is increased.

For replacement, the so called 'golden cage principle' is adopted. With this, the top performing individual is directly cloned to the next generation but all others are replaced. The best performing individual *is* subjected to the local improvement step, but recombination and random mutation is not performed.

The aim of this combination of a local optimisation procedure with the best individual in a 'golden cage' and a global optimisation scheme based on the EA is to improve the design in a targeted way and at the same time explore the global design space for solutions that might perform better - or constitute a global optimum at best. When the procedure finds a individual that performs better than the previous top performing, then it is placed in

the golden cage. In this way, a high degree of mutation can be imposed on the remainder of the population without loosing well performing design features and at the same time still improving that design.

Here, the procedure is stopped after sixteen generations. Convergence criteria could be added, but to fully explore the design space the iteration was left running for sixteen generations. Typically, between six and ten generations are needed to attain a performance that is higher than that of the reference design.

The optimisation is performed solely on the position of the stringers and a further comparison between the different runs on other parameters, such as amount of stringers and ribs and the feasibility of manufacturing is made afterwards.

B.2.3 Results

The optimisation procedure above was run for different stringer geometries and ribspacings. The different variations can be seen in Table B.2.

Geometry Parameter	Tested Values
Average sub -panel width	18, 21 & 25cm
Stringer height	8 & 10cm
Stringer width	10 & 12cm
Rib spacing	3 & 4m

Table B.2: Parameter variation in optimising the stringer position.

This results in 24 design variations which are all iterated over 16 generations. The result overview is presented in Figure B.8. On the left the results for 3m rib spacing and on the right for 4m. On the x-axis the average subpanel width is plotted and the results for different stringer geometries are plotted as different marker shapes. The reference CBL for the sandwich panel - 1140 - is plotted as dashed line.

One would expect the average sub-plate width to be the same for equal stringer width. However, when a stringer is dropped because of large subplate widths, the average subplate width will also change. Many designs attain the required load. Although the parameter variation is limited, already it can be seen that some designs converge towards a desired value very quickly, or do not attain the required buckling load at all. In general, a successful design has closely packed stringers near the sparbox, where the compression loads are maximum. As expected, the designs with 3m

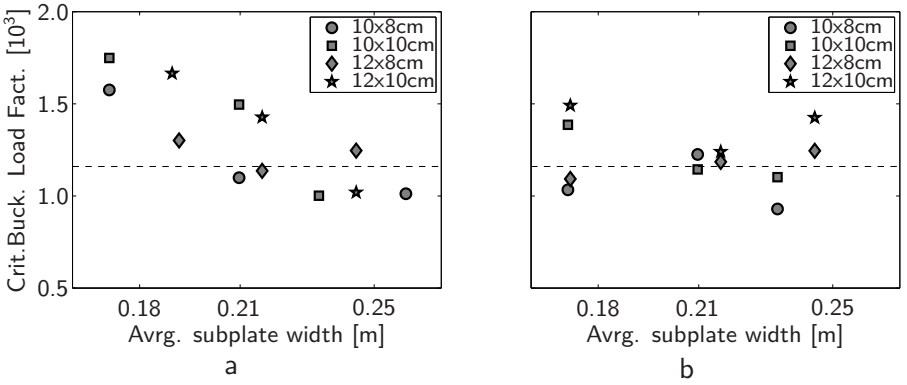

Figure B.8: Results of the different optimization studies for different stringer geometries and stringer spacings. The figure a) displays the result for a rib spacing of 3m and b) for 4m spacing.

rib spacing show higher CBL factors. However, the 4m ribspacing designs do not show a clear decrease of CBL with increasing subpanel width. This is to be expected because a larger subpanel width means that local buckling occurs at lower loads and that the resistance against global buckling is also smaller because the total added second moment of inertia (for a given stringer dimenstion) is smaller. On the other hand, the targeted mutation part of the algorithm tries to suppress local buckling modes. In principle, after many iterations, this leads to a design with a global buckling mode. Such a buckling mode will constitute a 'optimal' design for a relative small rib spacing and large subplate widths, because in this case the global buckling load is relatively high, if it can be found. However, for large rib spacings, the global buckling load factor might be low, and thus the algorithm is searching for a non-optimal design. This illustrated with the 4m rib spacing designs, with a large number of stringers, the highest CBL is found after about 10 generations, but this does not constitute a global buckling load. The designs that do show global buckling modes, have lower CBLs.

As can be seen in Figure B.8, there are several designs that meet the reference design load. A sub-selection is made, based on the following criteria:

1. The CBL of the design should exceed that of the reference buckling load, preferably with some margin.
2. The design should have as little as possible stringers.
3. Both 3m and 4m ribspacing designs are selected
4. Preferably, the design should have a well spread stringer distribution, to account for other load cases than the flapwise bending load case

that is considered here.

The resulting pre-selection with more details on the design, can be seen in Table B.3 Naturally, designs with bigger or a larger amount stringers

	Sub-plate width (cm)	Stringer width (cm)	Stringer height (cm)	Critical Buckling Factor	No. stringers
3m rib spacing	25	12	8	1246	10
	21	12	10	1427	11
	21	10	10	1496	12
4m rib spacing	25	12	8	1245	10
	25	12	10	1425	10

Table B.3: Result of the optimising procedure for 3m and 4m rib spacing

perform better. If a selection is made of designs that have a CBL which is equal to, or larger than the reference value, then a trade-off between closely packed ribs, large stringers or many stringers can be made. Of course, a thorough economic assessment will have to be made as well. Here the focus was on the technical feasibility of the concept, by studying what it takes in terms of ribs and stringers to attain the desired compressive load carrying capability.

B.3 Discussion on the modelling method

In this part of this appendix the modelling method as used in the optimisation procedure will be discussed because there are some critical remarks that can be made with the way that the panel is represented by single elements with a thick sandwich lay-up formulation for the stringers and by adjoining elements with a thin shell lay-up for the sub-plates in between the stringer. This modelling method will be referred to as the implicit model because the stringer's geometry is not modelled explicitly, but implicitly with the material formulation.

The implicit method is computationally more efficient because it requires less nodes, but the main issue with it, is that in local buckling the stringer normally poses elastic boundary conditions for the plate between the stringers because the stringer itself can deform in transverse direction [9]. This is not accurately captured when modelling the stringer as one shell element. In this section the implication for the analysis will be discussed by

comparing the the implicit modelling method to a more detailed FE model, where the geometry and laminate of the stringers are modelled *explicitly*.

The comparison is made on a panel that was also used in experiments that will be discussed in the final section of this appendix. The panel is a 0.96m high and 0.6m wide panel (a/b=1.6) with five top-hat stringers on it. In FEA only the top half of the panel is modelled and symmetry boundary conditions are applied along the bottom side of the model (at the horizontal plane of symmetry of the panel). Simply supported boundary conditions are applied along all edges of the panel. The models' details are discussed in the next two paragraphs.

B.3.1 Implicit stringer model

When modelling a laminate which has a finite thickness, with shell elements which have no thickness, an offset can be created between the center of the laminate and the shell surface. Here, the surface of the laminate is set to coincide with the shell elements to assure that the layers which form the plate are in one plane, and that the plies that represent the stringers are at the right distance from the plate. See Figure B.9.

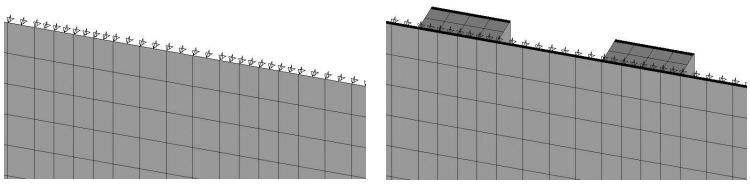

Figure B.9: Modelling of the stringers using a sandwich lay-up formulation. a) Elements with simply supported boundary conditions, b) the same elements, but with the material thicknesses plotted.

When the compressive load is applied, internally the loads are distributed over all layers. Thus, the stringers and plate receive the same loading in terms of stresses because their respective lay-ups are the same and the resultant of the stresses is on the neutral axis of the panel. In determining the nodal forces, this is taken into account because the element that form the stringers should take up more loading. The simply supported boundary conditions do pose an issue. Due to the method of modelling, the boundary conditions can only be imposed on the nodes, which coincide with the surface of the plate and therefore, the point of rotation is not on the neutral axis.

B.3.2 Explicit stringer model

For comparison, a similar FE model is set up in which the geometry and the laminate of the stringers is explicitly modelled. This model obviously is computationally more expensive because more nodes and elements are created to represent the stringers. To assure comparability with the implicitly modelled stingers, the simply supported boundary conditions are applied to the plate and the same offset between the laminate and shell surface is implemented. Therefore, both FE models are comparable, but the position of the point of rotation at the top of the models differs from what was implemented in experiments, in which the axis of rotation and the plane through which the loads are applied cannot be separated.

B.3.3 Materials and laminate lay-up

With both models the ply properties are derived from an experimental material study, which was described in Section B.1.1. Using those properties, a laminate is chosen which leads to a panel that will collapse under global buckling instead of local buckling or compression failure of the laminate itself. The chosen lay-up is [0,45,-45,0,-45,0,45,0,45,-45,0], which is a balanced laminate.

B.3.4 Results

Results of the FEA

The results for the first buckling mode of the FE analyses can be seen in Figure B.10, both for the explicit stringer model and the model where the stringers are modelled implicitely as part of a sandwich layup. For clarity, the implicit stringer model is depicted with the material thickness of the elements shown. As can be seen, the results are very similar, both in terms of buckling mode and buckling load. The same holds for the second mode, which constitutes two half-waves in transversal direction. However, the interesting comparison is in the local buckling load, which firstly occur as third mode with both modelling methods. After all, the optimisation algorithm of Appendix B is used to find the global buckling mode by suppressing the local ones. The results for the first mode in which local buckling occurs, can be seen in Figure B.11 below. As can be seen, both the location and load at which local buckling occurs, is different. On the other hand, This might also be related to the way that load and boundary conditions are applied to the respective models. Furthermore, with the implicit stringer modelling less GFRP material is modelled. Consequently,

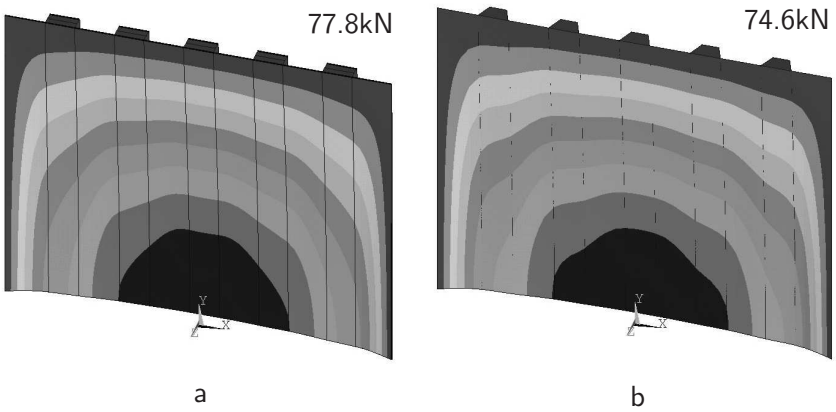

Figure B.10: First buckling modes of the panel with which the stringers are modelled in an implicit way (a) and explicit (b) way. Grey values are an indication of the out-of-plane displacement.

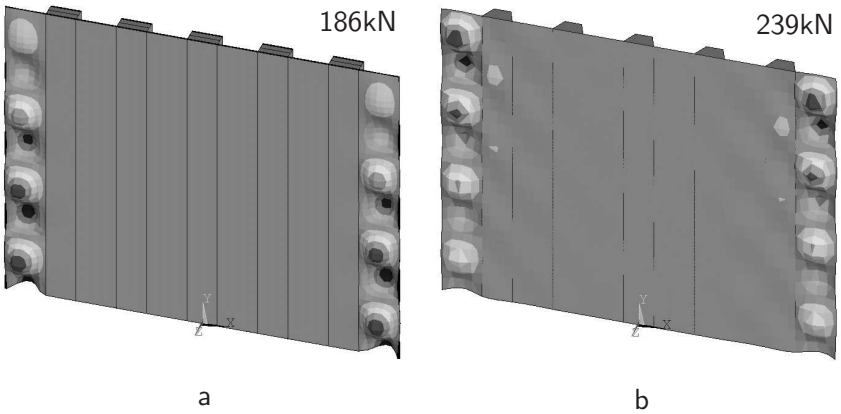

Figure B.11: Third buckling modes (first local one) of the panel with which the stringers are modelled in an implicit way (a) and explicit (b) way. Grey values are an indication of the out-of-plane displacement.

the loading on the plate part of the panel becomes higher for a given overall compressive load.

Mesh refinement study

To investigate the results of the local buckling load for different element size, a mesh sensitivity study is made. After all, besides the boundary conditions that the stringers pose for the sub-plate, the amount of elements that are used to model the subplate may also have a large influence of the

model. Using only few elements, leads to a high apparent stiffness of the subplate in bending. Therefore, the panel that is discussed here is analysed with different element sizes. In Table B.4 below, the result of the study on the model with the implicit stringer formulation can be seen.

Set element size [m]	Number of elements across sub-plate [-]	Buckling load first local mode [kN]
0.005	13	185
0.01	7	185
0.02	4	185
0.03	3	190
0.04	2	210

Table B.4: Results of the mesh refinement study

In the model of Appendix B has two elements across the sub-panel, in between the stringers. This results in a somewhat overpredicted local buckling load.

B.4 Experimental results

As mentioned before, the panel that was modelled in the FE analysis was also used in compression load experiments. Here a short overview of these experiments is presented for comparison with the FE analysis and to draw some conclusions about the performance of top-hat stiffened panels under compression - up to failure.

B.4.1 Experimental set-up

The compression test is performed on a manually controlled, 600kN MTS compression testing machine. The plate was mounted in a jig that posed simply supported boundary conditions. On the longitudinal edges, the plate is clamped between knife shaped edges. The plate is free to rotated between these edges. On the top and bottom sides where the load is applied, more precautions are taken. The load is introduced through bearings as depicted in figure B.12.

The bearing consist of a cylindrical rod placed between two plates in a V-shaped groove. The plate on which the panel is placed, is dissected in 10cm wide sections. During compression of a simply supported panel, a continuous rotation along the edge of the plate will occur. This enables a

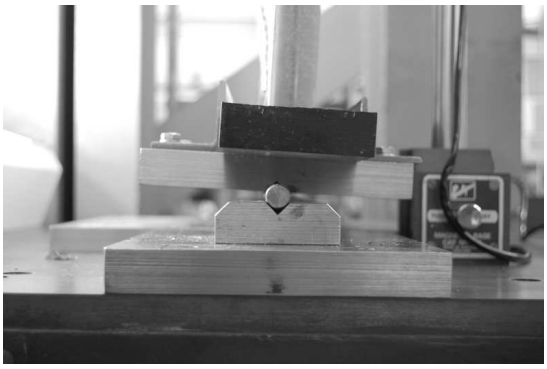

Figure B.12: Bearing set-up, seen from the side, after the panel has buckled. The center of the bearing is set at an offset of about 7mm from the surface of the plate, trough the neutral axis of the whole panel.

discretely varying rotation at the panel's edge. In order to prevent discontinuities in displacements in the panel at the transition from one support plate to the other, a section of several centimeters deep is made into the plate. This section also cuts though the panel's foot. The panel is placed such that the axis of the bearing lies in the predicted neutral plane. Thus, a panel is obtained with an effective length of 960 mm with simply supported edges. See Figure B.13 for a picture of the set-up.

At the bottom and top of the panel the cuts can be seen that allow for (piece wise) continuoes rotation of the edge of the panel. On the sides are the frames that prevent the out-of-plane displacement of the panel, while not restricting the rotation at the edges.

During the test several parameters are recorded. First of all displacement and force of the compression machine. Furthermore, strain is monitored along the transversal symmetry line at locations between the stringers. Strain gages are adhered to both sides of the panel and the deformation of a large part of the panel is monitored by the stereo Digital Image Correlation (DIC) system Vic3D (Limess Messtechnik and Software GmbH, Pforzheim, Germany). Through this system both the in-plane strain field and the out-of-plane displacement of a large surface can be recorded by tracking the displacement of an applied speckle pattern with two digital cameras. Finally, the out of plane displacement is monitored at the center of the panel by a LVDT displacement transducer. The installed LVDT can be seen on the stringer side in Figure B.13a.

a b

Figure B.13: Panel compression test set-up. a) Stringer side of the panel. b) Flat side of the panel with applied paint spatter for pixel tracking for the stereography equipment. The square is added digitally to the photo and it indicates the area of the panel that is in the field of view of the stereography system. The system was not able to observe the whole panel.

B.4.2 Elastic buckling load

The buckling load from the panel experiments was not conclusive. Only two panels were tested. In both cases the compression load increased linearly until the panel suddenly snapped into its buckled shape. This event could be predicted by monitoring the displacement at the centre of the panel, which was done by means of an LVDT. Just before buckling, the increase out-of-plane deflection with a certain load step would start to grow very rapidly. This displacement was in the order of magnitude of millimeters. After the buckling event, the compressive load on the panel would drop and when released would stay rather constant. Therefore, it was decided to derive the critical buckling load from the unloading curve and the critical buckling load was then derived from the intersection between the tangents at the start and the end of unloading curves. See Figure B.14. As can be

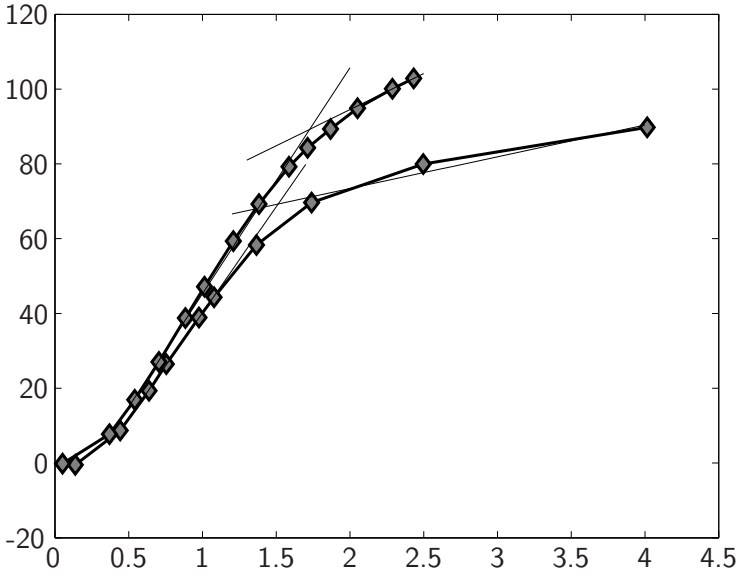

Figure B.14: Calculation of the buckling load from the unloading of the panel

seen, they are in the same range as the FE model predicts.

B.4.3 Loading until failure

Panel 2 was subsequently tested up to failure. Below, in figure B.15, the compression curve (load versus displacement) can be seen. The letter A to E indicate significant events which are further explained using the strain gage and camera data. Up to buckling, the panel showed the same linear behavior as before. The buckling event itself can be seen as an instantaneous drop in load at point A in Figure B.15 and Figure B.16 as a sudden, large out-of-plane displacement. Then, after buckling, the panel was further compressed. The load hardly increased with increasing compression. The first observable damage was a delamination between the stringer foot and the plate at the sides of the panel. This delamination slowly grew until first the first and then the second stringer foot separated and the panel bulged out. This can be seen in Figure B.17. The onset is hard to see in the compression curve because it hardly has an effect on the stiffness and load carrying capability of the panel. At point C the plate failed, indicated by a small drop in load. The crack can be observed as noisy spikes in Figure B.18 because the camera lost track of the pixel displacement.
Finally, after the panel was only slightly compressed further, the final failure of the material occured (event D and E in figure B.15) in two steps across

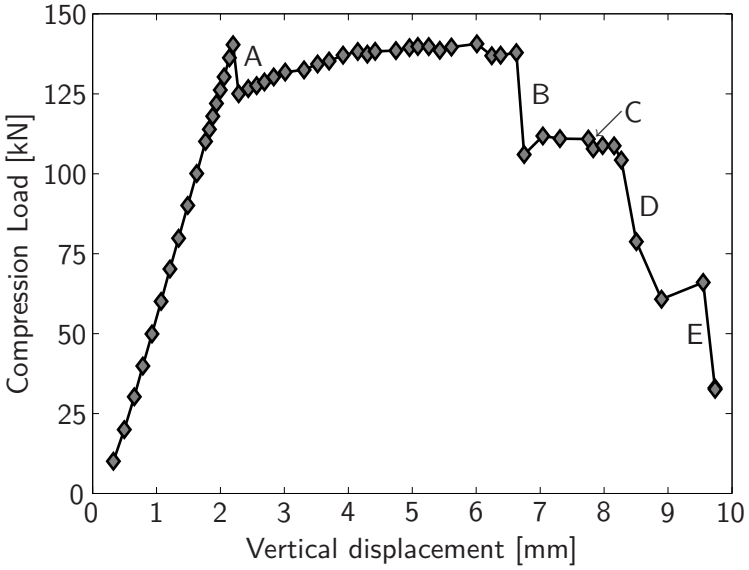

Figure B.15: Compression curve of panel 2 up to failure

the width of the plate, growing from the side of the separated stringer. Event D can also be seen in figure B.19.

B.5 Concluding remarks

B.5.1 Discussion of the modelling method

The conclusion with respect to the method of modelling is that the implicit stringer formulation predicts a lower local buckling load then when the stringers would be modelled explicitly. This constitutes a worse-case scenario for the optimisation procedure since it tries to suppress the local modes in favor of global ones. But again: a factor in the results may be the method of load introduction, which is inherent to the respective ways of modelling. By controlling the offset between the laminate and the shell surface, as good comparable conditions as possible were created.

A more important factor may be the stress in the sub-panel as a result of a given panel load. When the panel is modelled with the implicit stringer formulation, the amount of GRFP that is modelled, is smaller than in reality and than in the explicit stringer model. Thus, the stress on the plate for a given load is higher and the sub-plate will buckle at lower overall loads. This conclusion does not hold for all panel designs, because it is dependent on the height-to-width ratio of the stringer. Here, in all cases - in the optimisation

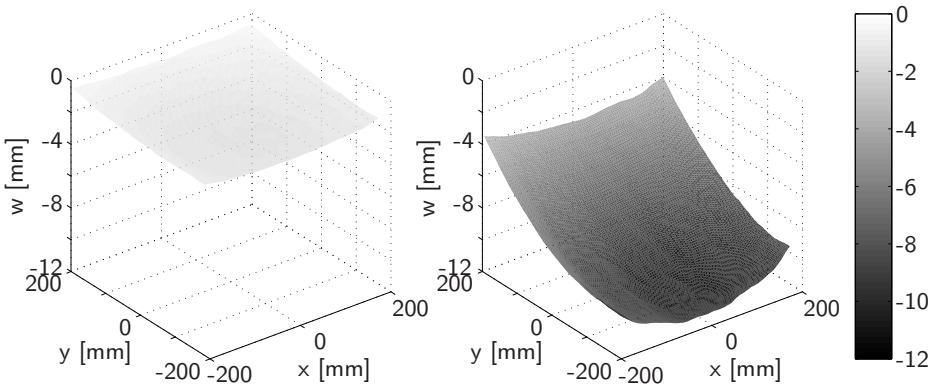

Figure B.16: Out-of-plane displacement just before and after buckling at point A in figure B.15

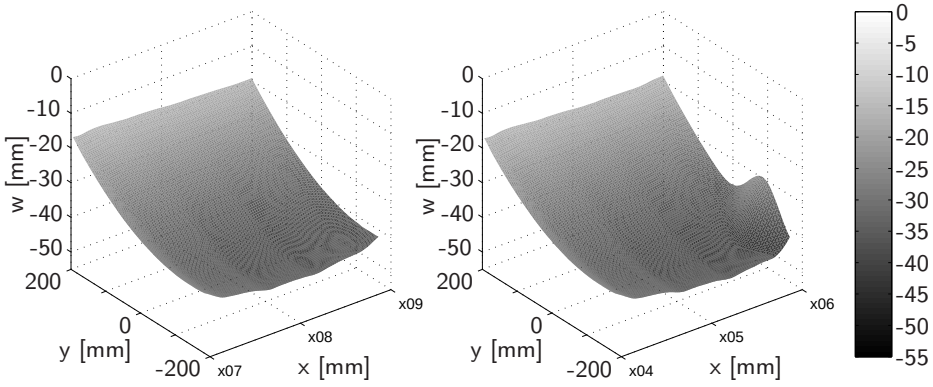

Figure B.17: Out-of-plane displacement just before and after first stinger foot separation at point B in figure B.15

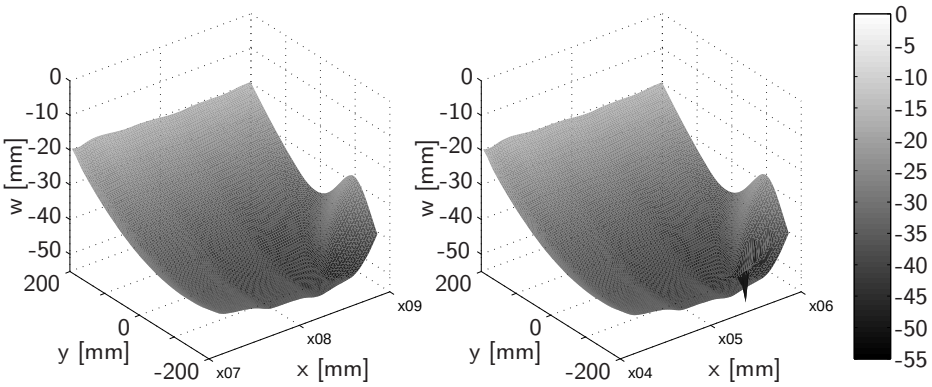

Figure B.18: Out-of-plane displacement just before fracture at the location of the stringer separation at point C in figure B.15

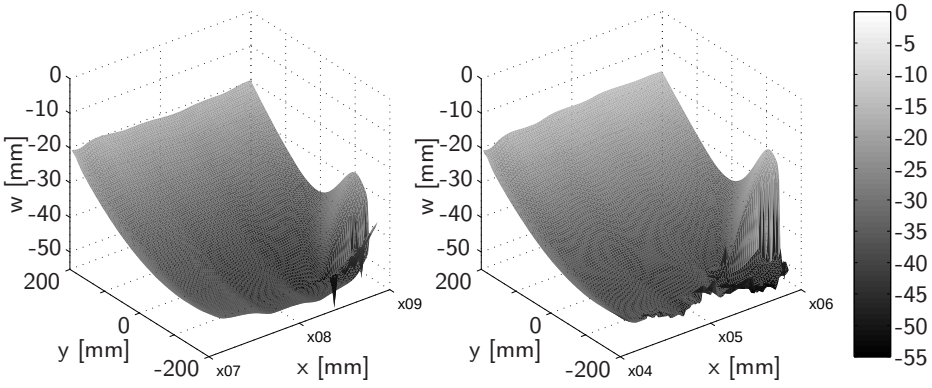

Figure B.19: Out-of-plane displacement just before propagation of the crack over the width of the plate (D in figure B.15)

procedure as well as the modelling method verification - a ratio of $\sim$1 was implemented.

B.5.2 Conclusions on the application of top-hat stiffened panels

There are several conclusions on the application of top-hat stringers to be drawn from the experiments. In the first part of this appendix it was already shown that through the use of top-hat stringers a similar buckling load capacity as with sandwich panels is attainable. However, based on the experimental results on an uncurved panel, it can also be concluded that the post-buckling behaviour of the panel is very good. The panel does not fail, even when the compressive load on the panel is increased. Moreover, the final failure of the panel does not occur suddenly, but the stringers fail one by one, incorporating some damage tolerance. With regard to this tolerance it is important to stress that with this panel the stringers were all applied independently; the material that formed the stringers was not one continuous drape, but separate strips of UD-fabric were draped over the trapezium foam pieces. If a continuous corrugated stiffening structure was applied, the peeling that caused the stringers to separate from the plate, which led to the final collapse, would have progressed across the stringers more easily.

References

[1] C. Kassapoglou. Simultaneous cost and weight minimization of composite-stiffened panels under compression and shear. *Composites Part A: Applied Science and Manufacturing*, 28A:419–435, 1997.

[2] Ö. Eksik, R.A. Shenoi S.S.J. Moy, and H.K. Jeong. Experiments on top-hat stiffened panels of fiber reinforced plastic boat structures. *Marine Technology*, 44:1–15, 2007.

[3] N. Uddin and A.M. Abro. Design and manufacturing of low cost thermoplastic composite bridge superstructures. *Engineering Structures*, 30: 1386–1395, 2008.

[4] R. Nijssen. WMC5MW laminate lay-out of reference blade for WP3. Technical report, Knowledge Centre Wind turbine Materials and Constructions, 2007. EC FP6 UpWind program document.

[5] Z. Hashin and B.W. Rosen. The elastic moduli of fiber-reinforced materials. *Journal of Applied Mechanics*, 31:223–232, 1964.

[6] ASTM d3039-07 - standard test method for tensile properties of polymer matrix composite materials.

[7] E. Lund and L.S. Johansen. *Mechanical Response of Composites*, chapter 12, On Buckling Optimization of a Wind Turbine Blade, pages 243–260. Springer Netherlands, 2008.

[8] M. Affenzeller, S. Winkler, S. Wagner, and A. Beham. *Genetic Algorithms and Genetic Programming Modern Concepts and Practical Applications*. Chapman and Hall/CRC, 2009.

[9] C. Mittelstedt and M. Beerhorst. Closed-form buckling analysis of compressively loaded composite plates braced by Omega-stringers. *Composite Structures*, 88:424–435, 2009.

List of publications

Journal publications

A.W. Hulskamp, J.W. van Wingerden, T. Barlas, H. Champliaud, G.A.M. van Kuik, H.E.N. Bersee and M. Verhaegen, *'Design of a scaled wind turbine with a smart rotor for dynamic load control experiments'*, Wind Energy, 2010, DOI: 10.1002/we.424

A.W. Hulskamp, A. Lara and H.E.N. Bersee, *'a high rate SMA actuator for aerodynamic load control on wind turbines'*, Journal of Intelligent Material Systems and Structures, accepted with minor revisions

J.W. van Wingerden, A.W. Hulskamp, T. Barlas, B. Marrant and G.A.M. van Kuik, D.-P. Molenaar and M. Verhaegen, *'on the proof of concept of a 'smart' wind turbine rotor blade for load alleviation'*, Wind Energy, 11, p265-280, 2008

J.W. van Wingerden, A. Hulskamp, T. Barlas, I. Houtzager, H. Bersee, G. Kuik, and M. Verhaegen, *'two-degree-of-freedom active vibration control of a prototyped 'smart' rotor'*, IEEE Transactions on Control Systems Technology, 2010, DOI: 10.1109/TCST.2010.2051810

Book chapter

A.W. Hulskamp and H.E.N. Bersee, *'Implementation of the 'smart' rotor concept'*, in Wind Power Generation and Wind Turbine Design, edited by Wei Tong, WIT Press, 2010

Patent

A.W. Hulskamp and H.E.N. Bersee, 09-027 activatable device

Conference proceedings

A.W. Hulskamp, *'Smart rotor and wind turbine blades - material and structures'*, 50th Topical Expert Meeting on the Application of Smart Structures for Large Wind Turbine Rotor Blades, December 2006, Delft, The Netherlands

A.W. Hulskamp, A.Beukers, H.E.N. Bersee, J.W. van Wingerden and T. Barlas, *'Design of a wind tunnel scale model of an adaptive wind turbine blade for active aerodynamic load control experiments'*, 16th International Conference on Composite Materials, July 2007, Kyoto, Japan

T. Barlas, J.W. van Wingerden, A.W. Hulskamp, and G.A.M. van Kuik, 'closed-loop control wind tunnel tests on an adaptive wind turbine blade for load reduction', 46th AIAA Aerospace Sciences Meeting and Exhibit, January 2008, Reno, NV, USA

A.W. Hulskamp, *'Smart rotor and wind turbine blades - material and structures'*, 56th Topical Expert Meeting on the Application of Smart Structures for Large Wind Turbine Rotor Blades, May 2008, Albuquerque, NM, USA

A.W. Hulskamp, H. Champliaud, H.E.N. Bersee, *Design and analysis of a scaled smart rotor blade for wind turbine load control*, 17th International Conference on Composite Materials, July 2009, Edinburgh, Scotland, UK

P. Wiwattananon, T.J. Ahmed, A.W. Hulskamp and H.E.N. Bersee, *'Investigation of a thermoplastic alternative for LiPCA'*, 20th International Conference on Adaptive Structures and Technologies, October 2009, Hong Kong, China

A.W. Hulskamp and H.E.N. Bersee, *'A shape memory alloy activated morphing surface for aerodynamic load control on wind turbine rotor blades'*, 20th International Conference on Adaptive Structures and Technologies, October 2009, Hong Kong, China

A.W. Hulskamp, H. Champliaud, J.W. van Wingerden, T. Barlas, H.E.N. Bersee, G.A.M. van Kuik and M. Verhaegen, *'Smart dynamic rotor control: Part 1, Design of a smart rotor'*, The Science of making torque from wind conference, June 2010, Herakleion, Crete, Greece

T. Barlas, J.W. van Wingerden, T. Hulskamp, G. van Kuik, M. Verhaegen and H. Bersee, *'Smart dynamic rotor control: Part 2, aeroelastic analysis'*, The Science of making torque from wind conference, June 2010, Herakleion, Crete, Greece

J.W. van Wingerden, A.W. Hulskamp, T. Barlas, I. Houtzager, H.E.N. Bersee, G.A.M. van Kuik and M. Verhaegen, *'Smart dynamic rotor control: Part 3, advanced controller design'*, The Science of making torque from wind conference, June 2010, Herakleion, Crete, Greece

Acknowledgments

"Hoe recht je staat
Heeft met zwaarte niets te maken
Hoogstens met de wind"
Uit 'Omarm', *van Bløf*

Het schrijven van een proefschrift, en het uitvoeren van het onderzoek wat eraan ten grondslag ligt, gaat niet altijd zonder slag of stoot. Bij mij niet in ieder geval. Ik heb de tegenslagen die ik gehad heb en de barrieres waar ik tegenop liep, echter nooit als een zware last ervaren, maar meer als een tegenwind; iets wat ooit zal moeten gaan liggen of iets wat je mee krijgt op het moment dat je een afslag kunt nemen. Dit was echter niet het geval geweest als er niet een aantal mensen in mijn omgeving waren aan wie ik veel steun kon ontlenen - binnen en buiten de faculteit.

First of all, I would like to thank professor Adriaan Beukers for giving me the opportunity to work in his group. Also many thanks to my colleagues of DPCS. Kjelt, Patricia, Darko, Giovanni, Witchie, Tahira, Natcha, Ab, Safqat, Didier, Nassira, Carlos, Lisette, Sotiris and Otto. Thank you all for the great times, in and outside the faculty. Especially the conferences in Edinburgh and in the Far East were definitely highlights for me over the last five years, not only from an academic point of view, but also because of the great times we had together. A special thanks to Irene, Julie and Jordy: letting me and my students getting involved your research really enriched this work and I enjoyed every bit of it. And to Nat and Adrian: it was a pleasure working on the smart-stuff together. Harald: thank you for keeping me on track the past five years. You sometimes called me a TGV hurtling ahead, but I could have easily derailed if it wasn't for your guidance. On the other hand I'm very grateful for the freedom you gave and the confidence you put in me. Also, the work on UpWind and our conversations about the content and the politics of things were always enjoyable and constructive. I'm also very grateful to you, Henri, for all work on blade modelling, as well as the warm welcome in Montreal.

I also want to thank Simon for laying the groundwork for the thermoplastic blade and smart rotor work. Voor de mensen van het Delft Aerospace Structures and Materials Laboratory en Demo; Marianne, Berthil, Bob, Hans, Johan, Ed, Peter, Rob, Herman, Cees, Frans, Serge en natuurlijk 'onze eigen' Sebastiaan en Fred: jullie zijn je gewicht in goud waard voor het *materials and structures* onderzoek op de faculteit, inclusief het mijne. Moreover, this thesis wouldn't have came about without the work of some very bright students. Gijs, Frederic, Nicolas, Roger, Andreas, Amir, Wouter, Ron and Robbe: I hope enjoyed working together as much as I did and thank you for your contribution to the research.

Outside the Vliegtuighal I owe a special 'thanks' to the other people working in the DUWind framework. Michiel, Carlos, Joost, Busra and Gerard: thank you for introducing me to the fascinating world of wind turbine technology and aerodynamics and for your occasional help. But my greatest gratitude must go out to professor Gijs van Kuik and Thanasis, together with Jan-Willem. Gijs: your professoring is an example to the whole academic community and beyond. To Thanasis and Jan-Willem: wind tunnel research is never easy, but I really enjoyed the cooperation and it may be a cliché, but this booklet literally wouldn't have been here to read if it wasn't for you guys. I would also like to acknowledge UpWind for its role. First of all because the research was funded through the project, but also because the interaction with the work package partners, especially Ludek Heller from IT-ASCR, has played an important role in this work.

Maar ook buiten de faculteit en het onderzoek zijn er velen bij wie ik steun vond of stoom af kon blazen, al was het maar door een rondje te fietsen. Dank aan m'n Bestuursgenoten, ook voor de relaxte weekendjes. Marc: het was mooi om nog een tijd in Delft te wonen en werken. De autoritten naar weekendjes waren altijd mooie momenten om het over de leuke en minder leuke kanten van het promotiewerk te hebben. In Delft waren de tijden langs de Schie en op de Bosbaan, met name met Licht2007 en MGL, onvergetelijk. Peter en Eloïne: het was fijn om zo af en toe even over het promotieproces te kunnen hebben, tijdens een wijntje en een bordspel met Martijn en Dorien. Tijmen en Suzanne; bedankt voor jullie hulp, vooral bij het zoeken en vinden van 'iets nieuws' en voor de inburrrgerrríng in Leiden.

Claar, Noor: dank dat ik altijd op jullie kan rekenen, maar ook voor de geregelde kritische noot. Ik hoop stiekem dat jullie trots zijn. Maar mijn allergrootste dank gaat toch uit naar Mylène. Voor je steun, flexibiliteit, voor je vrolijkheid en de knuffels als ik er een nodig had, maar ook voor de relativering. Kortom: dank je dat er de afgelopen vier jaar voor me was. Ik kijk er naar uit om samen met jou en Anna nieuwe avonturen aan te gaan.

About the author

Anton Werner Hulskamp (Teun) was born on the 21st of April, 1980 in Amsterdam. He grew up in Baarn were he obtained his Grammar school diploma from the Baarnsch Lyceum. In 1998 he moved to Enschede to study Mechanical Engineering at the University of Twente. He graduated on fiber reinforced polymers at the chair of Professor Akkerman, doing an internship on the preliminary design of an composite emergency exit hatch at Airbus GmbH in Hamburg, Germany in 2003 and writing his thesis in 2005 on moulded-in holes in composites with woven fiber structures.

In 2006 he started his PhD-research with the Design and Production of Composites group at the Faculty of Aerospace Engineering of the TU Delft, which has resulted in this thesis.

During his study in Enschede, he pursued a semi-professional career in lightweight rowing as a member of the student rowing club Euros, winning several national titles and competing at World Cup regattas. After moving to Delft he continued in the sport as a coach with Proteus-Eretes for several years, while enjoying road cycling himself.

After finishing his PhD dissertation, in January 2011 he joined the Technology team of the Rotating Equipment department of Shell Projects and Technology.